WEAR OF HIGH ALUMINIUM ZINC-BASED ALLOYS IN PLAIN BEARING APPLICATIONS

Rodney Antonio Balanza Erquicia

Doctor of Philosophy

THE UNIVERSITY OF ASTON IN BIRMINGHAM

April 1993

THE UNIVERSITY OF ASTON IN BIRMINGHAM

WEAR OF HIGH ALUMINIUM ZINC-BASED ALLOYS IN PLAIN BEARING APPLICATIONS

Rodney Balanza Erquicia

A thesis submitted for the Degree of Doctor of Philosophy 1993

SUMMARY

Two zinc-based alloys of high aluminium content, Super Cosmal alloy containing 60% Al, 6% Si, 1% Cu, 0.3% Mn and HAZCA alloy containing 60% Al, 8% Si, 2% Cu, 0.06% Mg were produced by sand casting. Foundry characteristics in particular, fluidity, mode of solidification and feeding ability were examined. Metallographic analysis of structures was carried out using optical and scanning electron microscopy and their mechanical properties were determined using standard techniques. Dry wear characteristics were determined using a pin-on-disc test, and boundary-lubricated wear was studied using full bearing tests. Results from casting experiments were evaluated and compared with the behaviour of a standard ZA-27 alloy and those from tribological tests with both ZA-27 alloy and a leaded tin-bronze (SAE 660) under the same testing conditions.

The presence of silicon was beneficial, reducing the temperature range of solidification, improving feeding efficiency and reducing gravity segregation of phases. Use of chills and melt degassing was found necessary to achieve soundness and enhanced mechanical properties. Dry wear tests were performed against a steel counterface for sliding speeds of 0.25, 0.5, 1.0 and 2 m/s and for a range of loads up to 15 kgf. The high aluminium alloys showed wear rates as low as those of ZA-27 at speeds of 0.25 and 0.5 m/s for the whole range of applied loads. ZA-27 performed better at higher speeds. The build up of a surface film on the wearing surface of the test pins was found to be responsible for the mild type of wear of the zinc based alloys. The constitution of the surface film was determined as a complex mixture of aluminium, zinc and iron oxides and metallic elements derived from both sliding materials.

For full bearing tests, bushes were machined from sand cast bars and were tested against a steel shaft in the presence of a light spindle oil as the lubricant. Results showed that all zinc based alloys run-in more rapidly than bronze, and that wear in Super Cosmal and HAZCA alloys after prolonged running were similar to those in ZA-27 bearings and significantly smaller than those of the bronze.

Key Words: High-aluminium zinc alloys, sand casting, dry wear, lubricated wear.

DEDICATION

Dedicada a mi amada esposa Miriam y a Eduardo, Jose Antonio y Gustavo mis queridos hijos

ACKNOWLEDGEMENTS

I am greatly indebted to my Supervisor Dr Sam Murphy, for his continued guidance and encouragement throughout this project.

I wish to thank Dr K. Sawalha for his friendly and active support.

I wish to thank the academic and technical staff of the Mechanical and Electrical Engineering Department of Aston University, for their advice and help. In particular my thanks are due to members of the technical staff: Messrs. D. Farmer, P. Pizer, R. Howell, J. Jeffs, J. Foden, A. Evitts and K. Harrison.

My gratitude to Miss C. Rouse for her co-operation and excellent typing.

Finally, I would like to thank the British Government's Overseas Development Administration for the award, and the Universidad Mayor de San Andres of La Paz - Bolivia for its sponsorship.

LIST OF CONTENTS

LIST OF FIGURES

LIST OF TABLES

CHAPTER 1

INTRODUCTION

Commercial zinc-aluminium alloys can be classified into three families, namely Conventional pressure die casting zinc alloys, ZA alloys and High-aluminium Cosmal alloys.

The pressure die casting zinc alloys have been developed from practically disastrous characteristics to the adequate properties offered at present. The most important alloys today are the Zamak 3 and Zamak 5. They show a unique combination of properties which permits the rapid economic casting of strong, durable and accurate parts.

The family of the ZA alloys were originally developed as sand and gravity casting alloys but it was found later that they could also be used in the pressure die casting process. They have achieved great success in the non-ferrous foundry industry because of many attractive properties such as lower initial cost, good mechanical properties, excellent bearing behaviour and reduced cost in finishing operation. These facts have made them very competitive against traditional foundry alloys like cast irons, copper-based alloys and aluminium-based alloys.

During the mid-1980s, under the trade mark of Cosmal-Z, a new family of zinc-aluminium alloys was developed for the die casting process in search of high strength and high damping capacity materials. Apart from those qualities, others like good fluidity and castability, good creep resistance and high hardness were also reported. There is no information available about the use of these alloys as gravity castings.

It is remarkable the considerable increase in the use of zinc-aluminium alloy as plain bearing materials in recent years. Particularly the ZA-27 alloy has been demonstrated to perform exceptionally well under high load-low speed conditions. Features such as high mechanical properties, high resistance to wear and seizure as well as its ease of fabrication, excellent machinability and low cost have made the alloy a potential substitute for conventional materials.

Among others, resistance to wear and seizure are important requirements for plain bearing materials because in practical situations, some direct contact between the journal and bearing surfaces is unavoidable. Bearings which normally work at hydrodynamic lubrication regime, undergo metal to metal interaction only during short periods of engine start up or during emergency situations of lubricant starvation. Meanwhile, lubricated journal bearings which

work under high load-low speed conditions have to survive more or less extended periods of solid-to-solid contact.

Many pieces of heavy duty equipment such as mechanical presses, ore crushers, pellitizers, road machinery, water turbines, locomotives, etc., incorporate journal bearings that run under boundary lubrication conditions therefore tribological properties are critical.

Based on the successful experience of zinc-aluminium alloys from the zinc-rich side of the Zn-Al system as bearing materials, there have been a number of preliminary works, particularly at Aston University, devoted to investigate the wear characteristics of other groups of alloys within the Zn-Al system. Monotectoid zinc-aluminium alloys with additions of silicon and copper offered the possibility of improved wear behaviour relative to the established alloys and their more traditional competitors.

With the present work it is intended to extend the research programme on wear resistant zinc-aluminium alloys to alloys of higher aluminium contents. For this purpose two high aluminium zinc-based alloys are proposed as testing materials; the Super Cosmal alloy containing 60% Al, 6% Si, 1% Cu, 0.3% Mn and an experimental alloy containing 60% Al, 8% Si, 2% Cu, 0.06% Mg, named as HAZCA alloy.

In the experimental HAZCA alloy silicon is added to reduce the melting temperature and increase fluidity, copper to strengthen the matrix and magnesium to reduce tendency to intergranular corrosion.

The experimental programme comprised of the following steps:

1. Examination of the casting behaviour of the alloy when cast in sand moulds.
2. Examination of the metallurgical structure of the alloys.
3. Determination of the mechanical properties of the alloys.
4. Examination of the wear resistance of the alloy in unlubricated sliding conditions.
5. Examination of the bearing characteristics of the alloys under boundary conditions of lubrication.

CHAPTER 2

SAND CASTING OF HIGH ALUMINIUM ZINC-BASED ALLOYS

2.1 LITERATURE REVIEW

2.1.1 Introduction

Zinc alloys are used extensively in both gravity and pressure die castings. When used as general casting alloys, zinc alloys can be cast using such processes as high pressure die casting, low pressure die casting, sand casting, permanent mould casting (iron, graphite and plaster moulds), spin casting, investment (lost wax) casting, continuous or semi-continuous casting and centrifugal casting. New processes involve semi-solid castings and squeeze castings [1].

Pressure Die Castings

Zinc alloys have been used for die casting for over 60 years. Until recently, all zinc alloys were based on a hypoeutectic composition but not long ago a family of hypereutectic zinc-aluminium alloys, originally designed as gravity casting alloys, have become widely used as die casting alloys. They possess higher strength than hypoeutectic zinc alloys. Very recently new high damping capacity zinc-aluminium alloys of high aluminium content were developed for die casting processes. Chemical compositions of the alloys mentioned are included in Table 1.

Zinc alloys have low melting points, require relatively low heat input, do not require fluxing or protective atmospheres, and are non-polluting. Because of their high fluidity, zinc alloys can be cast in much thinner walls than other die casting alloys and they can be die cast to tighter dimensional tolerances. The rapid chilling rate inherent in zinc die castings results in minor property and dimensional changes with time. It should be noted that the strength performance of zinc alloys drops significantly with increase in temperature. At 100°C tensile and yield strengths are typically 65 to 75% of those at room temperature, and creep strength is similarly reduced.

Table 1. Nominal Compositions of zinc-aluminium foundry and die casting alloys

	Additions %						Impurities %			
Alloy Common Designation	**Al**	**Cu**	**Mg**	**Si**	**Mn**	**Zn**	**Fe max**	**Pb max**	**Cd max**	**Sn max**
ZAMAK 3	3.5-4.3	0.25	0.02-0.05	-	-	Bal	0.100	0.005	0.004	0.003
ZAMAK 5	3.5-4.3	0.75-1.25	0.03-0.08	-	-	Bal	0.100	0.005	0.040	0.003
ZA 8	8.0-8.8	0.8-1.3	0.015-0.030	-	-	Bal	0.075	0.006	0.006	0.003
ZA 12	10.5-11.5	0.5-1.2	0.015-0.035	-	-	Bal	0.075	0.006	0.006	0.003
ZA 27	25.0-28.0	2.0-2.5	0.010-0.020	-	-	Bal	0.075	0.006	0.006	0.003
COSMAL	40.0	1.0	0.005 max	3.0	0.3	Bal	0.100	0.003	0.001	0.001
SUPER COSMAL	60.0	1.0	0.005 max	6.0	0.3	Bal	0.200	0.003	0.001	0.001

Zamak-3 (BS 1004 Alloy A) is the most widely used zinc die casting alloy. It provides the best overall combination of strength, castability, dimensional stability and ease of finishing.
Zamak-5 (BS 1004 Alloy B) produces castings that are both harder and stronger than those made from Zamak-3 but at the expense of ductility.
ZA-8 is the only member of the hypereutectic alloys that can be hot chamber die cast. It has higher tensile, fatigue and creep strengths, is more dimensionally stable and has lower density than hypoeutectic alloys.
ZA-12 has very good castability in cold chamber die casting machines, frequently specified for castings that must combine casting quality with optimum performance.
ZA-27 is the lightest, hardest and strongest of all the family, but has relatively low ductility and impact strength when pressure die cast.
Finally, Cosmal alloys were developed as high damping capacity die castings and have demonstrated good castability and relatively high values of strength and hardness but low ductility [2].

Gravity Castings

With the exception of forming die alloys, slush casting alloys, and speciality alloys developed and use for bearings, no general-purpose gravity casting zinc alloy existed until the 1960s. Alloy ILZRO-12 (now ZA-12) was the first to appear, then ZA-8 and ZA-27 were quickly added. Alloy ZA-12 was developed first as a prototyping alloy for alloy ZAMAK-3 pressure die castings [1].
Alloy ZA-27 was developed specifically as sand casting alloy, and ZA-8 was turned into a permanent mould casting alloy. All three alloys are now used more extensively as pressure die castings. There is no information available about the use of the high aluminium Cosmal alloys as gravity castings.

The same requirements concerning impurities, melt cross contamination and general handling as for die casting alloys apply equally to the gravity casting alloys. Also the microstructural changes with time can alter the properties and dimensions of cast parts. However, property changes are normally very small over the normal life span of a component and dimensional changes, except in ZA-27 are negligible [1].
Alloy ZA-8 is used mostly with ferrous and graphite permanent mould casting. It can also be sand cast if needed. With the exception of creep resistance, the strength of a permanent mould casting is lower than that of pressure die castings due to the coarser microstructure of the former.
Alloy ZA-12 is more versatile than ZA-8 because it can be either sand cast or permanent mould cast. Its strength properties are high and its ductility and impact strength are acceptable. The

wear and damping properties are both high. Alloy ZA-12 can also be semi-continuous cast in solid and hollow rounds.
Alloy ZA-27 develops its optimum properties when it is sand cast. However, care must be taken when producing heavy section castings to ensure maximum soundness and minimal underside shrinkage. In a sound casting, ductility and impact strength are both higher than the other two alloys of the family. Alloy ZA-27 has excellent wear and bearing properties.

Other zinc-aluminium alloys for gravity casting include the following:
Kirksite alloy which is used as forming die alloy and can be sand cast to shape as well. It has an almost identical composition to the Zamak 2 die casting alloy.
Kayem 1 and Kayem 2 are similar alloys used in Europe.
Slush casting alloys (4.5-5.75% Al, 0.2% Cu) are used for the production of hollow castings such as table lamp bases.
Speciality alloys such as Main metal alloy and Alzen alloy are still used in Europe for the production of continuously cast bearing stock and other sliding elements.

2.1.2 Solidification of Sand Cast Aluminium Zinc-based Alloys

Unlike the pure metals, most alloys do not solidify at a single temperature. This difference is usually termed the solidification range of temperature and it affects the structure of the casting and the way shrinkage cavities are distributed in it.
Although equilibrium conditions do not occur at the rates that castings cool, the constitutional diagrams of alloys can be used to give a general explanation of the different patterns of solidification.

The zinc-aluminium system shown in Figure 1 has a eutectic at 5% aluminium, so that the temperature range over which freezing of alloys occurs increases as the aluminium content increases.

Gervais et al.[3] reported melting ranges for the commercial alloys as the difference between the liquidus and the eutectic temperatures because of the segregation that normally occurs in foundry practice as the following: ZA-8, 29°C; ZA-12, 55°C and ZA-27, 112°C. Using the same principle the high aluminium-zinc binary of 60% Al would present roughly a freezing range temperature of 200°C.

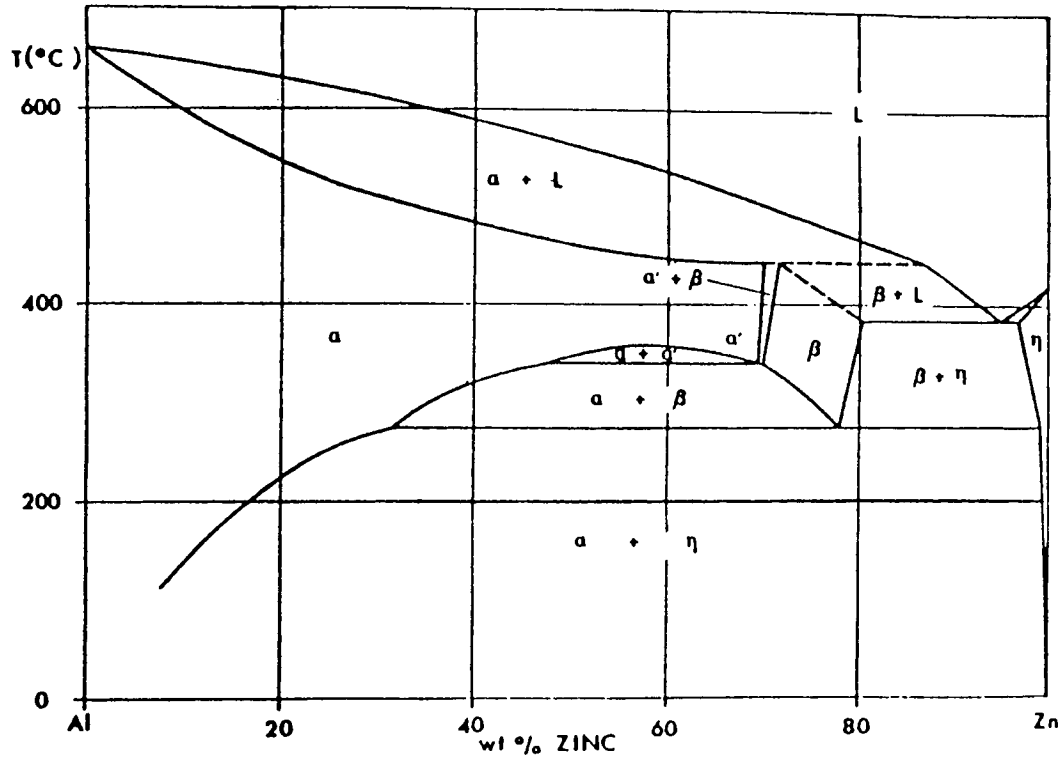

Figure 1. Zinc-Aluminium Phase Diagram.

Nieswaag [4] has characterised the solidification of alloys into two types: exogenous (from the mould wall to the centre by forming columnar grains) and endogenous (crystal growth throughout the section). These types are shown in Figure 2 where the mode of solidification depends upon the type of alloy, its composition, and the cooling conditions. Only high-purity metals and a few eutectics solidify as type I, while long freezing range alloys solidify as type Va.

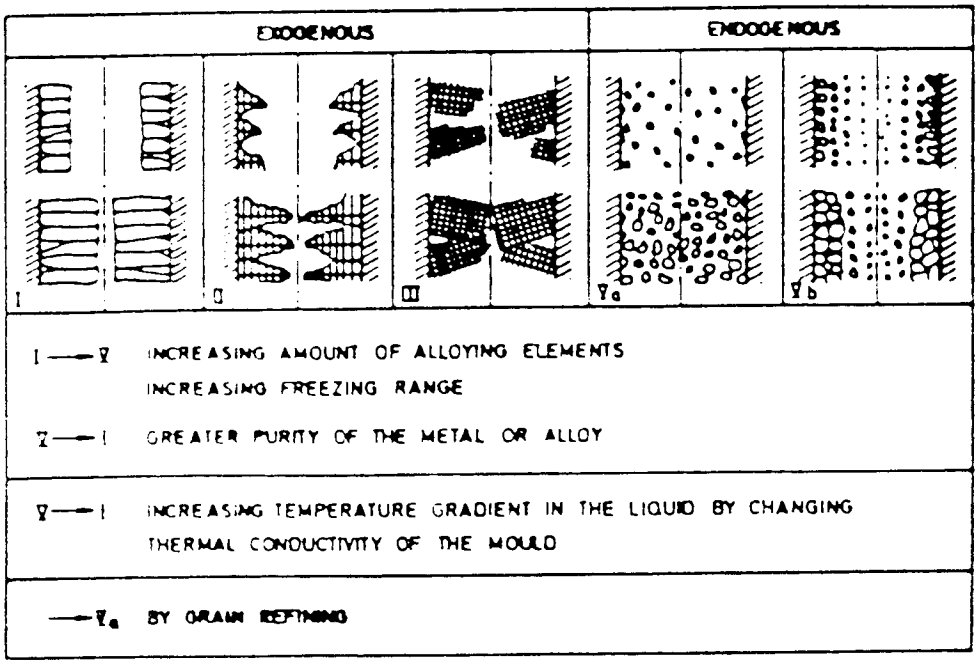

Figure 2. Illustration of the main types of solidification for metals and alloys [4].

Since most metals contract in volume during solidification, a continuous flow of liquid to the solid-liquid interface is necessary to avoid shrinkage porosity. For alloys that solidify as Type III or V, a mushy zone is created where the flow of liquid is blocked early during solidification so that these alloys tend toward having microporosity. The blockage of feed metal also depends upon the complexity of the dendrite maze established and the mode of solidification of the eutectic [5].

Possible feeding mechanisms have been discussed by Campbell [6] and illustrated in Figure 3. Not all the processes are to be expected in any given casting.

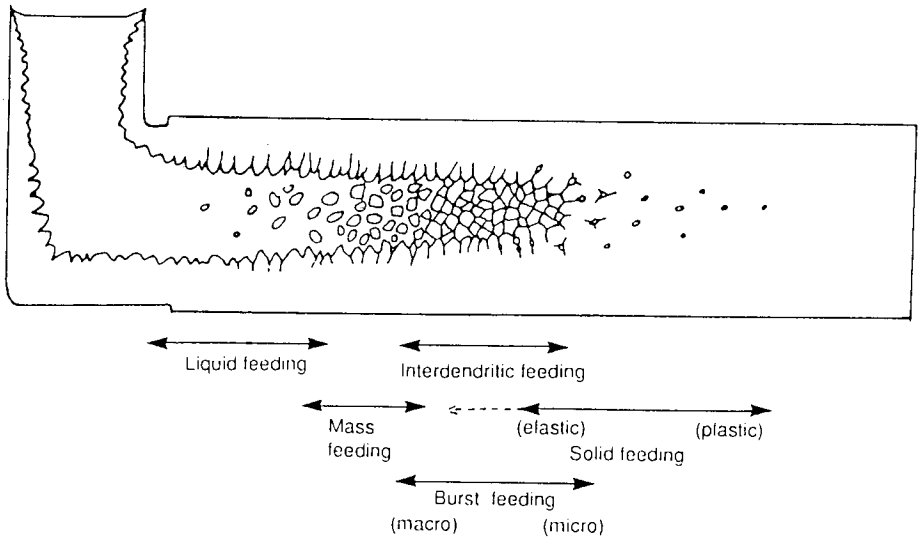

Figure 3. Schematic representation of the five feeding mechanisms in a solidifying casting [6].

Liquid feeding is applicable only in short freezing range alloys where the liquid can flow as a result of pressure gradients. Mass feeding denotes the movement of a slurry of solidified metal and residual liquid and can take place until the solid crystals impinge upon each other and form a rigid network. When this occurs, feed metal must be transported by the interdendritic flow of liquid. Burst feeding is the result of the local collapse of the network structure allowing feed metal to flood into the poorly fed region. Solid feeding is the flow into the poorly fed region. Solid feeding is the flow of solid as a result of creep in response to pressures attempting to form a shrinkage cavity.

In zinc-aluminium sand castings feeding becomes more complex not only because of their long freezing range but for the occurrence of macrosegregation during solidification.

ZA sand castings of large section thickness when cast under low thermal gradients, present an unusual spongy shrinkage on the bottom surface better known as Underside Shrinkage Defect. The severity of it increases with increasing aluminium content.
During the solidification of ZA-27 alloy, the first material to solidify is rich in aluminium and has a substantially lower density than the liquid from which it forms; 3400 and 4500 Kg/m^3 respectively [7].
Under these conditions, segregation can occur by flotation of aluminium-rich dendrites during the early stages, or by the interdendric flow of heavy zinc-rich liquid during the later stages of solidification. Both forms of segregation are driven by the density difference between the liquid and the solid phases and by the solidification shrinkage [8]. Underside shrinkage results from surface tension forces which, in order to compensate for the solidification volume change, cause the remaining liquid to be drawn into the interdendritic spaces producing an inverted pipe in large castings or a ragged bottom surface in smaller ones.

Another important experimental result reported in Reference 8, is that during the time that underside shrinkage was taking place, the casting was progressing from 75-90% solid approximately. Therefore, underside shrinkage occurred in castings which were nearly completely solid. In this condition, the channels to the region where the shrinkage was taking place were no longer open and risers have little effect on opposing it.
It is for this reason that the control of this defect requires the macrosegregation to the bottom of the casting to be prevented.

In castings of thin section and in permanent mould castings the time for solidification is too short to permit macrosegregation and underside shrinkage is not a problem. In sand castings it is advisable to use chills and risers to generate temperature gradients within the casting to prevent gravity segregation.

Barnhurst and Gervais [9] found that underside shrinkage could be eliminated by a proper use of chills. A cooling rate exceeding 0.25°C/s was necessary to achieve total elimination of the defect in the areas susceptible to its formation in ZA-27 castings. Other authors [10] suggested that a thermal gradient of 2.5°C/mm also prevents underside shrinkage formation. When a low thermal gradient is present, interdendritic shrinkage results from the inability of risers to feed the solidifying casting especially in the last 10 to 15% of the solidification process [11].

Underside shrinkage can also occur in the ZA-8 and ZA-12 alloys, but it is more easily controlled by proper attention to riser volume, pouring temperature and sand system [7]. In general terms, zircon sand with its relatively high thermal conductivity produces a chilling action on the casting, so the underside defect is minimised. On the other hand, reducing the

pouring temperature reduces the amount of heat transferred to the mould walls hence maintaining the thermal gradient.

Sahoo et al.[12] studied the addition of rare earth elements as modifying agents which could be able to hinder underside shrinkage. In their experiment it was found that Li, Na, K and Cs from Group IA and Be, Ca, Sr and Ba from group IIA in the concentration range 0.02-0.1% eliminated underside shrinkage. Although no influence of the trace elements on macrosegregation was observed, the underside shrinkage defect appeared to be prevented by the formation of a strong skin of metal at the bottom of the castings. However dross formation even at concentrations as low as 0.03-0.06% was reported as the main disadvantage when these modifying elements were used.

From the point of view of availability, cost and reactivity, it was concluded that modification of Zn-Al alloys by Sr or Ca may be the preferred treatment.

2.1.3 Foundry Parameters for Casting Zinc-Aluminium Alloys in Sand

Zinc-aluminium alloys are low melting temperature materials. Table 2 shows that their melting point as well as other thermal properties increase with increase in aluminium content.

Melting of zinc-aluminium alloys may be done in gas, oil or induction furnaces. Since the alloys react with iron at normal bath temperatures it is not recommended to use cast iron pots. Also overheating the melt at around 700°C should be avoided in order not to produce fuming of zinc.

Prior to any metal transfer operation, it is essential to vigorously stir the bath to prevent gravity segregation and ensure homogeneity in melt composition.

Zinc alloys are not prone to gas absorption; thus no special treatment such as degassing or fluxing is needed. However, the melt surface should be skimmed to remove oxides and any solids floating on the melt [3].

The preparation of sand moulds for use with zinc-based foundry alloys can follow general non-ferrous practice. Due to the excellent fluidity and low pouring temperature of the alloys, it is preferable to use fine grain sands for optimum surface quality and minimum penetration [3].

Table 2. Physical and thermal properties of standard zinc-aluminium alloys

Properties	Units	ZAMAK 3	ZAMAK 5	ZA 8	ZA 12	ZA 27
Density	kg/m^3	6600	6700	6300	6030	5000
Melting Range	℃	381-387	380-386	375-404	377-432	375-484
Thermal Conductivity at 24°C	W/m K	113	109	115	116	125.5
Specific Heat 24-100°C	J/kg K	419	419	435	450	525
Latent Heat of Fusion 380-415°C	kJ/kg	-	-	112	118	128
Solid Contraction	%	1.17	1.17	~1.0	~1 to 1.3	~1.3

Fluidity and Pouring Temperature

With other liquids fluidity simply means low viscosity, but in foundry terms can be defined as that quality of the liquid metal which enables it to flow through mould passages and to fill interstices of the mould [13].

Neglecting factors related to the mould into which a metal is cast, the factors strongly affecting fluidity are; degree of superheat, composition of the alloy and mechanism of freezing. Other factors that exert certain influence on fluidity are; viscosity of the molten metal, surface tension of the molten metal, formation of surface oxide films and presence of non-metallic inclusions in the liquid metal.

The influence of the type of solidification was identified by Potervin and Bastien [14] who concluded that the greater the freezing range of an alloy, the lower the fluidity and that solidification with dendritic crystals reduce fluidity more than if compact crystals were formed. High fluidity is commonly found to be associated with pure metals and some eutectics. Mollard et al.[15] have reproduced interesting documented data from Lang [16] about the fluidity of pure metals as a function of superheat, one example of that is given in Figure 4 where pure zinc shows better fluidity than aluminium and lead for the same pouring temperature. The presence of alloying elements decreases fluidity rapidly initially but the proximity of the eutectic composition increases fluidity again as is the case of pressure die casting zinc-aluminium alloys.

Results from fluidity tests are generally used to determine optimum pouring temperatures. Regarding ZA gravity castings, various authors [17,18] have reported fluidity-degree of superheat relationships of the type shown in Figure 5.

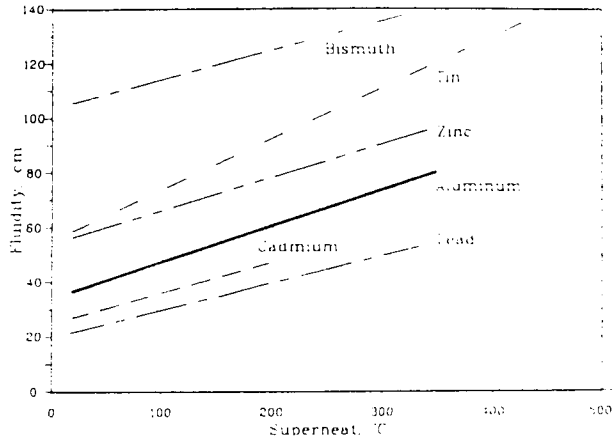

Figure 4. Fluidity of some pure non-ferrous metals as a function of superheat [15].

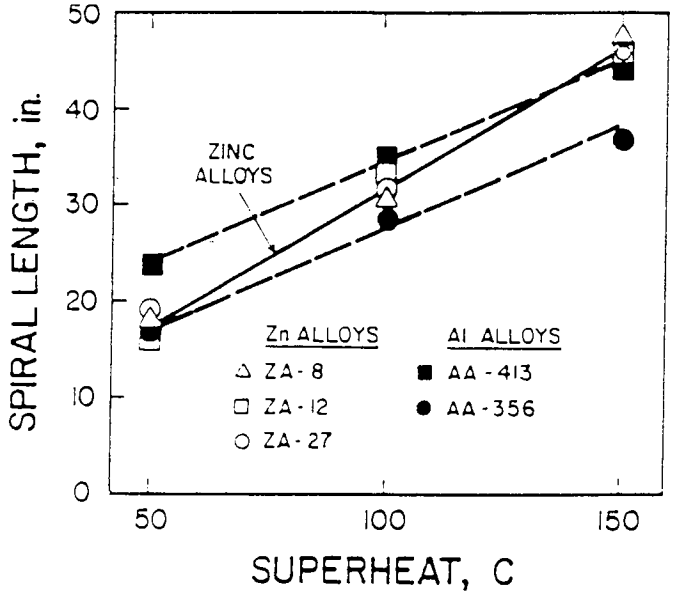

Figure 5. Fluidity of ZA alloys in comparison to aluminium alloys[19]

The three alloys of the ZA family present about similar fluidity values and are comparable to well known highly fluid aluminium alloys. Because of this quality ZA alloys easily flow along thin section parts of the mould and in larger sections can be poured at lower temperatures without misruns.

Running, Gating and Risering

Casting ZA alloys is compatible with all casting systems used for aluminium and bronze alloys but the design of patterns and running and risering systems is of critical importance in obtaining sound castings.

It is recommended to use a non-pressurised running and gating arrangement with a 1:3:3 to 1:4:4 gating ratio [17].

The riser requirements to compensate solidification shrinkage of ZA sand castings were studied by Barnhurst and Jacobs [20] as a function of casting geometry and presence or absence of copper chills. Based on radiographic analysis they established NRL type risering curves as shown in Figure 6.

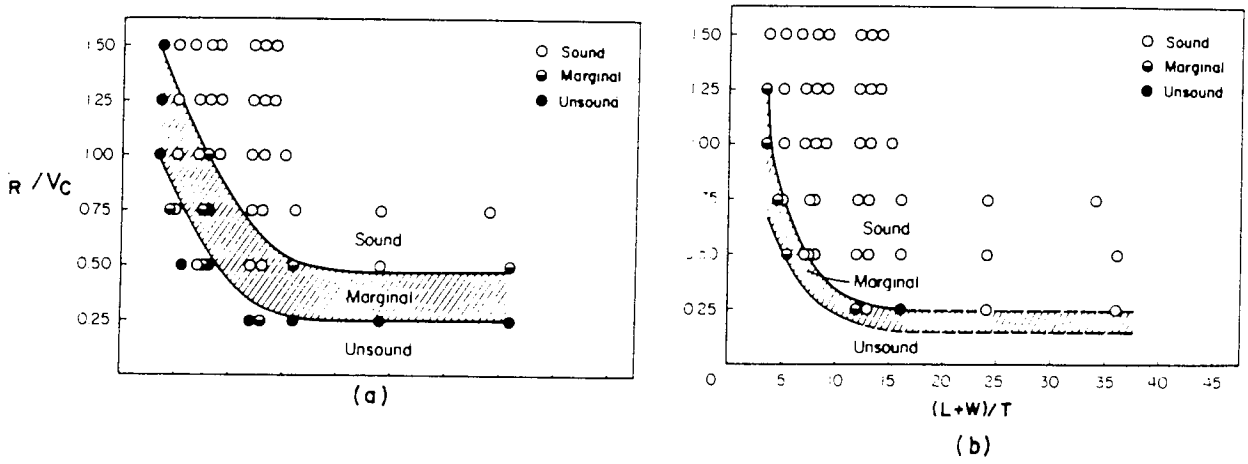

Figure 6. NRL type risering curve (a) unchilled (b) chilled for ZA-27 castings [20].

In the NRL (Naval Research Laboratory) method, the casting shape factor (L+W)/T ((length+ width)/thickness) represents the surface-to-volume ratio. Here the relative soundness of the ZA castings was found to be dependent on the presence or absence of end chills. The use of end chills gave lower values of Vr/Vc.

Optimum riser H/D ratios for bar and plate castings were also reported, the best cylindrical risers having a height-to-diameter ratio of 0.5-1.0.

Regarding the effective feeding distance, Barnhurst's report states that the most important parameter that influences it in ZA sand castings, is the section or wall thickness of the pattern. For the range of geometries tested, curves of the type shown in Figure 7 were reported.

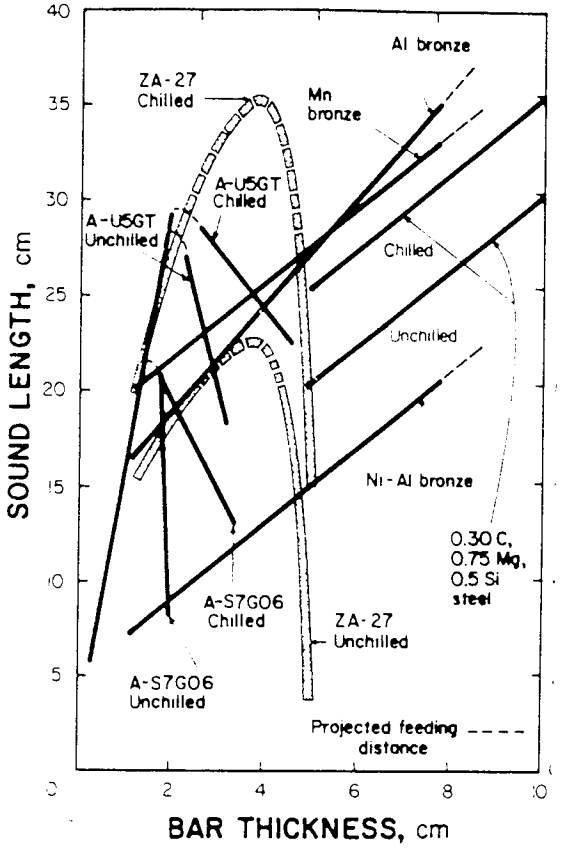

Figure 7. Feeding distance of ZA 27 sand castings based on radiographic analysis. Data of common ferrous and non-ferrous alloys are provided for comparison [20].

In thick section castings, the feeding distance is reduced mainly due to the lack of sufficient thermal gradient to foster directional and rapid solidification which is to a certain extent achieved by the use of chills.

2.1.4 Sand Casting of High Aluminium Zinc-based Alloys

As stated in the Introduction to this Chapter two families of high aluminium zinc-based alloys have been introduced to the market; the Alzen and the Cosmal alloys respectively. The first family was developed by Voest AG[21] during the 1940's and consisted of a zinc base containing 27%-70% Al, 0%-5% Cu and 0%-5% Si. Of this range of alloys, that containing 32% Al and 5% Cu (Alzen 305) has been manufactured in the UK by means of continuous casting processes. In the other case, Cosmal alloys whose compositions are given in Table 1, were recently developed by Mitsubishi Metal Corporation for high damping capacity die castings. Therefore, there is no information available about the industrial use of these high aluminium zinc-based alloys as sand castings.

2.1.5 Sand Casting of Aluminium-Silicon Alloys

The zinc-based alloys studied in the present research work contained as major additional elements aluminium and silicon at levels of 60% and 6-8% respectively, therefore a brief literature review of the sand casting practice of aluminium-silicon alloys is considered worth including. Particular attention is paid to the influence of silicon on foundry characteristics such as solidification shrinkage, metal feeding and fluidity.

The aluminium-silicon phase diagram of Figure 8 provides a simple eutectic-forming system, which makes possible the commercial viability of most aluminium castings. Silicon contents ranging from 4% to the eutectic level of about 12% reduce scrap losses, permit production of much more intricate designs with greater variation in section thickness, and yield castings with higher surface and internal quality. These benefits derive from the effects of silicon in increasing fluidity, reducing cracking and improving feeding to minimise shrinkage porosity[22].

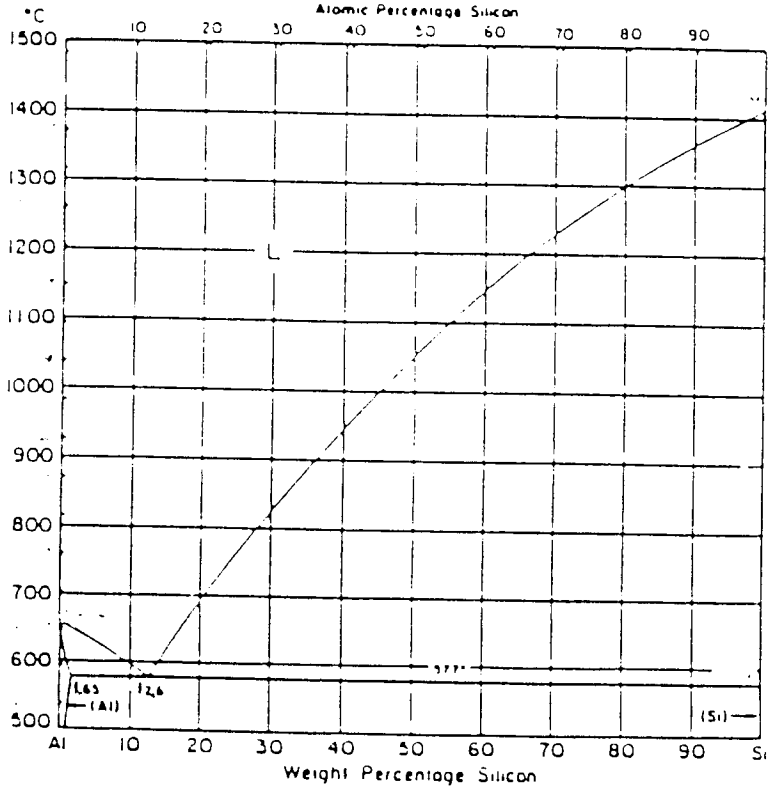

Figure 8. Equilibrium phase diagram for the binary Al-Si system.

Figure 4 show that aluminium has better fluidity than cadmium and lead, but less fluidity than zinc, tin and bismuth for the same pouring temperature. It can be seen also that pure metals, including aluminium, still have a considerable degree of fluidity at temperatures just above their liquidus.

The fluidity of unalloyed aluminium decreases with decreasing purity [15], and in binary alloys apparently, fluidity at a given pouring temperature decreases rapidly as the amount of alloying element increases, as in the case of the Al-Cu and Al-Mg binaries shown in Figure 9. As composition approaches the eutectic, fluidity increases again.

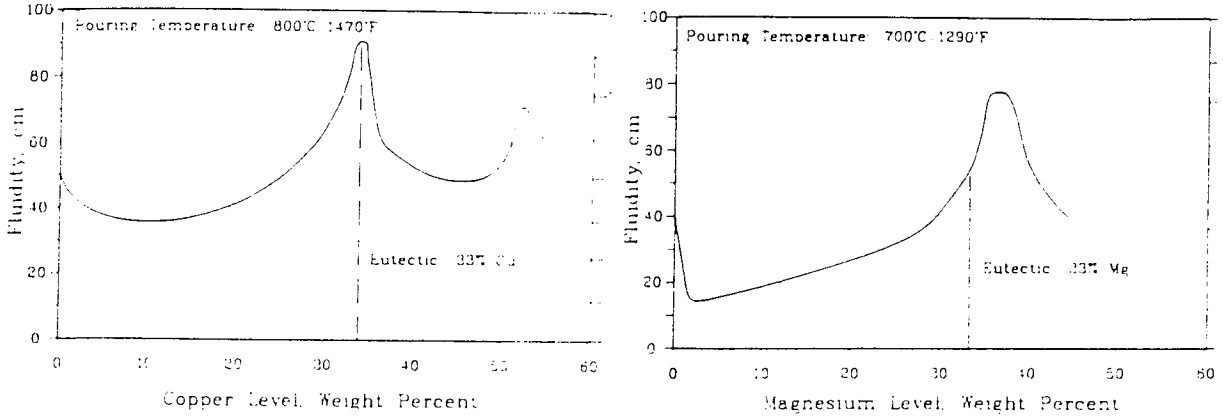

Figure 9. a) Fluidity of Al-Cu alloys as a function of copper level [15]. Pouring temperature 800°C.

b) Fluidity of Al-Mg alloys as a function of magnesium level [15]. Pouring temperature 700°C.

The Al-Si alloys, probably the most important aluminium alloy family, displays a similar trend shown in Figure 10. The lowest fluidity value corresponds to the 5-7% Si range, typical of most commercial hypoeutectic Al-Si casting alloys. However, the highest fluidity value occurs not at the 12% eutectic but rather around 18% Si, typical of commercial hypereutectic Al-Si alloys [15].

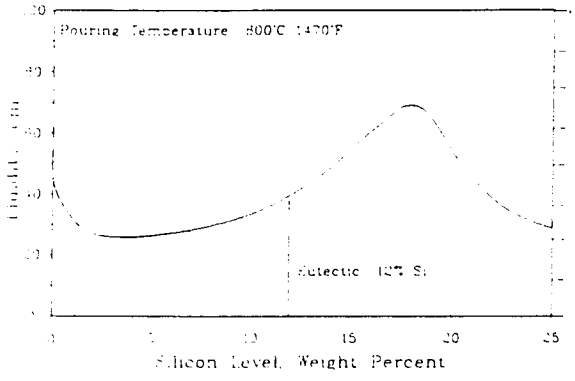

Figure 10. Fluidity of Al-Si alloys as a function of silicon level [15]. Pouring temperature 700°C.

Consequently, in casting alloys with silicon as the major additional element, relatively high values of fluidity are imparted due to the presence of large volumes of Al-Si eutectic.

Aluminium-silicon alloys have low solidification temperatures compared with Cu-based alloys and ferrous alloys, so that smaller differences in temperature between metal and mould are involved. They solidify over a relatively wide freezing range, and therefore their solidification mode is of the mushy type They also have high specific heat and latent heat of solidification which give them the tendency to cool slowly. Added to this, their thermal conductivity is high so that heat is rapidly transferred from the centre to the outside of the casting This combination tends to produce very shallow temperature gradients during casting solidification.

In general, feeding of castings to compensate the liquid-to-solid contraction becomes inefficient in this type of solidification. As a consequence, macro and/or micro shrinkage porosity are expected to be developed.

When suitably designed, risers will eliminate macro shrinkage, but they are not too effective in preventing microporosity from forming in the interdendritic regions. Other means, such as chilling the casting to establish proper temperature gradients, are required to achieve soundness.

In the specific case of Al-Si alloys, the formation of the silicon phase during solidification is accompanied by an increase in volume, thereby reducing the feed metal volume that must be supplied. If a stable mould is assumed, and minimum superheat is used to pour the casting, the expansion accompanying the formation of the silicon phase could be used for self feeding of the castings [5].

The positive influence of silicon on feeding ability in some aluminium alloys was observed by Fortina [23] who used thermal analysis to obtain the solidification curves displayed in Figure 11.

The Al-Si alloy solidified with the formation of about 55% alpha aluminium within the first 40°C of cooling, followed by the formation of Al-Si eutectic. The Al-Cu alloy solidified with the formation of alpha aluminium dendrites over a wider temperature range consuming about 85% of the liquid before the formation of the eutectic Al-$CuAl_2$. Clearly, in the Al-Si solidifying alloy, passages between the alpha dendrites were maintained open allowing the flow of feed metal to the mushy zone.

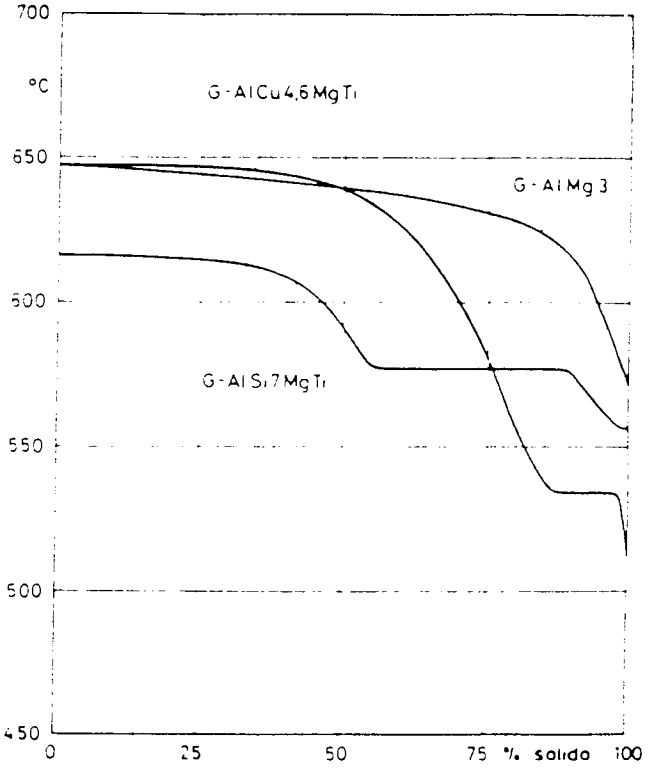

Figure 11. Solidification curves for three aluminium casting alloys illustrating differences in solid fraction formed at various temperatures.

Iwahori et al.[24] reported Figure 12 to show that as silicon content is increased, there is lesser volume of solid alpha aluminium formed at temperatures above the eutectic therefore leaving sufficient space for feed metal delivery.

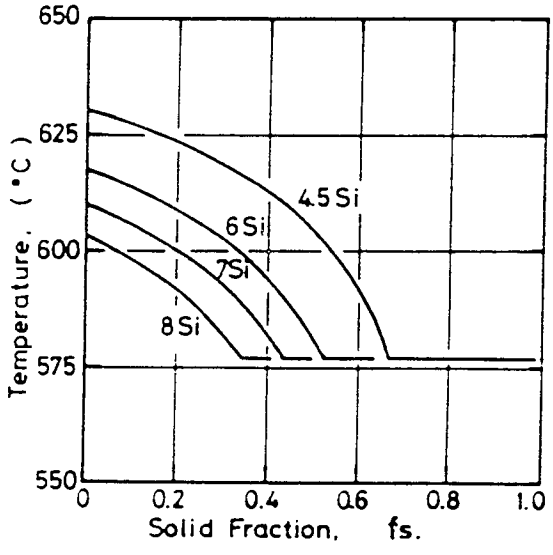

Figure 12. Relationship between temperature and solid fraction for Al-Si alloys [24].

2.2 SPECIFIC AIM OF THE SAND CASTING WORK

From this review of the casting behaviour of existing Zn-based alloys and Al-based alloys, the important influence of Si and Al on the casting behaviour of the alloys was demonstrated. For high-Al zinc-based alloys the very large freezing range would entail considerable difficulties in producing sand castings. However addition of sufficient Si would be expected to reduce the freezing range considerably, and improve the fluidity of the alloys. Accordingly for an alloy designed to be broadly similar to existing commercial alloys based on the Zn-Al-Cu-Mg system, an addition of 8% Si was chosen. This would also put this alloy closer to the Super Cosmal alloy and make a more direct comparison possible.

Thus the specific purpose of this part of the work was to examine some foundry characteristics of the following two high aluminium zinc-based alloys when cast in sand:

Super Cosmal Alloy	:	Zn, 60% Al, 6% Si, 1% Cu, 0.3%Mn
Hazca Alloy	:	Zn, 60%Al, 8% Si, 2% Cu, 0.06% Mg

The casting behaviour of these alloys was investigated through the following features:

1. Determination of fluidity as a function of degree of superheat
2. Examination of gravity segregation and solidification shrinkage in a slow cooling casting.
3. Examination of feeding characteristics and porosity distribution as a function of melt preparation, cooling condition and casting geometry.

Results were compared to those of standard ZA-27 alloy obtained under the same experimental conditions.

2.3 EXPERIMENTAL PROCEDURE

2.3.1 Preparation of Alloys

Alloys to be used in the experimental work, were obtained by melting the appropriate charges in an electrical induction furnace fitted with a graphite crucible and then cast into iron moulds to form ingots for further use. Samples for chemical analysis were taken from every melt at the time of pouring.

Charges were prepared using commercial grade zinc (99.99%), high purity aluminium (99.99%), commercial magnesium (99.8%) and Al-Si (50/50), Al-Cu (50/50) and Al-Mn (90/10) master alloys.

In order to make the Super Cosmal alloy, the aluminium and the Al-Si, Al-Cu and Al-Mn master alloys were melted together. Subsequently zinc was added at around 600°C bath temperature.

The HAZCA alloy was prepared by melting the aluminium along with the Al-Si and Al-Cu master alloys to begin with, and magnesium was introduced to the melt just before casting.

In all cases, prior to being ingoted, the alloyed bath was vigorously stirred and properly skimmed.

2.3.2 Fluidity Test

Fluidity of Super Cosmal, the experimental HAZCA and ZA-27 alloys was evaluated using standard spiral fluidity test for sand castings.

The sand mixture used as in all casting experiments comprised of fine silica sand, 12% bentonite and 5-7% moisture.

Melts were obtained by remelting the pre-prepared ingots in an induction furnace. After stirring the melt, spirals were cast at superheats of 50, 100 and 150°C for each alloy. Bath temperature was carefully monitored with a chromel-alumel thermocouple and castings were poured when the correct superheat was reached.

2.3.3 Gravity Segregation and Solidification Shrinkage

In order to observe the extent of gravity segregation and the development of solidification shrinkage, an experiment was conducted consisting of casting four alloys in a slow cooling system which would enlarge the occurrence of the phenomena. A Zn-Al binary alloy of 60% Al is included for comparison. Figure 13 illustrates the cylindrical pattern used which in turn, simulates a top risered heavy section cylinder.

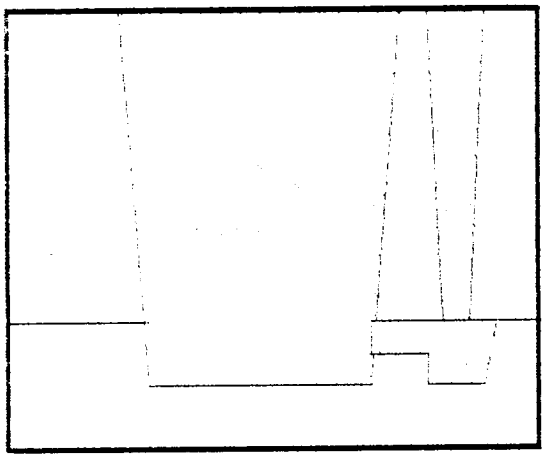

Figure 13. Heavy cylindrical pattern to observe development of shrinkage.

The sand mixture used was prepared in the same manner as in previous points.

A thermocouple tip was positioned in the centre of the casting to monitor its cooling rate and to obtain information about freezing changes.

Once at room temperature, the chunky castings were sectioned vertically to better observe the solidification shrinkage formed and to obtain samples for chemical analysis from top, centre and bottom locations necessary to evaluate long-range segregation of alloy components.

2.3.4 Evaluation of Horizontal Feeding Characteristics

Casting of test bars.

Feeding characteristics of the experimental alloys when cast in sand, were evaluated through degree of soundness measurements along square-section test bars of variable length and thickness. Figure 14 shows a schematic configuration of the pattern used.

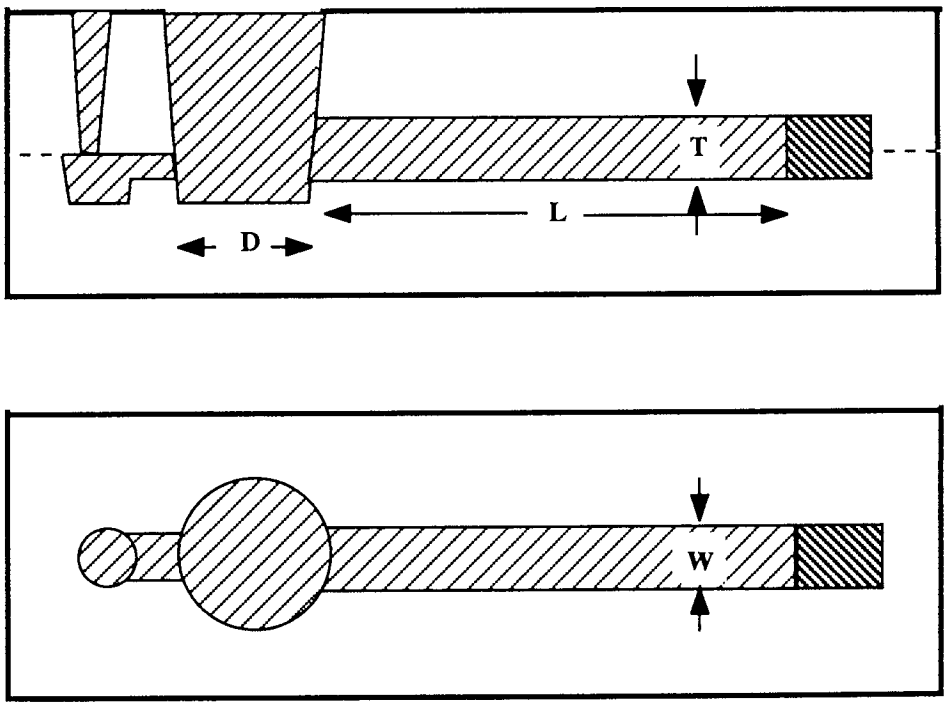

Figure 14. Pattern details and mould assembly.

A single open riser design to give sufficiently long solidification time was used. To ensure the riser to contain feed metal during the period of freezing, a large ratio of modulus riser : modulus casting ratio was employed.

The selection of riser size for the heaviest of the castings was done using NRL type risering curves developed for ZA-27 alloy [20].

Calculations assuming unchilled conditions were as follows:

Volume of casting	$Vc = 50x50x300 \text{ mm} = 750\,000 \text{ mm}^3$	
NRL shape factor	$(L+W)/T = (30+5)/5 = 7$	
Freezing ratio	$Vr/Vc = 1.25$	(from Figure 5)

Required volume of riser	Vr = 936 000 mm^3
Riser height/diameter ratio	H/D = 1
Riser dimensions	H = 10 cm, D = 10 cm
Horizontal Running System	1:4:4 A (choke) = 130 mm^2 , 12 mmØ A (runner) = 520 mm^2 , 40x13 mm

Dimensions of the bar patterns used along with their calculated freezing ratios (Mr/Mc) are given in Table 3.

Table 3. Dimension of the bar patterns.

T (mm)	W (mm)	L (mm)	Mc (mm)	Mr/Mc
15	15	150	3.65	4.57
15	15	200	3.68	4.53
15	15	250	3.69	4.52
25	25	200	6.06	2.75
25	25	250	6.09	2.74
25	25	300	6.20	2.70
50	50	100	11.10	1.50
50	50	250	11.90	1.40
50	50	300	12.0	1.40

Two conditions of melt preparation were applied for the high-aluminium Super Cosmal and HAZCA alloys, namely degassing the melt and not degassing the melt. The ZA-27 melt was not subjected to any kind of degassing treatment since it is reported that the alloy is not prone to gas absorption [3,17].

Two conditions of solidification were imposed by chilling and not chilling the castings. When needed, copper chills were used at the cold end of the cast bars.

Finally, the following three combinations were applied to evaluate the feeding ability of the alloys and the resulting porosity distribution:

1. Not degassing and not chilling
2. Degassing and not chilling
3. Degassing and chilling.

Moulding was carried out by hand ramming using the sand mixture before mentioned.

Once again, melts were obtained in an induction furnace remelting pre-prepared ingots. Before casting, degassing (when scheduled), stirring and skimming were applied.

Appropriate pouring temperatures for each alloy were obtained from the fluidity test results. It was judged that 50-60°C of overheat was sufficient and safe in all cases. Therefore, 550-560°C for ZA-27 alloy and 620-630°C for both Super Cosmal and HAZCA alloys were used as casting temperatures.

The castings produced were knocked out after two hours from pouring, cleaned of retained sand and left to cool at room temperature.

Determination of Porosity Occurrence along Cast Bars

Density measurements according to Archimedes' Method were applied to determine porosity content at consecutive locations along the cast bars from riser end to chill end. Percentage porosity was calculated by the equation 100x(Ds-D)/D (%), where Ds was density of standard specimen and D was density of the specimen with unknown porosity content.

To produce density specimens the cast bars were cut into slices of approximately 10 mm thickness. All slices were properly numbered, roughly ground and bored as shown in Figure 15.

Density measurements were carried out using a balance of 0.01 mg of resolution and at constant room temperature.

Standard specimens were considered those having the maximum density value and where porosity was not visible by naked eye when ground and polished.

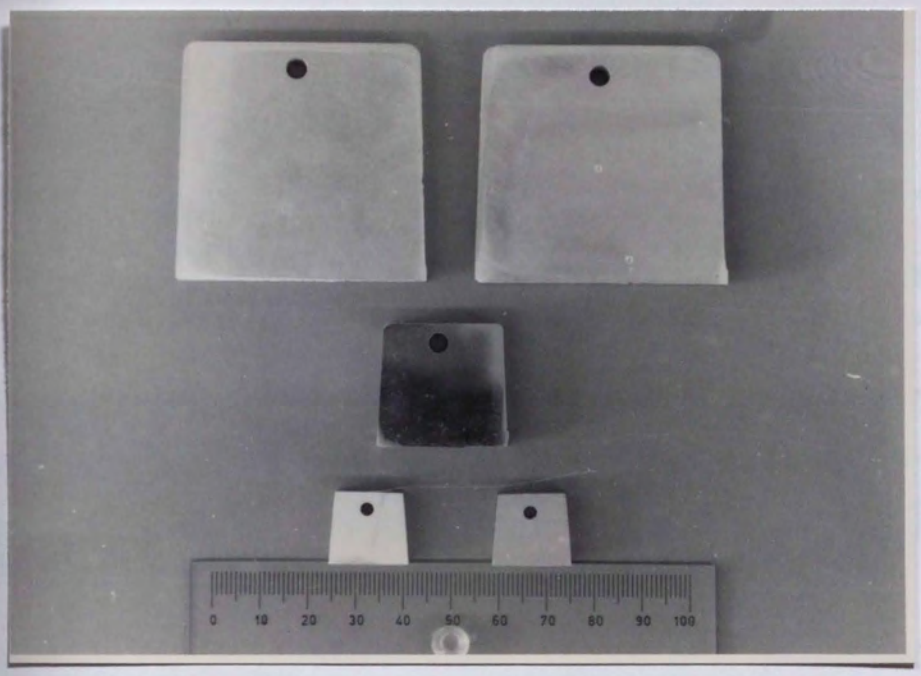

Figure 15. Specimens for density measurements.

2.4 EXPERIMENTAL RESULTS

2.4.1 Chemical Composition of the Alloys

The chemical composition of the alloys produced was determined by Atomic Absorption Spectroscopy in the ISC Alloys Division of PASMINCO EUROPE. The results are given in Table 4 where the composition of commercial MAZAK ZA-27 ingot is included.

Table 4. Composition of the alloys produced.

	Additions wt.%					
Alloy	**Al**	**Si**	**Cu**	**Mn**	**Mg**	**Zn**
Super Cosmal	60.8	5.97	0.98	0.35	-	31.40
HAZCA	57.50	8.12	2.10	-	0.04	32.17
ZA-27	25.5- 28.0	- -	2.0- 2.5	- -	0.015- 0.020	69.50- 72.50

Impurity levels were below the permissible maximum

2.4.2 Fluidity Test Results

Results of the fluidity tests are given in Figure 16a. The fluidity of the alloys, as measured by the length of the spiral arm following casting is given as a function of superheat. An example of a cast spiral is shown in Figure 16b.

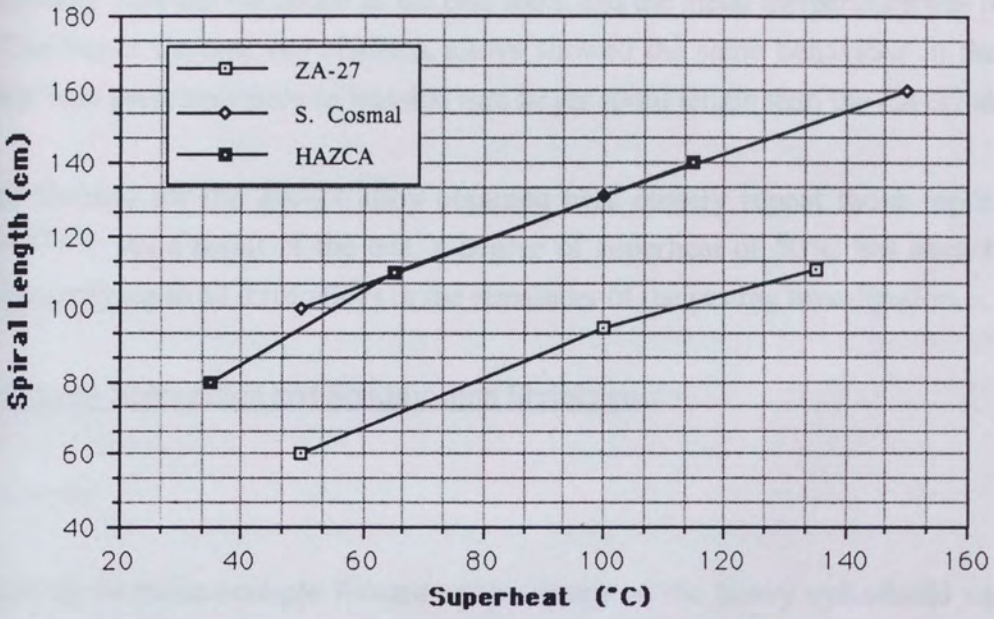

Figure 16a. Casting fluidity for ZA-27, Super Cosmal and HAZCA alloys as a function of superheat.

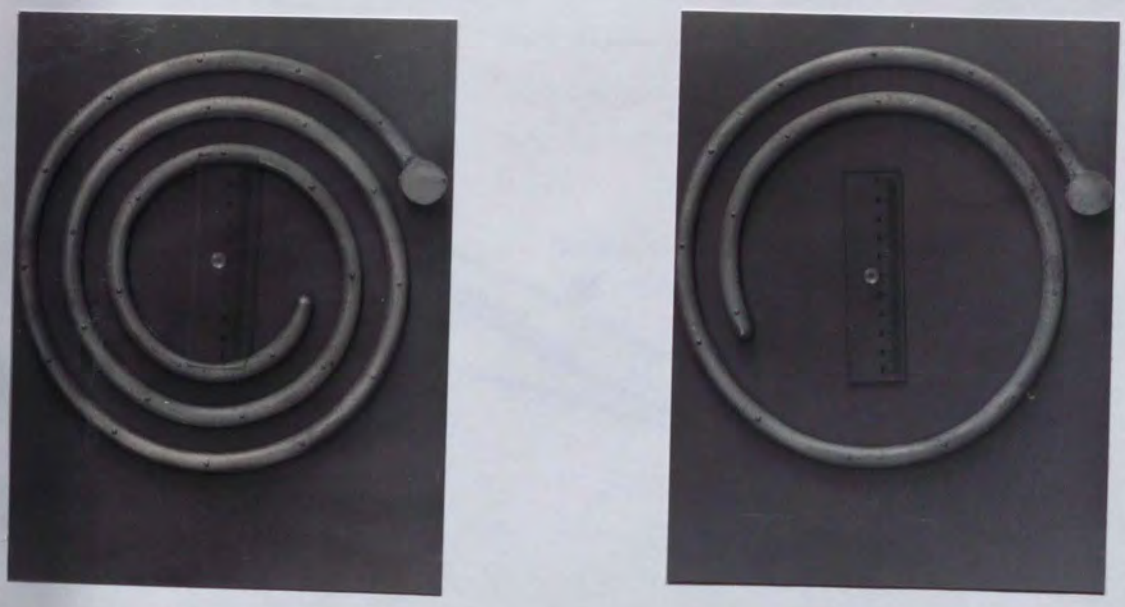

Figure 16b. Super Cosmal alloy fluidity spirals cast at superheats of 150 and 50°C respectively.

The relationship between the length of the cast spiral and the metal temperature was found to be linear. The Super Cosmal and HAZCA alloys showed the same behaviour in their casting fluidity but both presented more or less 400 mm larger spiral length than the ZA-27 alloy.

Values of fluidity for the ZA-27 alloy obtained here closely repeat those reported in the literature[17,18]. As a result of the test, a degree of superheat of 50°C has been considered appropriate applying to all three alloys in the remainder of the casting investigation.

2.4.3 Gravity Segregation and Solidification Shrinkage

Cooling Curves

The output of the thermocouple located at the centre of the heavy cylindrical casting was recorded as a function of time so cooling curves during solidification were obtained as shown in Figure 17.

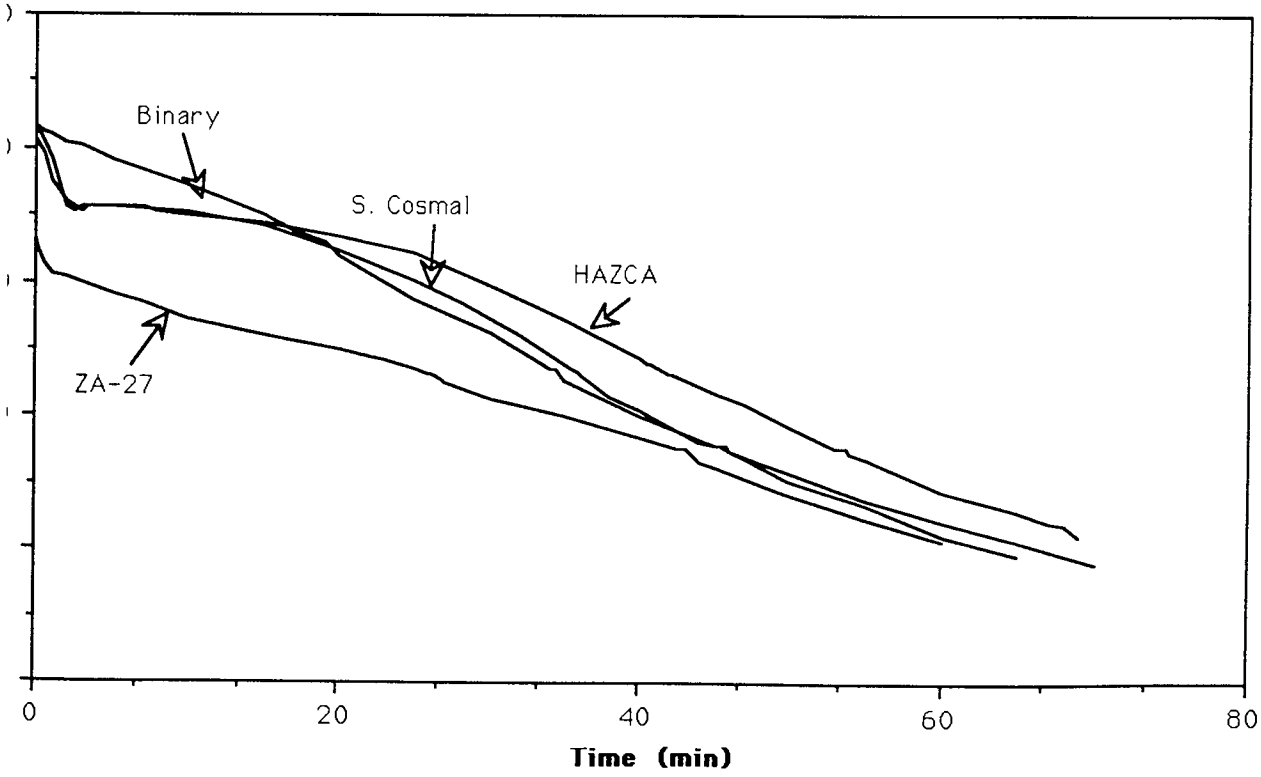

Figure 17. Cooling curves for ZA-27, Super Cosmal, HAZCA and 60Al40Zn Binary alloys when cast the cylindrical mould of Figure 12.

From a close examination of the curves the following apparent observations can be noted:

1. ZA-27 alloy solidifies in accordance with its equilibrium diagram. Thermal arrests are not definitely clear but slope changes approximately coincide with solidification transformations of the phase diagram, such as : peritectic ß formation at around 430°C and eutectic transformation at around 380°C.

2. The Zn60%Al binary showed a practically constant cooling rate during solidification but still very short thermal arrests could be detected at around the theoretical peritectic and eutectic temperatures.

3. Presence of silicon in Super Cosmal and HAZCA alloys strongly modified the solidification mode of the high-aluminium zinc binary, lowering the liquidus temperature by approximately 45°C and establishing a thermal arrest which is assumed to be due to aluminium-silicon eutectic solidification and growth. The greater the silicon content the longer the period of Al-Si eutectic arrest. Subsequently, cooling rate increased during solidification of the remaining zinc-rich liquid until the Zn-Al eutectic temperature was reached.

4. Bearing in mind that the method here employed was not very accurate to determine structural transformation during solidification, a rough approximation of freezing ranges can be given as follows:

ZA-27	500-380°C
Zn/Al Binary	600-380°C
Super Cosmal	556-380°C
HAZCA	556-380°C

Considering the period of time between liquidus and eutectic temperatures as solidification time, average cooling rates during freezing at the centre of the experimental casting were identified as the following:

ZA-27	2.8°C/min
Zn/Al Binary	5.0°C/min
Super Cosmal	4.0°C/min
HAZCA	3.5°C/min

Gravity Segregation and Development of Shrinkage Solidification

Longitudinal sections of each of the slowly cooled castings under study are shown in Figure 18. They reveal the appearance of shrinkage cavities developed during solidification. Aluminium analyses obtained at three different locations from top to bottom are also included.

As expected, the ZA-27 alloy exhibited a large inverted shrinkage cavity at the bottom of the casting due, as it is well known now, to gravity separation of primary aluminium crystals towards the top part of the casting and zinc-rich eutectic towards the bottom at slow cooling rates. As Figure 18 (a) shows, analysis reported large differences in aluminium concentrations along the vertical axis. Aluminium content at the casting base is 36% less than that of the melt.

The 60%Al-Zn binary alloy presented a relatively lesser degree of gravity segregation. In this case, the aluminium content at the bottom of the casting was 25% less than that of the original melt. Furthermore, segregation seemed to have occurred only from centre to bottom. As a result, although different in shape and apparently smaller than that of the ZA-27 alloy, underside shrinkage also developed in this alloy.

In Super Cosmal and HAZCA alloys where silicon contents are as high as 6 and 8% respectively, solidification of the heavy castings took place similarly to most aluminium-silicon alloys [25] when cooled at very slow rates. Firstly, a drop in the overall casting height and some pipe formation and secondly development of a gross shrinkage cavity near the surface and dispersed microshrinkage around it. In both cases, the base of the castings appeared sound with no signs of underside shrinkage. As illustrated in Figure 18 (c) and (d) in both alloys gravity separation of aluminium and zinc was minimal but flotation of primary silicon occurred. Note, that having obtained the compositional analysis by X-Ray energy dispersive spectrography from the SEM, results for silicon reported unrealistic values in spite of averaging numerous readings at the lowest magnification possible.

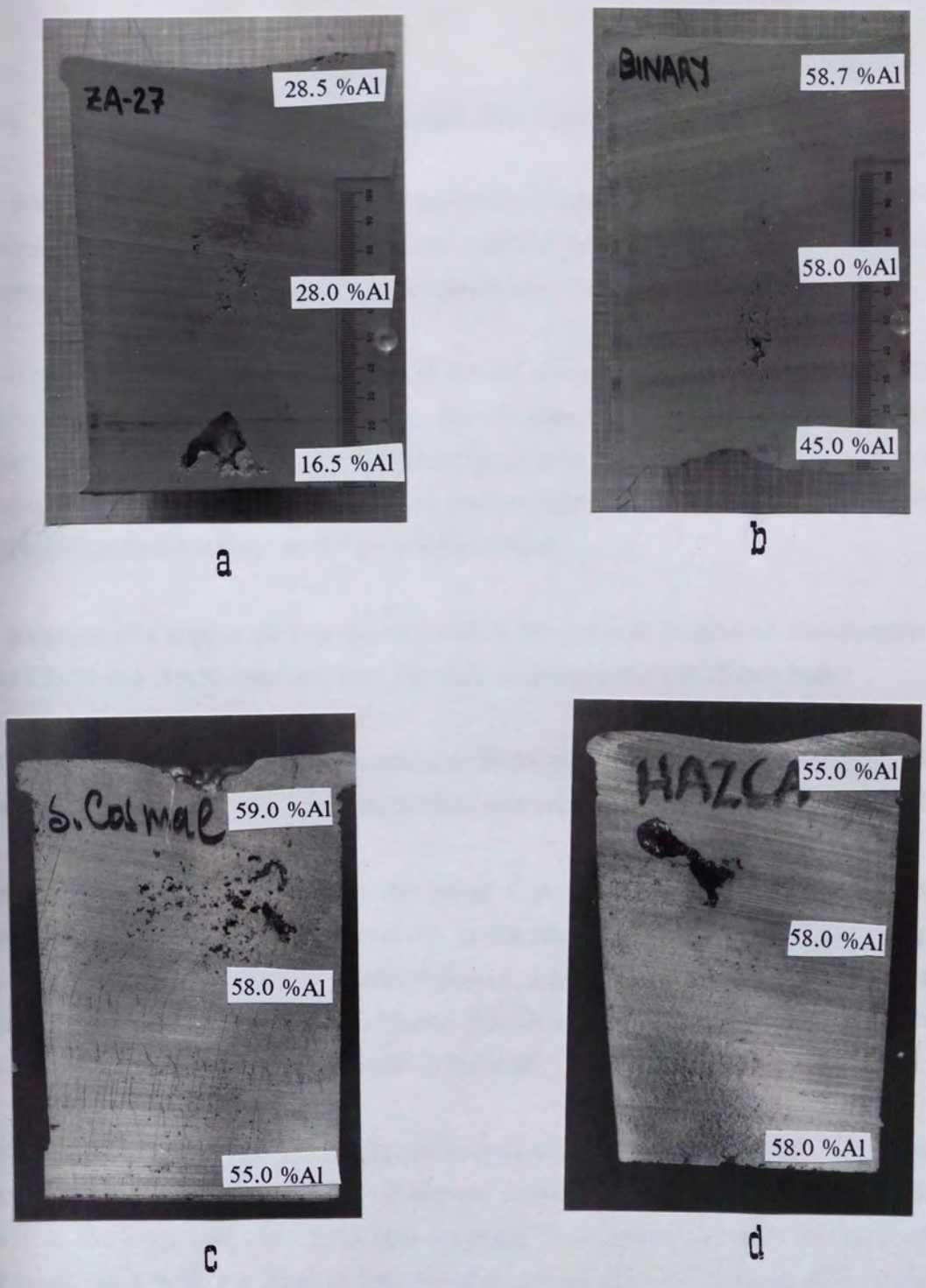

Figure 18. Vertical sections from slowly solidified heavy castings
(a) ZA-27 (b) 60%Al-Zn Binary (c) Super Cosmal (d) HAZCA

2.4.4 Feeding Characteristics and Porosity Distribution in Castings

The distribution of porosity in all the experimental castings is given in Figures 19 to 27 as a function of size, absence or presence of end chill and application or not of degassing treatment. Curves represent porosity levels at regular positioned intervals along the bar castings.

Porosity content curves for the standard ZA-27 alloy are shown in Figures 19, 20 and 21, where, regarding the influence of size, the thickest 50x50 mm bars exhibited the lowest porosity levels and a more gradual variation from cold end to hot end. Clearly, the longest of the 15x15 and 25x25 mm bars were very porous near the casting mid point, possibly due to centreline dendritic blockage to the path of feed metal.

The presence of a copper chill at the cold end of the castings, improved soundness remarkably in the 25x25 and 50x50 mm cast bars, but only slightly in the 15x15 mm bars.

In all cases, maximum porosity occurred next to the riser because of the heating influence of it, which induced very slow cooling rates at that location. Chilling did not modify this effect.

Corresponding porosity curves for the Super Cosmal alloy cast in the experimental sand moulds are given in Figures 22, 23 and 24. In the unchilled and not degassed casting condition only the longest of the 15x15 mm bars exhibited high porosity of irregular distribution on its central zone while the thicker 25x25 and 50x50 mm bars presented a smooth and almost constant porosity increase from cold end to hot end.

Degassing treatment applied to the Super Cosmal melt, notably decreased porosity contents at all locations along the bar castings. However, a small uneven porosity distribution was still present in the longest of the 15x15 mm castings. The gradual porosity increase towards the riser takes place within a band of low porosity values showing feeding effectiveness of the alloy even at temperature gradients established by the unchilled sand mould system.

Chilling lowered porosity even more at all locations, enlarging the sound zone of all cast bars. Particularly the 25x25 mm castings responded very well to the applied copper chill action.

Direct riser-casting contact brought about a slow cooling zone where directionally shifted porosity from the solidifying casting could not be eliminated.

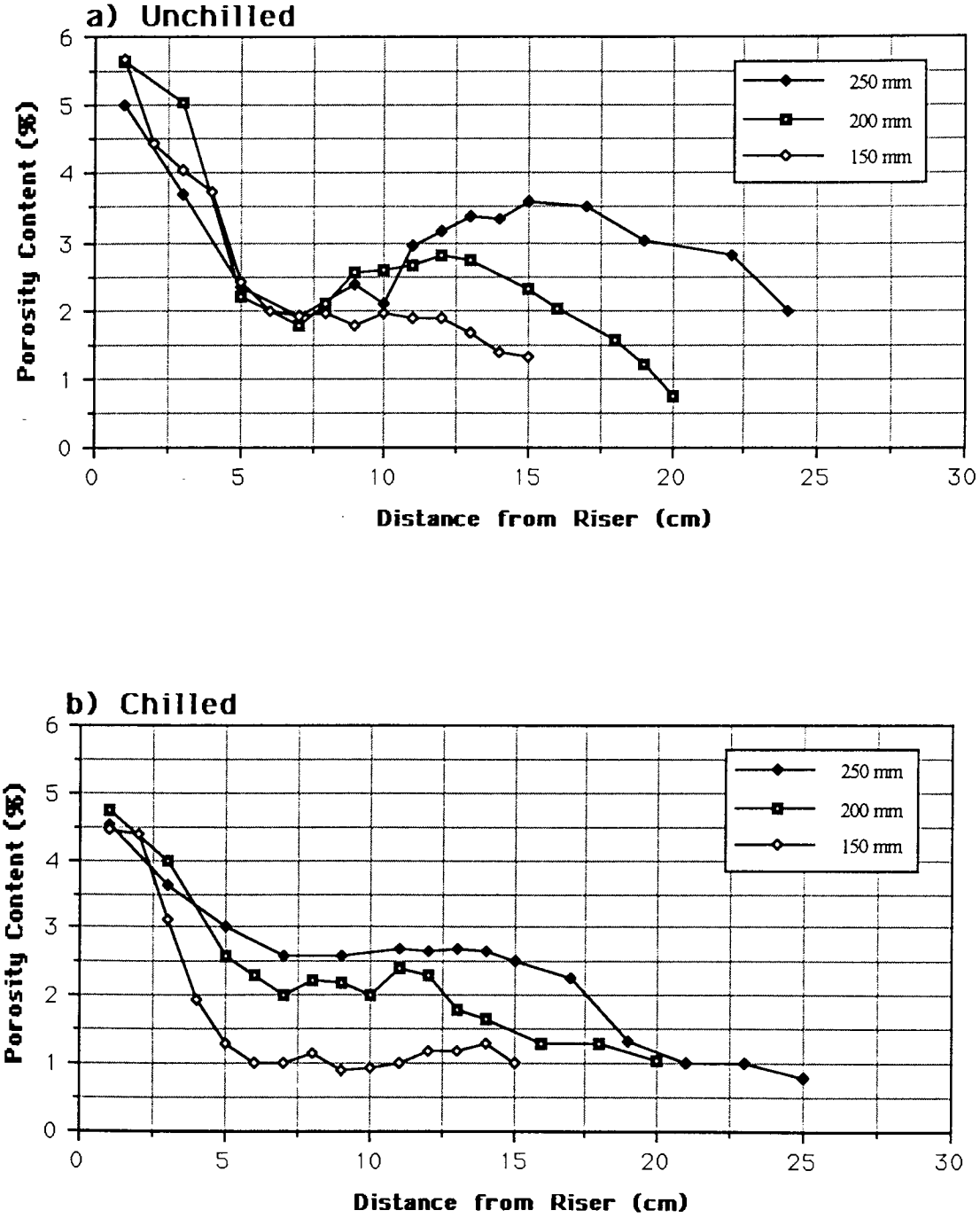

Figure 19. Porosity distribution in ZA-27 15 mm square cast bars of variable length.

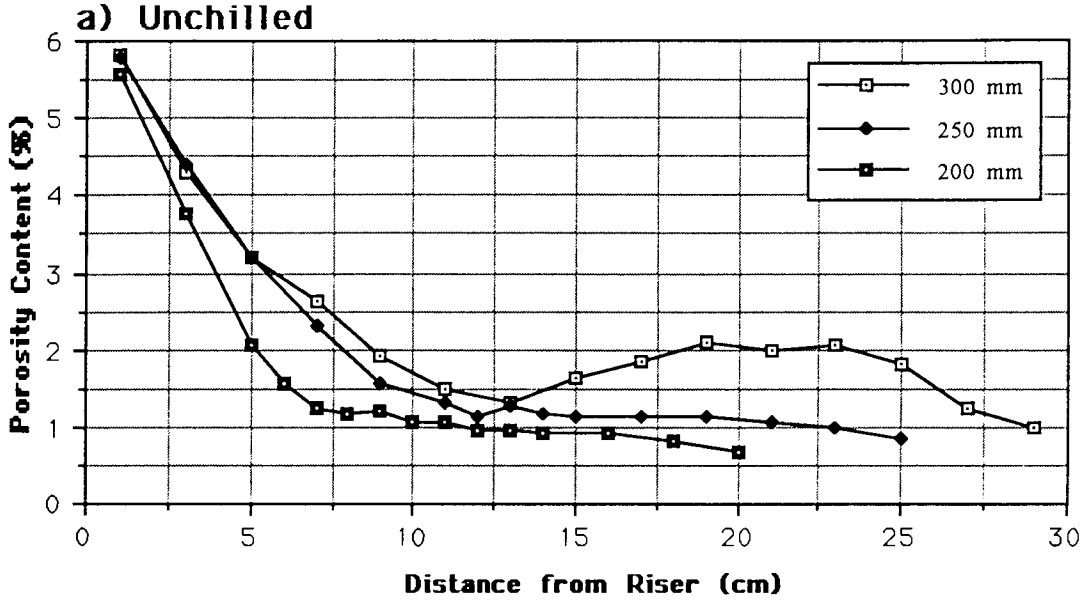

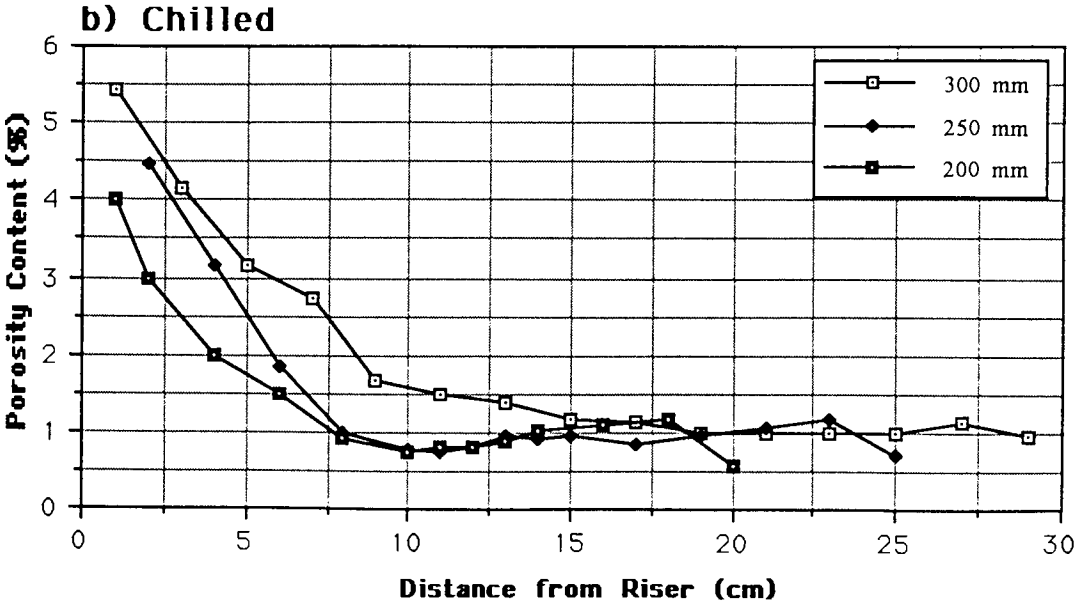

Figure 20. Porosity distribution on ZA-27 25 mm square cast bars of variable length.

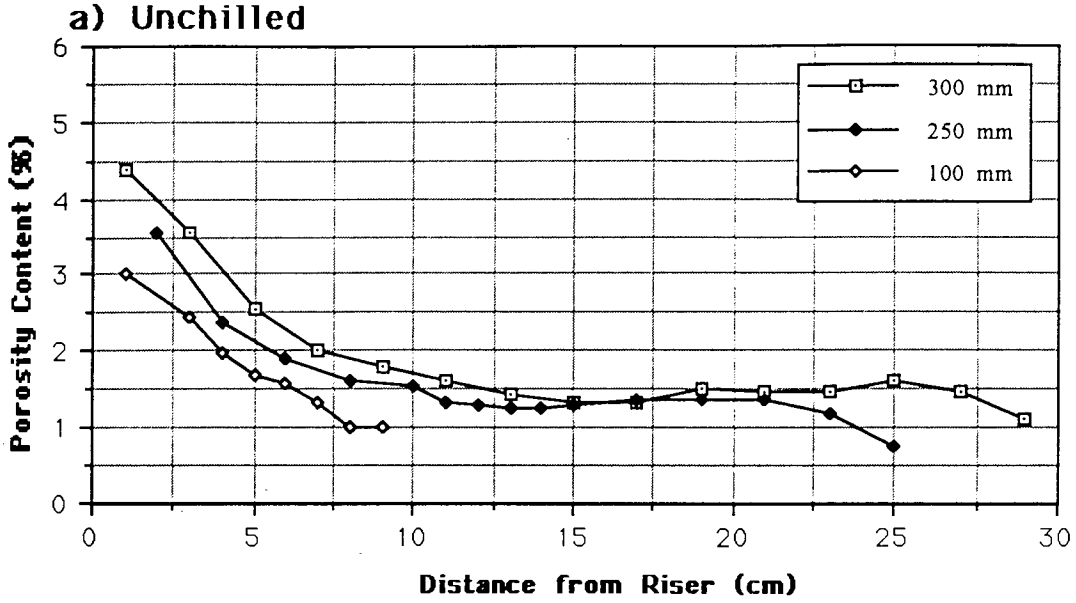

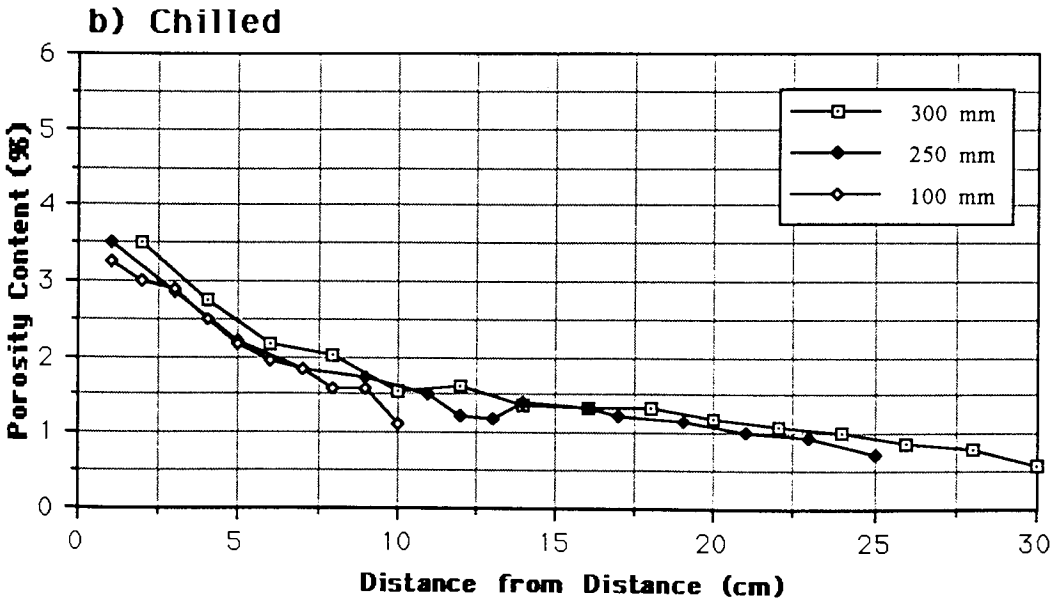

Figure 21. Porosity distribution in ZA-27 50 mm square cast bars of variable length.

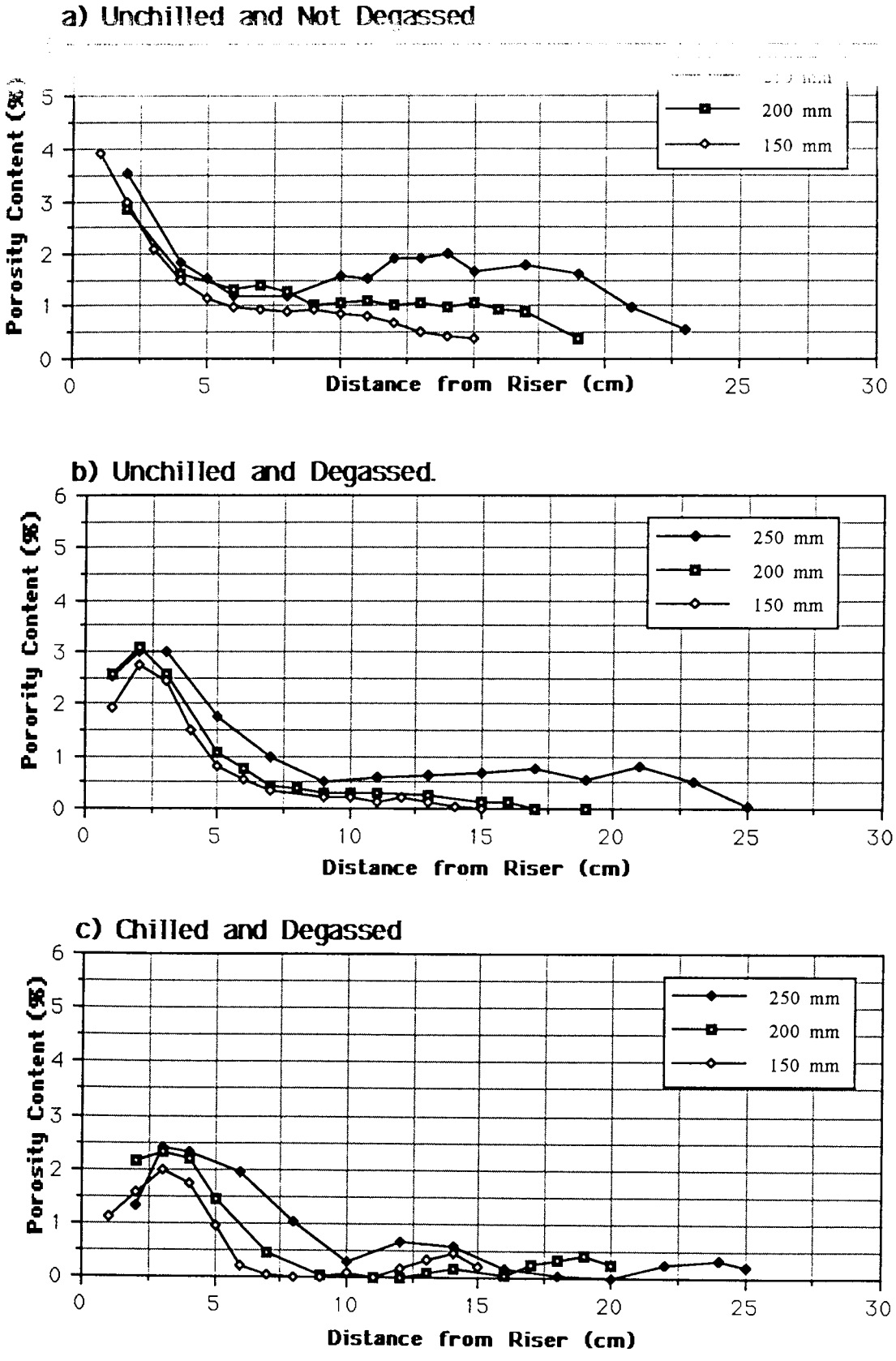

Figure 22. Porosity distribution in Super Cosmal 15 mm square cast bars of variable length.

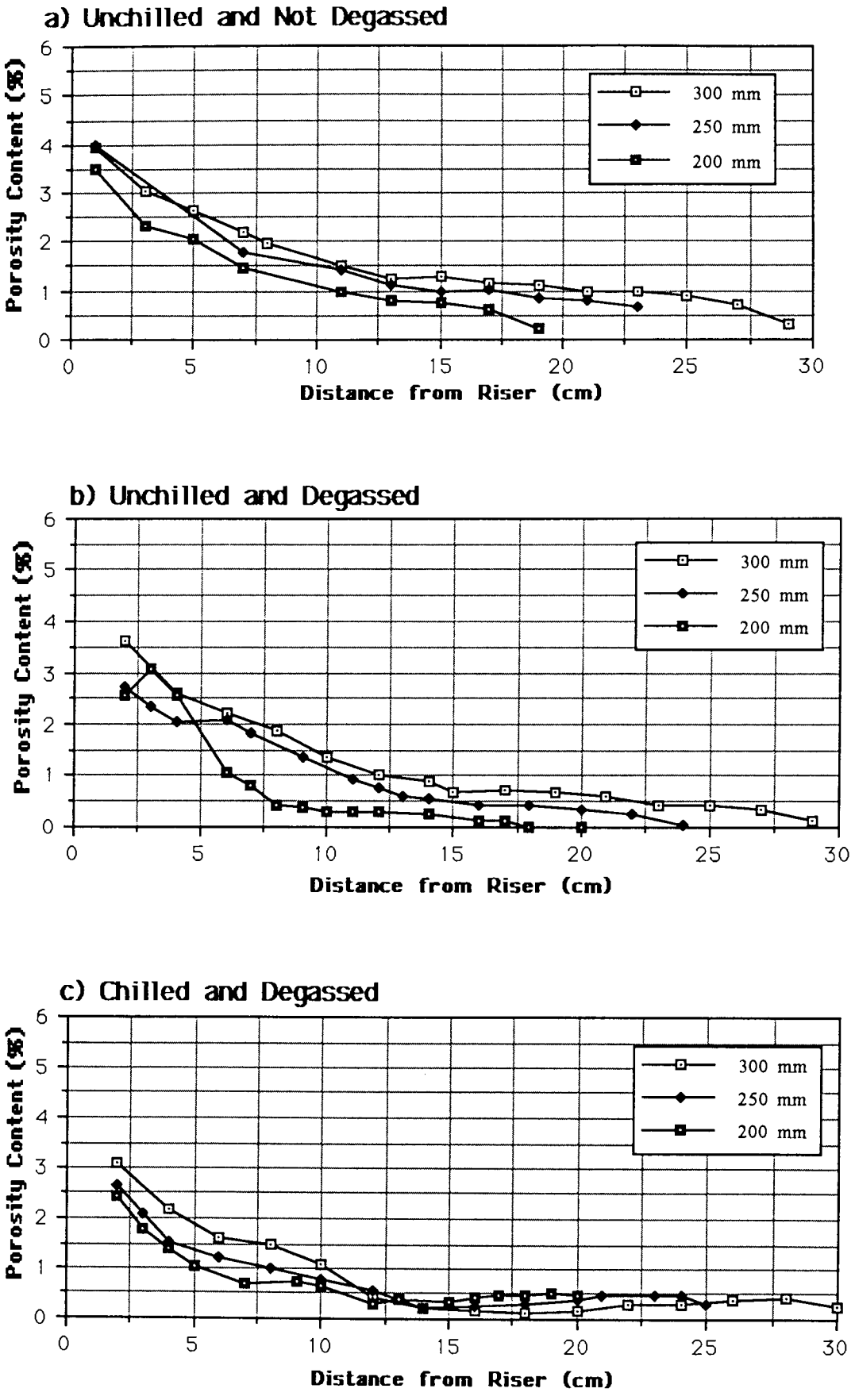

Figure 23. Porosity distribution in Super Cosmal 25 mm square cast bars of variable length.

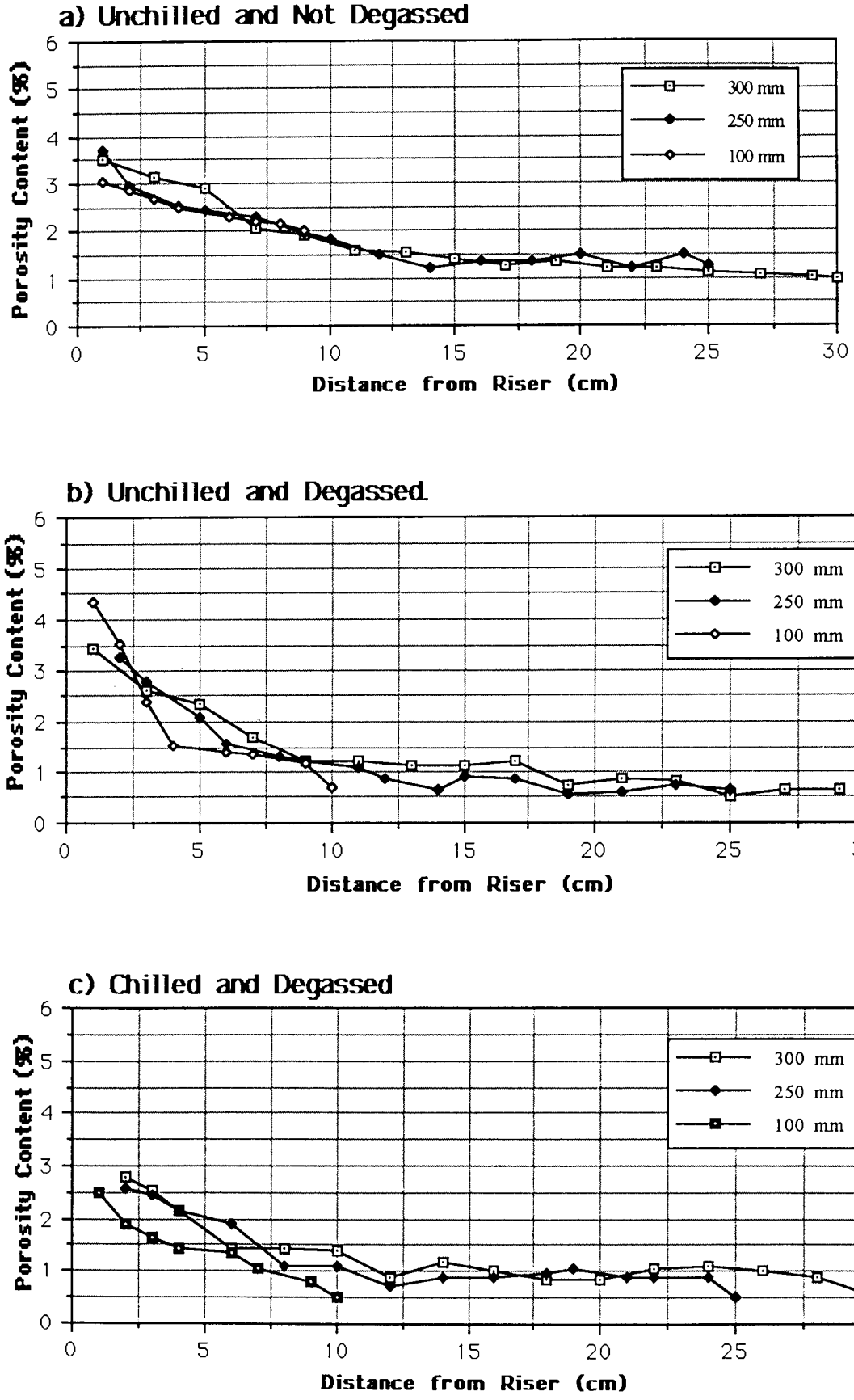

Figure 24. Porosity distribution in Super Cosmal 50 mm square cast bars of variable length.

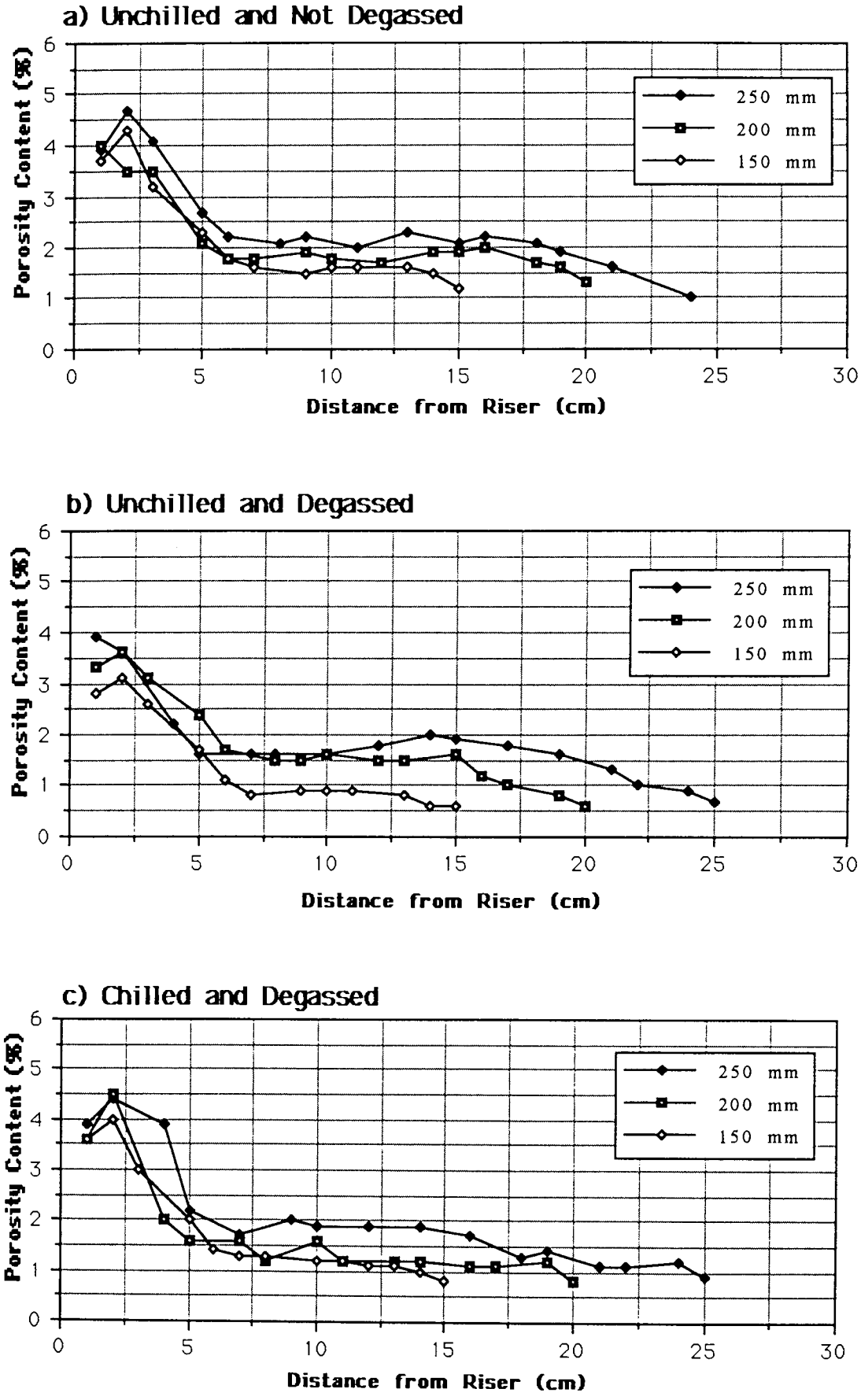

Figure 25. Porosity distribution in HAZCA 15 mm square cast bars of variable length.

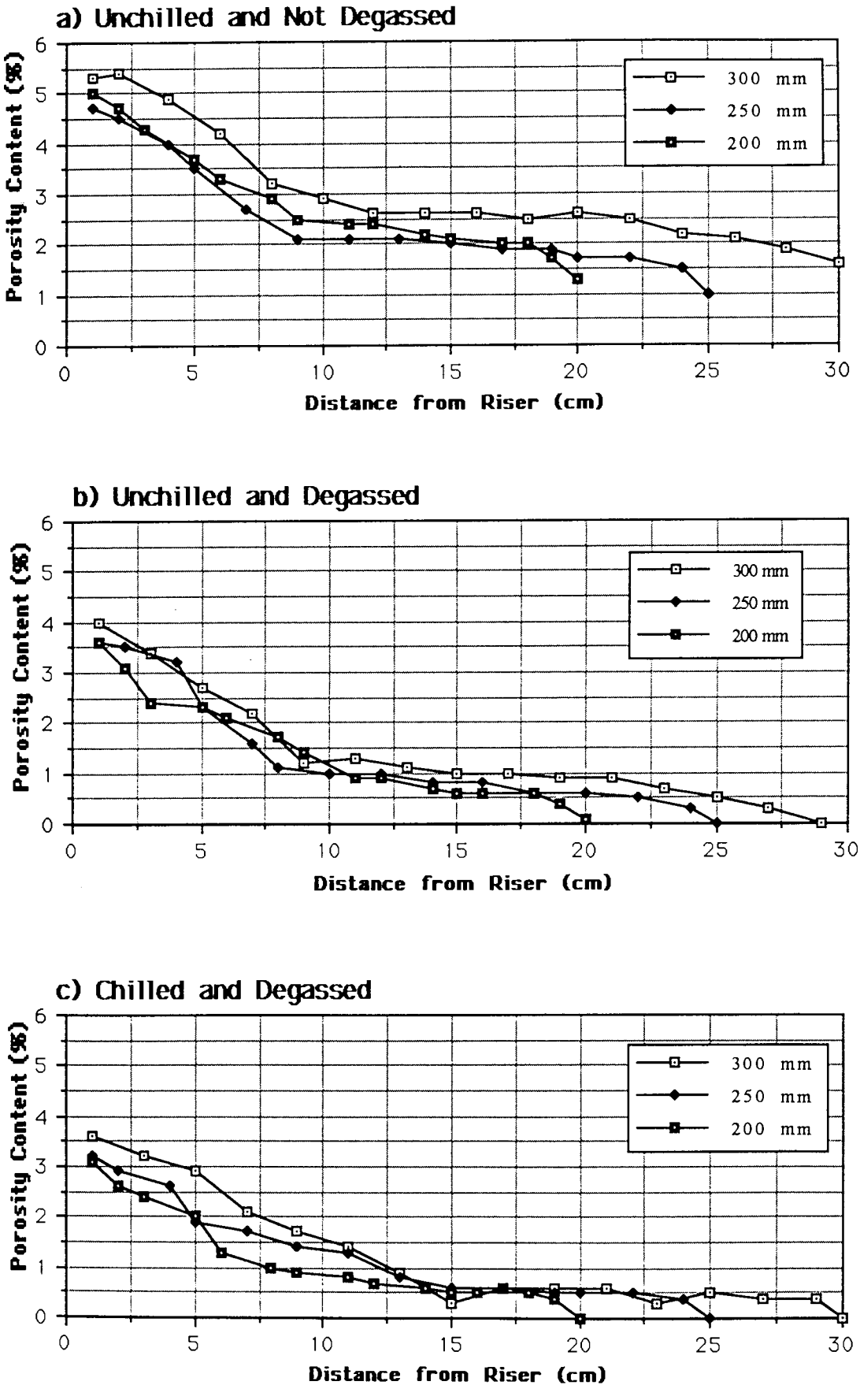

Figure 26. Porosity distribution in HAZCA 25 mm square cast bars of variable length.

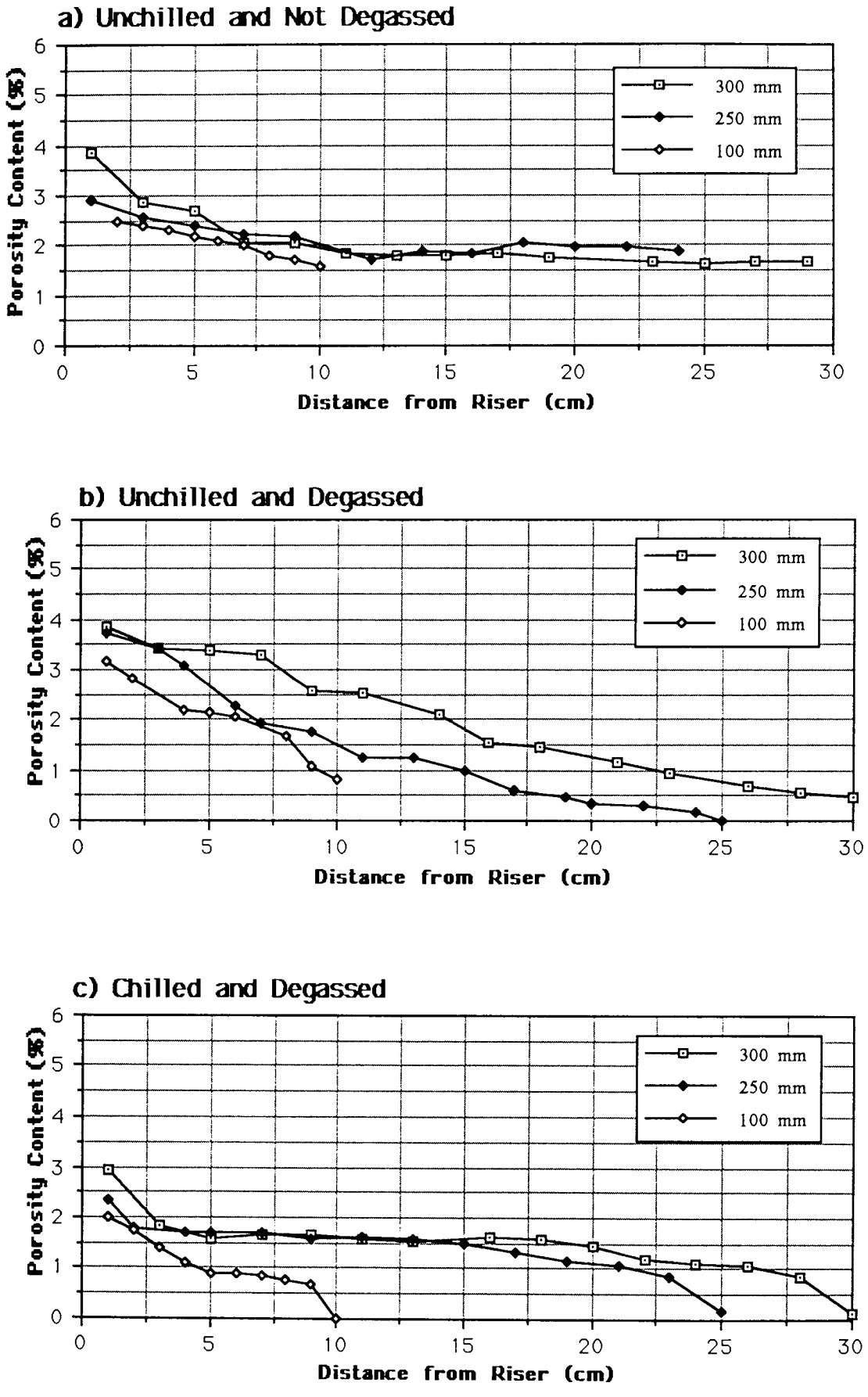

igure 27. Porosity distribution in HAZCA 50 mm square cast bars of variable length.

Experimental HAZCA alloy castings as melted in a gas-fired furnace exhibited the casting behaviour shown in Figures 25, 26 and 27. The general trend is similar to that of the Super Cosmal alloy but with slightly increased porosity contents mainly due to the greater possibility of gas pick-up during melting.

As in the case of the ZA-27 and Super Cosmal alloys and within the experimental range, the thicker the casting the more uniform the porosity distribution along cast bars. In the unchilled and not degassed casting condition porosity levels in most bars practically did not change, excluding the riser side portion. This is most probably due to the obstruction of feeding paths by the gas evolved from the solidifying casting.

The latter is confirmed by the curves corresponding to the unchilled and degassed casting condition where porosity gradients demonstrate a more effective directionality in solidification leading to better feeding.

The use of end chill was also benefited in producing higher levels of soundness and again, the copper chills used were most effective for the 25x25 mm castings.

2.5 DISCUSSION

From the cooling curves shown in Figure 17 the following points of discussion concerning the solidification mode of the Super Cosmal and HAZCA alloys can be drawn:

1. The binary Zn-Al alloy of 60%Al presented a wide range of solidification of around 220°C and solidified in a very pasty manner. Rapidly, solid aluminium-rich dendrites formed a massive network throughout the casting, leaving the zinc-rich liquid to drain down through small interdendritic channels so the thermocouple tip at the centre of the casting could not detect further thermal changes other than a constant cooling rate.

   The absence of pipe in this alloy used for comparison, is characteristic of systems with no clear solidification front. On the other hand, the development of an inverted pipe at the bottom of the heavy casting revealed gravity separation of phases. However, the magnitude of this segregation, at the same cooling rate, was less than in the ZA-27 casting mainly because of a much greater density of aluminium dendrites impinging on each other.

2. The addition of silicon as in the Super Cosmal and HAZCA alloys significantly changed the solidification of the binary Zn60%Al. Firstly the liquidus temperature dropped approximately 45°C. Secondly, and immediately after nucleation and growth of aluminium dendrites, liquid of composition near to the Al-Si eutectic remained at the central zone of the casting and began to solidify producing a thermal arrest. The highly fluid silicon-rich liquid, must feed the wide primary interdendritic spaces just before freezing. Thirdly, once the Al-Si eutectic had solidified, there still remained a liquid rich in zinc of low freezing temperature which solidified interdendritically at around 380°C.

   It seems that the influence of silicon in the high aluminium-based alloys is similar to that in aluminium-silicon alloys concerning their feeding ability. For example, Figure 12 shows that in alloys with 6-8% Si, the solid fraction formed just before the eutectic temperature of only 0.35 to 0.50 is a favourable fact for the transference of feed metal. If this is accompanied by a positive temperature gradient, filling of interdendritic channels is ensured.

No marked difference in solidification between the Super Cosmal alloy and the experimental HAZCA was found. Only the thermal arrest at the early stages was longer, due to a greater quantity of eutectic.

In both the Super Cosmal and the HAZCA alloys neither massive gravity segregation nor underside shrinkage were detected. It is thought that the rapid flow and freezing action of the silicon-rich liquid hindered gravity separation of phases.

The solidification mechanism discussed above for both high aluminium zinc-based alloys becomes the main explanation for their excellent fluidity level obtained through spiral tests. Fluidity results for both of these alloys compared favourably with those of the ZA-27 alloy which has already been shown as having a very good behaviour on this respect.
Although the HAZCA alloy is 2% higher in silicon, its fluidity results were similar to those of the Super Cosmal. This is in close agreement with Figure 10 where no significant variations of fluidity in the range of 6-8% silicon were reported.

In consequence, the alloys studied here will not contain casting defects due to incomplete filling of thin sections. Furthermore, it will be possible to use lower pouring temperatures to promote soundness.

Porosity curves obtained in bar castings showed the influence of casting size, melt degassing and use of end chills upon the degree of soundness obtained from riser end to chill end.
As no macroshrinkage was developed in any of the castings, the riser design calculated for the largest piece, was demonstrated to be effective for it and for smaller castings as well. However, signs of over-risering were noticed in the region next to riser zones.

In general, it was found that directional solidification was more difficult to achieve in thinner bars due to rapid lateral formation of dendrites blocking the flow of feed metal. Therefore and within the experimental limits here accounted, the thicker the bars the easier the feeding process under all conditions.

Another apparent fact, is that both the Super Cosmal and the HAZCA alloys are prone to gas porosity, undoubtedly due to the high hydrogen solubility in the aluminium present in these alloys. During solidification, dissolved hydrogen segregates to the interdendritic regions where gas pores are formed. Then, due to its internal pressure, they can obstruct feeding as is the case of Figure 26a.

The use of chills increased both solidification cooling rate and temperature gradient thus reducing the size of the pasty zone, increasing time for feeding and the opportunity to produce higher levels of soundness.

Although observed distribution of porosity in the casting bars was closely related to the solidification pattern of the alloys, it was considered insufficient to quantify feeding distances as a function of bar thickness and be able to compare with reported curves for ZA alloys shown in Figure 4.

2.6 CONCLUSION

Study of some foundry characteristics of high aluminium zinc-based alloys when cast in sand indicated the following:

1. Casting fluidity of both Super Cosmal and HAZCA alloys was found to be remarkably good.

2. The presence of silicon in both alloys was of primary importance in facts like: reducing the temperature range of solidification, improving feeding efficiency, reducing gravity separation of phases and eliminating underside defect.

3. High aluminium zinc-based alloys were found to be prone to gas absorption hence melt degassing is necessary.

4. Proper riser design and the use of chills to promote directional solidification constitute the most important factors to achieve sound castings.

5. No marked differences in casting behaviour were found between the Super Cosmal and the experimental HAZCA, but both behaved slightly better than the ZA-27 alloy under the experimental conditions used.

CHAPTER 3

METALLURGICAL STRUCTURE AND MECHANICAL PROPERTIES OF HIGH ALUMINIUM ZINC-BASED ALLOYS

3.1 INTRODUCTION

As in the general case of alloys, zinc-aluminium alloys not only solidify over a range of temperatures but also after becoming solid, they undergo constitutional changes which affect their properties and use. The binary Zn-Al provides information of considerable importance about structures and composition of phases that exist in equilibrium for all commercial Zn-Al based alloys. But equally as important are the ternary and quaternary systems generated by the addition of copper and silicon which show the development of new phases and changes in some metallurgical transformations that influence the engineering properties of these materials.

3.1.1 The Binary Zn-Al System

The phase diagram of Figure 1 obtained by Presnyakov et al. and confirmed by Goldak and Parr [26] is considered the most accurate constitutional representation of the Zn-Al binary at equilibrium conditions.

This equilibrium diagram shows the following characteristics and phase transformations:

1. Eutectic transformation at 5% Al and 382°C:

$$L \Leftrightarrow ß + \eta$$

where, ß is a zinc-aluminium solid solution of f.c.c. structure which contains up to 81% Zn at the eutectic temperature and is stable only at temperatures above 275°C. η is a solid solution of aluminium in zinc with the c.p.h. lattice of zinc.

2. Peritectic transformation at approximately 30% Al and 443°C:

$$L + \alpha \Leftrightarrow ß$$

where α is an aluminium-rich solid solution of f.c.c. structure.

3. Eutectoid transformation at 22% Al and 275°C:

$$\beta \Leftrightarrow \alpha + \eta$$

4. Monotectoid transformation in a range of 30% - 50% Al:

$$\alpha' \Leftrightarrow \alpha + \alpha'$$

where α' is an α phase enriched in zinc and different in lattice parameter. The lattice parameter of pure aluminium at 25°C is 4.014 Å decreasing to 4.000 Å at 65% Zn in the α region.

5. Second eutectoid decomposition at about 340°C with the eutectoid point at 30% Al:

$$\alpha' \Leftrightarrow \alpha + \beta$$

The Zn-Al system is characterised by the presence of high-temperature phase-fields extending across the phase diagram up to 80% Zn represented by α, α' and β phases all of which have the f.c.c. structure of aluminium, and a large two phase field of $\alpha + \eta$ below the horizontal eutectoid.

3.1.2 The Binaries Zn-Si and Al-Si

According to the Zn-Si phase diagram of Figure 28 zinc and silicon are insoluble in each other. Figure 7 presents the Al-Si system which forms a simple eutectic with limited solid solubility at both ends. The eutectic occurs at 580°C and 12.5% Si. At the eutectic temperature, the aluminium and silicon solutions contain 1.65% Si and about 0.5% Al, respectively. Other intermetallics do not exist in the pure binary system [27].

3.1.3 The Binaries Zn-Cu and Al-Cu

The Zn-Cu system of Figure 29 shows the existence of four intermediate phases, β, γ, δ and ε which are compound-like associations of zinc and copper atoms and are hard and brittle [28]. At the zinc-rich end of the diagram, the maximum solid solubility of copper is 2.7% at 423°C.

The aluminium-rich part of the Al-Cu system shown in Figure 30 exhibits a eutectic Al-$CuAl_2$ at 548°C and 33% Cu. The maximum solid solubility of copper in aluminium is 5.7% at the eutectic temperature under conditions of equilibrium, falling to 0.45% at 300°C.

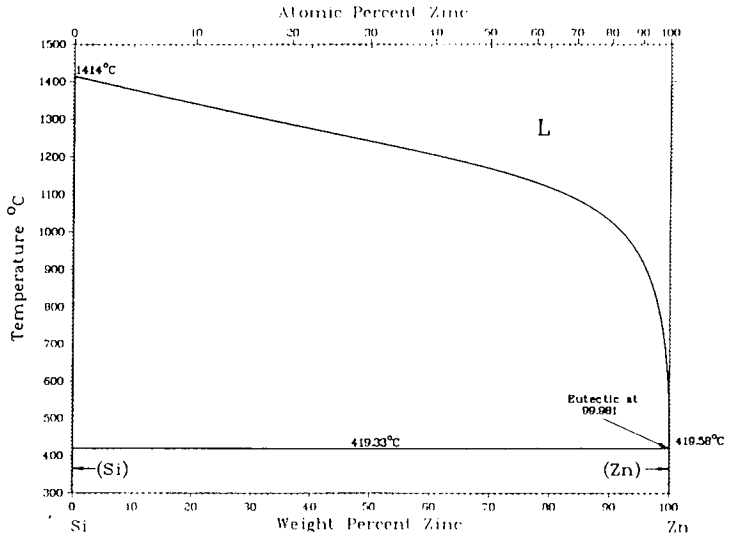

Figure 28. Equilibrium diagram for the binary Zn-Si.

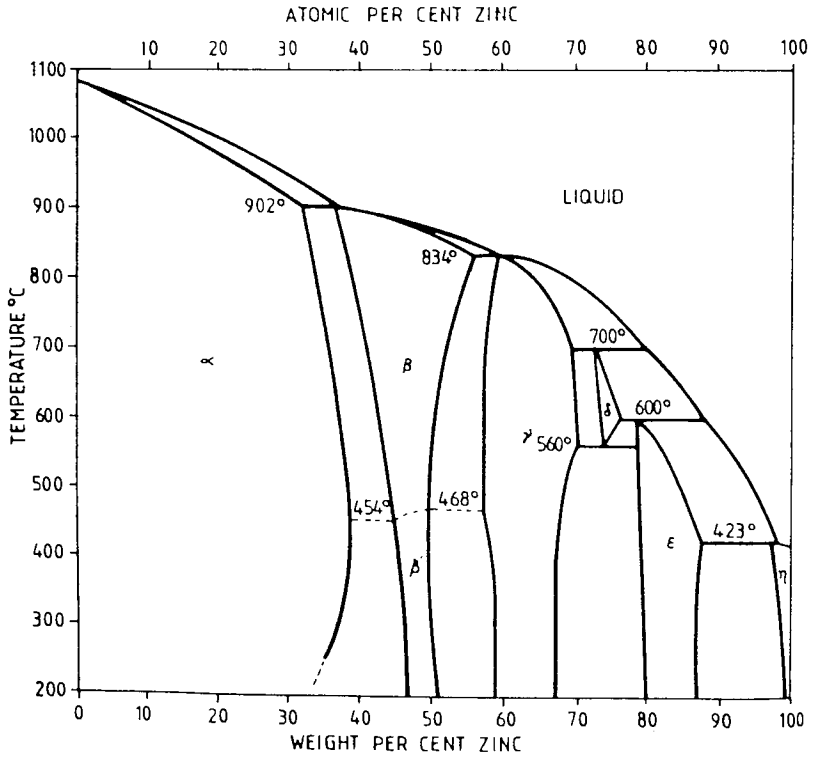

Figure 29. Equilibrium diagram for the Zn-Cu system.

3.1.4 The Ternary Zn-Al-Cu System

Many important studies of Zn-Al-Cu ternary carried out since the 1940s gave rise to the now well known isothermal sections published by Willey [29], which mainly refer to the copper-rich side of the system. The low copper part of the Zn-Al-Cu ternary was investigated by Murphy [30] who reported the isothermal sections reproduced in Figures 31-35.

As seen in the isothermal at 350°C, not only was the coexistence of the T' phase with the α and ß of the Zn-Al system at relatively high copper contents determined, but also a considerable solubility of copper in the α and ß phases, which increased with zinc content to a maximum of 4.5% at 70.9% Zn.

The isothermal section at 290°C of Figure 32 shows that the development of the α + ß field in the Zn-Al system has introduced a broad α + ß + T' field in the ternary diagram. The solubility of copper in the α and ß solid solutions has decreased to 2.5%. The ß + T' two phase field has narrowed extremely, indicating an imminent Class II four-phase reaction:

$$ß + T' \Leftrightarrow \alpha + \varepsilon$$

Figure 33 shows the 280°C isothermal section at which the four-phase reaction had been completed and a narrow α + ε phase field separates two three-phase fields; α + T' + ε, and α+β+ε.

At 270°C the isothermal section shows that ß phase had disappeared forming an α + ε + η phase field and the α+ ε phase field has narrowed, indicating another four-phase reaction just below 270°C:

$$\alpha + \varepsilon \Leftrightarrow T' + \eta$$

which resulted in a large α+ T'+ η three-phase field, shown in the isothermal section at 250°C in Figure 35.

Murphy also observed that ß decomposition in the ternary system took place at higher temperature than in the Zn-Al binary through the following four-phase reaction:

$$ß + \varepsilon \Leftrightarrow \alpha + \eta$$

A summary of the reaction sequences in binary and ternary systems is given in Figure 36.

The crystal structure of the ε phase is the c.p.h. of zinc containing 16% Cu and with an approximate formula $CuZn_4$ and a c/a ratio of 1.567 Å.

The structure of the T' phase as established by Murphy [31] is an ordered rhombohedral with a =8.676 Å and $\alpha = 27.41°$, based on an assembly of five small CsCl type cells, joined corner to corner along [111] direction. The composition of the T' was measured as 30% Al, 58% Cu and 12% Zn.

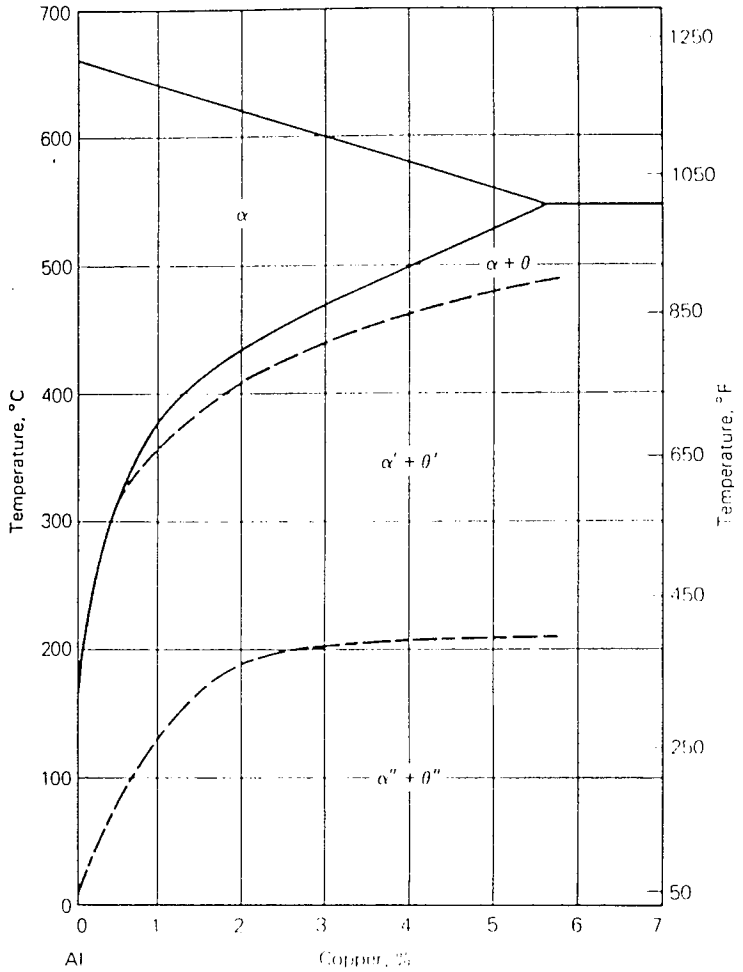

Figure 30. Equilibrium phase diagram for the Al-rich side of the Al-Cu system.

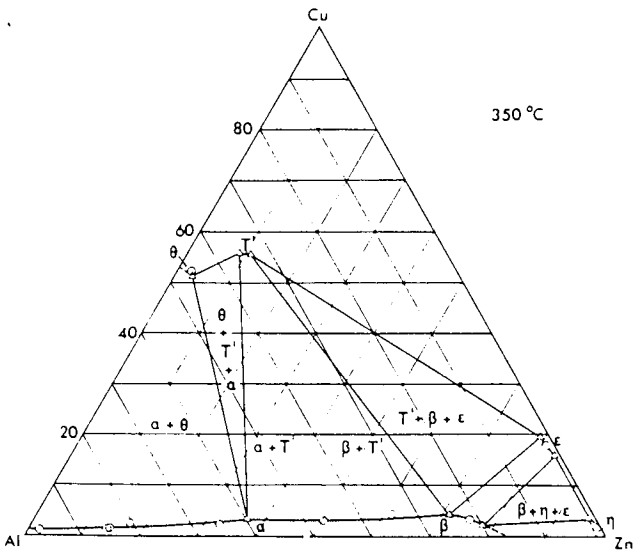

Figure 31. Isothermal section of the Zn-Al-Cu system at 350°C.

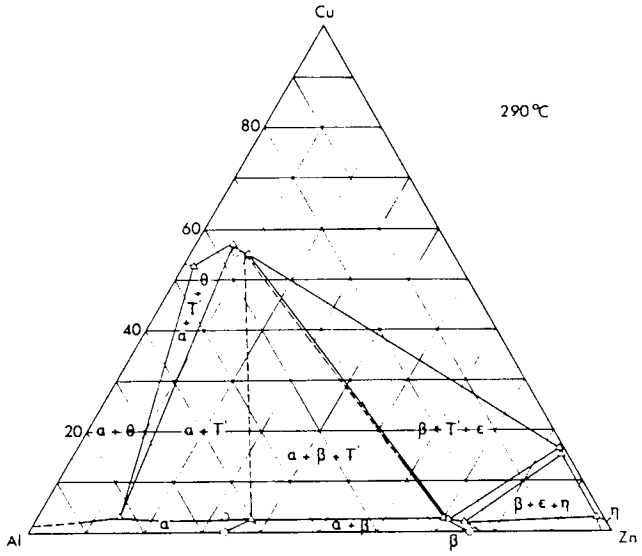

igure 32. Isothermal section of the system Al-Zn-Cu at 290°C.

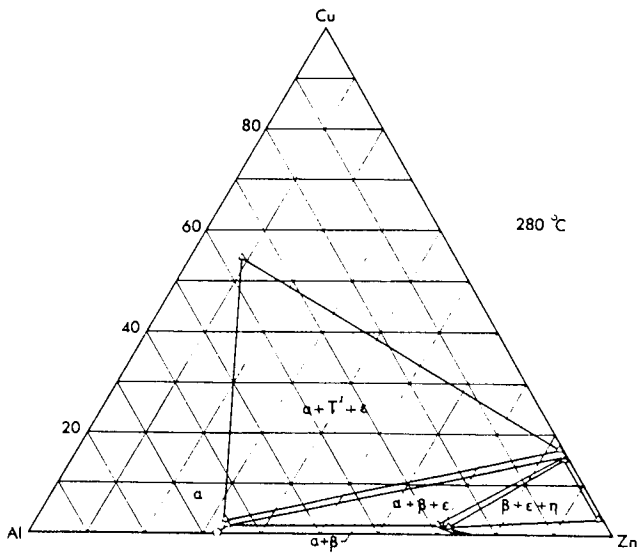

gure 33. Isothermal section of the system Al-Zn-Cu at 280°C.

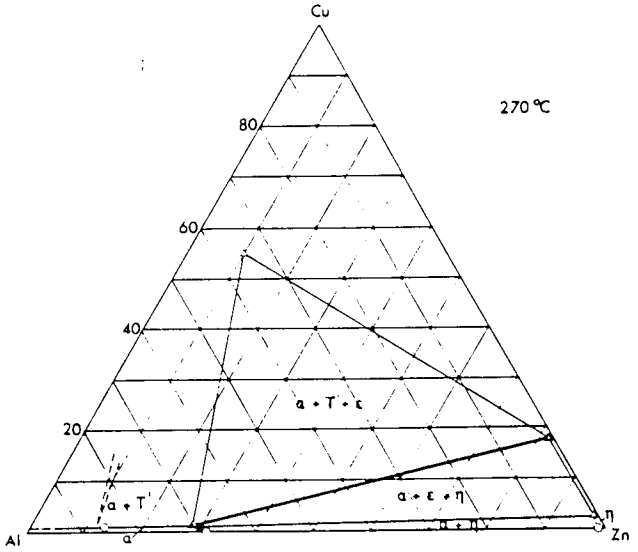

Figure 34. Isothermal section of the Zn-Al-Cu system at 270°C.

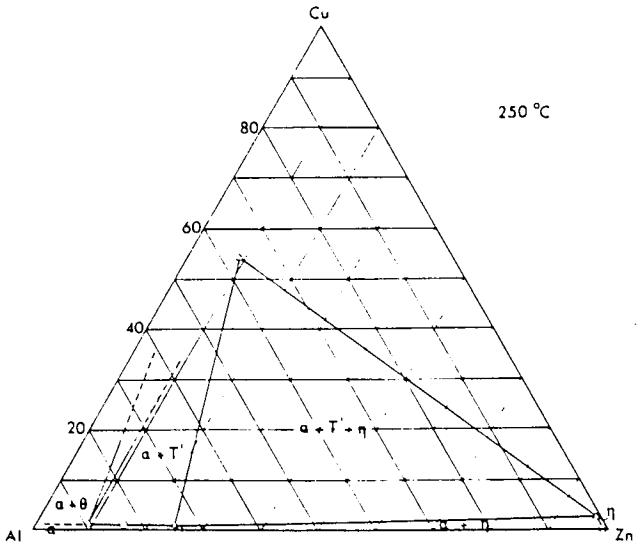

Figure 35. Isothermal section of the Zn-Al-Cu system at 250°C.

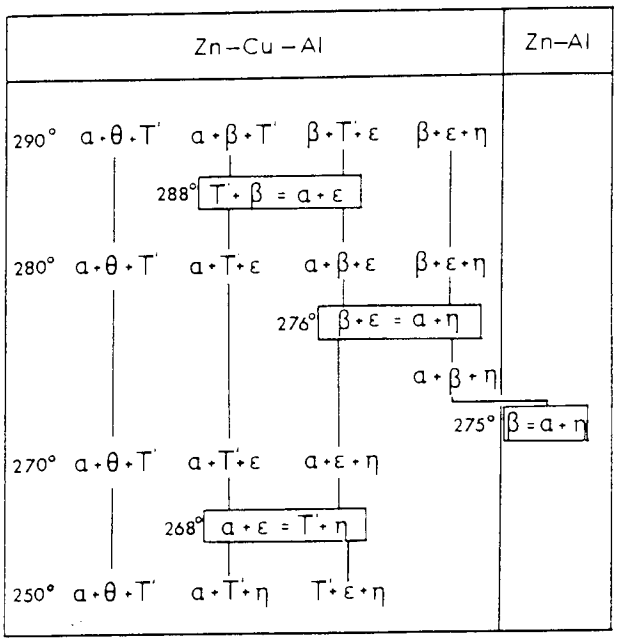

Figure 36. Solid-state reactions in the low-copper part of the Zn-Al-Cu system.

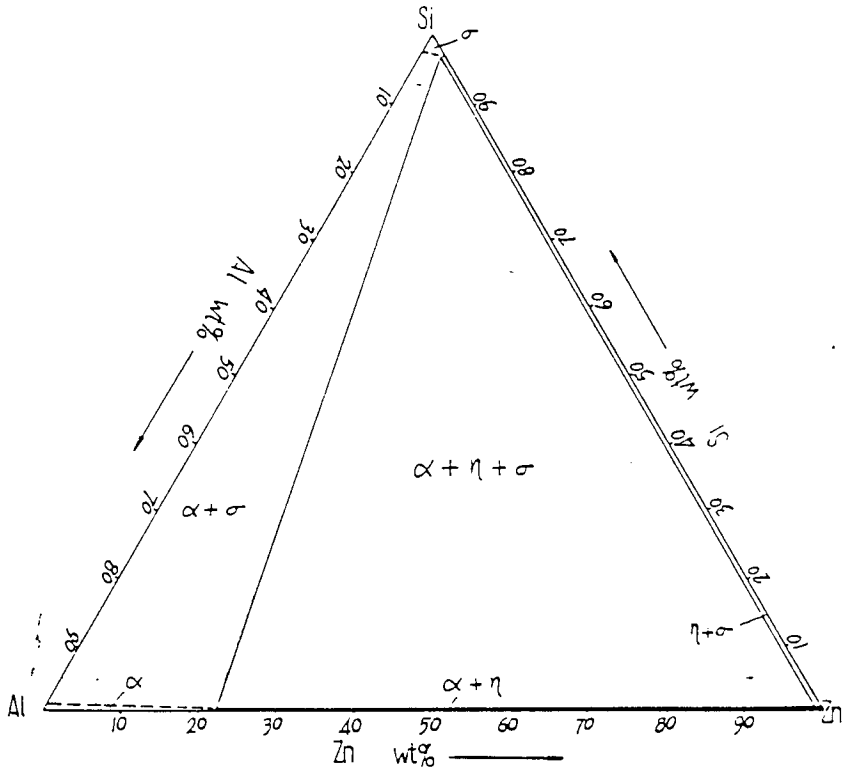

Figure 37. Isothermal sections of the Al-Zn-Si system at 350°C.

3.1.5 The Ternary Zn-Al-Si

Zhu [32] identified phases in the Zn-Al-Si system by SEM, EPMA and X-Ray diffraction studies of a number of ternary alloys at temperatures below the solidus. As a result the sothermal sections of Figures 37-41 were reported.

n all isothermal sections of the Zn-Al-Si phase diagram a terminal solid solution of Al and Zn n Si was found. It is represented by the symbol σ and exists in equilibrium with the Zn-Al ystem phases. The silicon-rich σ phase has a diamond cubic structure with a lattice parameter f 5.437 Å at 70% Zn and 27% Al and 5.402 Å at 22% Zn and 70% Al. The lattice parameter f pure silicon being 5.430 Å. These variations confirmed the fact that silicon formed a nterstitial solid solution with zinc and a substitutional solid solution with aluminium.
An increase in the solubility of Al and Zn in Si at various temperatures was found compared to he values of the respective binary systems.

he isothermal sections feature two three-phase fields which enlarge with decreasing emperature down to the eutectic point. The transformation $\beta \Rightarrow \alpha + \eta$ was detected at 266°C o that at 230°C a large three phase field of $\alpha + \eta + \sigma$ was formed.

rom the analysis of a vertical section of the Zn-Al-Si diagram at 0.2% Si, Zhu concluded that licon presented little effect on the phase boundaries of the Zn-Al system except that ß ecomposition occurred at a lower temperature.

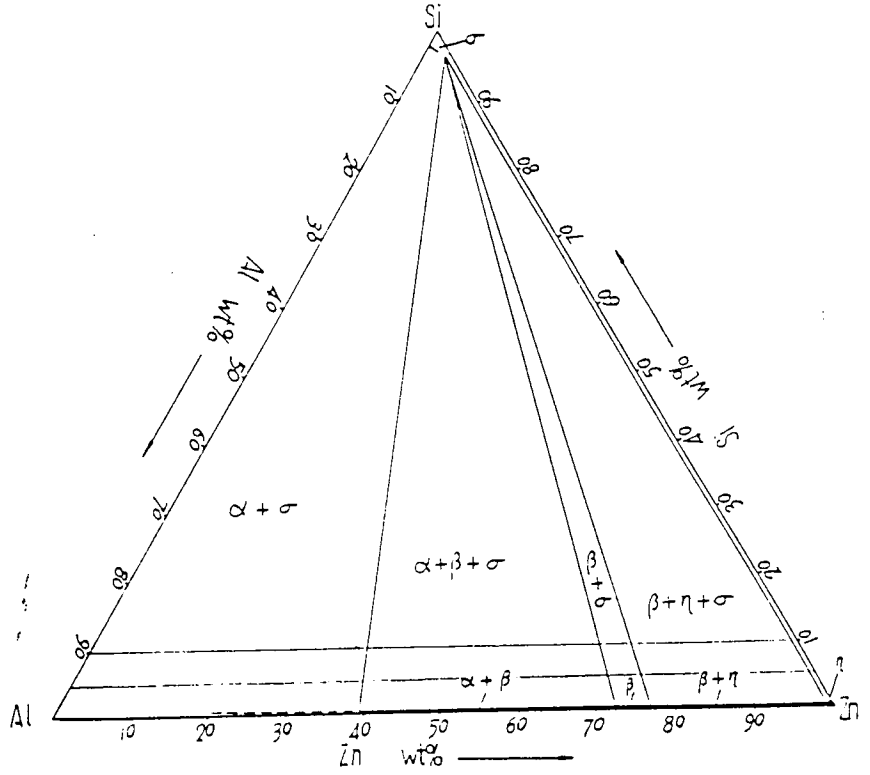

igure 38. Isothermal section of the Al-Zn-Si system at 300°C.

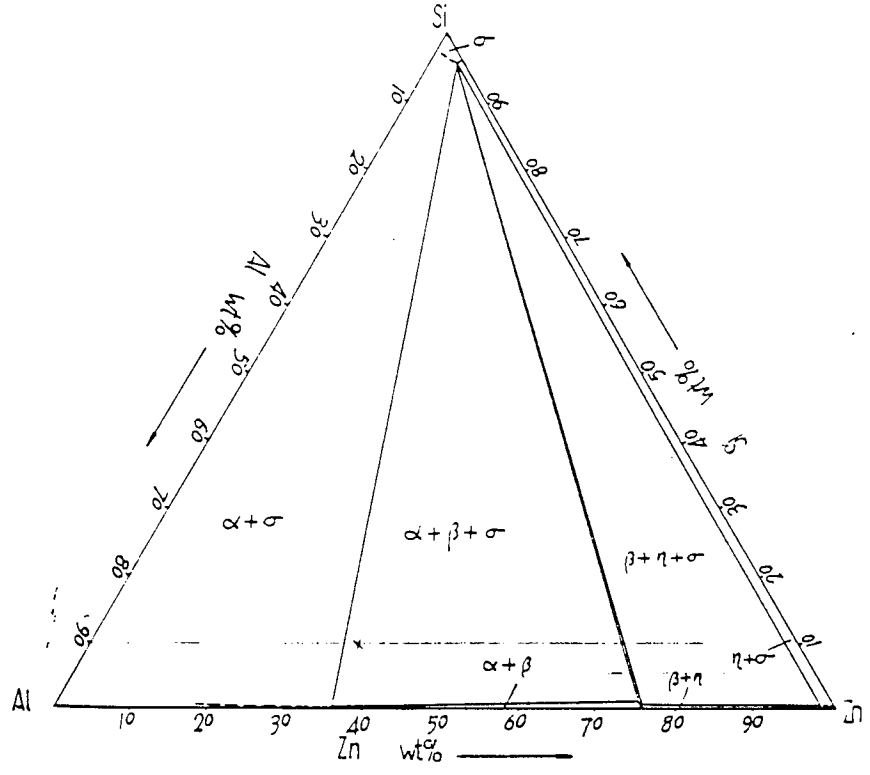

igure 39. Isothermal section of the system Al-Zn-Si system at 280°C.

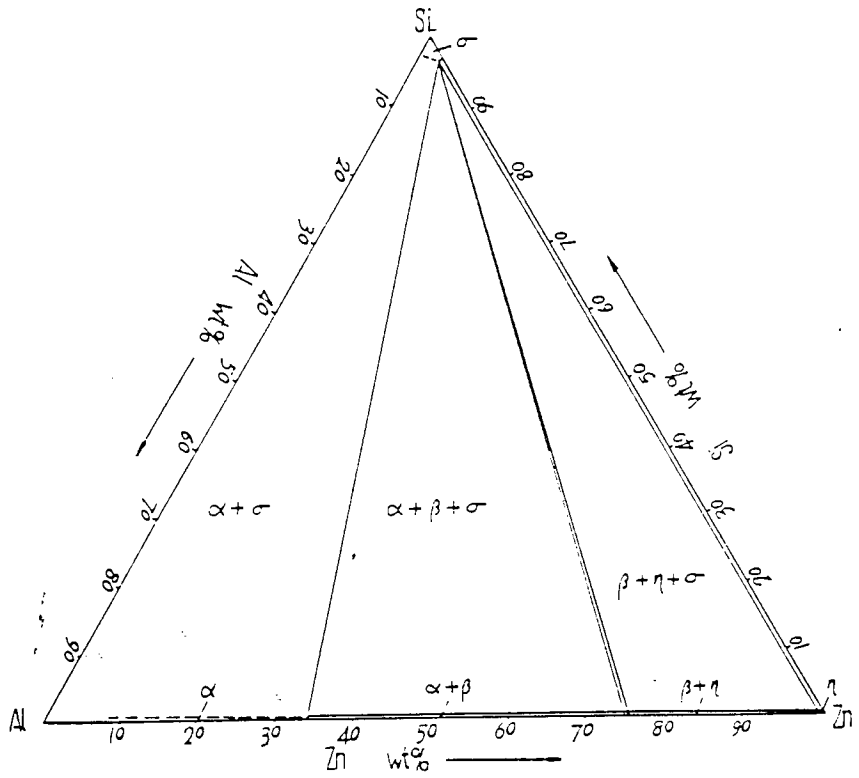

igure 40. Isothermal section of the Al-Zn-Si system at 272°C.

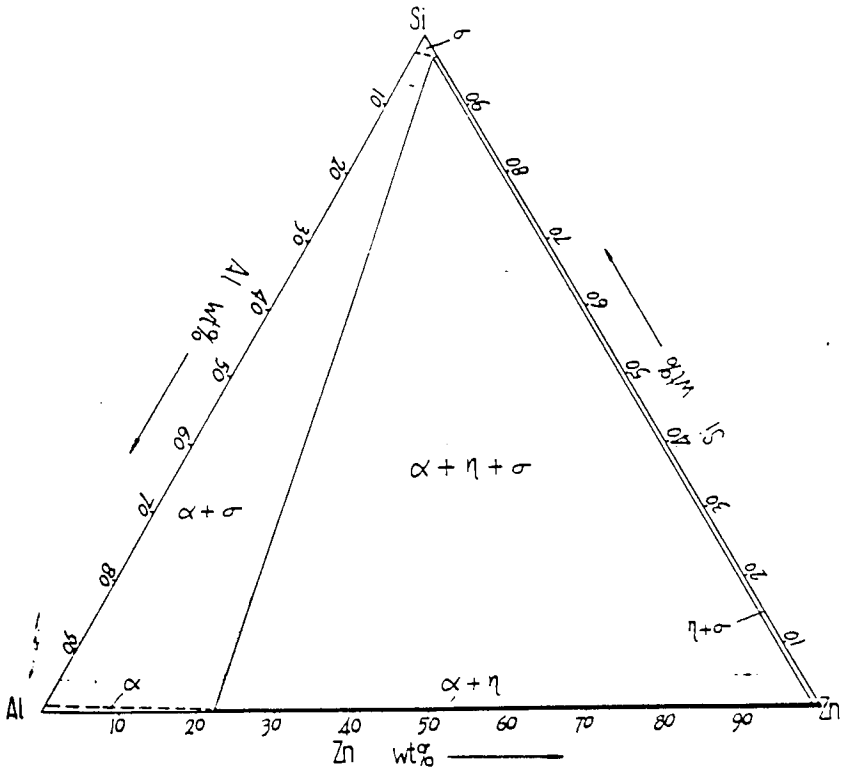

igure 41. Isothermal section of the Al-Zn-Si system at 230°C.

.1.6 The Zn-Al-Cu-Si Phase Diagram

hu also investigated the quaternary system in which phase relationships at various mperatures were represented by a pseudo Al-Zn-Cu ternary. Comparing the isothermal ctions obtained with those of the actual Al-Zn-Cu diagram determined by Murphy, no ifferences in the construction and in the position of the phase fields were found except for the ntent of Cu in the T' phase which was slightly different at 280°C and 275°C.

.1.7 Phase Transformations in Commercial Zn-Al base Alloys

lost of the high temperature phases of the Zn-Al system are retained either after casting or after uenching, i.e. they become thermodynamically metastable with the tendency to transform into stable state. Mykura, Zhu and Murphy [33] have established the occurrence of short term ansformations and long term transformations in the solid state:

hort term transformations

- The decomposition of eutectoid phase ß into stable constituents $\alpha + \eta$.

- The precipitation of excess zinc from the supersaturated α solid solution to the equilibrium constituents $\alpha + \eta$.

- Decomposition reactions of high-aluminium alloys on slow cooling via a monotectoid reaction, two eutectoid reactions and a solubility change.

ng term transformations

The transformation of the epsilon phase ($CuZn_4$) formed during cooling into a new copper-rich T' phase stable at room temperature. Under equilibrium conditions the transformation has been reported as:

$$\alpha + \varepsilon \Leftrightarrow T' + \eta$$

This reaction is responsible for the dimensional metastability of the commercial zinc-aluminium alloys with high copper contents because the product phases have lower specific gravity than the reactant phases resulting in a net expansion on ageing [33].

Toldin et al. [34] studied the process of decomposition of supersaturated solid solutions in Al-Zn alloys with 40, 50 and 60% Zn (AlZnII) and in an alloy containing 73% Zn (AlZn III). They generalised the possible sequences of transformation that could occur depending on composition, cooling rate and heat treatment temperature Phase transformations occur through metastable phases R, α'_m and G.P. zones which are formed from the supersaturated state by nucleation or spinodal decomposition.

2. Dilute f.c.c. Al-rich alloys, on ageing, decompose to give the Al-rich solid solution (α) and the following series of precipitations:

Spherical G.P.→ zones	Rhombohedral Transition→ phase α''_m	f.c.c. Transition→ phase α'_m	Zn-rich stable precipitates

The rhombohedral α''_m phase differs only slightly in lattice parameters (a = 3.992Å , α =91.31°) from the cubic α'_m phase (a = 3.995Å).

3.1.8 Phase Transformations in the Zn-Al-Cu-Si System

Zhu and Murphy [35] have reported a study of the decomposition of supersaturated phase during quench-ageing of a monotectoid alloy of composition AlZn60Cu3Si2 in which a cellular reaction $\alpha'_S \rightarrow \alpha'_T + \varepsilon + \eta$ as the first stage of transformation was found. On the subsequent ageing a fine scale clustering of zinc atoms formed GP zones then followed by the precipitation of transitional α''_m and α'_m phases as shown in the sequence that follows:

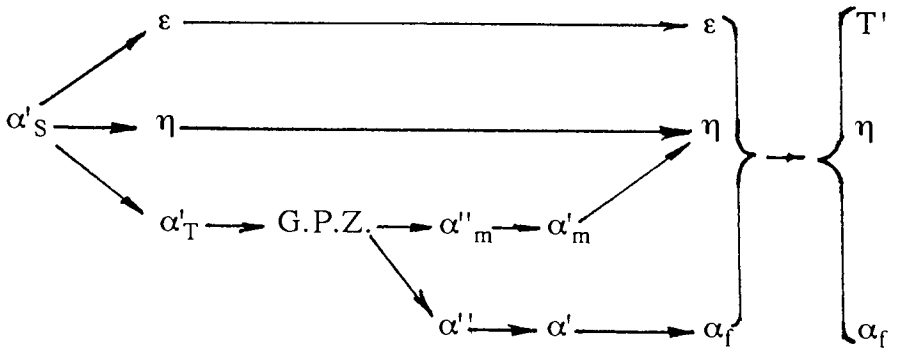

For an Al-rich alloy (AlZn30Cu3Si2) which is out of the $\alpha + \beta + \varepsilon + T'$ phase field the decomposition of the supersaturated solid phase starts with a different sequence [32] as shown in the summary that follows:

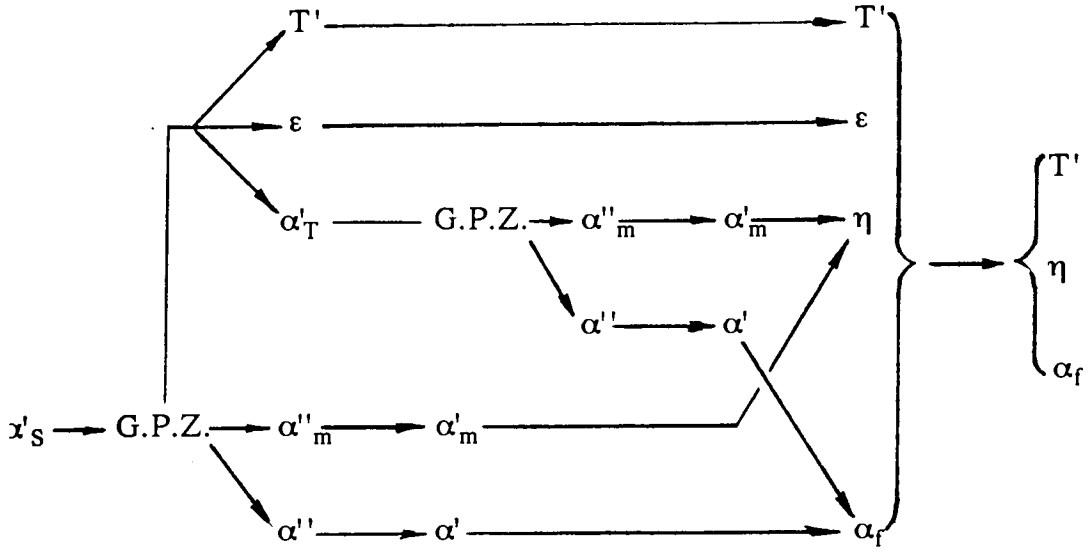

α'' and α' are Al-rich matrix phase in equilibrium with α''_m and α'_m respectively.

3.1.9 Effect of Alloying Elements on General Properties of Zn-Al Based Alloys

Copper and Magnesium

Koudelis and Dallen [35] have reported that magnesium and copper of 0.25% and 3.0% respectively alloyed with zinc containing 30-50% Al, can decrease the rate of decomposition of the high temperature phases therefore affecting the mechanical properties of the zinc alloy after solution heat treatment. They reported a significant increase in strength and hardness but the alloy suffered a decrease in ductility.

Copper additions are also made to increase creep strength and to improve corrosion resistance. However, the addition of too much copper to zinc-aluminium alloys influences the ageing characteristics; so that mechanical properties decrease and dimensional growth with time occurs.

Durman and Murphy [36] carried out a TEM and electron diffraction study of a hypereutectic Zn-Al alloy containing copper and determined the role of copper in improving the mechanical properties of the alloy. The identification of a dense dispersion [illegible] copper-rich ε-phase particles in the η_f matrix, indicated that the improvements were due to the effects of this precipitate on the strength of the η phase which is the major phase in the zinc-rich commercial alloys.

Magnesium is mainly used as an alloying element in small concentrations to improve hardness, U.T.S. and creep strength as well as to retard intergranular corrosion.

In a development program that led to the formulation of sand cast ZA alloys, contents of copper and magnesium were optimised with respect to their effect on tensile properties [3]. Some results are shown in Figure 42 where copper additions of up to 3-4% significantly increased tensile strength but reduced ductility. It was also shown that the influence of small additions of magnesium on tensile strength was strong, and that beyond a magnesium level of 0.01% there was no further increase in tensile strength. The effect of Mg in Cu-containing alloys was similar to that noted on the binary alloys and because of the independent strengthening effect of copper, higher levels of tensile strength were attained.

In the recently developed Cosmal alloys magnesium was considered not applicable because of its detrimental effects on damping capacity, instead copper was added to prevent intergranular corrosion [2].

Silicon

There is little information about the influence of silicon on the mechanical properties of zinc-aluminium alloys and mentioned above, Zhu [32] found that silicon appears to have minor effect on the phase equilibria of Zn-Al based alloys. However, in the high aluminium Cosmal alloys 1.5% - 6% Si was added not only to improve castability but also high temperature strength and creep strength without negative effects on damping capacity [2].

In aluminium based alloys silicon contents of up to 10 - 12% increase tensile strength and hardness at the expense of ductility. When the alloy is modified the improvement of strength is more noticeable and the drop of ductility is less pronounced as shown in Figure 43 [27].

The presence of hard, but brittle, silicon crystals in the eutectic matrix of Al-Si alloys provides the wear resistance which makes these alloys so attractive for automobile components such as engine block and heads, pistons and transmissions.

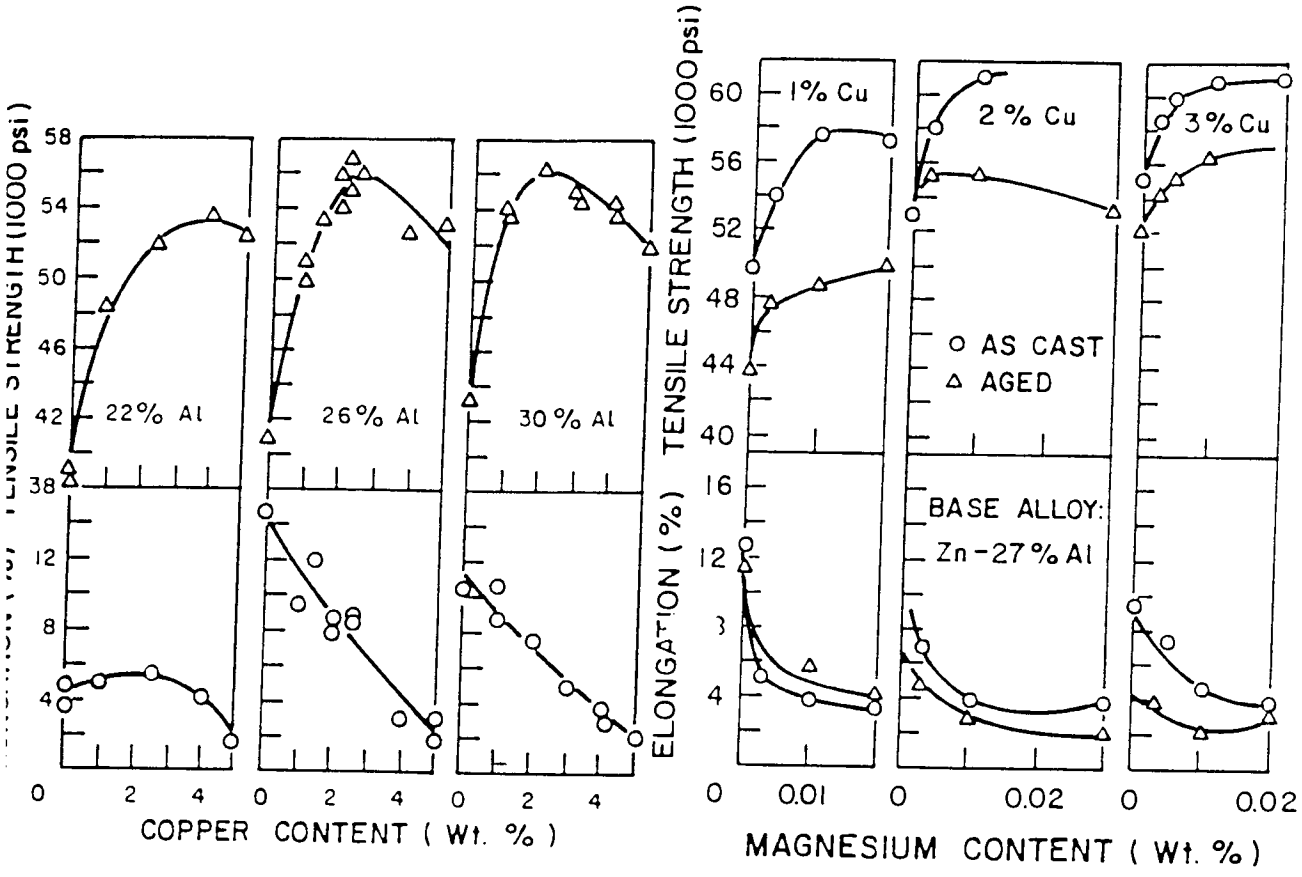

Figure 42. Tensile properties of sand cast Zn-Al alloys as a function of copper and magnesium content [3].

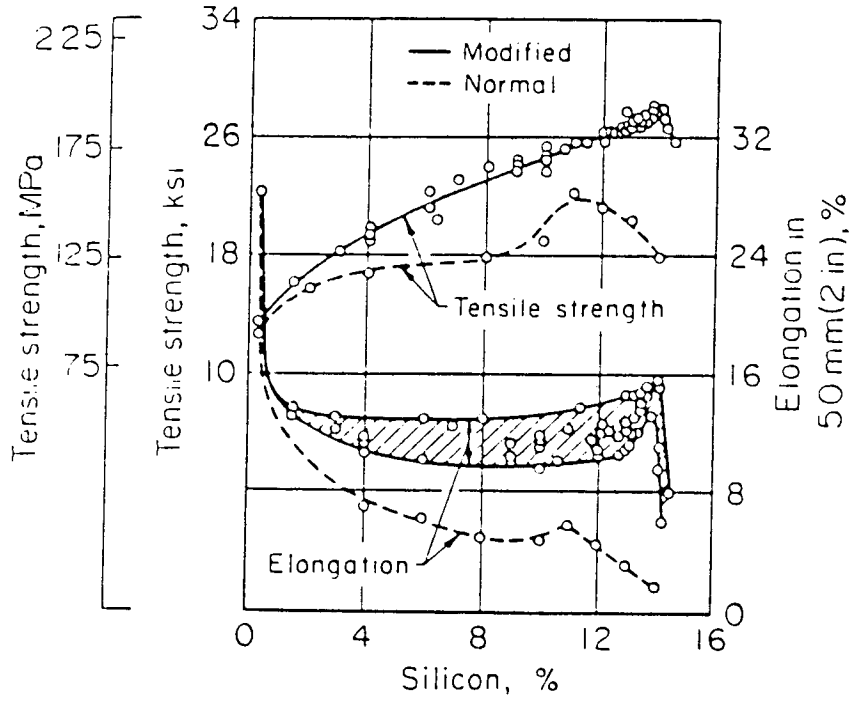

Figure 43. Tensile properties of sand cast Al-Si alloys as a function of the silicon content [27].

Manganese

From a value of 0.47% at 400°C, the solubility of manganese in zinc decreases with temperature to a very small value, and it gets even smaller when zinc is alloyed with aluminium. Therefore the use of manganese as an alloying element in Zn-Al based alloys is very limited. Once again, Mae and Sakono-oka [2] reported that a value of 0.3% Mn in the high aluminium Cosmal alloys was effective to improve high temperature strength and creep resistance.

Manganese in aluminium reduces the susceptibility to intergranular or stress corrosion [27].

Impurities

Lead and tin are considered to be impurities in zinc-aluminium based alloys and should not exceed 0.07% and 0.05% respectively. The solid solubility of lead in zinc is very low and its presence in Zn-Al alloys result in a massive corrosion which can spread quickly along the grain boundaries.

The presence of cadmium exceeding 0.005% badly affects the castability and mechanical properties of Zn-Al alloys.

The presence of iron to a degree of more than 0.02% can be harmful, as it tends to form the $FeAl_3$ compound with aluminium.

Arsenic, indium, antimony, bismuth and mercury are considered harmful impurities as they cause intergranular corrosion.

3.1.10 Effect of Casting Conditions on Mechanical Properties

Casting variables like thermal gradients, cooling rates and riser-gating arrangements have a marked effect on the soundness and microstructure of zinc-aluminium alloys. When present, porosity or interdendritic shrinkage can lead to a reduction in properties of castings, in particular tensile ductility and impact strength. On the other hand, dendrite arm spacing, grain size, presence of impurities or precipitates and inclusion content are microstructural factors that can alter the mechanical performance of castings.

Barnhurst and Gervais [36] studied the effect of soundness level, secondary dendrite arm spacing and inclusion content on the mechanical properties of ZA-27 alloy employing semi-continuously cast, sand cast and permanent mould cast specimens. Figure 44 reproduce some results of this study where impact toughness and percent elongation display a large decrease as a function of increased porosity. The sand cast material shows higher impact strength at equivalent soundness levels up to a porosity level of about 1.6 vol. %. The structural factor that explains this difference is that the sand cast material showed not only larger dendrite size, but that much greater quantities of ß and ε phases were formed in the cast structure with a corresponding reduction in the amount of eutectic. Tensile strength shows little dependence on soundness up to a level of 1-1.5% for both sand cast and concast material. However porosity levels greater than 2% results in the lowest strength. The authors of the work found as well, that only where soundness fell below 0.5% did the dendrite arm spacing play a role in property development. Finally, the report establishes that the presence of iron exceeding 0.05% reduced ductility and impact strength, but did not influence the tensile strength.

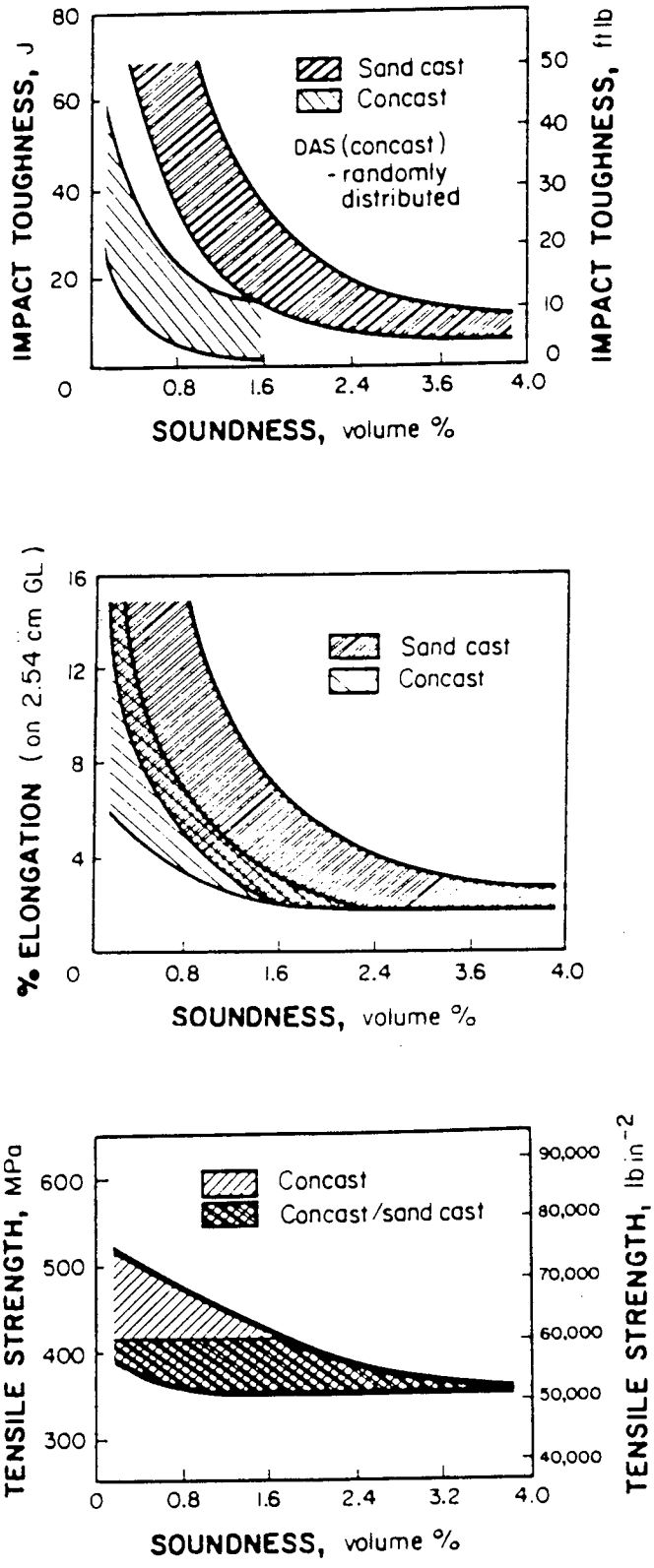

Figure 44. Influence of soundness on impact strength, % elongation and tensile strength in sand cast ZA-27 alloy [36].

3.1.11 Typical Mechanical Properties of Casting Alloys

A comparison of typical mechanical properties of zinc-aluminium based alloys with some common casting variables is given in Table 5 where the UNS number designation corresponds to the following:

Al-based alloy 319 has 6% Si and 3.5% Cu as major alloying elements.
Al-based alloy 357T6 is a heat treated alloy of 6.5-7.5% Si and 0.5% Mg.
Cu-based alloy C83600 is a leaded red brass of 5% Zn, 5% Sn and 5% Pb.
Cu-based alloy C93200 (SAE660) is a high-lead tin bronze of 3% Zn, 7% Pb and 7% Sn.
Cu-based alloy C95300 is an aluminium bronze of 10% Al and 1% Fe.
Cu-based alloy C86500 is a manganese bronze of 39% Zn, 1% Al and 1% Mn.

Strength and hardness of ZA-27 alloy compares favourably with most casting alloys. Its toughness strength and ductility are similar to Al-based alloys and gray iron but very low compared to Cu-based alloys.

Cosmal and Super Cosmal alloy as die castings possess medium strength and high hardness but are low in ductility.

3.1.12 Effect of Temperature in Mechanical Properties

The low melting point of zinc alloys is clearly an advantage in the foundry, but it also makes the properties of the alloys very temperature sensitive. The values in Table 5 are measured at 20°C but as can be seen in Figure 45 strengths are significantly reduced at 150°C. Hardness follows similar pattern. Elongation, however is greatly increased with temperature.

Table 5. Mechanical properties of zinc-aluminium alloys and other casting materials [37,2]

Alloy	Tensile Strength (MPa)	0.2% Yield Strength (MPa)	Elong. in 50 mm (%)	Youngs Modulus (MPa)	Impact Strength (J)	Hardness HB/HV
Zn-Alloys						
ZA-8 (S)	250	200	1	85	20	85
ZA-8 (P)	255	207	1	85	--	88
ZA-8 (D)	372	290	8	--	42	100
ZA-12 (S)	300	207	2	83	25	100
ZA-12 (P)	320	207	2	83	--	100
ZA-12 (D)	400	317	5	--	28	100
ZA-27 (S)	410	365	3	75	--	115
ZA-27 (P)	420	365	2	--	--	115
ZA-27 (D)	421	365	2	--	--	115
Cosmal (D)	294	235	1	72	--	120V
S. Cosmal D)	335	294	0.5	82	--	130V
Al-Alloys						
319 (S)	185	124	2	74	5	70
357-T6 (P)	262	185	5	72	11	80
Cu-Alloys						
C83600 (S)	255	117	30	83	--	60
C86500 (S)	490	193	30	103	42	98
C93200 (S)	240	124	20	100	8	65
C95300 (S)	450	70	20	110	31	81
Cast Irons						
Gray Iron	214	124	--	100	--	210
Malleable ron (S)	345	221	10	172	60	130

D) Die casting, (P) Permanent mould, (S) Sand casting.

The high temperature characteristics of die cast Cosmal alloys are shown in Figure 46. In the same way as ZA alloys, strength decreases rapidly beyond 80°C.

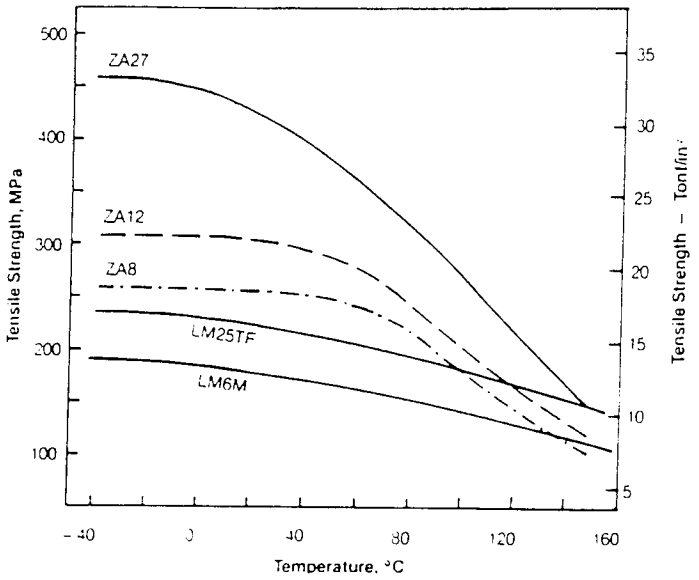

Figure 45. Variation of tensile strength of the ZA alloys and two aluminium alloys with emperature [38].

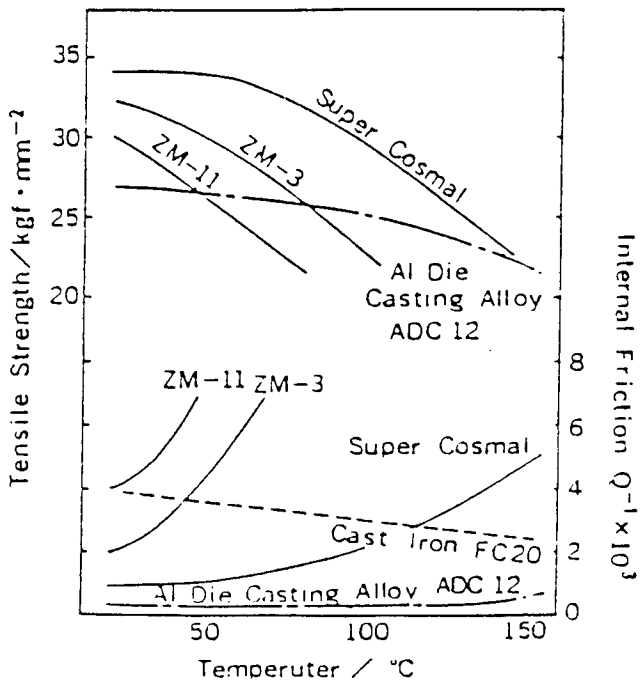

igure 46. Tensile strength and internal friction of Cosmal alloys at elevated temperatures [2].

3.2 EXPERIMENTAL PROCEDURE

n this part of the investigation, the Super Cosmal, HAZCA and ZA-27 alloys produced by and casting were subjected to metallographic examination using optical and scanning electron nicroscopy and to mechanical testing using standard techniques.

n order to analyse the influence cooling rate on the resulting microstructure, samples were aken from the extremes of a bar casting, i.e. one from a zone near to the riser and another from . zone near to the copper chill.

Aechanical tests were carried out on samples taken from consecutive locations along a cast bar. 'his was to observe the influence of cooling rates and porosity content on mechanical roperties.

.2.1 Optical and Scanning Electron Microscopy

he preparation of samples for metallographic examination was carried out following standard chniques until a highly polished surface was obtained.

or optical microscopy examination, specimens of ZA-27 alloy were etched in 2% Nital for bout 10 seconds. Specimens of Super Cosmal and HAZCA alloys were swab etched with a ft cotton saturated with Keller's solution (1 vol % HF, 3 vol % HCl, 5 vol % HNO_3). The ptical metallography was performed on a Reichart-Jung Polivar metallurgical microscope.

Cambridge Instruments SEM 150 was used to obtain better resolution of structures. Contrast uld be achieved from the difference in the atomic number of phases in the sample using the ck-seattered electron detector fitted to the instrument.

2.2 Mechanical Testing

bsized round ASTM B567 tensile test pieces and un-notched impact specimens (10 x 10 mm) re machined from slices cut from 50 x 50 mm bars cast in a chilled and degassed condition. gure 47 shows an example of the test samples obtained.

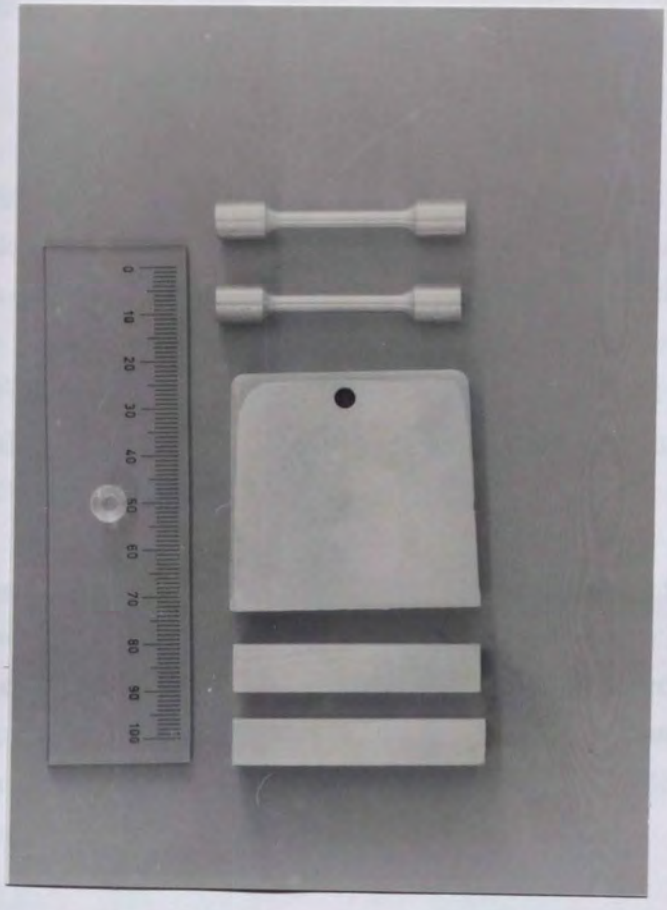

Figure 47. Test pieces for mechanical testing.

Tensile tests were carried out at room temperature in an INSTRON 1197 machine at a crosshead speed of 1mm/min.

Charpy tests to measure toughness were made in an AVERY machine using a striking velocity of 300J.

Hardness measurements were performed on the same slices from which tensile and impact test pieces were machined. Brinell hardness values were obtained applying a load of 250 kgf on a 5 mm diameter ball using a Wolper hardness tester on samples ground to 600 grit.

3.3 EXPERIMENTAL RESULTS

3.3.1 Metallographic Structures

ZA-27 Alloy

The general structure of the ZA-27 alloy obtained from a zone of relatively slow cooling rate during the production of bar castings, is shown in the light optical micrograph of Figure 48. The alloy has a coarse dendritic-eutectic structure where the Al-rich α -cores (light grey) are surrounded by a grey band of former ß phase and dark interdendritic zinc. At bigger magnification Figure 49 reveals the presence of white particles of ε phase in the interdendritic eutectic. Also along the dendritic edges the decomposition of former ß phase into lamellar and particulate structures of α and η phases can be observed.

The sample corresponding to a zone near to the chill presented a finer structure than that of a zone near to the riser. It is also dendritic with fine dispersion of white ε particles in the interdendritic eutectic η phase as shown in the optical micrograph of Figure 50. The interdendritic spaces are smaller but the ε particles appear to be similar in size when structures of Figure 49 and 51 are compared. The latter also shows that the light α and grey ß phases had decomposed into fine particulate structures.

Viewed in atomic number contract in the SEM, the structure in Figure 52 appears similar but with reversed contrast. The zinc-rich phase in the interdendritic area has the highest atomic number and looks white while the former ß regions adjacent to the zinc are mottled grey and the Al-rich α cores are dark grey. Also some shrinkage voids can be observed. Figure 53 shows the same sample (slow-cooled) at higher magnification. Here the dark dendrite core contains some zinc-rich precipitates and sub-grain boundaries. The prior ß phase in the vicinity of eutectic pools appears decomposed into particles. Furthermore, the edges of the eutectic η phase exhibit a rim of tiny aluminium particles.

The structure of the ZA-27 cast alloy from a zone of relatively more rapid cooling is shown by the SEM micrograph of Figure 54. The general structure is the same as shown by the optical micrograph of equal magnification with the exception that the ε particles can not be distinguished from zinc by atomic number contrast and both appear as white constituents. Clearly the predominant phase in the structure is the decomposed ß of mottled grey appearance. In Figure 55 at higher magnification, rims of aluminium particles around both the eutectic zinc and the cores of Al-rich former α' phase can be seen and also in sub-grain boundaries.

Super Cosmal Alloy

A sample of Super Cosmal alloy from a zone near to the riser is shown in the optical micrograph of Figure 56 which consists of a multiphase structure of primary silicon particles and eutectic silicon laths in a cored Al-rich matrix, grey prior ß phase and dark interdendritic η phase which contains small rounded white particles. At higher magnification in Figure 57 the above mentioned particle is shown at the centre of the interdendritic η phase and is believed to be $CuZn_4$ ε phase.

At zones near the chill (Figure 58), the structure contained finer dendrites with smaller eutectic silicon precipitates and few primary silicon particles. Coring by zinc segregation to the interdendritic spaces appears to be less developed than in slow-cooled zones. The predominance of the decomposed ß phase and eutectic silicon can be seen in the optical micrograph of Figure 59 where the presence of ε particles and sub-grain boundaries are also noticed.

When observed in the SEM, the structure of the Super Cosmal alloy shown in Figure 60 comprises of large dark areas of Al-rich matrix, small light grey areas of decomposed ß, interdendritic zinc-rich areas in the centre of which there are particles of intermediate atomic number, eutectic silicon, few primary silicon particles and some light grey particles clustered in the Al-rich matrix. These particles are shown in Figure 61 together with a primary silicon particle. Semi-quantitative EDS analysis in the SEM gave a composition which corresponds approximately to the formula $CuAl_2$ for these particles.

A micrograph of an interdendritic boundary is shown in Figure 62 where the former ß phase appears decomposed into α and η phases in some parts as a lamellar structure, and in some others as a particulate structure. In this same Figure, the presence of an irregular particle surrounded by zinc which is assumed to be T' phase based on EDS analysis is visible. This particle occurs in the centre of most interdendritic pools. At higher magnification, Figure 63 shows in more detail the eutectoid decomposition of ß phase and also the precipitation of aluminium particles in the interdendritic borders and part of a decomposed α' phase.

HAZCA Alloy

The general structure of HAZCA alloy from a place near to the riser is shown in the optical micrographs of Figures 64 and 65. The multiphase structure consisted of primary and eutectic silicon particles embedded in the predominant Al-rich phase, and a zinc-rich interdendritic phase

where rounded particles of $CuZn_4$ phase and irregular T' particles had formed. Blades of Fe-Si-Zn intermetallic were also found in this dark etched region.

The general structure corresponding to a sample of faster cooling is shown in the optical micrograph of Figure 66. The structure was finer and coring appeared less developed than that of slow-cooled zones. The presence of bright rounded particles and some blades can also be noticed. Here silicon particles were predominantly eutectic but there were some clusters of primary silicon particles in some parts of the structure as shown in Figure 67. Figure 68 shows an ε phase particle right in the centre of the interdendritic bands of prior ß phase.

At reversed contrast, Figures 69 and 70 show the SEM micrographs of the general structure of the HAZCA alloy where the grey Al-rich α phase associated with eutectic silicon prevailed. At higher magnification the SEM micrograph of Figure 71 reveals the formation of Fe-Si-Zn intermetallic as long blades in the middle of zinc-rich interdendritic spaces. This is magnified in Figure 72 where high atomic number particles had also formed along the intermetallic blades and in the junction of sub-grain boundaries. Figure 73 shows this in more detail and also the particulate decomposition of what had solidified as ß phase. The EDS analysis of the triangular particle gave a composition approximately corresponding to a T' phase.

Figure 48. Optical micrograph of ZA-27 alloy from a zone of relatively slow cooling rate showing a coarse dendritic structure of α-cored ß dendrites with darker eutectic zinc. x 100.

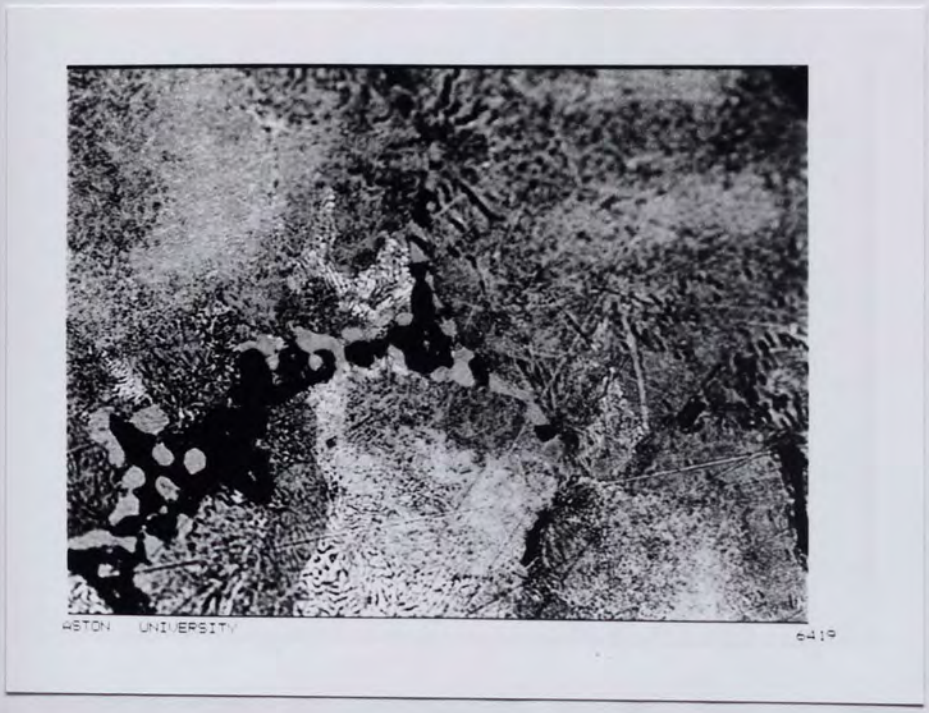

Figure 49. Optical micrograph showing the presence of ε phase as white particles in the interdendritic eutectic and decomposition of former ß phase into lamellar and particulate structures of α and η phases. x 500.

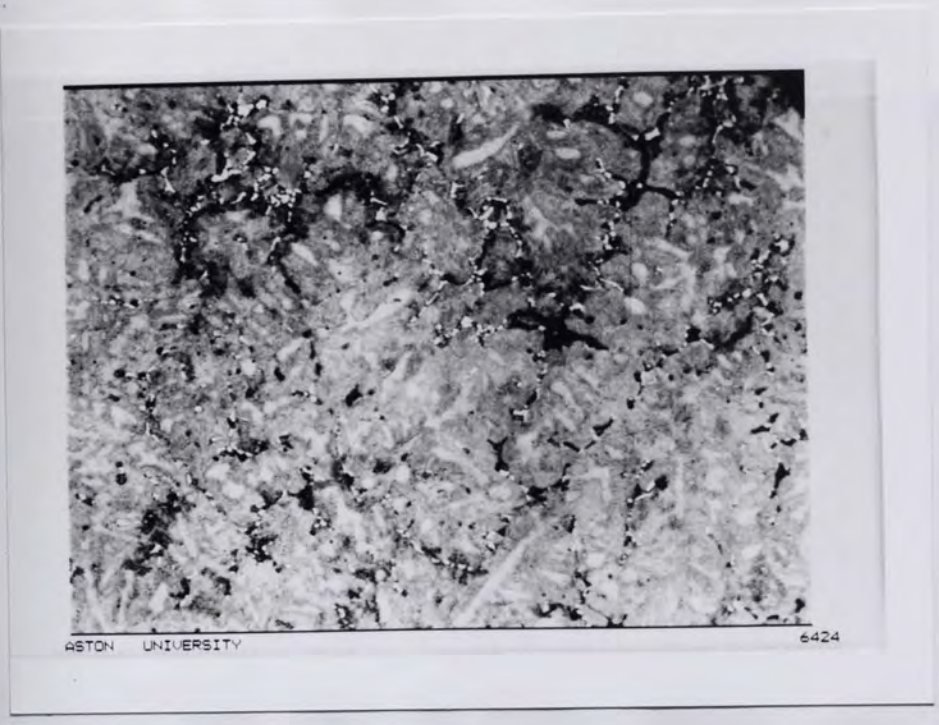

igure 50. Optical micrograph showing the fine dendritic structure of ZA-27 alloy from a zone ear to the chill with fine dispersion of white ε particles in the interdendritic η phase. x 100.

igure 51. Optical micrograph showing fine decomposition of α' and ß phases into α and η articles. x 500.

igure 52. SEM micrograph of ZA-27 alloy from a relatively slow solidification rate casting ıowing a typical cored dendritic structure. Al-rich α cores (dark grey), peritectic ß (grey), ıterdendritic eutectic η (white) and some shrinkage porosity.

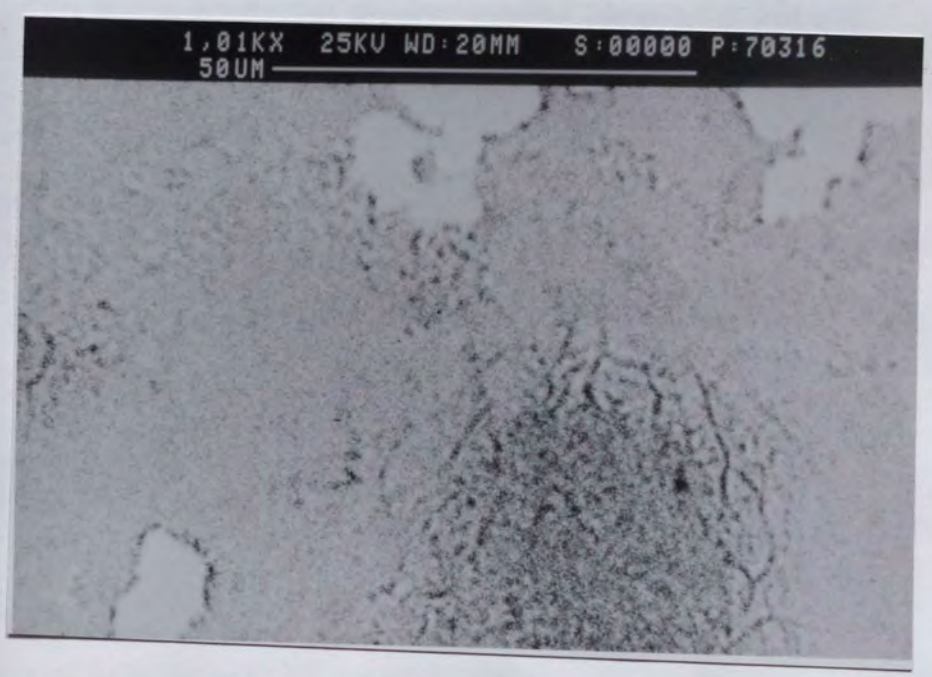

gure 53. SEM micrograph showing some zinc-rich precipitates within the dark dendritic re. The grey area is decomposed ß. A rim of tiny aluminium particles at the edges of the tectic zinc is also shown.

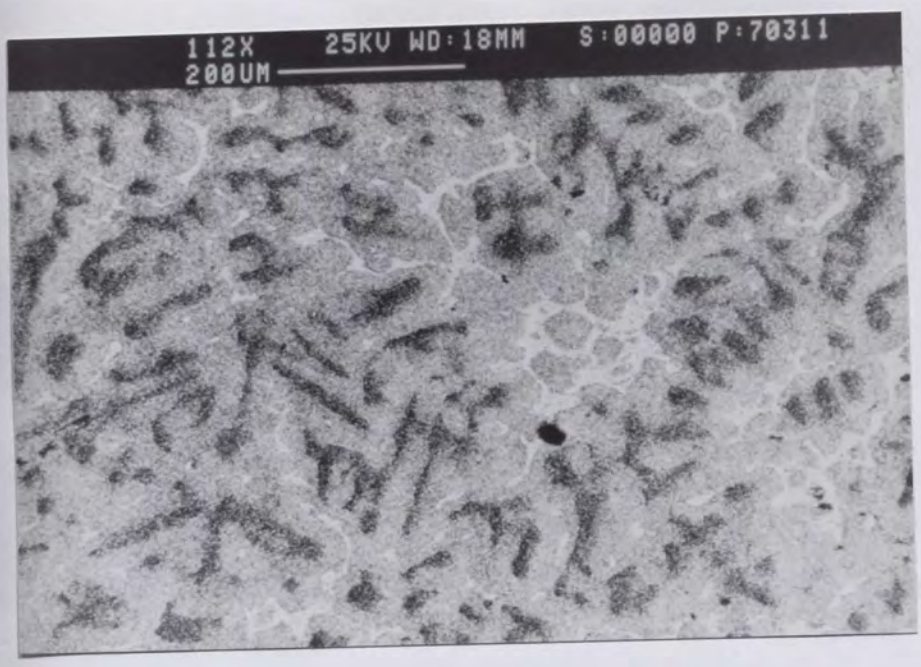

gure 54. SEM micrograph of ZA-27 taken from a zone near to the chill showing a finer endritic structure and narrower interdendritic spaces filled with eutectic η.

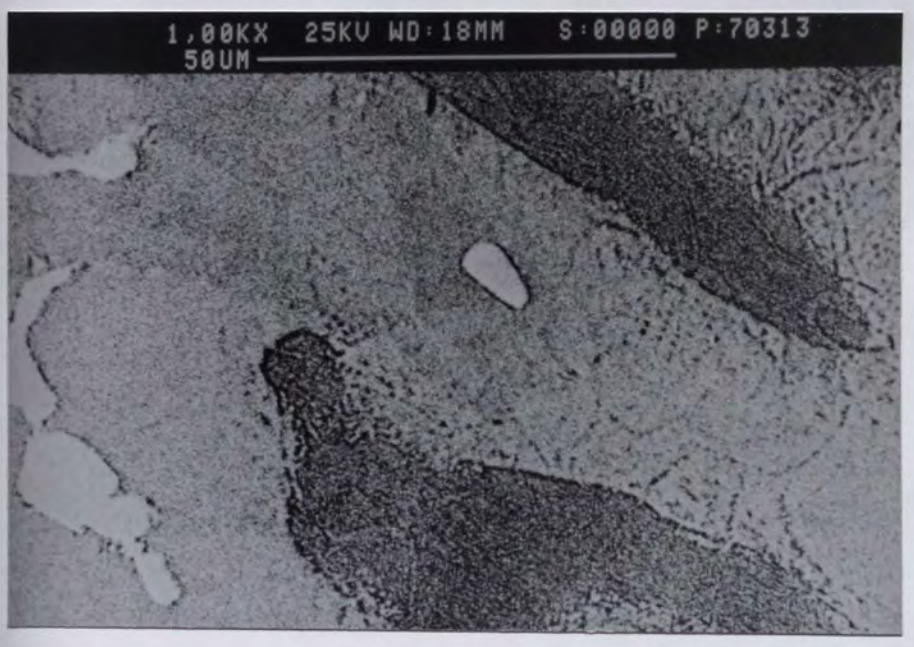

gure 55. SEM micrograph showing rims of aluminium particles around both the eutectic zinc d the cores of the Al-rich former α' phase. Precipitation of Al particles in sub-grain undaries.

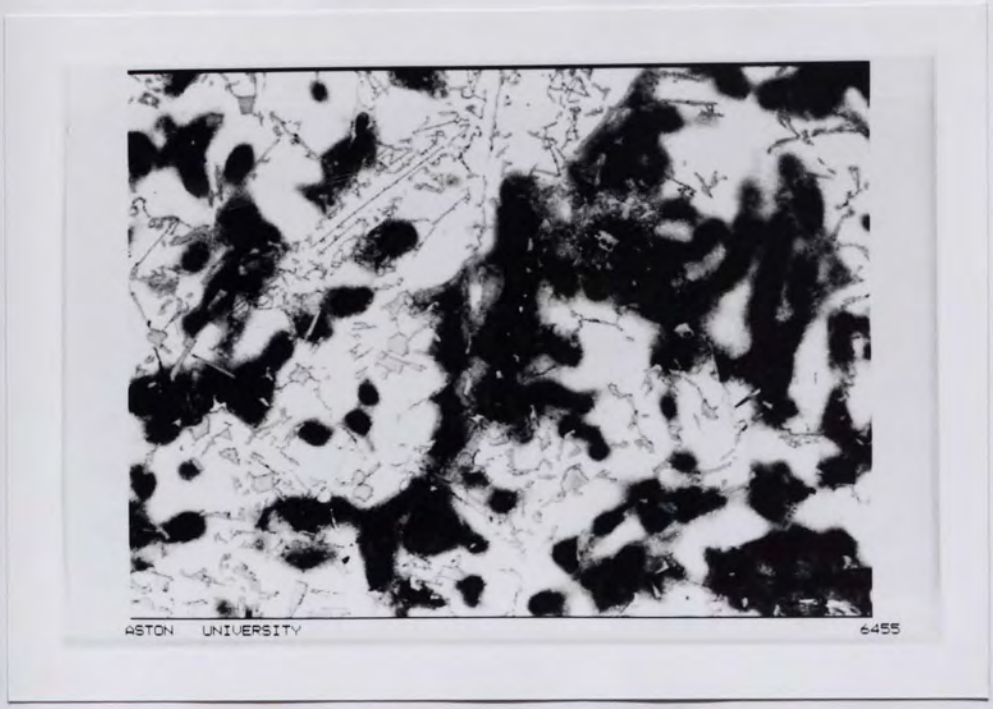

'igure 56. Optical micrograph of a Super Cosmal alloy from a relatively slow cooling rate asting showing a multiphase structure of primary silicon particles, small rounded particles, utectic Si laths in Al-rich matrix, grey prior ß and dark interdendritic η phases. x 100.

igure 57. Optical micrograph of Super Cosmal alloy showing the Al-rich α phase associated ith silicon particles and the presence of a bright rounded particle in the centre of the terdendritic pools which is thought to be either ε or T' phase. x 500.

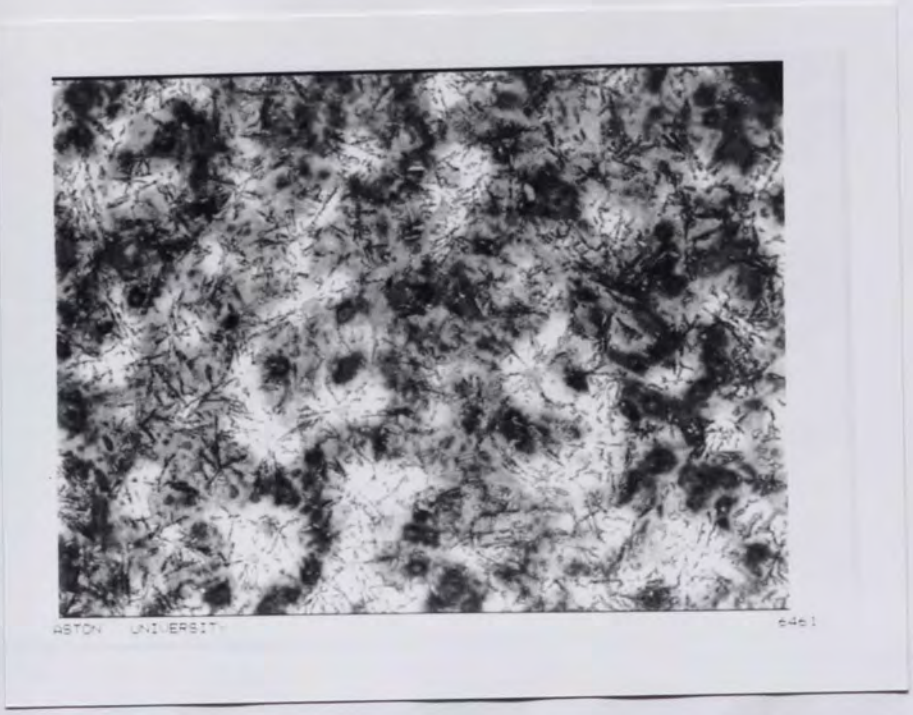

Figure 58. Optical micrograph of Super Cosmal alloy from a zone near to the chill showing a finer structure with smaller eutectic silicon precipitates. x 100.

Figure 59. Optical micrograph of Super Cosmal alloy showing the predominance of decomposed ß phase around the Al-rich cores and eutectic silicon. x 500.

Figure 60. SEM micrograph of Super Cosmal alloy from a slow cooling rate zone showing the general structure consisting of Al-rich matrix, eutectic silicon, primary silicon, other light grey precipitates in the Al-rich matrix and zinc rich interdendritic phase.

Figure 61. SEM micrograph of Super Cosmal alloy showing particles of clustered $CuAl_2$ intermetallics in the Al-rich phase.

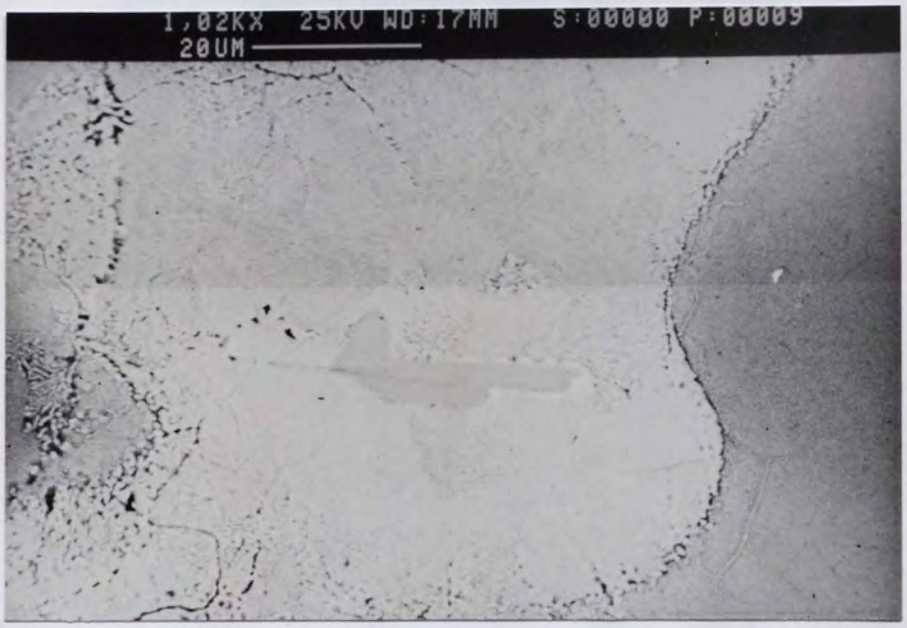

Figure 62. SEM micrograph of Super Cosmal alloy showing the structure of the zinc-rich interdendritic. The irregular particle was identified as T' which is in part surrounded by zinc.

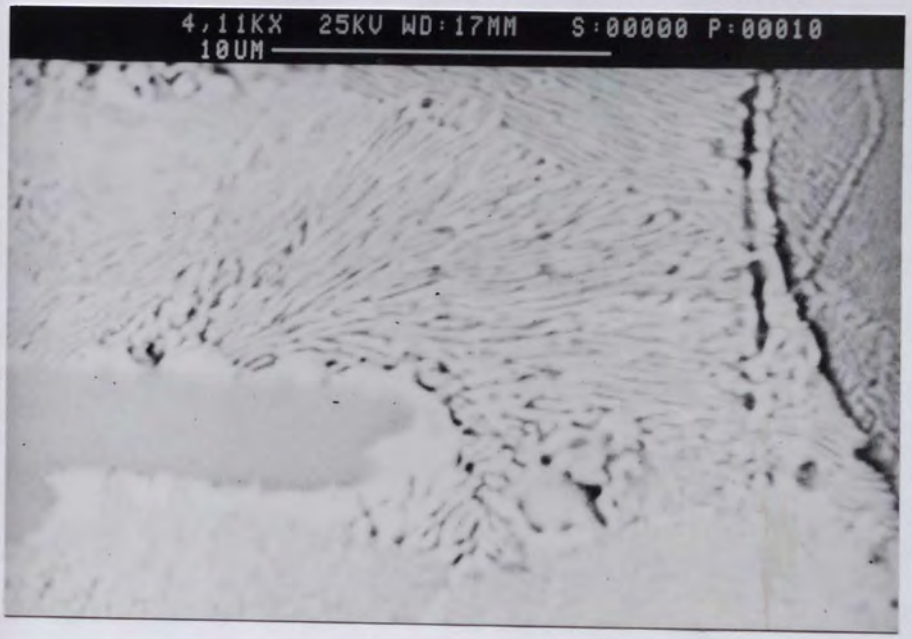

igure 63. SEM micrograph of the zinc-rich interdendritic structure of Super Cosmal alloy, nowing the lamellar decomposition of the peritectic ß phase. The dendrite boundary shows luminium particles and a portion of a decomposed former α' phase.

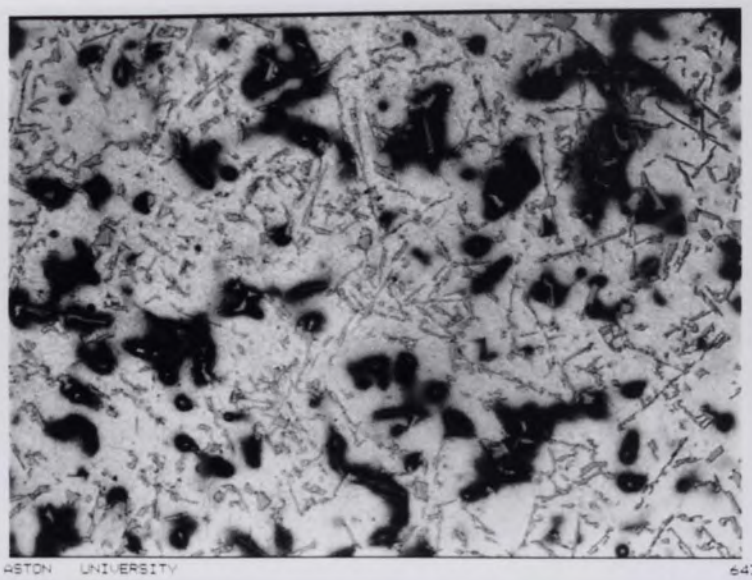

Figure 64. Optical micrograph of HAZCA alloy from a zone of slow cooling rate showing a multiphase structure. Primary and eutectic silicon in the Al-rich matrix and in the dark zinc-rich interdendritic phase, blades of a Fe-Si-Zn intermetallic, rounded ε particles and irregular T' particles. x 100.

Figure 65. Optical micrograph of HAZCA alloy showing zinc segregated to the interdendritic spaces where particles of either ε phase or T' phase have been formed. x 500.

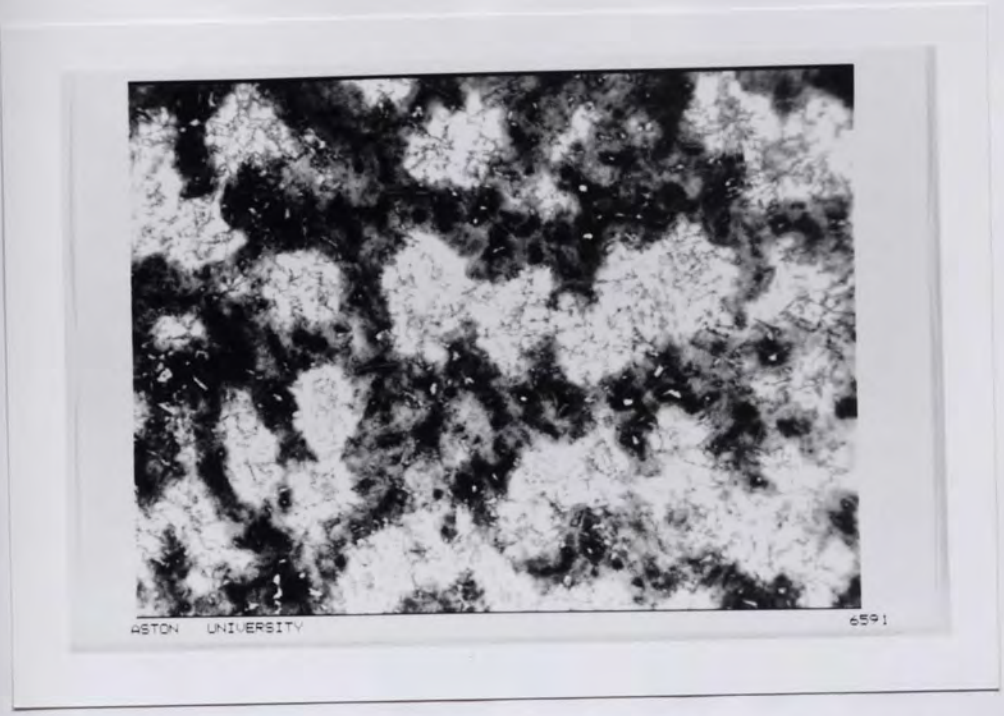

igure 66. Optical micrograph of HAZCA alloy from a zone of fast cooling. The structure is ne and coring is less developed than that of slow-cooled zones. Blades of intermetallic Fe-Si-n in the dark interdendritic zinc can also be seen. x 100.

gure 67. Optical micrograph of HAZCA alloy showing a cluster of large primary silicon rticles and eutectic silicon in the Al-rich matrix. x 200.

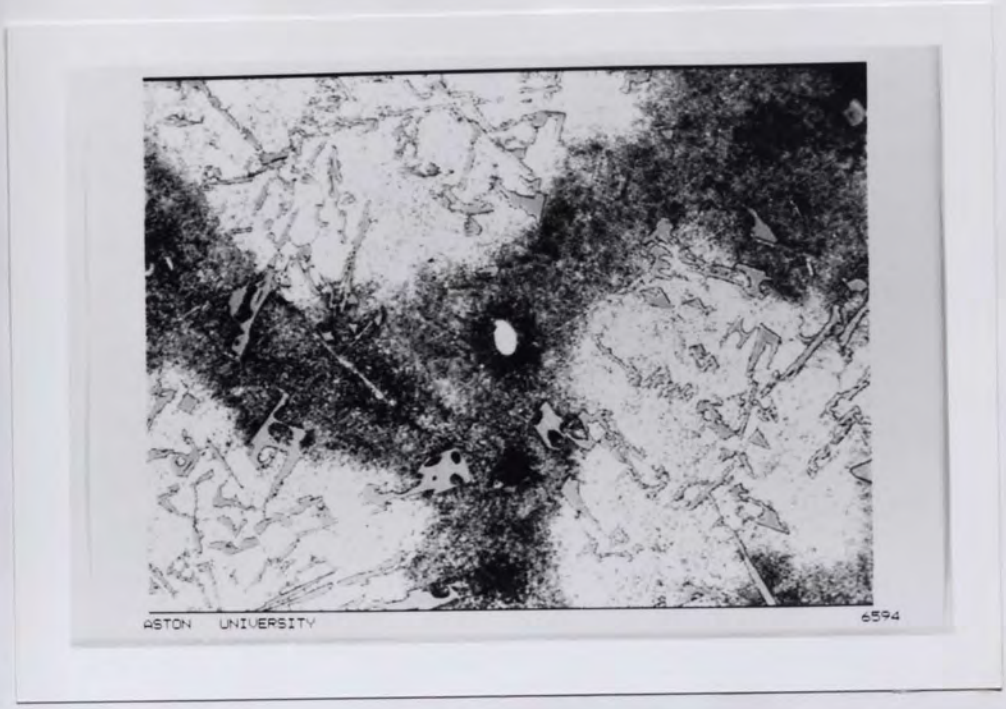

igure 68. Optical micrograph of HAZCA alloy showing interdendritic bands of prior ß phase ı the centre of which a particle of ε phase has been formed. x 500.

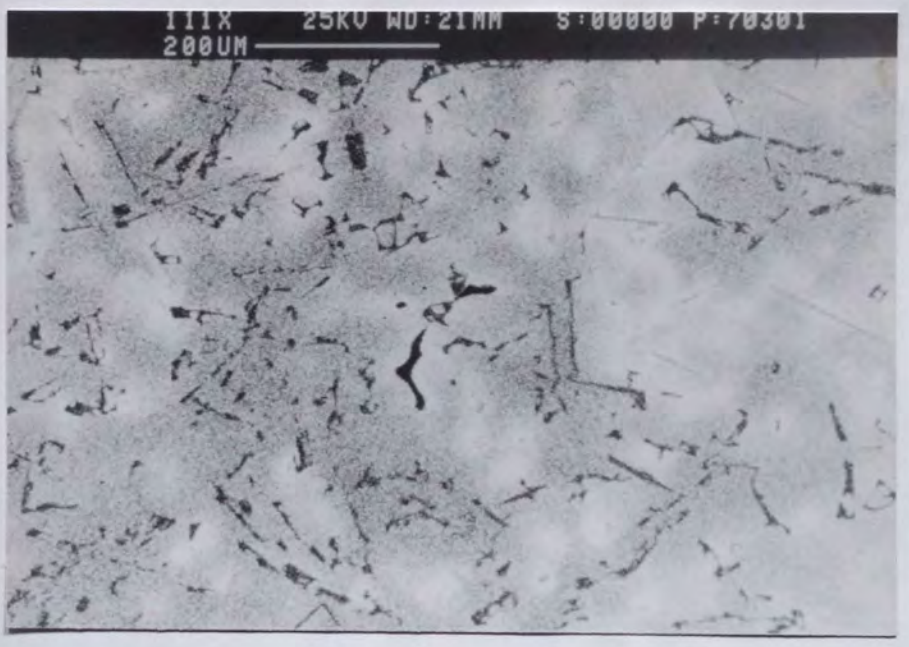

igure 69. SEM micrograph of HAZCA alloy showing at low magnification general ıultiphase structure consisting mainly of Al-Si eutectic. The interdendritic zinc-rich phase ppears white.

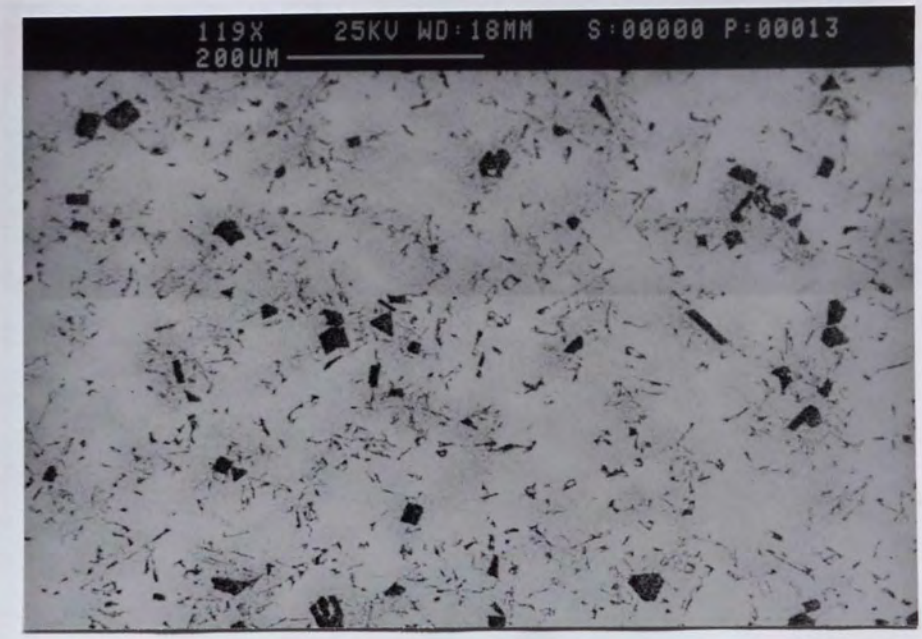

igure 70. SEM micrograph of HAZCA alloy. General structure showing primary silicon articles.

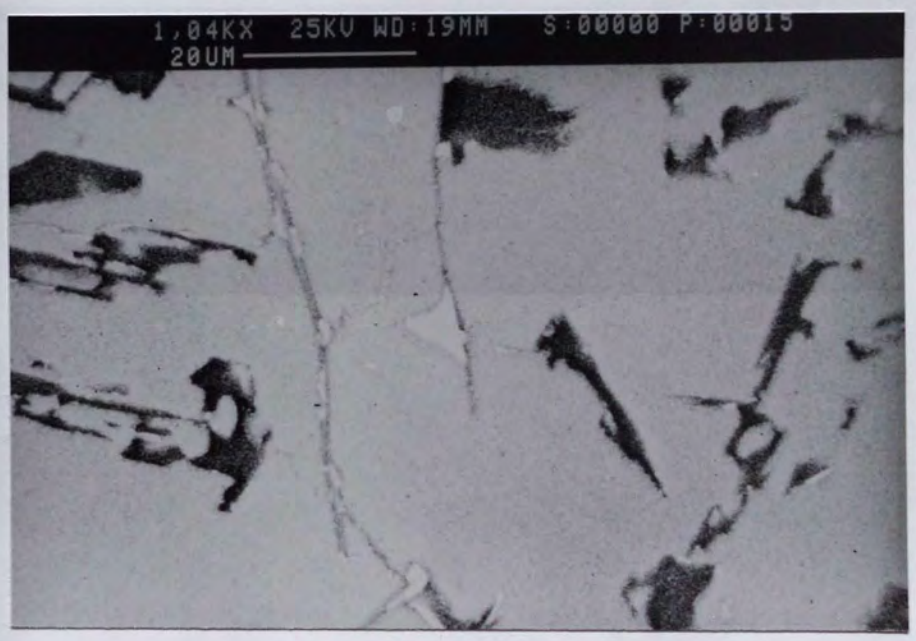

gure 71. SEM micrograph of HAZCA alloy showing an interdendritic region where blades Fe-Si-Zn have formed.

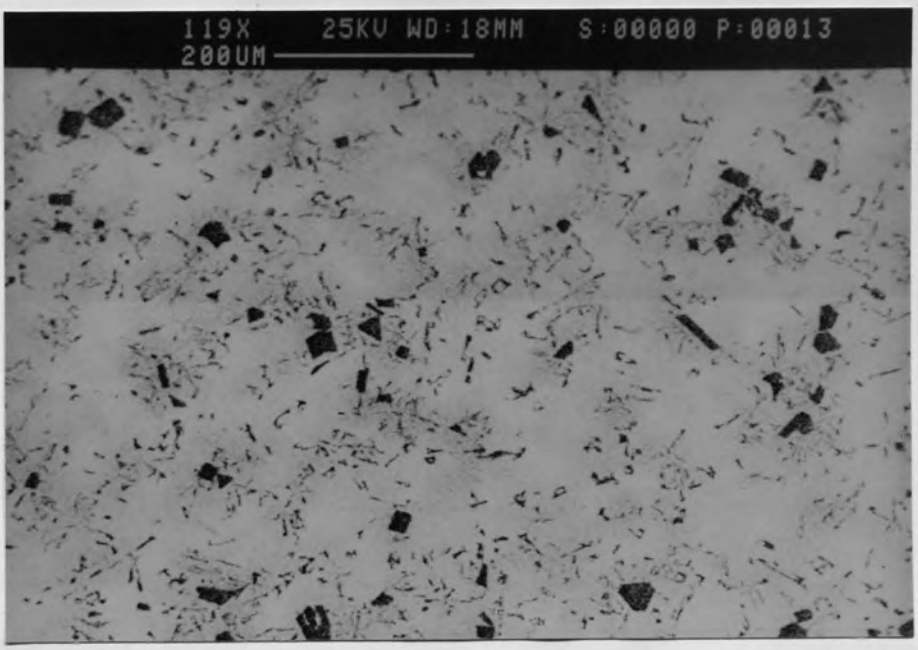

Figure 70. SEM micrograph of HAZCA alloy. General structure showing primary silicon particles.

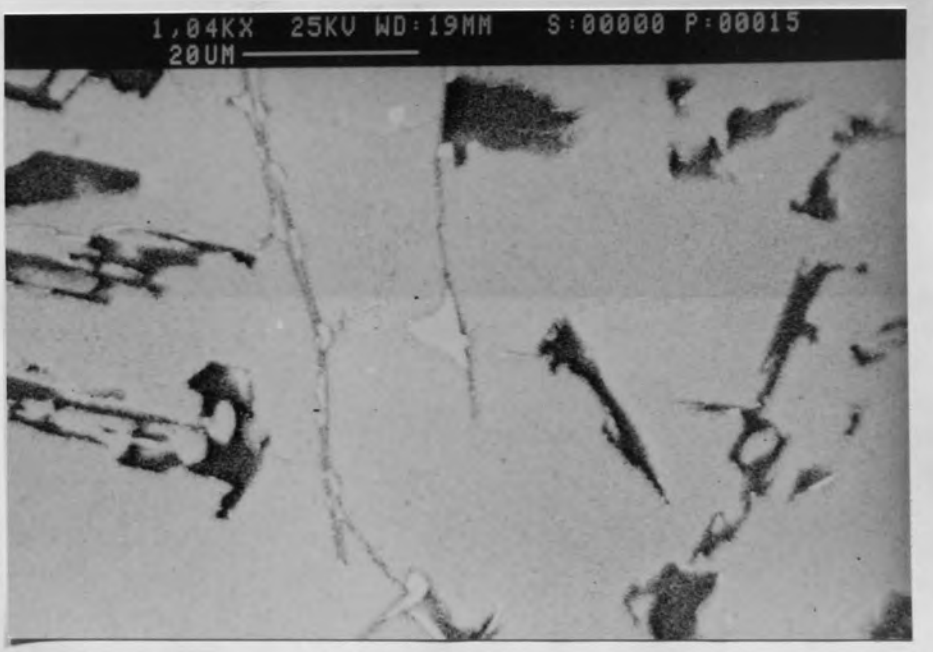

Figure 71. SEM micrograph of HAZCA alloy showing an interdendritic region where blades of Fe-Si-Zn have formed.

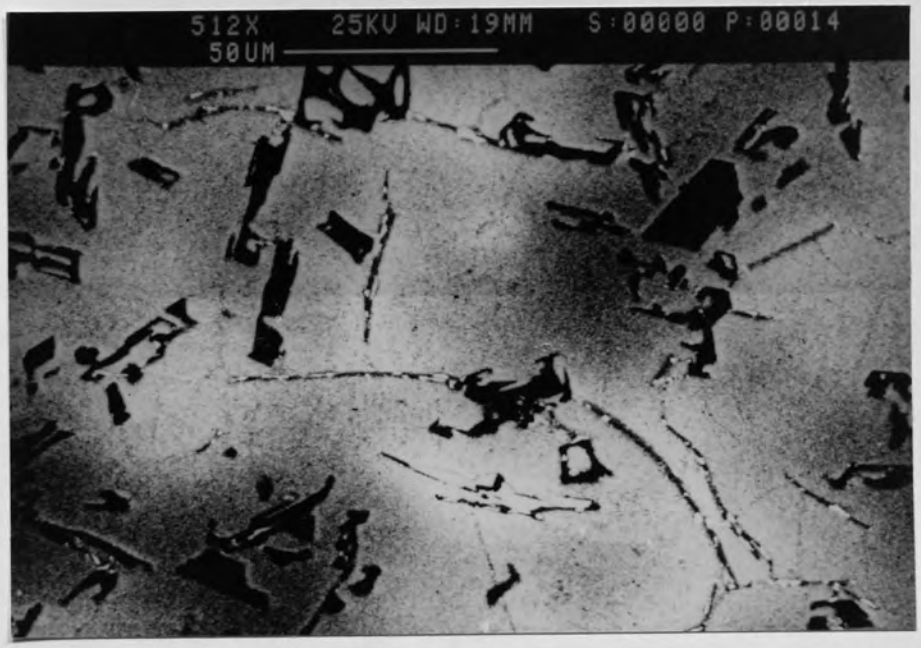

Figure 72. SEM micrograph of HAZCA alloy showing a zinc-rich area with blades of Fe-Si-Zn intermetallic and particles of T' phase.

Figure 73. SEM micrograph of HAZCA alloy showing the particulate structure of the eutectoidal decomposition of ß phase.

3.3.2 Mechanical Properties

Mechanical testing results are reported as a function of the porosity content corresponding to locations from which test pieces were machined. As samples were taken from consecutive locations along chilled cast bars, the highest porosity values corresponded to zones near to the riser.

The influence of porosity on tensile strength of the three alloys under study is shown in Figure 74. Apparently the strength of ZA-27 alloy was not strongly affected by porosity, whilst in Super Cosmal and HAZCA alloys, tensile strength decreased rapidly with increasing content of porosity. Within the limits shown in the graph, at porosity levels higher than 1.5%. The UTS of Super Cosmal was as low as 250 MPa, but remained constant while that of the HAZCA alloy dropped drastically. Maximum values of tensile strength were found in the chilled areas of the casting where shrinkage porosity was low and the microstructure was finer.

Yield strength in ZA-27 was also found not to be very dependent on porosity content within the range of porosities tested (Figure 75). On the other hand, only the Super Cosmal specimens from chilled zones presented some yielding while HAZCA alloy exhibited no yielding at all.

Figure 76 show that tensile ductility of ZA-27 alloy displayed a large change as a function of porosity content and/or dendrite, as cell size. Super Cosmal alloy showed small values of elongation in those samples obtained from zones near to the chill.

Super Cosmal and HAZCA alloys exhibited a brittle behaviour compared to ZA-27 alloy in the unnotched Charpy test, the results of which are shown in Figure 77. However, toughness of ZA-27 decreased with increasing porosity.

Hardness as measured by a Brinell tester was shown not to be porosity dependent in the range of soundness levels tested. However, the highest levels of hardness were found on chilled parts of the castings. HAZCA alloy showed the highest values of hardness of 120-135 HB, Super Cosmal the second hardest with 120-130 HB and ZA-27 with hardness values of 100-110 HB. The drop in hardness values at around 1.5% porosity apparently occurred at the limit of the chilled zone in the casting. This is displayed in Figure 78.

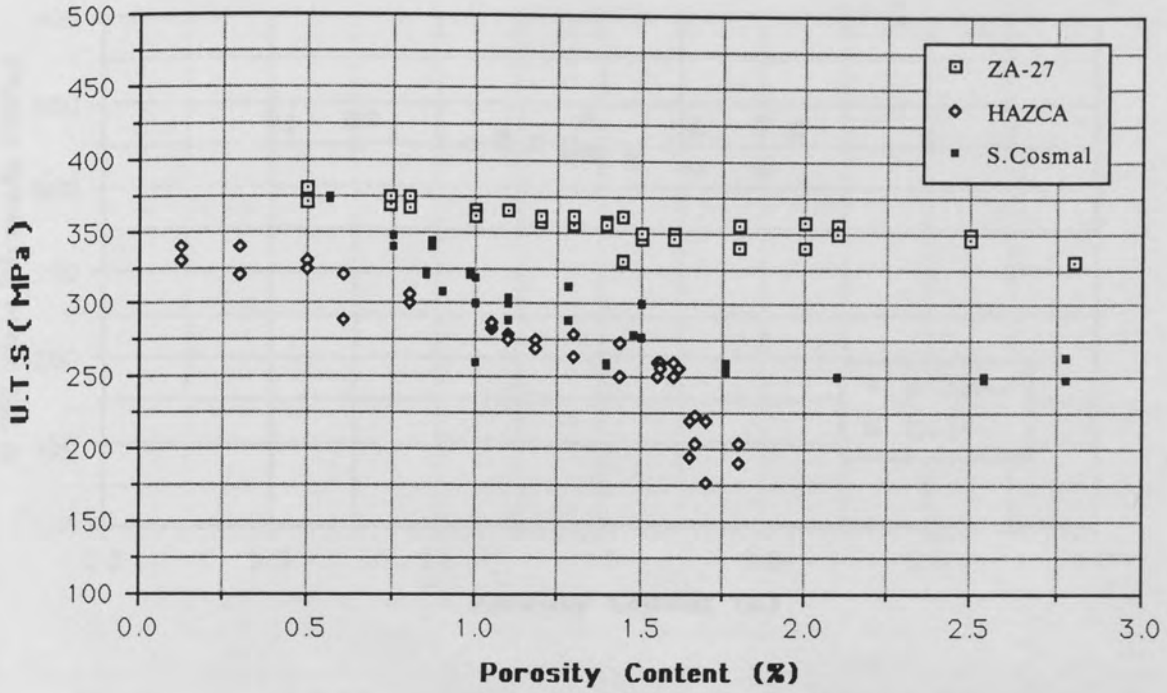

Figure 74. Variation of tensile strength with porosity level in ZA-27, Super Cosmal and HAZCA alloys.

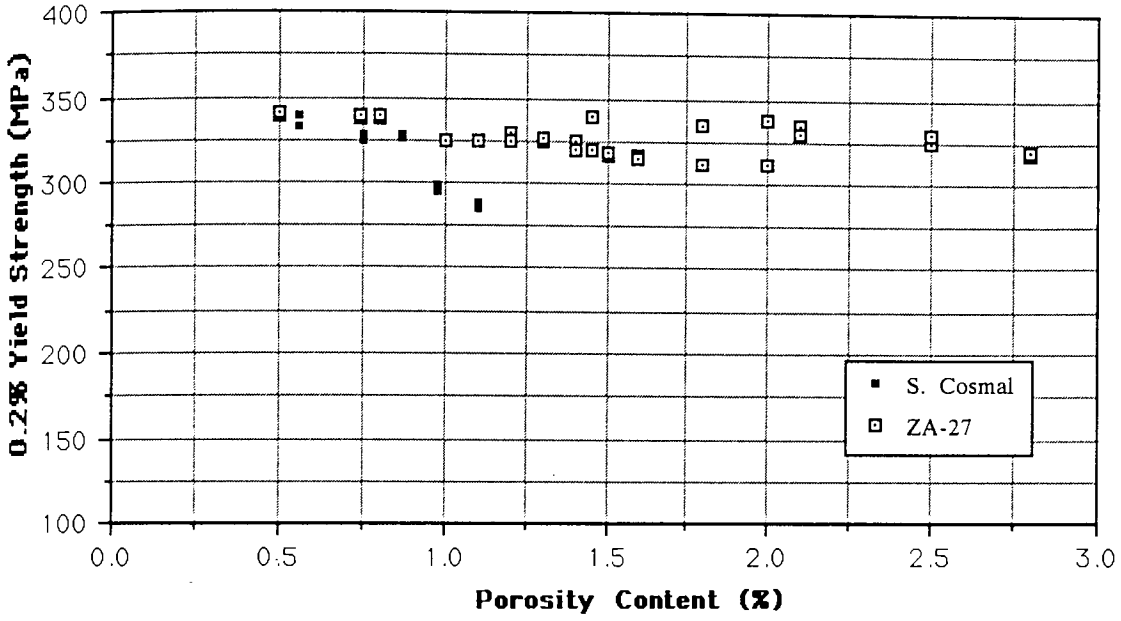

Figure 75. Variation of 0.2% yield strength with porosity level in ZA-27 and Super Cosmal alloys.

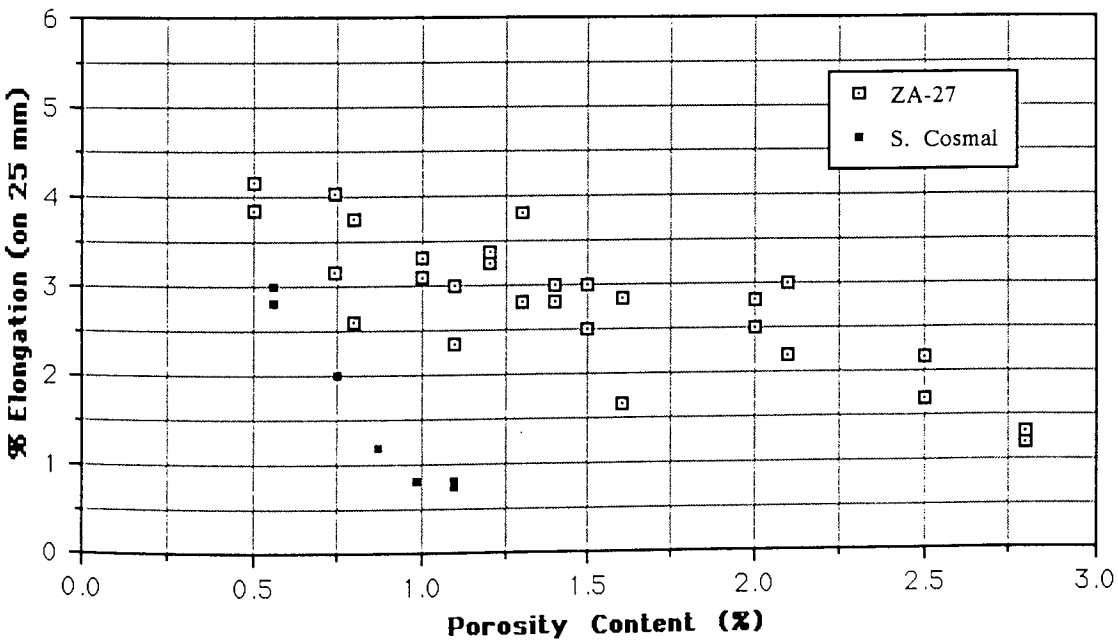

Figure 76. Variation of percentage elongation with porosity content in ZA-27 and Super Cosmal alloys.

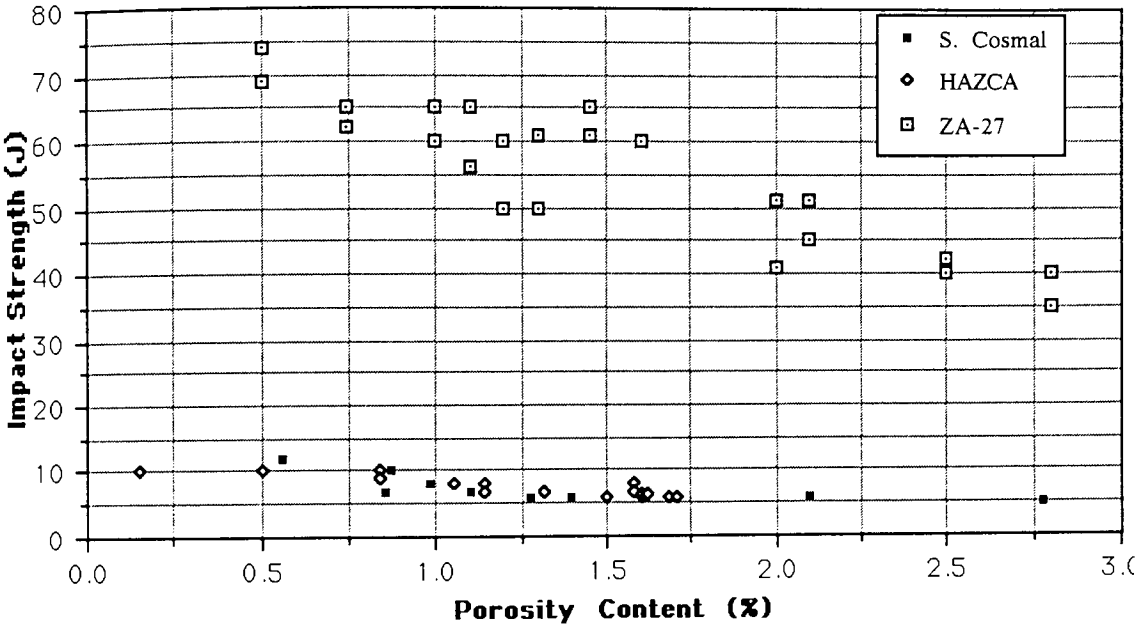

Figure 77. Variation of impact strength with porosity level of ZA-27, Super Cosmal and HAZCA alloys.

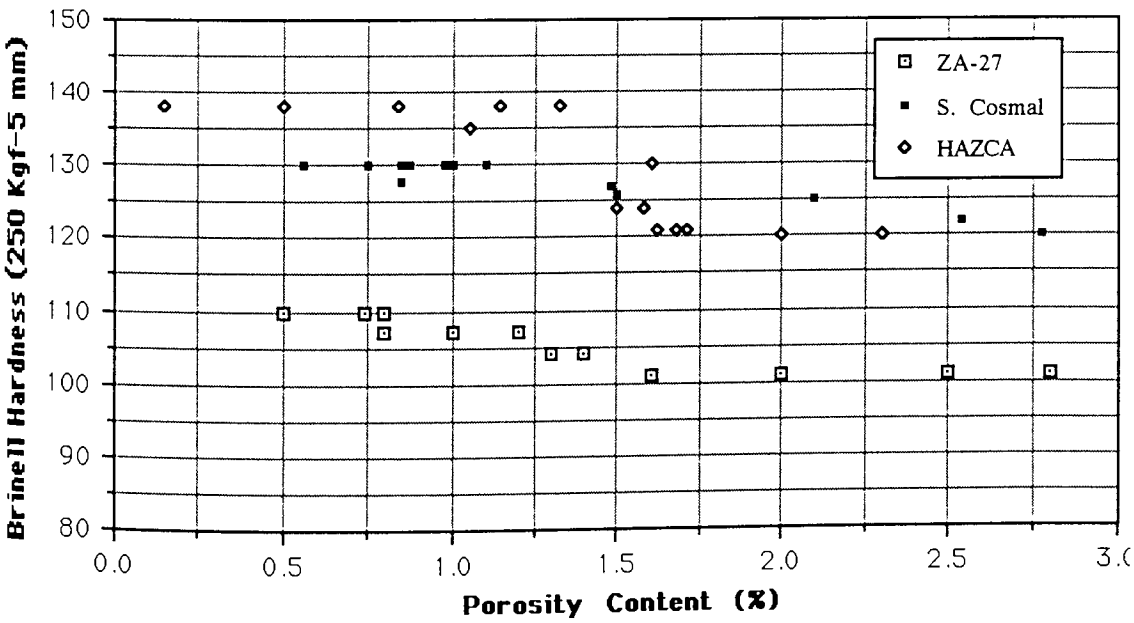

Figure 78. Brinell Hardness of ZA-27, Super Cosmal and HAZCA alloys as a function of porosity.

3.4 DISCUSSION

3.4.1 Metallography and Mechanical Properties of ZA-27 Alloy

The microstructure of the ZA-27 alloy cast in sand moulds consisted of α cored dendrites, with broad ß rims and an interdendritic matrix consisting largely of zinc where ε particles were concentrated.

Solidification of this alloy started with the nucleation and growth of Al-rich α dendrites in a liquid progressively enriched in zinc which subsequently reacted with the original α phase to form the peritectic zinc-rich ß phase around the original dendrites. The coring produced a zinc eutectic which occupied the remaining interdendritic channels. Precipitation of copper as ε phase was also concentrated in the interdendritic regions following solidification.

On further cooling after solidification, the supersaturated α cores have decomposed by precipitation of small zinc particles and the ß phase has formed in some parts lamellar structures and in others particulate structures of α and η phases.

Regarding the cooling rate effect, in zones near to the chill, faster solidification developed a more sound and finer structure with equally fine dispersion of ε particles to that in the opposite side of the casting. These features had a positive effect on the mechanical properties of the alloy.

Results of the tensile tests showed that maximum values of strength in ZA-27 sand castings were achieved at regions of low porosity content and refined structure. U.T.S. values of 370-380 MPa obtained in this work are in close agreement with reported values in the literature (Figure 44). Furthermore, the influence of porosity on tensile strength was found not to be marked especially in the range of 1-2% (considered as a normal level of porosity in sand castings) where an average U.T.S. of 350 MPa was obtained.

The combined effect of porosity and large interdendritic η pools in slowly-cooled parts of the castings were responsible for the rapid drop in tensile ductility and impact strength as the distance from the chill increases.

Hardness was shown not to be dependent on the degree of soundness but slightly dependent on microstructural parameters. Rapidly cooled zones near the chills produced fine structures where the dispersion of the hard ε particles was more uniform, resulting in improved hardness.

3.4.2 Metallography and Properties of Super Cosmal Alloy

The Super Cosmal alloy of composition Zn, 60% Al, 6% Si, 1% Cu, 0.3% Mn developed a complex multiphase microstructure following casting.

The manner in which this Zn-Al-Cu-Si alloy solidified in sand moulds can be described as the following: the first phase to form is silicon, often referred as primary silicon because it appears in the microstructure before the silicon which is part of the eutectic. This primary silicon grows within the liquid melt and acts as a site of nucleation. The aluminium phase nucleates here and on other heterogeneous sites and grows into dendritic grains until the temperature reaches the Al-Si eutectic temperature. At this temperature, silicon in the liquid mass nucleates on first-formed small dendrite arms and grows together with α and α' phases leading to the formation of the Al-Si eutectic phase. The residual liquid enriched in zinc in contact with the solid α phases undergo the Al-Zn peritectic reaction to form the zinc-rich ß phase around the original dendrites. Segregated copper is present in the last zinc-rich eutectic liquid where it forms $CuZn_4$ (ε) and/or Al_4Cu_3Zn (T') intermetallic phases. In the solid state, the monotectoid α' phase passed through two consecutive eutectoidal transformations into α + ß and then into α + η phases. At the same time the peritectic ß decomposes eutectoidally into α + η phases. The decomposed ß phase appears as an interdendritic area of lamellar and particulate cells containing copper-rich particles in its centre. The occurrence of the afore-mentioned solid transformation is shown in Figures 62 and 63.

Throughout the structure of Super Cosmal alloy, silicon appears in primary and eutectic forms. Both of them are essentially pure silicon and as such are very hard and brittle. Primary silicon grows in a faceted manner by the propagation of twin planes that emerge at the crystal surface [39]. In slowly cooled Al-Si alloys, primary silicon crystals grow with {111} facets so that the perfect crystal would be octagonal [40]. However, the primary silicon particles can be found in a variety of shapes ranging from blocky to star-shape crystals depending upon process variables and presence of additional elements in the alloy as is the case of the Super Cosmal where some primary silicon particles appeared as hexagonal, triangular and rectangular according to the sectioning angle during sample preparation. Others have polygonal shapes with branches that formed pockets containing α aluminium (Fig. 57 and 60). Growth of eutectic silicon took place from the first formed aluminium dendrites and because of its co-

precipitation with α-aluminium, faceted growth did not occur producing needle-like structures as in Figure 57.

Other intermetallics detected in the structure of the Super Cosmal alloy were scarce clusters of $CuAl_2$ embedded in the Al-rich matrix.

An increase in the solidification cooling rate (zone near to the chill) was found to produce a finer general structure. Both the primary and eutectic silicon were refined and more uniformly distributed (Figure 58). In slowly cooled zones the coarse structure not only presented shrinkage voids, but also a very well developed segregation of zinc to the interdendritic spaces so that former ß rims were thinner than in more rapidly solidified structures.

Although tensile strength values as high as 370 MPa were achieved at low soundness levels, this property was shown to be strongly affected by porosity.

In the range of 0.8-1.5% porosity there was a big scatter of U.T.S. results (Fig. 74) due to the fact that subsized test pieces did not represent exactly the local porosity on cast bars. However, within this range a U.T.S. of 300-320 MPa can be taken as representative of the Super Cosmal alloy when cast in sand. During tensile tests the Super Cosmal specimens did not yield except those obtained from zones in contact with the chill. The lack of ductility of this material was confirmed by its low capacity of energy absorption at shock loading conditions. Even at such low levels of impact resistance (Fig. 77) an increase in soundness increased toughness.

As in ZA-27, the Brinell hardness of Super Cosmal alloy was found not to be a function of porosity but a function of solidification cooling rate. Zones influenced by the copper chill gave the highest hardness value of 130 HB, but in the riser side the material was 10 HB units softer.

Disregarding porosity, the main microstructural feature responsible for the hard and brittle nature of Super Cosmal alloy is the occurrence of coarse and hard particles of silicon and other intermetallic compounds in the dendritic structure.

3.4.3 Metallography and Mechanical Properties of HAZCA Alloy

The experimental HAZCA alloy of composition ZA, 60% Al, 8% Si, 2% Cu, 0.06% Mg had undergone the same type of solidification process as the Super Cosmal alloy after being cast in sand moulds.

Basically HAZCA alloy revealed the same structural phases than Super Cosmal, i.e., primary silicon particles and eutectic silicon laths in an Al-rich matrix, and prior ß and η phases in the interdendritic boundaries. Nevertheless, because of the higher content of silicon, the solid fraction formed between the liquidus and eutectic temperatures was smaller (Fig. 12) leaving a larger mass of Al-Si eutectic to solidify. Growth of the Al-Si eutectic left smaller and more separated interdendritic pools (Fig. 64). The longer period of eutectic growth at around 560°C shown also in the cooling curve of Figure 17, might have accelerated the dendritic segregation of zinc and copper from the forming Al-rich α-α' phases into the remaining liquid. Solidification of this liquid produced thinner rims of prior ß phase and zinc rich interdendritic pools where copper-rich intermetallic particles were deposited. Due to the higher content of copper in this alloy and the thermal effect mentioned, the copper-rich particles appeared large in size as in Figures 65, 66 and 68. The SEM micrograph of Figure 73 shows at high magnification the structure of a interdendritic pool where a copper-rich particle was identified from semi-quantitative EDS analysis as T' phase. The matrix in this area shows a particulate structure which is though to be the result of the decomposition of zinc rich ß formed at around the eutectic solidification point. Another particular feature in the HAZCA structure was the presence of a blade-like intermetallic not identified, but assumed to be an Fe-Si-Zn compound according a previous study on the metallography of zinc-based alloys[41].

The tensile strength of the experimental HAZCA alloy was found to bevery dependent on the degree of soundness. It decreased linearly up to 1.5% porosity and then dropped drastically to values under 200 MPa. Again, the highest values of U.T.S. (320-340 MPa) were obtained in samples of chilled zones of the bar castings. In the range of 1 - 1.5% porosity an averaged value of 270 MPa could represent the strength of medium quality sand cast HAZCA alloy. It is evident that careful casting techniques and chilling and degassing are necessary to achieve the best tensile properties of the alloy. However, not even tensile samples corresponding to zones in contact with the chill showed any yielding. Furthermore the response of this alloy to the impact tests was very low and also dependent on the degree of soundness.

The chilling action on HAZCA sand castings produced the hardest structure of all three alloys tested. The harder and more brittle nature of HAZCA alloy was due to its higher content of silicon and it seems that the increment of copper in respect to the Super Cosmal alloy to increase strength had been counterbalanced by the influence of more silicon particles and other intermetallics in the structure. However, the conservative level of 270 MPa compares favourably with modified commercial Al-Si alloys.

3.5 CONCLUSIONS

1. Both Super Cosmal and HAZCA alloys presented a similar general multiphase microstructure consisting of primary silicon particles and eutectic of silicon laths in an Al-rich α matrix and decomposed ß and interdendritic η phases. The HAZCA alloy developed relatively larger amounts of α phase and lesser amounts of prior ß phase and eutectic zinc pools than the Super Cosmal.

   In both alloys ε and T' intermetallic compounds were found at the α/ß boundaries. Silicon was present as primary polyhedral particles and eutectic laths the size and distribution of which depended on the solidification rate. Combined with iron, curved blades of intermetallic compounds of Si were also detected in the HAZCA alloy.

   Super Cosmal alloy showed a more definite decomposition of the prior ß phase into particulate and lamellar structures of α and η phases than in HAZCA alloy. In this alloy the zinc-rich spaces exhibited mainly a particulate structure. The reason for this is thought to be to the influence of magnesium retarding the discontinuous ß-decomposition and the overall rate of zinc precipitation. This was found by Zahra et al.[42] in studying isothermal ageing in Al-(40-50)% Zn alloys.

2. In all alloys directional solidification and the use of chills produced zones of low porosity and refined structure in which mechanical properties were improved. It has been confirmed that with up to 2.5% porosity, the tensile strength of ZA-27 castings was not strongly influenced. Meanwhile, Super Cosmal and HAZCA were significantly affected by the presence of shrinkage pores within the same range.

   Considering a realistic level of 1-1.5% porosity for ordinary sand castings, a summary of averaged mechanical properties for all alloys is presented in Table 6 where density is also included.

Table 6. Summary of mechanical properties of sand cast ZA-27, Super Cosmal and HAZCA alloys.

Properties	ZA-27	Super Cosmal	HAZCA
Density (Kg/m^3)	4 980	3 380	3 280
U.T.S. (MPa)	350	310	270
0.2% Yield Strength (MPa)	325	-	-
% Elongation	2 - 3	-	-
Strength/weight ratio	70.3	91.71	82.3
Impact Strength (J)	50	7	7
Brinell Hardness	105	130	137

Clearly the combined effect of silicon and copper strengthened and hardened the Zn-Al binary, but changing the composition from Super Cosmal to HAZCA by adding 2% more of Si and 1% more of Cu with small amounts of Mg instead of Mn did not improve strength, did not modify brittleness but increased hardness.

Analysing the strength to weight ratio, Super Cosmal and HAZCA alloy become more attractive as hard and strong light materials.

CHAPTER 4

UNLUBRICATED SLIDING WEAR OF HIGH ALUMINIUM ZINC-BASED ALLOYS

4.1 LITERATURE REVIEW

4.1.1 Introduction

Friction, wear and lubrication of interacting surfaces are principal subjects of the wide interdisciplinary science of tribology. As such they have received a great deal of interest by scientists and engineers and a vast quantity of information has been produced showing the complexity of tribological problems.

Friction is the resistance to motion which occurs whenever one solid body slides over another. There are two basic laws of friction which are basically obeyed to a good approximation [42]. The first law states that the friction force is independent of the apparent area of contact of the two bodies, and the second states that the friction force is proportional to the normal load between them. The latter is formulated as $F=\mu W$ where the constant of proportionality μ is known as the coefficient of friction.

The friction force is due to interactions between the opposing asperities of the two sliding surfaces, and the reason why friction forces are often constant, is because the number of asperity interactions taking place at any time is so large that the statistical distribution of the contact process is almost constant. There are two types of asperity interactions: adhesion and deformation and their contributions to friction are not simply additive, but interactive [42].

Adhesion of asperities takes place by chemical or structural affinity between the two surfaces loaded together. Strong cold welds are formed at some asperity junctions and for the sliding to continue these welds must be broken. The break will occur at the weakest part of the junction, which may be the original interface or in the weaker of the two materials.

In the absence of adhesion, the other asperity interaction that results in a resistance to motion is the deformation and displacement of material during relative motion. A microscopic interaction is the deformation and displacement of interlocking surface asperities, and a more macroscopic interaction is the ploughing of grooves in the surface of the softer material by the harder. Another source of ploughing of one or both surfaces are the wear particles trapped between

Quinn [49] understanding classification as a method of grouping together items which have at least one feature in common, proposed that all new classifications of types of wear can be reduced to a more basic and easy to apply classification first given by Archard and Hirst in 1956, namely those of mild wear and severe wear. This classification is based on phenomenological observations like (a) contact resistant measurements, (b) analysis of the wear debris as regards size and composition (severe wear debris normally consist of large particles approx. 10 μm, mild wear debris particles consist of small particles of approx. 100 nm) and (c) microscopic examination of the surfaces (severe wear produces rough deeply torn surfaces while mild wear produces extremely smooth surfaces); this classification can readily be applied to actual wear situations without recourse to any wear mechanisms.

Barwell [50] has suggested that the terms mild and severe wear apply to the form of surface damage rather than the rate of material loss for wear in a mild wear regime can be higher than that in a severe wear regime.

Here a brief description of the classification discussed by Arnell et al. [43] will be reproduced.

Adhesive Wear

The theory of adhesive wear has the same basis as the adhesion theory of friction. Strong cold welds are formed at some asperity junctions and these welds must be sheared for sliding to continue. The amount of wear then depends on where the junction is sheared; if shear takes place at the original interface, then wear is zero, whereas if shear takes place away from the interface, a fragment of material is transferred from one surface to the other. This transfer of material is observed in practice normally from the softer material to the harder.

Abrasive Wear

There are two types of abrasion, known respectively as two-body abrasion and three-body abrasion, in each of which a soft surface is ploughed by a relatively hard material. In two-body abrasion a rough hard surface slides against a relatively soft opposing surface, whereas in three-body abrasion rough hard particles trapped between the two sliding surfaces cause one of them to be abraded.
This kind of damage is usually described by other authors as scratching scoring, or gouging, the difference being mainly in the degree of severity [44].

Surface Fatigue

Surface fatigue is an important phenomenon on two scales, macroscopic and microscopic. Macroscopic fatigue wear occurs at non-conforming loaded surfaces, whereas microscopic fatigue occurs at the contacts between sliding asperities. In loaded sliding contacts because of the asperity height distribution these are strained to different extents, so that, in general, the contact stresses will vary from a very low level of elastic stress up to a level of fracture stress of the weaker of the materials. The elastic stresses will cause no damage, while the fracture stress will cause the formation of a wear particle, during a single interaction. However, at intermediate stresses, the asperity will be subjected to a single fatigue cycle. The accumulation of such cycles during sliding will cause the formation of a wear particles by local surface fatigue fracture.

Delamination Wear

Delamination wear takes place as a result of relative sliding between two surfaces under a normal contact load. It is a process consisting of the following mechanisms:

1. When two sliding surfaces interact, the asperities in the softer surface are flattened by repeated plastic loading, until the sliding condition corresponds to that of a harder, rough surface sliding against an approximately plain softer surface. Thus, at each point on the softer surface there is repeated surface cyclic shear loading.

2. As this cyclic loading continues, voids and cracks are nucleated below the surface.

3. Further cycling causes these voids and cracks to link up, to form long cracks at an approximately constant distance below the surface.

4. When the cracks reach some critical length, the stress situation at the crack tip causes the crack to break through to the free surface, resulting in the formation of the thin plate like wear particles which are often observed in practice.

Corrosive Wear

When rubbing takes place in a corrosive environment, either liquid or gaseous, then surface reactions can take place and reaction products can be formed on one or both surfaces. These

reaction products can be removed by rubbing and the cycle of removal can be repeated indefinitely.

One important point to note is that oxidation of sliding surfaces is usually beneficial. The oxide film prevents metal-metal contact and thus mitigates against the severe adhesion-enhanced wear which would otherwise occur.

Very often, when surfaces are oxidised, the wear debris is finely divided oxide, the rubbing surfaces remain smooth and the rate of loss of material is low.

4.1.3 Wear Equations

Based on simple models for the three basic mechanisms of adhesion, delamination and abrasion, wear relationships of the type Archard formulated in 1953 were developed by various workers. A general mechanical wear law is now known as the following:

$$Q = K\frac{W.S}{H}$$

Where:

- Q = Wear volume
- W = Normal load
- S = Sliding distance
- H = Hardness
- K = Wear constant

The equation suggests that the volume of material worn is proportional to the applied normal load and the sliding distance and inversely proportional to the hardness of the softer material. The constant K is interpreted as the probability of producing a wear particle at any given asperity encounter.

Wear rate is usually related as the volume removed per unit sliding distance (w) and since the real area of contact can be written as $A = W/H$ (where hardness H represents the yield pressure of the softer material) another way to express wear rate in terms of the real area of contact is as $w = KA$.

Wear coefficients (K) in most engineering situations are found to be of the order of 10^{-3} - 10^{-7} with the upper value of 10^{-3} corresponding to unacceptably high wear.

Quinn [49] suggested that the knowledge of the factors influencing K is of the highest priority in understanding the fundamentals of wear. For instance, he reported the following expression for the mild wear of steels based on the oxidational wear theory:

$$W = \left[\frac{dAp\ \exp(-Q_p/RT_o)}{\xi^2 \rho_o^2 f^2 U}\right] A$$

Where ρ_o is the density of the oxide, f the fraction of oxide which is oxygen. U is the linear sliding speed, d is the distance of a sliding contact during which oxidation occurs at a temperature T_o, A_p is the Arrhenious constant, Q_p is the activation energy for oxidation and R the gas constant. In the same article an expression for severe wear based on the delamination theory is reproduced as:

$$W = \left[\frac{B_1 h_1}{dc_1} + \frac{B_2 h_2}{dc_2}\right] A$$

Where the expression for K between brackets contain factors like; thickness of removed layers (h), critical plastic displacements (d) and topography constants (B).

Although the theoretical wear equations increase the understanding of wear processes, it is still generally agreed that the only safe way to select materials to resist wear is on the basis of tests.

4.1.4 Wear Rate and Mechanical Properties

As the removal of material from metallic surfaces by any mechanism occurs by deformation and fracture of wear particles from the wearing material, then the wear rate must depend on mechanical properties such as flow stress, hardness, strain hardening capability, ductility and toughness of the wearing material [48]. As a general rule the adhesion, delamination and abrasion rates are inversely proportional to the hardness. This relationship is only applicable if the increased hardness does not severely affect other mechanical properties. It has been observed that increasing hardness by introducing many hard second phase particles may increase delamination rate, because the hard particles may act as void nucleation sites. The effect of ductility and toughness has not been studied extensively. It may be expected that an increase in ductility should decrease the wear rate. However, this may not be observed since by increasing ductility, the hardness of the alloy is usually decreased, which may increase the

wear rate. Jahanmir points out as well that the lack of a simple relationship between the wear rate and some of the mechanical properties is partly due to the interdependence of mechanical properties and partly due to the difference in the state of stress during wear and during mechanical property testing.

4.1.5 Wear Testing

There are two kinds of laboratory wear tests. First, tests in which specimens with convenient geometries are run against each other, varying parameters one at a time, and then attempting to correlate wear rate with them. This kind of tests range from simple comparative wear studies to closely controlled experiments aimed at a better understanding of fundamental wear mechanisms. Second, tests which simulate the practical situation where the conditions simulated are often the worst wear conditions that are likely to be met in practice [51].

Czichos [47] distinguished four groups of parameters to be taken into account in any tribological testing; namely:

1. Technical functions of the tribo-system.
   Transmission of motion, transmission of energy, transport of materials, etc.

2. Operating variables.
   Type of motion, load, velocity, temperature and time.

3. Structure of the tribo-system:
   a) Elements: tribo-element 1, tribo-element 2, lubricant, atmosphere
   b) Properties of elements: Relevant geometrical and materials properties
   c) Relationship between elements.

4. Tribological characteristics.
   Data which have to be measured in tribo-testing as changes in properties, changes in contact topography, friction, materials losses, etc.

It is necessary to keep uniform the testing methodology in order to obtain reliable results.

The most common specimen geometries used for simple wear tests are pin-on-disc, pin-on-cylinder and crossed cylinder arrangements.

4.1.6 Previous Sliding Wear Studies on Zinc-Aluminium Alloys

It is widely known that the ZA-12 and ZA-27 alloys have been demonstrated to have excellent wear and bearing properties. Most of the published research work about the tribological behaviour of these materials accounts for comparative wear rate evaluations in lubricated conditions or simulative bearing testings. However, only a few studies regarding dry sliding wear tests are known in the literature, in spite of its valuable contribution to the understanding of the mechanisms of sliding interaction.

Barnhurst and Farge [52] carried out lubricated wear tests on a variety of zinc-based alloys and other standard bearing alloys using a block-on-ring equipment. A load of 6.9 MPa and sliding speed of 0.15 m/s were applied as experimental conditions and wear was measured by weight losses. A steel ring was used as the counterface material. The study showed that sand cast ZA-27 alloy presented equivalent wear resistance to aluminium bronze and was superior to SAE 660 lead-tin bronze.

The variation in performance of the ZA alloy as a function of the production process was found to be dependent on the amount of ε phase and the matrix hardness.

Mani et al. [53] have reported a study on the tribological properties of cast zinc-aluminium alloys of 12% and 27% Al, both with three different levels of copper content. The friction and wear tests were carried out on a pin-on-disc arrangement at 8.5 m/s of speed and 7.5 kg/cm^2 of loading stress, wear being expressed as percentage of mass loss. As a result, an improvement in wear resistance with increasing copper was found in both Zn-Al alloys. A comparison with two copper-based alloys gave favourable results for the ZA alloys.

Zhu [32] has investigated the sliding wear behaviour of various Zn-Al-Si and Zn-Al-Cu-Si alloys against a hardened steel counterface. A pin-on-disc apparatus was used in dry conditions and at 0.84 m/s of sliding speed and 2 kgf load. Wear rate was reported as volume loss per unit sliding distance. It was found that the wear resistance of alloys in the Zn-Al-Cu-Si system was higher than that of the Zn-Al-Si system. Particularly alloys of monotectoid composition showed the best resistance to wear. It was explained that the combined effect of T' and Si-rich phases increasing hardness and tensile strength were responsible for such a behaviour.

Regarding Zn-Al alloys of higher aluminium contents than those of the ZA family, Marczak and Ciach [54] studied the wear and friction properties of ZnAl40Cu alloys. Samples were rubbed against a rotating steel ring in lubricated conditions and at high loads until seizure occurred.

The ZnAl38Cu2 alloy was found to have the best anti-seizure response. This result was explained to be due to the formation of a net of oxides on the aluminium and zinc precipitates which resulted from the spinodal transformation of supercooled zinc-rich α phase during heat treatment. The hard aluminium oxide contributed to wear resistance and the softer zinc oxide because of its hexagonal structure acted as a lubricating agent.

4.1.7 Sliding Wear Studies on Aluminium-Silicon Alloys

It is well known that Al-Si alloys are extensively used in applications requiring good sliding resistance such as cylinder blocks, cylinder heads, pistons, and others. Recently Al-Si-based alloys are also finding applications as bearing materials.

Wear resistant Al-Si alloys are complex alloys of near eutectic composition containing other alloying elements like copper, nickel and magnesium.

Sarkar [55] tested a number of Al-Si alloys under dry sliding conditions and found that hypereutectic alloys wear more than hypoeutectic alloys. The predominant mode of wear was found to be by separation of all or part of the work-hardened layers from random patches on the wear track.

Shivanath et al. [56] carried out dry wear tests on a number of binary Al-Si alloys using a pin-on-disc technique, where the material of the rotating disc was a heat-treated steel. They found that all alloys exhibited two wear mechanisms; one oxidative and the other metallic. The oxidative wear rate was shown to be independent of the silicon content and its particle size. Metallic wear occurred on a fairly massive scale because the yield strength had been exceeded and fracture produced separation of large fragments of metal.

Beesley and Eyre [57] in a similar study on Al-based alloys established the fact that during mild wear, protective surface films were produced and maintained on the wear pin surface. Then they found that the transition from mild to severe wear was associated with the breakdown of these protective layers which could be oxides or even Al/Fe compounds.

Regarding the influence of soft phases on bearing materials Davies and Eyre [58] conducted dry and lubricated wear tests using a pin-on-disc machine at low speeds and a range of loads comparing the behaviour of soft phase-containing alloys like leaded bronze and aluminium-tin, with hard aluminium-silicon alloys. It was found that the soft alloys presented low wear rates during running-in because the soft phases provided a kind of solid lubricant film which controlled metallic wear. In contrast the Al-Si alloy exhibited a high wear rate during running-

in which decreased with the onset of equilibrium conditions owing to the build-up of oxide films.

4.2 SPECIFIC AIM OF THE DRY WEAR-TESTING WORK

The main objective of the present work was to establish the wear characteristics of high aluminium zinc-based alloys having in mind their use as plain bearing materials that work under boundary conditions of lubrication.

Boundary conditions of lubrication in plain bearings are generated by low speed-high load combinations or by conditions of lubricant starvation leading to metal-to-metal contact between journal and bearing. Therefore it is of great importance to assess the bearing materials' behaviour in an extreme situation of friction where a small sample of the testing material is rubbed against a material representing the journal in the absence of lubricant.

In this work a pin-on-disc machine was used to study the wear resistance of the Super Cosmal and HAZCA alloys in a comparable way under unlubricated conditions and at relatively high load-low speed combinations. Sand cast ZA-27 alloy and a bearing leaded-tin bronze (SAE 660) were used as standard materials for comparison since they have been demonstrated to behave well under severe conditions.

A separate set of tests were carried out to obtain information about temperatures generated by frictional heating on the test pin.

Finally, microscopic analyses were carried out on pin worn surfaces and transversal sections of worn pins to observe the type of the surface damage which had occurred on the wear pin.

4.3 EXPERIMENTAL DETAILS

Pin-on-Disc Apparatus

The arrangement of the pin-on-disc machine used for wear testing is shown in Figure 79. The friction force and the amount of wear were measured by two linear variable differential transducers; (a) and (b) respectively. Both transducers were connected to a potentiometric recorder.

Figure 79. Pin-on-disc wear machine.

The friction force between pin and disc produces a torque on the load arm which acts on the cantilever (c). The cantilever deflection is measured by the horizontally positioned linear transducer.

Wear was measured as the change in length of the test pin by means of the vertical linear transducer.

Frictional forces were calibrated on the chart recorder by applying static loads against the cantilever using an arrangement of pulley and weights. The relationship found was 1Kgf=13.4 mm displacement on the chart at a full scale sensitivity of 5 mV.

The vertical displacement of the carriage arm was calibrated on the chart using a set of feeler gauges. The relationship found was 1 mm wear = 63 mm on the chart at a full scale sensitivity of 200 mV.

Operating Variables

Load :- Load was varied in a range of 0.6 - 15 kgf which represented a range of 1.8 - 4.6 MPa of loading stress on the pin.

Sliding Speed :- Sliding speed was varied in four steps of 0.25, 0.50, 1.0 and 2.0 m/s.

Sliding Distance :- At continuous sliding, the distance travelled was maintained at 5400 m in all cases.

Tribological Elements

Wear Pins:- Wear pins (p) were machined as cylindrical rods 6.33 mm in diameter and 50 mm long. The contact surface of the pin was ground to 0.3 μm c.l.a using grinding paper stuck to some discs on the same wear machine. This was done to ensure conformability between pin and disc surfaces.

Wear Disc:- Wear discs (d) were made of hardenable steel EN31 and heat-treated to approximately 60 Rc of hardness. A new surface finish was obtained by grinding to 0.3-0.4 μm c.l.a. of surface roughness.

Lubricant:- No lubricant was intentionally used during wear testing.

Atmosphere:- Wear tests were run at laboratory atmosphere at an average room temperature of 22°C.

Evaluation of Tribological Characteristics

Wear rates were obtained as volumetric loss of material per unit of sliding distance. Wear rates were measured as a function of load at four constant levels of sliding speed.

Coefficients of friction as a function of load and sliding speed were also obtained.

The appearance of pin worn surfaces were observed after each test.

Wear Testing Procedure

1. A conformal pin and disc contact was obtained by grinding the test pins over disc carrying abrasive paper on the same wear testing machine. Grinding on each paper took only a few seconds using a small load of 1N. The resulting surface roughness was 0.3 μm which was maintained constant for all pins and materials.

2. Both test pin and disc were ultrasonically cleaned in methyl alcohol.

3. In order to calculate mass losses after testing and to double check wear results given by displacement measurements, the initial mass of the pin to be tested was determined using a balance of 0.01 mg of resolution.

4. The test pin was mounted on the loading arm of the wear machine and the required load and speed were set up.

5. Friction and wear linear transducer signals were zeroed on the chart recorder and test was started full load.

6. Tests were stopped when the required sliding distance was achieved.

7. After each test, the wear lips were carefully removed from worn pins which were then, ultrasonically cleaned in methyl alcohol and weighed again.

8. Pins were sectioned at 4-5 mm from the worn surface for microscopic observation of wear scars.

In order to measure the temperature rise on the test pin due to frictional heating, a microthermocouple was welded to the exposed lateral face of it at 3-4 mm away from the contact surface. Temperature rise was monitored during a 1 hour run at constant sliding speed and different levels of normal load.

Analysis of Worn Surfaces

Standard Scanning Electron Microscopy was applied to observe the appearance of wear scars on pins after test. The backscattered electron mode was used to obtain views of subsurface structures.

In order to find out the elemental composition of the surface layer of worn pins and their chemical state, selected samples were sent for surface analysis in the Applied Physics Department where Auger Electron Spectroscopy was applied for that purpose.

4.4 EXPERIMENTAL RESULTS

Volumetric wear rates and coefficients of friction were calculated from the chart recorder output of both displacement transducers. An example of the friction and wear profiles on the chart is shown in Figure 80. The friction trace show the typical type of fluctuation found in most metal-to-metal frictional interactions. For a given condition of load and speed the mean frictional force was practically constant throughout the test.

Super Cosmal, HAZCA and ZA-27 alloys showed the same type of friction traces, whereas bronze produced smoother frictional behaviour but louder screeching.

In all cases, linear wear traces started with a period of running-in, the extension of which depended mainly upon the applied load. After this period the wear curve showed a nearly constant rate of variation. Under conditions of severe wear the curve showed a progressive increase in slope.
Wear rates calculated from graph traces compared very well with those calculated from mass loss determinations. Discrepancies between these results were found to be in the range of 0.2-5% with a mean value of 1.5%.

4.4.1 Wear and Friction

The wear behaviour of ZA-27 alloy expressed as volumetric loss of material per unit sliding distance (in kilometres) is shown in Figure 81 to be proportional to the applied load at all constant sliding speeds.

Wear rates decreased with increasing speed from 0.25 m/s to 1 m/s, however, at 2 m/s this tendency was no longer obeyed and a severe type of wear occurred.

Wear of Super Cosmal alloy as a function of the applied normal load at speeds of 0.25, 0.50, 1.0 and 2.0 m/s is shown in Figure 82. It can be observed that at 0.25 m/s and 0.5 m/s there was a linear relationship between wear and load within the whole range of loads applied and that at a sliding speed of 1 m/s, two wear regimes were established; at loads of up to 7 kgf a mild wear regime similar to that of ZA-27 pins, and a more severe loss of material at higher loads. High wear rates even at low loading stresses at 2 m/s of sliding speed are also shown in this graph.

The wear behaviour of the experimental HAZCA alloy as shown in Figure 83, was similar to that of the Super Cosmal at sliding speeds of 0.25, 0.5 and 2 m/s. The exception lay on the curve corresponding to 1 m/s speed where the transitional load from low to high wear rate had shifted down to 5 kgf. The lowest wear rates of this alloy were obtained at 0.5 m/s at all loading stresses tested.

The wear testing conditions used in the present work, were too severe for the bearing bronze SAE 660. As shown in Figure 84, tin-leaded bronze pins showed heavy loss of material even under low loads when dry rubbed against a steel counterface.

Figure 85 shows the variation of the coefficient of friction (μ) at constant speed and increasing load. It can be observed that μ practically remained constant within the range of loads applied. This of course is the result of a proportional relationship between friction force and load. On the other hand, for a given load at increased speed levels higher coefficients of friction were obtained except when sliding speed was 2 m/s.

The coefficients of friction corresponding to the dry sliding tests of the Super Cosmal alloy are plotted in Figure 86. There is not a clear correlation between them and speed and load changes but it appears that high wear rates were associated with relatively low frictional coefficients.

Coefficients of friction relative to the pin-on-disc test on HAZCA alloy also showed the same pattern as those of the Super Cosmal alloy. As shown in Figure 87 they fluctuated within a band of 0.4 to 0.55 with the lowest values corresponding to high wear rates. Strangely, the coefficients of friction for 2 m/s sliding speed were higher that those of the Super Cosmal and similar to those of the ZA-27 alloy.

The coefficients of friction were as high as 0.6 to 0.7 at low stresses, but dropped to relatively low values in higher wear situations.

4.4.2 Temperature Rise on Test Pin during Dry Sliding

Figures 89 to 92 show the temperature evolution in the test pins due to frictional heating during tests of 1 hour duration at different experimental conditions for ZA-27, Super Cosmal, HAZCA and Bronze (SAE 660) alloys respectively.

The temperature traces followed approximately a fluctuating pattern similar to that shown by the friction force so that each temperature point on the graph represents the mean value between the highest and lowest peaks at a given time.

On starting the test, the temperature increased suddenly to a value dependent on applied normal load and sliding speed, with continued sliding temperature increments becoming smaller until a near to equilibrium condition was established by the end of the test.

In all zinc-based alloys the temperature of the test pin increased with increasing load and speed, whereas the bronze pin showed smaller temperature changes with load and speed variations.

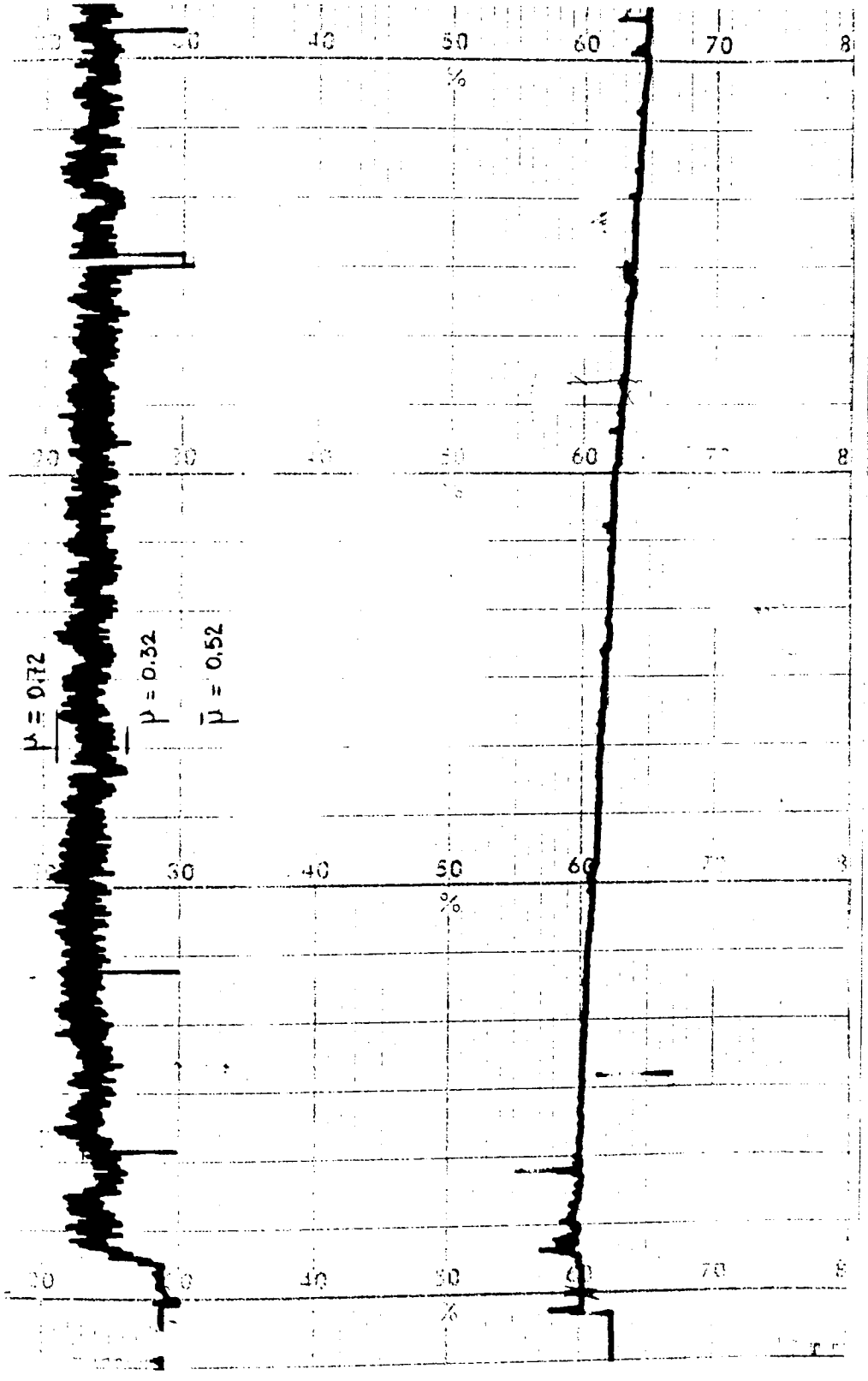

Figure 80. Characteristic friction and wear drifts on chart recorder during dry sliding test.

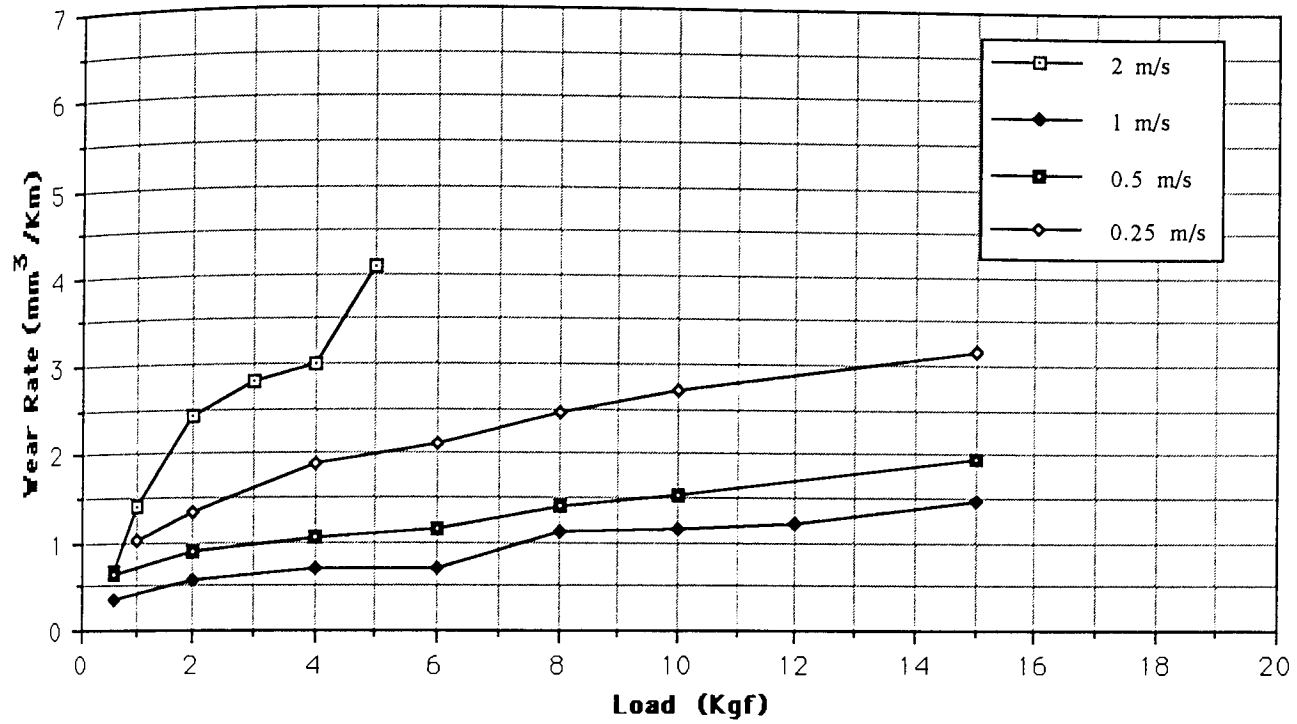

Figure 81 ZA-27 alloy. Volumetric wear rate as a function of load and sliding speed.

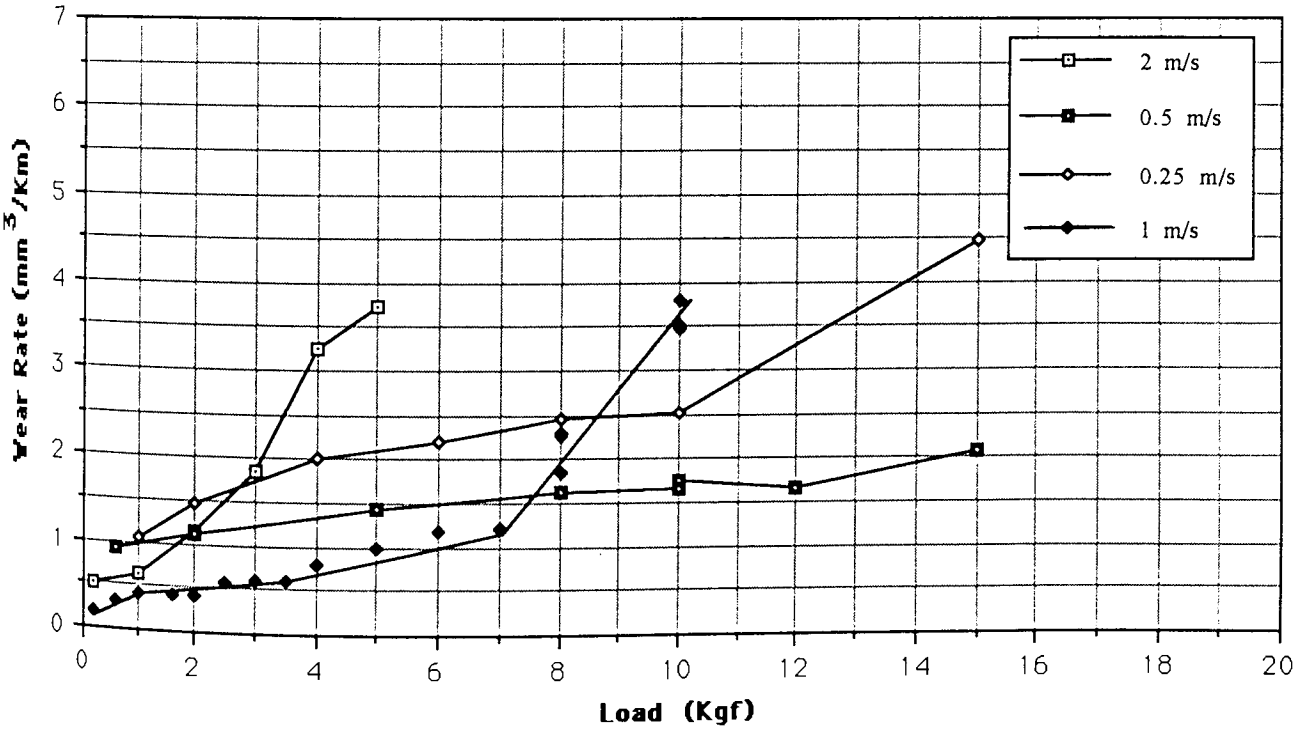

Figure 82. Super Cosmal alloy. Volumetric wear rate as a function of load and sliding speed.

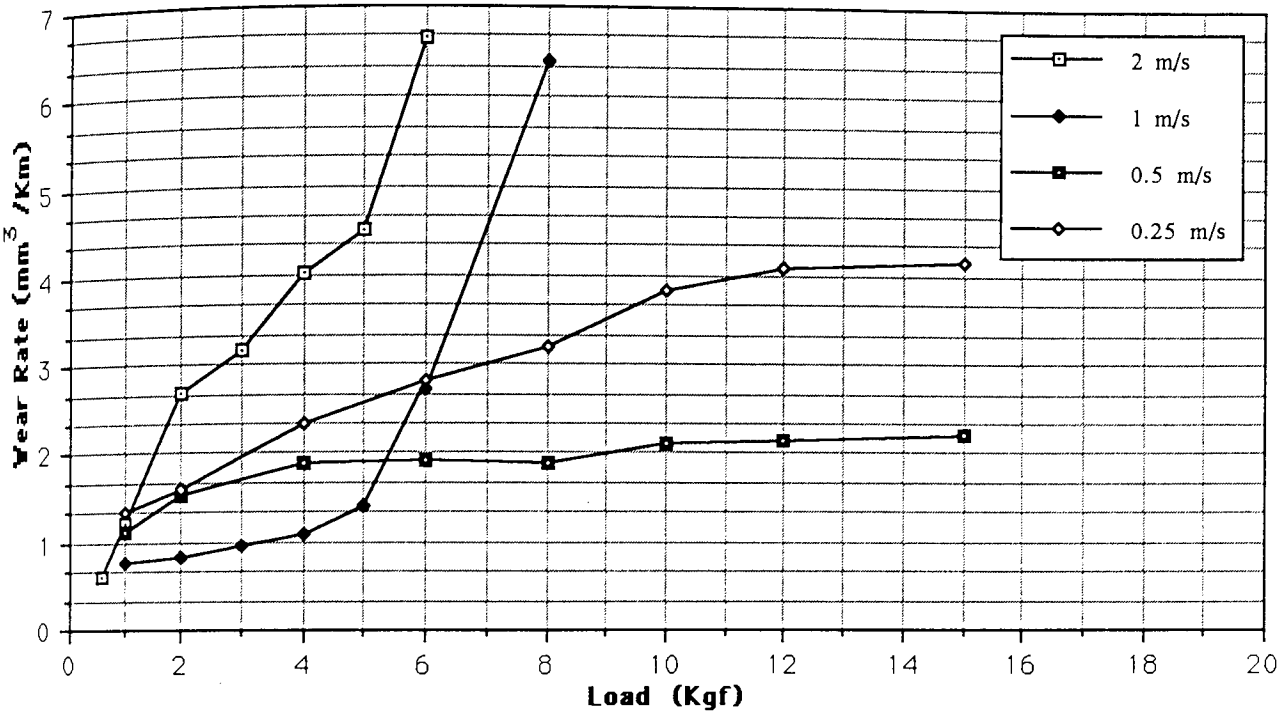

Figure 83. HAZCA alloy. Volumetric wear rate as a function of load and sliding speed.

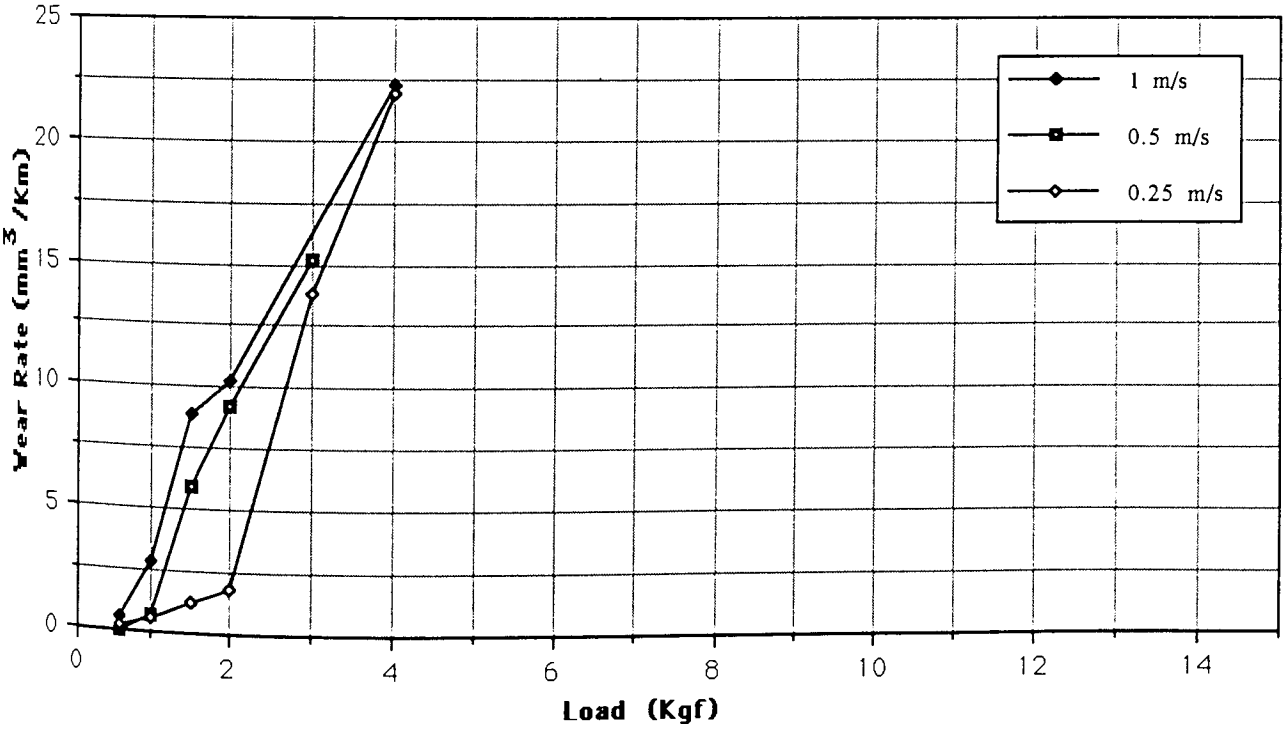

Figure 84. Tin-leaded bronze (SAE 660). Volumetric wear rate as a function of load and sliding speed.

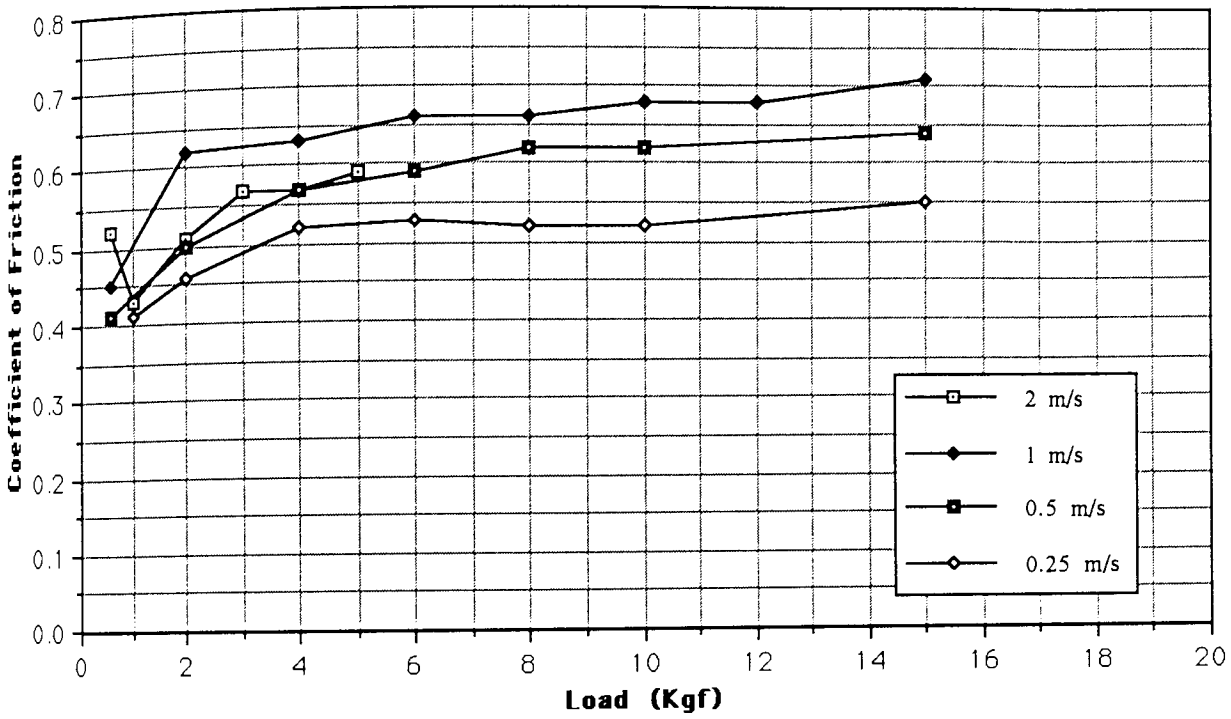

Figure 85. ZA-27 alloy. Coefficient of friction as a function of load and sliding speed.

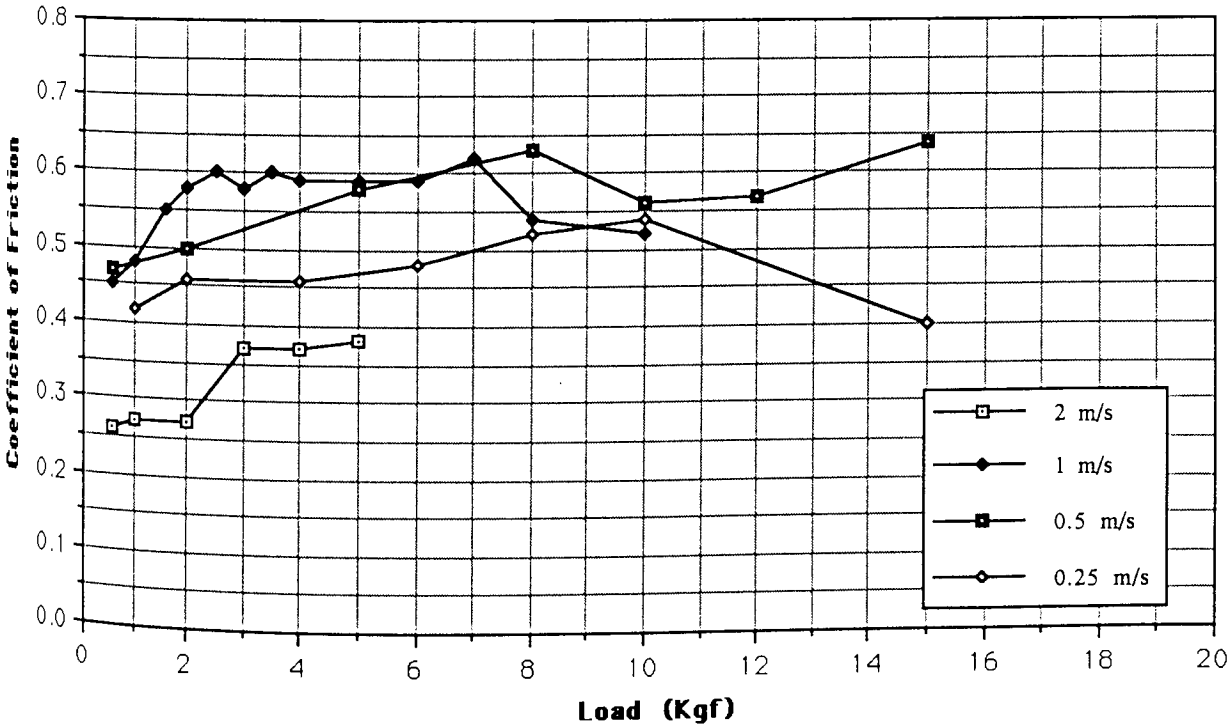

Figure 86. Super Cosmal alloy. Coefficient of friction as a function of load and sliding speed.

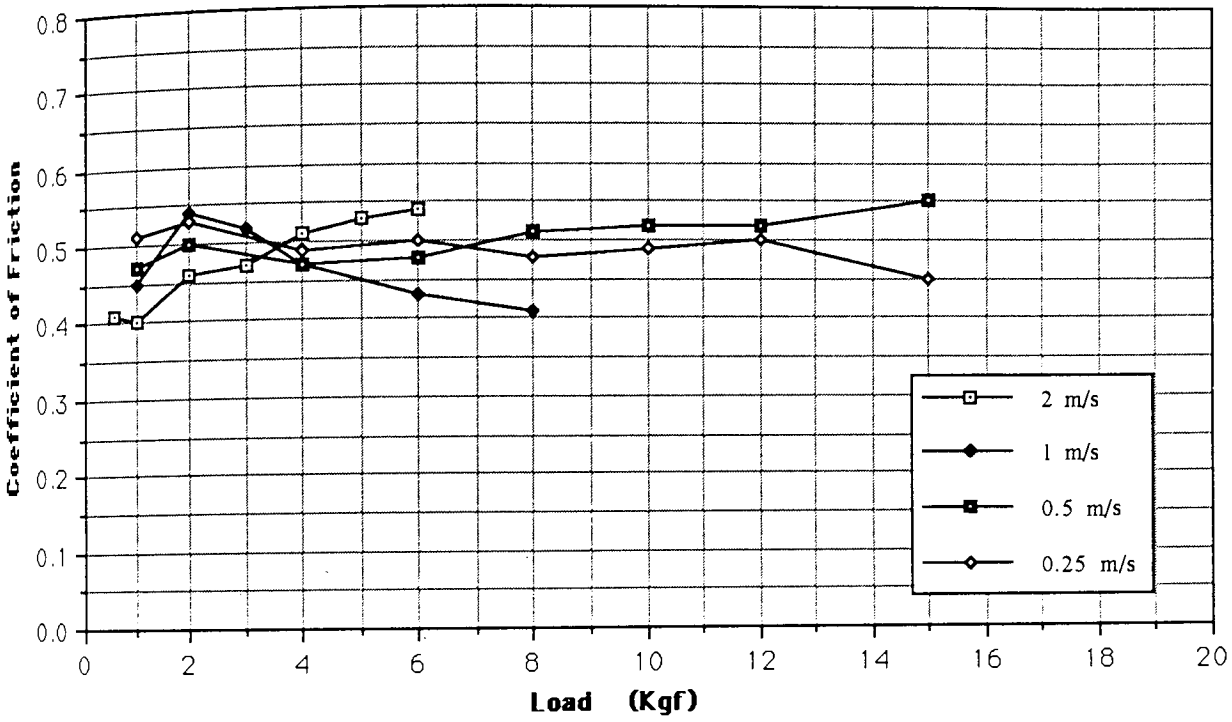

Figure 87. HAZCA alloy. Coefficient of friction as a function of load and sliding speed.

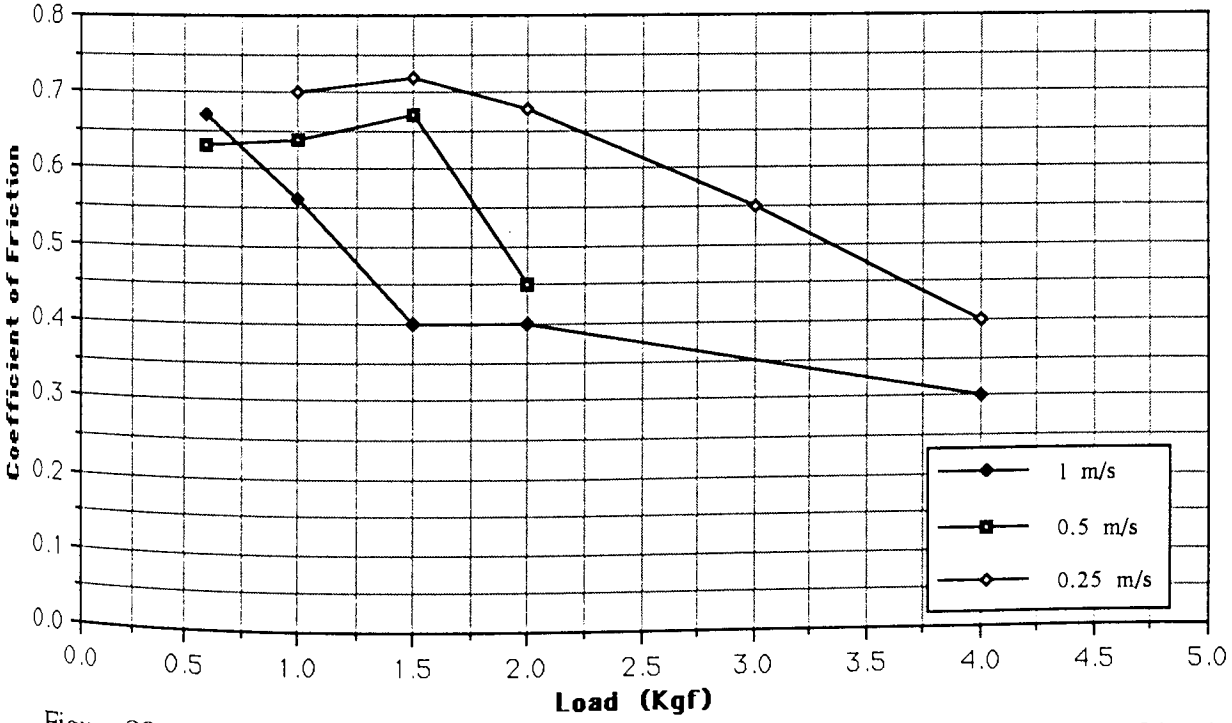

Figure 88. Leaded-Tin bronze (SAE 660). Coefficient of friction as a function of load and sliding speed.

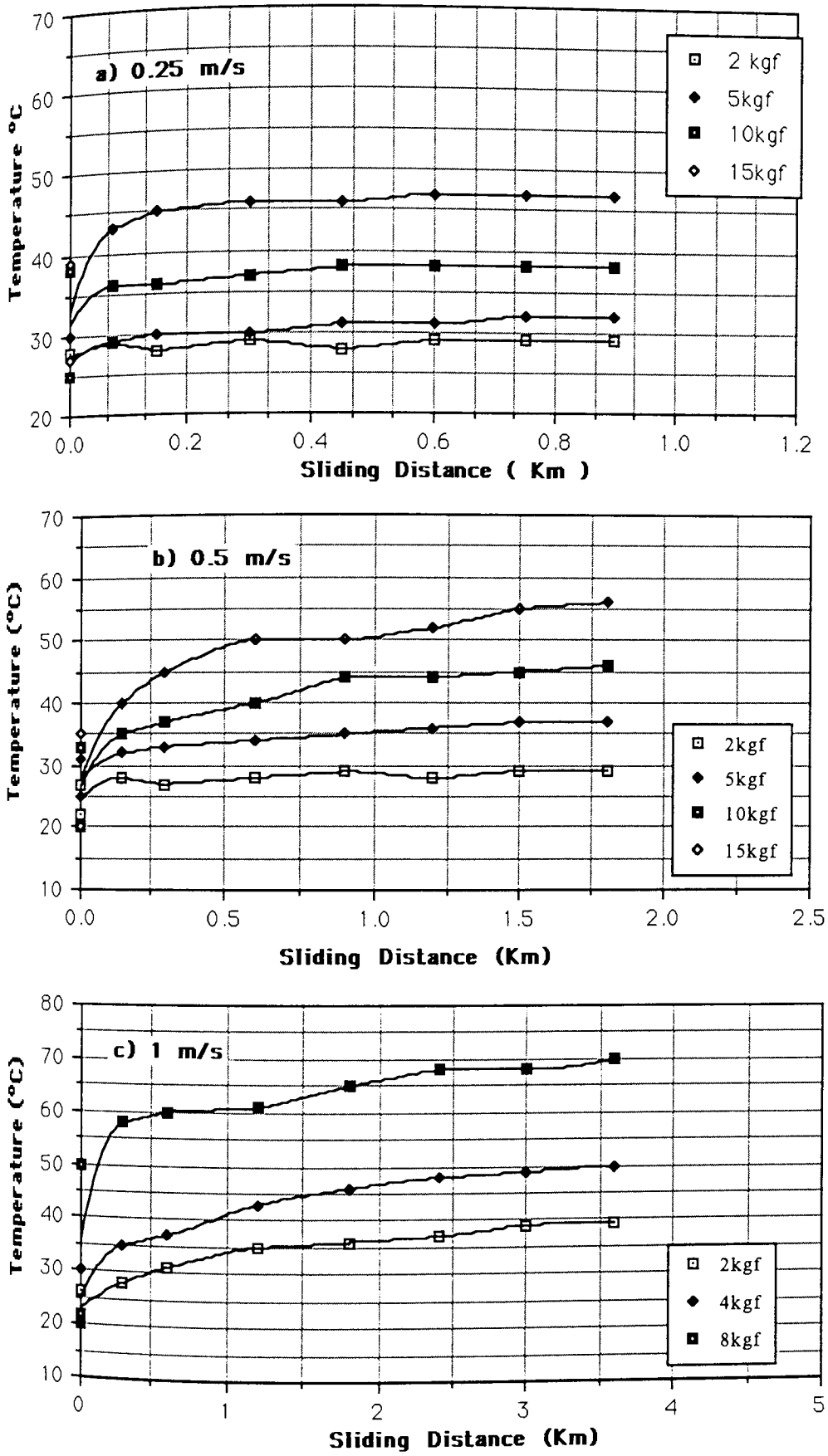

Figure 89. Temperature rise in ZA-27 test pin during 1 hour dry sliding run as a function of load at a) 0.25 m/s, b) 0.5 m/s and c) 1 m/s.

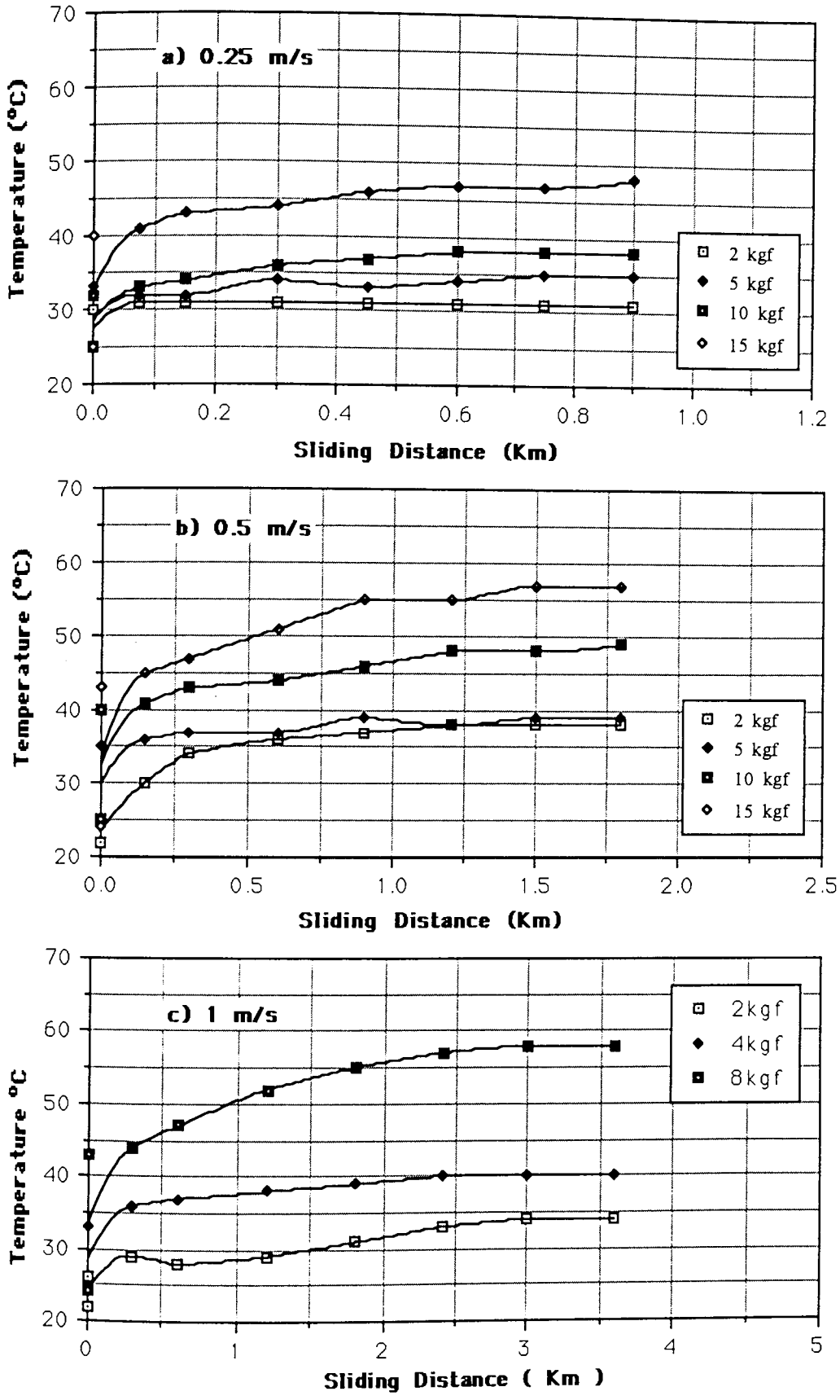

Figure 90. Temperature rise in Super Cosmal test pin during 1 hour dry sliding run as a function of load at a) 0.25 m/s, b) 0.5 m/s and c) 1 m/s.

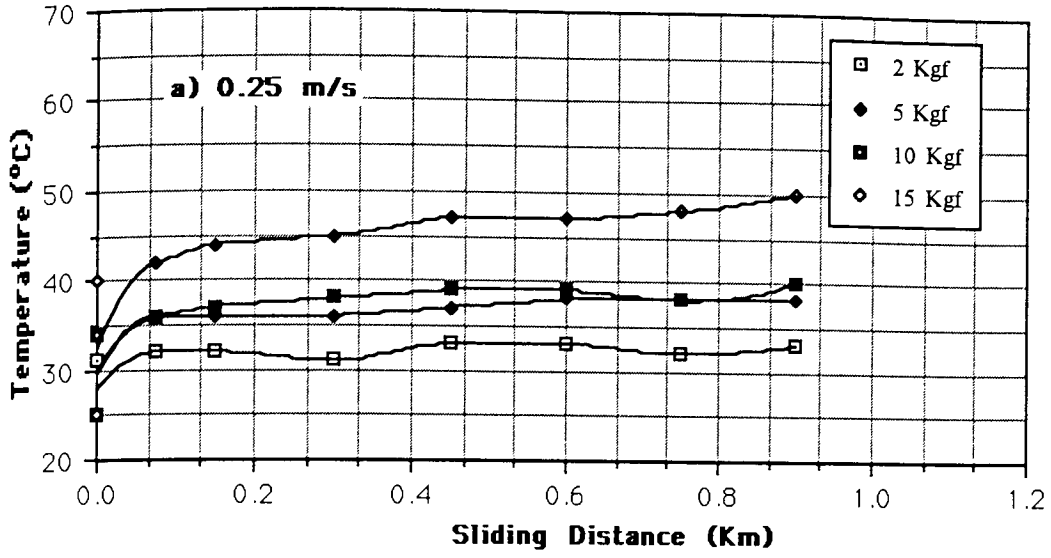

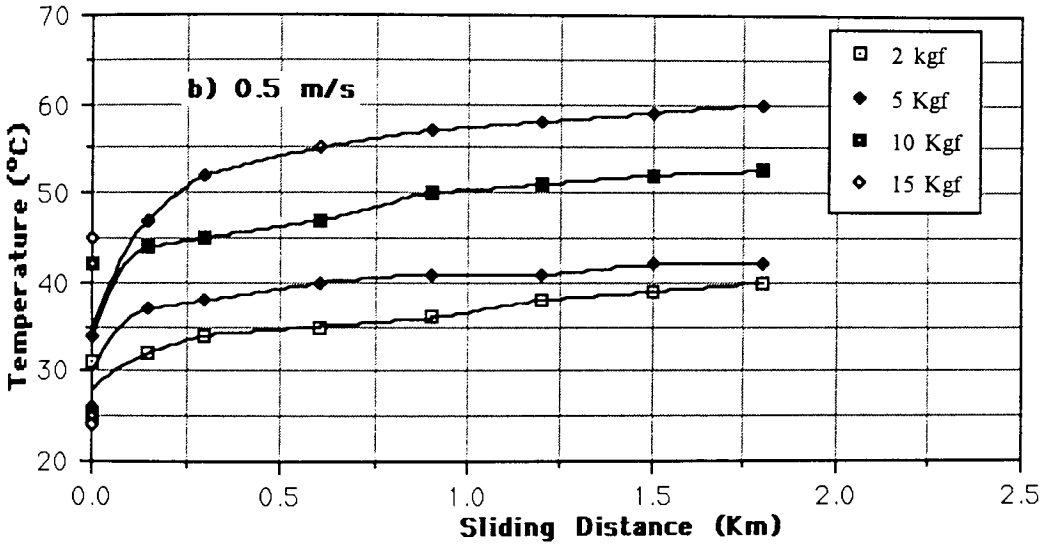

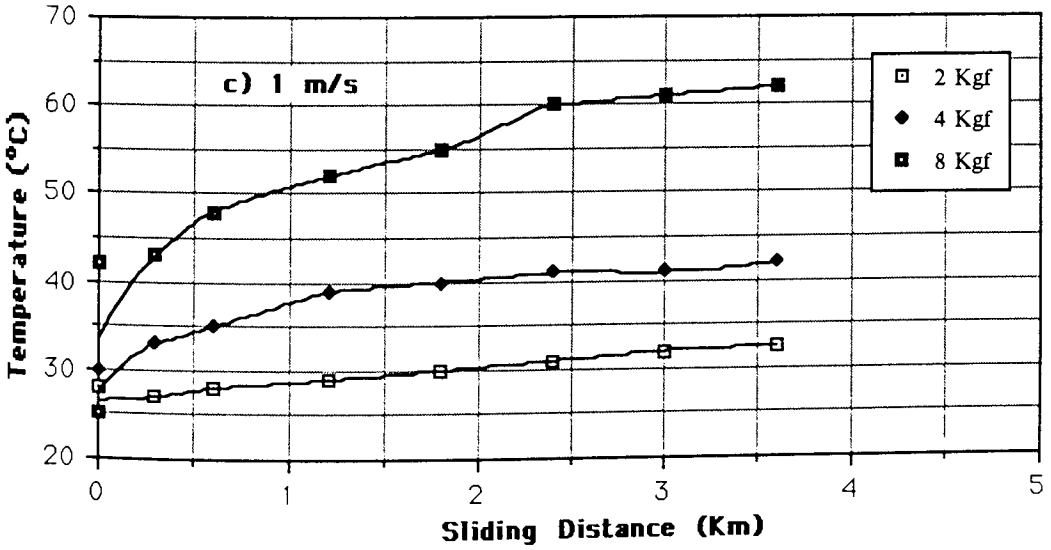

Figure 91. Temperature rise in HAZCA test pin during 1 hour dry sliding run as a function of load at a) 0.25 m/s, b) 0.5 m/s and c) 1 m/s.

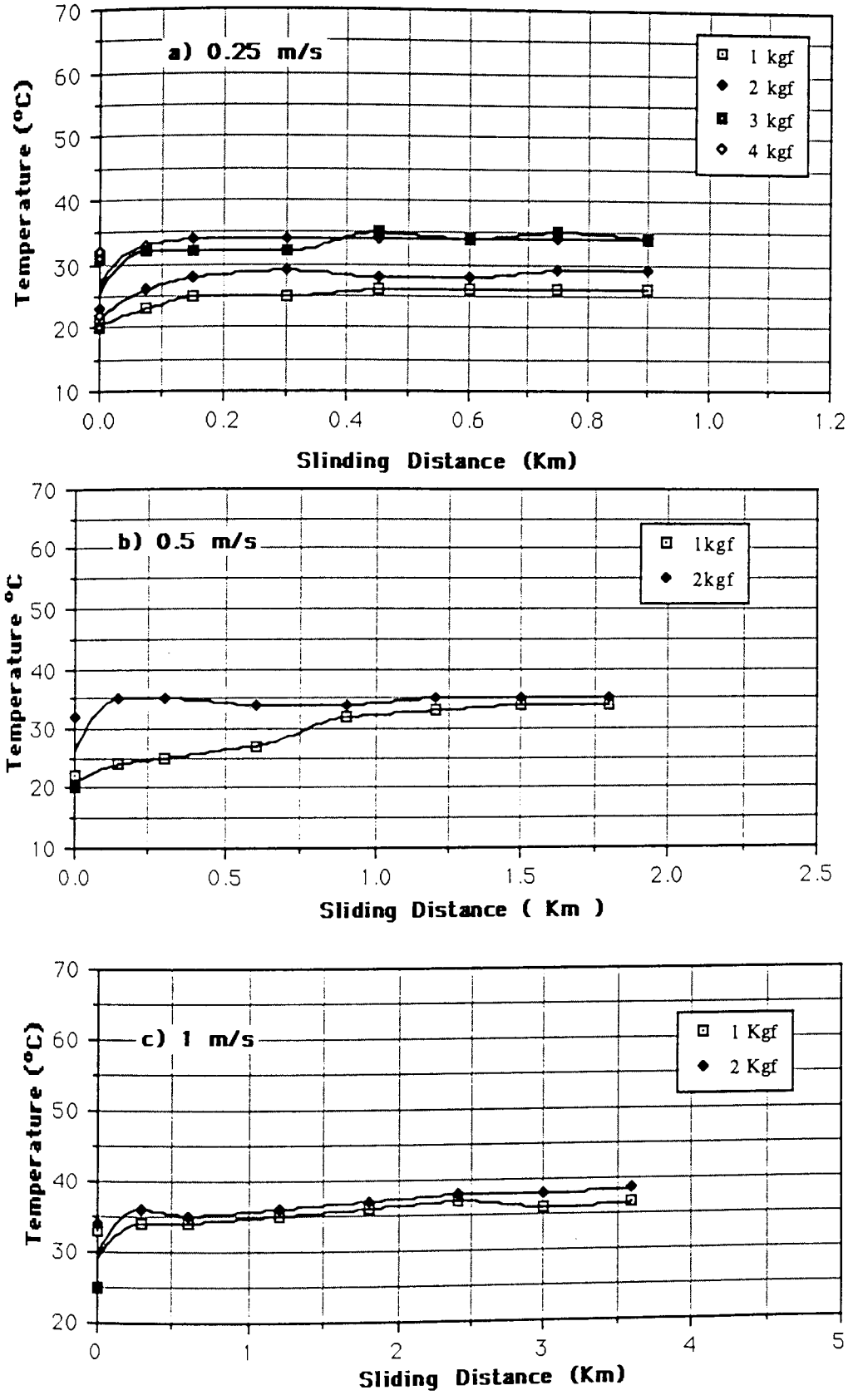

Figure 92. Temperature rise in bronze (SAE 660) test pin during 1 hour dry sliding as a function of load at a) 0.25 m/s, b) 0.5 m/s and c) 1 m/s.

Temperature increments in the ZA-27 pins appeared to be slightly higher than in both Super Cosmal and HAZCA alloys, but in general at low speeds temperatures at the point on the pin measured did not exceed 60°C even at loading stresses as high as 4.5 MPa.

4.4.3 Pin Worn Surface Appearance and Subsurface Structures

ZA-27 Alloy

The wear rate curves have shown that wear of ZA-27 pins at 0.25 m/s of sliding speed was higher than at 1 m/s. This is qualitatively verified by the appearance of wear scars shown in Figures 93 to 96.

The surface of a ZA-27 pin worn at 0.25 m/s and 10 kgf is shown in Figure 93 where pits of irregular shape probably developed by surface spalling can be observed. It is apparent as well that grooves had formed by the ploughing action of disc asperities and hard wear particles. Figure 94 shows at higher magnification the virgin material left by detached wear particles.

In contrast, the worn surface of a low wear rate pin subjected to 15 kgf load at 1 m/s disc speed presented a different appearance. A layer of black material covering most of the surface could be observed by the naked eye. This is better shown in the SEM micrograph of Figure 95 and 96 where surface spalling and grooving appear not to be severe, besides large and small patches of black material firmly adhered to the wearing surface.

The transverse section of a pin slid at the above mentioned conditions is shown in Figures 97 and 98. It is evident that deformation of the subsurface structure had taken place in the sliding direction, with transportation of material to the interface and the formation of a complex surface layer. The elemental composition of this layer and the chemical state of the elements in it are presented further on.
The pin-disc interaction at 2 m/s has been demonstrated to cause high wear rates in the ZA-27 pins. Evidence of this is shown in the worn surface of Figure 99 where wide bands of metallic appearance exhibit plastic flow of material due to thermal softening leading to scuffing. Heavy ploughing of the surface has also occurred.

Super Cosmal

The wear rate curves of the Super Cosmal alloy have shown that wear of pins at 0.25 m/s of speed was higher than that at 0.5 m/s. This fact was confirmed by the resulting appearance of

pins slid at those conditions. Figure 100 shows that wear particles were produced mainly by separation of large fragments of metal due to surface spalling or by adhesion to the steel counterface, whereas at 0.5 m/s conditions seemed to have been adequate to build up a protective layer that prevented metallic wear. This is shown in Figures 101 and 102. The same situation occurred at 1 m/s speed and low loads at which low wear rates were measured. Figure 103 shows the worn surface in such a case where no severe damage can be seen. However, at 1 m/s but at loads higher than the transitional load, wear became severe by a change in the dominant mechanism of wear which according to Figures 104 and 105 was a combination of plastic deformation of material and surface cracking.

The transverse section of a low wear rate Super Cosmal pin slid at 1 m/s speed is shown in Figure 106 where two zones can be distinguished: 1) a surface layer of complex structure, which composition is presented later and 2) a thin layer of plastically deformed structure. Beneath the latter lies a region of essentially undeformed bulk material. Silicon particles had become shattered in the interface to form part of the topmost layer by the mixing action of the two sliding surfaces.

HAZCA Alloy

Wear rate curves have shown that HAZCA alloy had a similar behaviour to that of Super Cosmal under the same testing conditions. The worn surface appearance of HAZCA pins all presented the same features as those of the Super Cosmal. Figures 107 and 108 show a low wear rate sample slid at 0.5 m/s and 8 kgf on which worn surface pits and valleys produced by metallic fragment detachment appear shallow and small. In contrast a high wear rate pin surface such as the one shown in Figure 109, presented extensive flow of metal and signs of scuffing.

The transverse section of a HAZCA pin worn at 1 m/s and 4 kgf (low wear rate) is shown in Figure 110. Here the surface layer material filled a valley previously formed by fragment detachment. In the next section an analysis of the surface layer is presented.

Bronze SAE 660

The worn surface of a bronze pin which presented a high wear rate during sliding at 1 m/s speed and 4 kgf load is shown in Figure 111. The flat and smooth surface of the wear track is typical of plastic flow of metal in the sliding direction. The severity of the deformation was such that at the trailing edge of the test pin a large lip of wear material has accumulated. As most of the frictional energy was dissipated through plastic deformation of the pin surface, the

subsurface structure was not deformed plastically as is shown in Figure 112. Apart from lead globules smeared on the wearing surface no protective layers could be noticed.

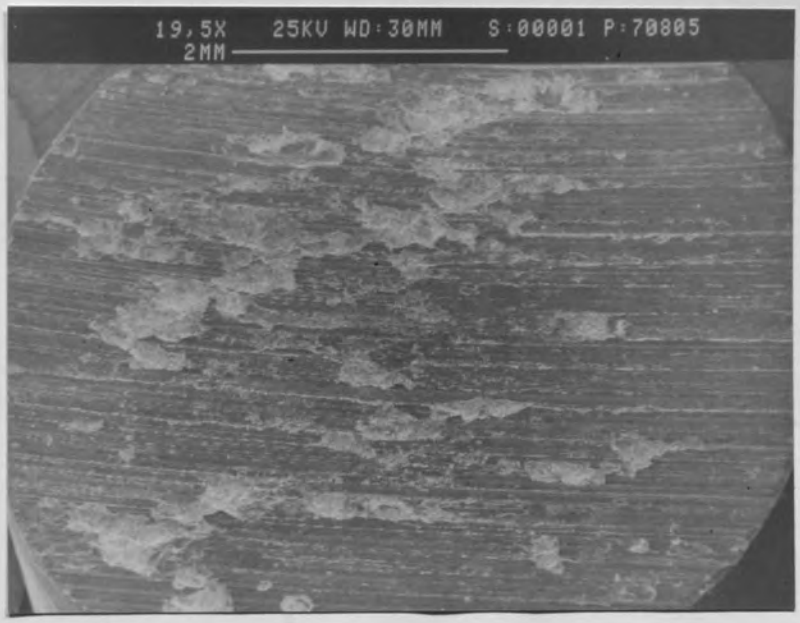

Figure 93. SEM micrograph of the worn face of a ZA-27 pin after sliding at 0.25 m/s speed and 10 kgf load. Sliding direction left to right.

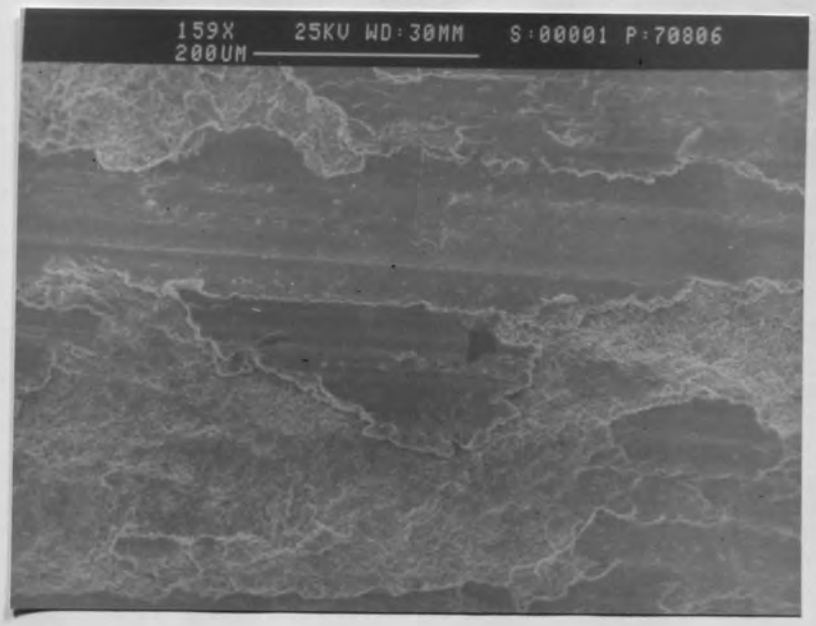

Figure 94. Higher magnification of Figure 93 showing spalling of the pin surface.

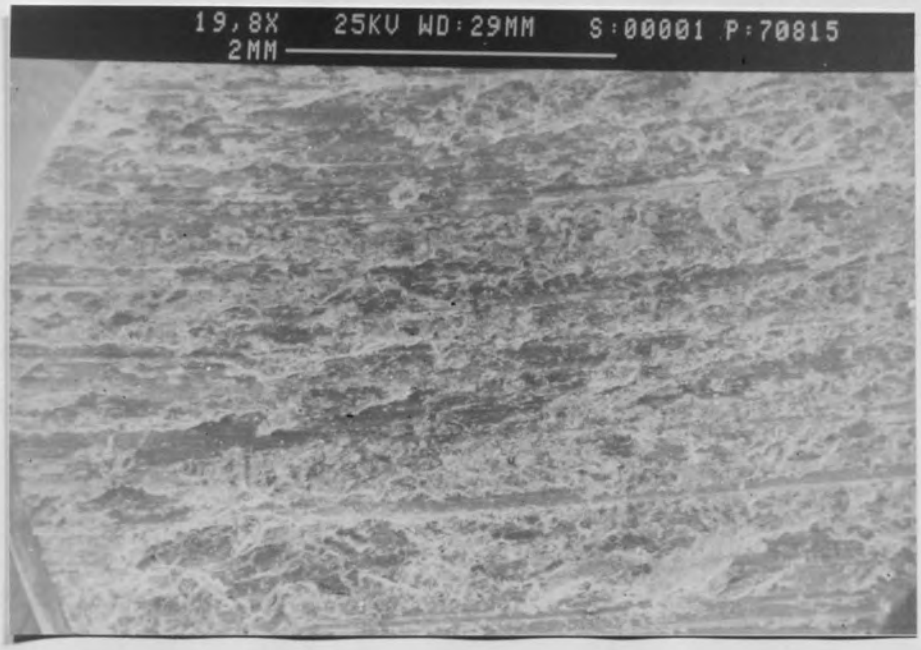

Figure 95. SEM micrograph of the worn surface of a ZA-27 pin after sliding at 1 m/s speed and 15 kgf load. Sliding direction left to right.

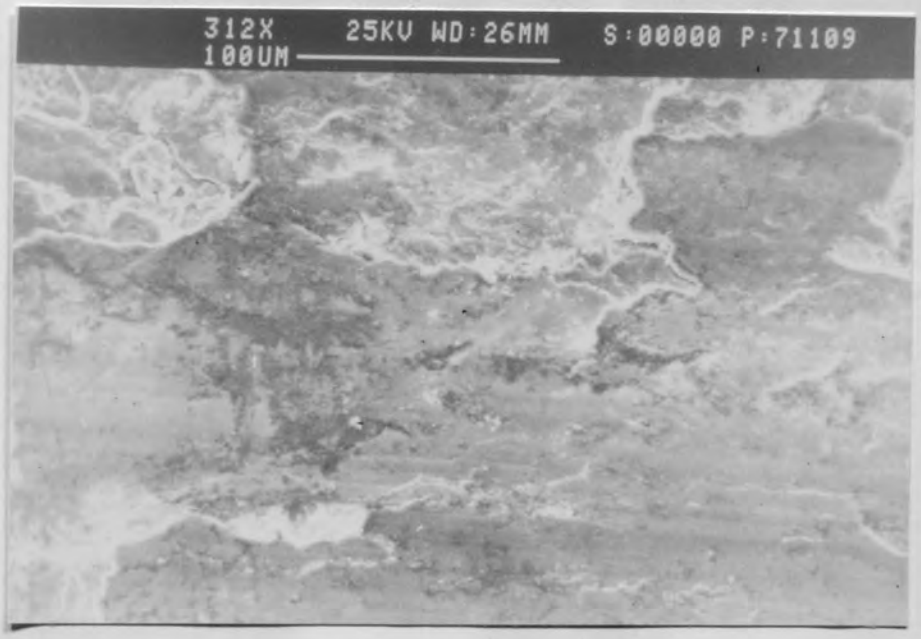

Figure 96. Increased magnification of Figure 95 showing patches of oxide debris adhered to the wearing surface.

Figure 97. Backscattered electron image of the transverse section of a ZA-27 pin worn at 1 m/s and 15 kgf load. Sliding direction right to left.

Figure 98. Backscattered electron image of the same sample of Figure 97 showing a section of a thick surface layer where steel fragments are embedded.

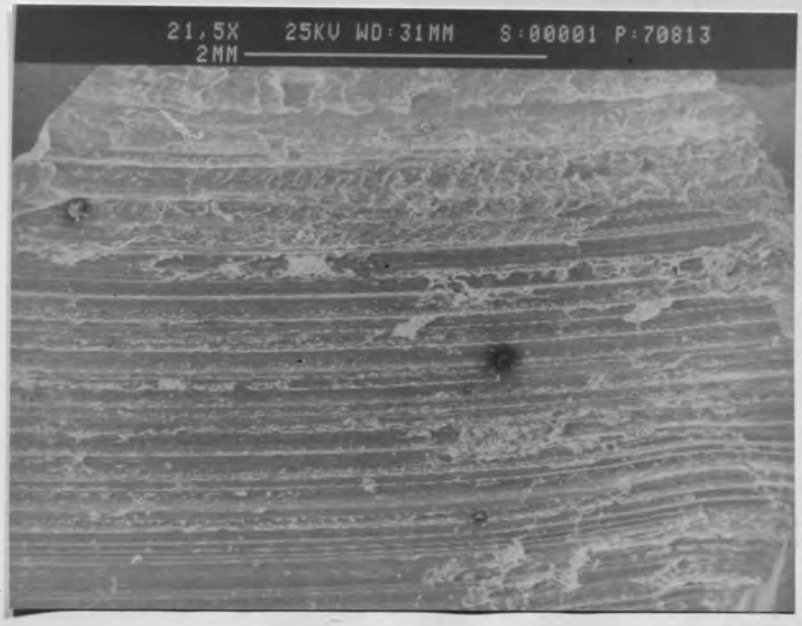

Figure 99. SEM micrograph of the worn surface of a ZA-27 pin after sliding at 2 m/s speed and 3 kgf. Sliding direction left to right.

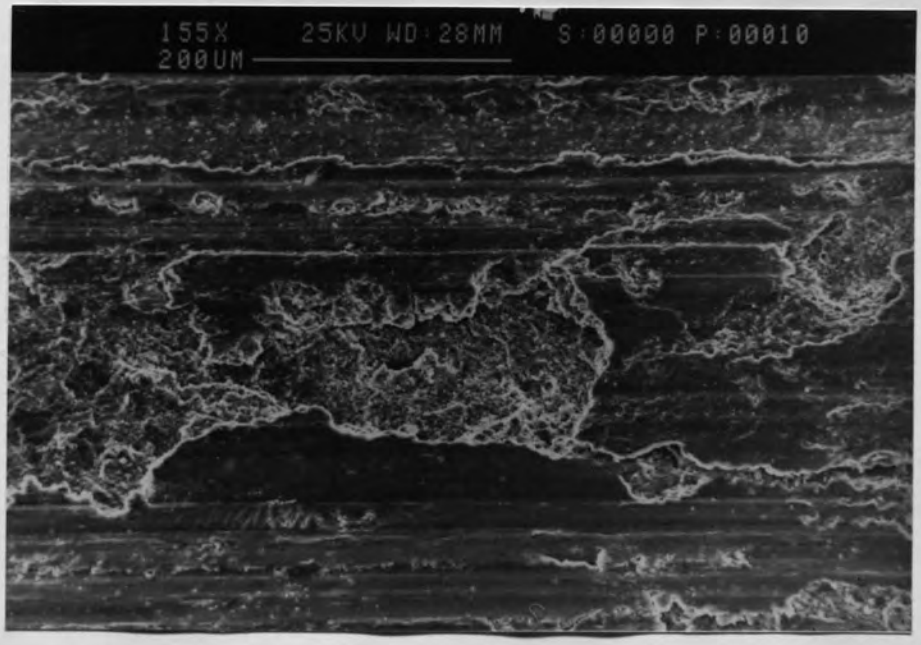

Figure 100. SEM micrograph of the worn surface of a Super Cosmal pin after sliding at 0.25 m/s and 10 kgf showing severe local spalling.

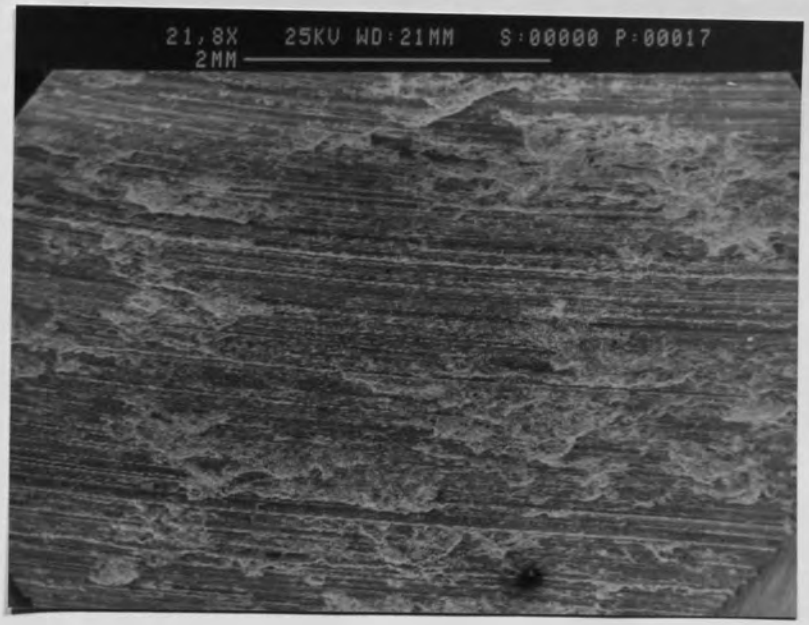

Figure 101. SEM micrograph of the worn surface of a Super Cosmal pin after sliding at 0.5 m/s and 15 kgf load. Sliding direction left to right.

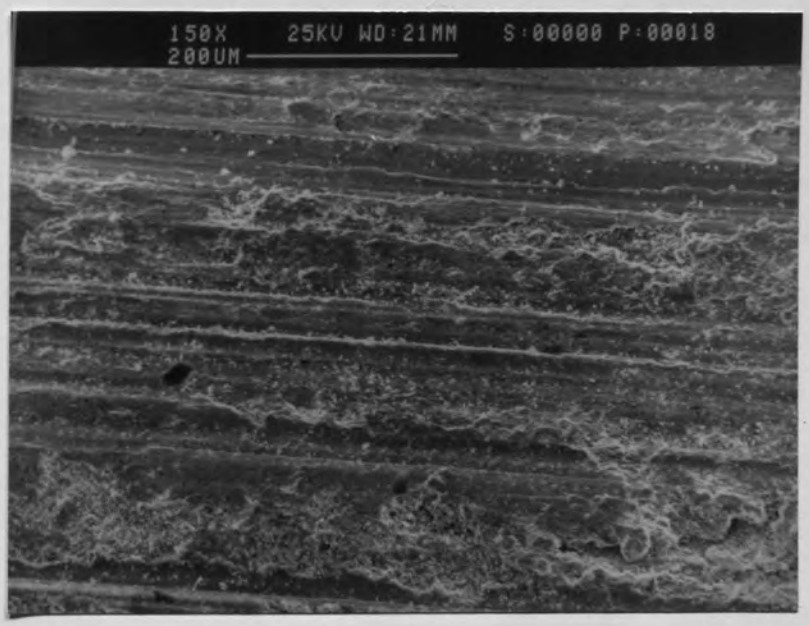

Figure 102. Increased magnification of Figure 101 showing shallow scars generally covered by a black layer of debris.

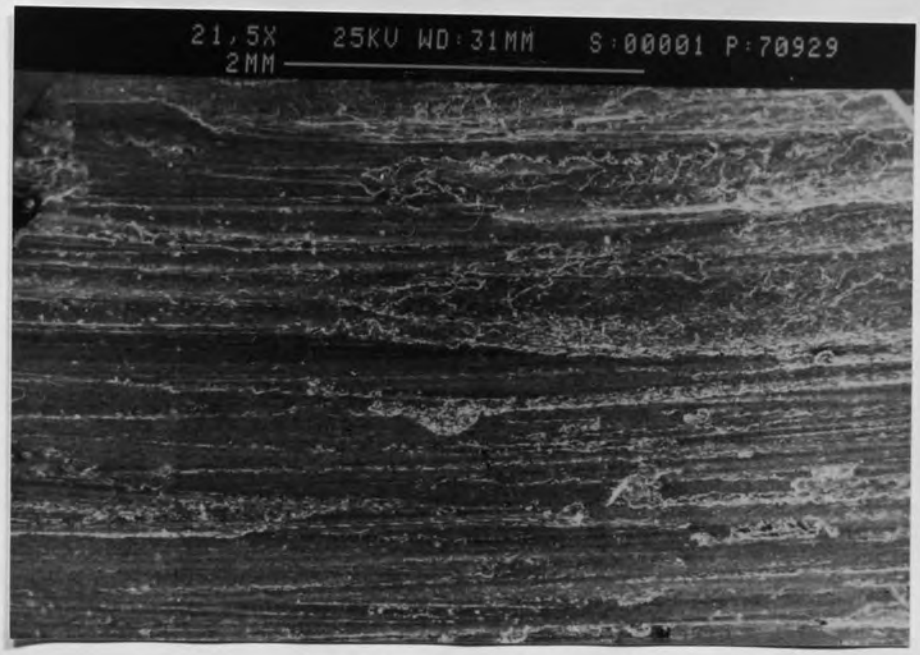

Figure 103. SEM micrograph of the worn face of a Super Cosmal pin after sliding at 1 m/s and 4 kgf. Sliding direction left to right.

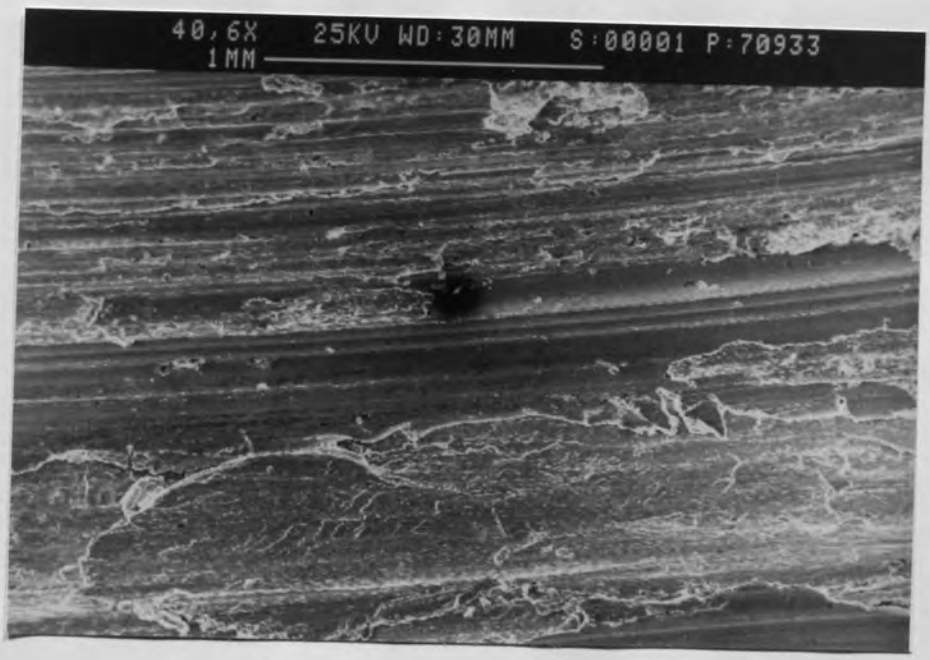

Figure 104. SEM micrograph of the worn surface of a Super Cosmal pin after sliding at 1 m/s speed and 8 kgf. Sliding direction from left to right.

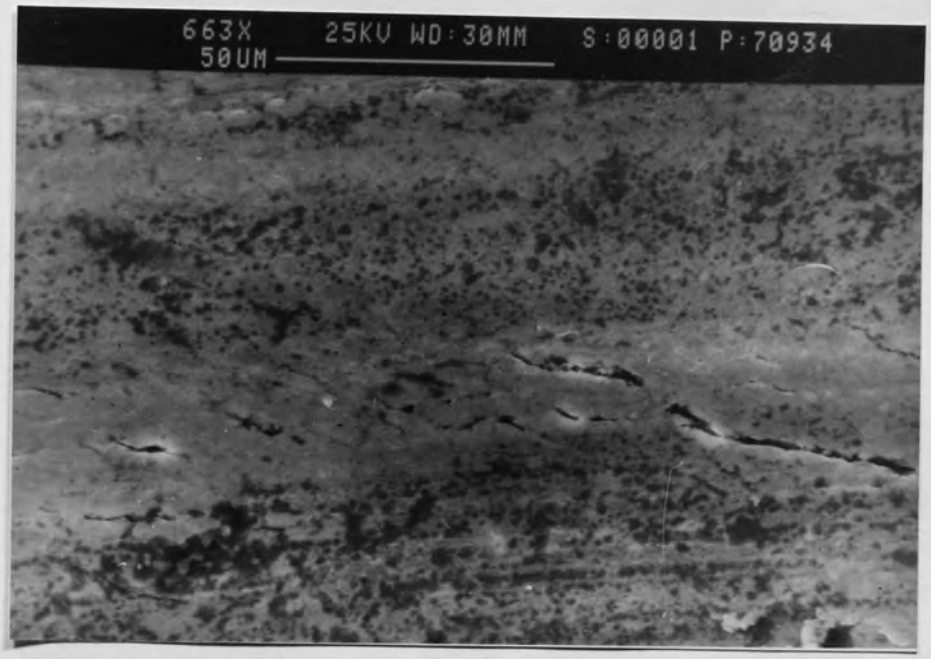

Figure 105. Increased magnification of Figure 104 showing cracks in the transverse direction of sliding.

Figure 106. Backscattered electron image of the transversal section of a Super Cosmal pin worn at 1 m/s and 4 kgf.

Figure 107. SEM micrograph of the worn face of a HAZCA pin after sliding at 0.5 m/s and 8 kgf load. Sliding direction left to right.

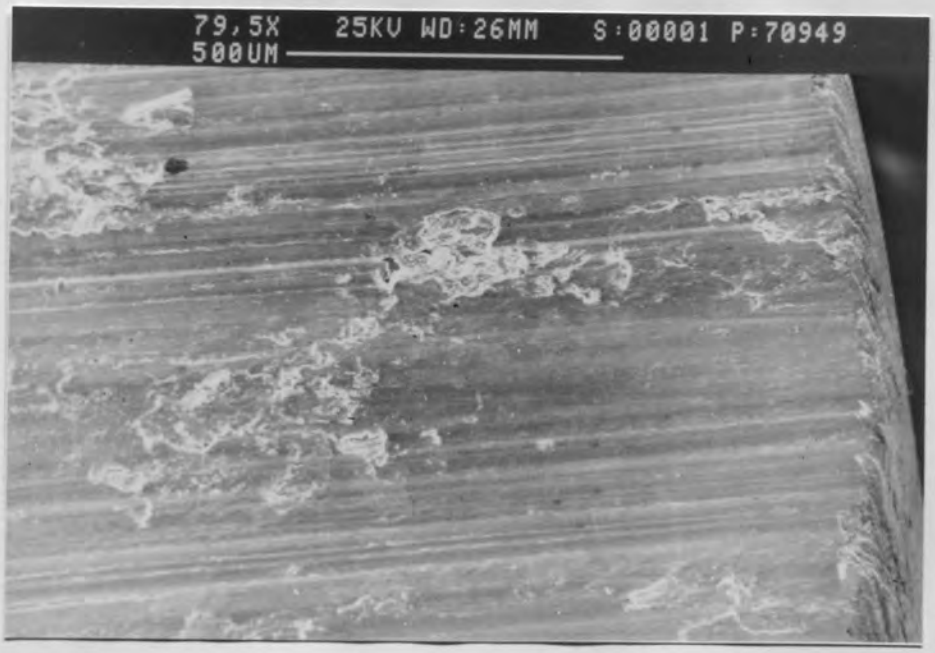

Figure 108. Increased magnification of Figure 107 at the trailing edge of the pin.

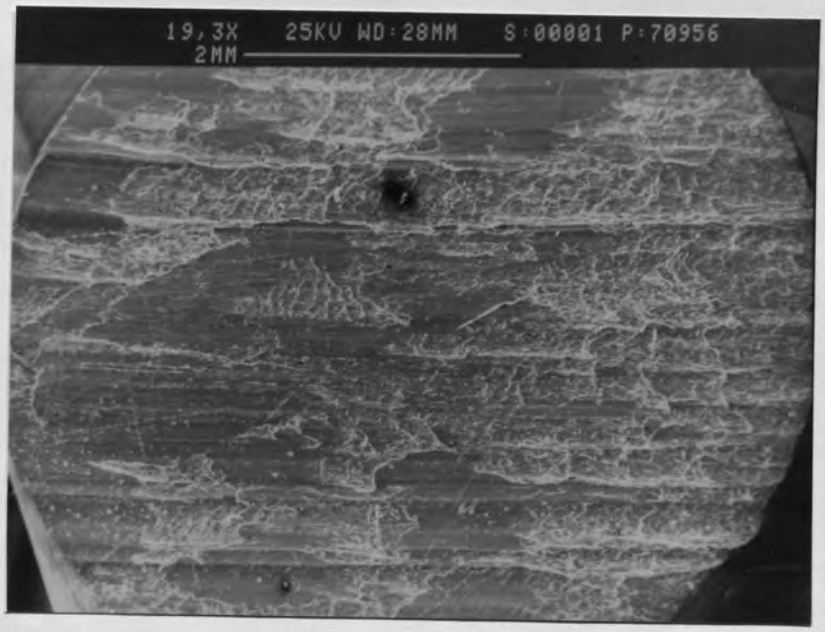

Figure 109. SEM micrograph of the worn surface of HAZCA pin after sliding at 1 m/s and 8 kgf. Direction of sliding left to right.

Figure 110. SEM Backscattered electron image of HAZCA pin worn at 1 m/s and 4 kgf load.

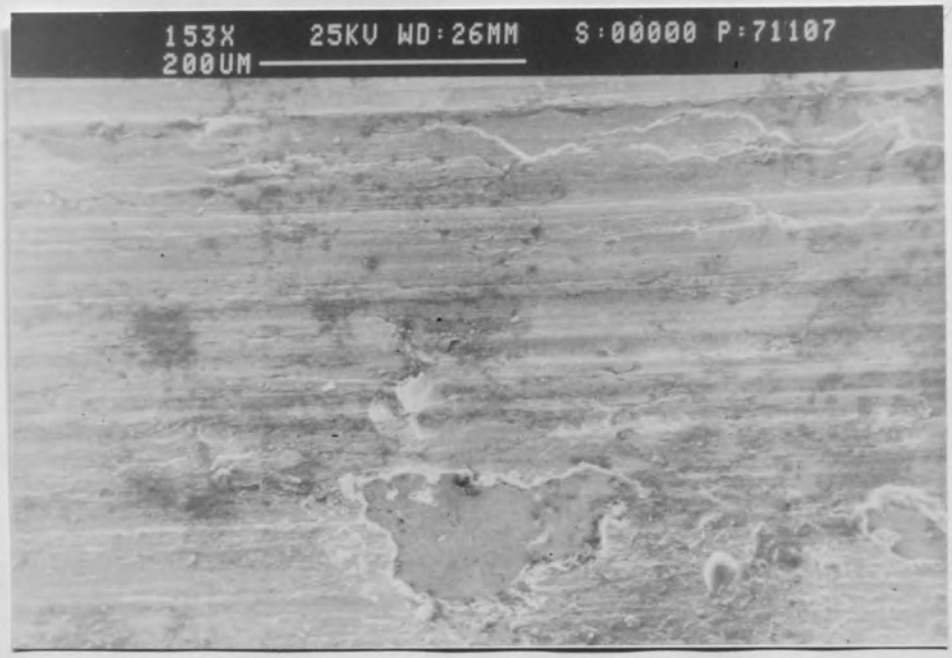

Figure 111. SEM micrograph of the worn surface of a bronze pin after sliding at 1 m/s and 4 kgf.

Figure 112. Optical micrograph of the transverse section of a bronze pin worn at 1 m/s and 4 kgf load.x200

4.4.4 Results of Auger Electron Spectroscopy on Worn Surfaces

Samples which showed low wear rates at high loads were selected for their worn surface to be analysed by Auger Electron Spectroscopy. With this method of surface analysis elements can be detected only at a depth of approximately 5-30Å. Table 7 present the elemental composition of the worn surfaces of ZA-27, Super Cosmal and HAZCA test pins.

Table 7. Elemental composition of worn surface pins

Element	ZA-27 At.(%)	Super Cosmal At.(%)	HAZCA At.(%)
C	24.7	37.9	19.8
Si	--	1.4	2.7
Al	20.6	26.0	33.7
Zn	7.5	1.0	2.2
Cu	0.5	0.14	0.3
Fe	8.3	3.2	4.0
O	38.4	30.6	37.7

The presence of carbon was due to unavoidable atmospheric contaminants and from solvents or residues of sample cleaning.

Aluminium was the predominant metallic element in all three alloys and its content increased as we move from ZA-27 to HAZCA alloy.

In the same instrument of analysis, X-ray Photoelectron Spectroscopy was used to determine the chemical nature of the surface atoms.

XPS spectra for aluminium corresponding to each of the three analysed surface layers showed the following distribution of chemical states:

Al in ZA-27 worn surface 8% metallic and 92% oxide
Al in Super Cosmal worn surface 11% metallic and 89% oxide
Al in HAZCA worn surface 19% metallic and 81% oxide.

An example of the spectra for aluminium is given in Figure 113.

A very diminished proportion of zinc was detected on worn surfaces relative to its proportion on the parent alloys. The chemical state of zinc was as follows:

Zn in ZA-27 worn surface 48% metallic and 52% oxide
Zn in Super Cosmal worn surface 38% metallic and 62% oxide
Zn in HAZCA worn surface 27% metallic and 73% oxide

The spectra of zinc in the ZA-27 worn surface is given in Figure 114.

Silicon was detected on the worn surfaces of the Super Cosmal and HAZCA alloy in two forms; as pure silicon the major proportion and as silicide the small proportion. A XPS spectrum for silicon on the worn surface of a HAZCA pin is shown in Figure 115.

The second highest atomic content on the sliding surfaces was that of iron apparently as a result of transference from the steel disc counterface. The ZA-27 alloy seem to be more prone to iron pick-up during sliding. Iron also was found to be present in metallic and oxide states:

Fe in ZA-27 worn surface 9% metallic and 91% oxide
Fe in Super Cosmal worn surface 34% metallic and 66% oxide
Fe in HAZCA worn surface 28% metallic and 72% oxide

Here it is important to note that the iron oxide identified in all cases was FeO whose formation takes place at temperatures as high as 800°C. A spectrum for iron on a Super Cosmal worn surface is shown in Figure 116.

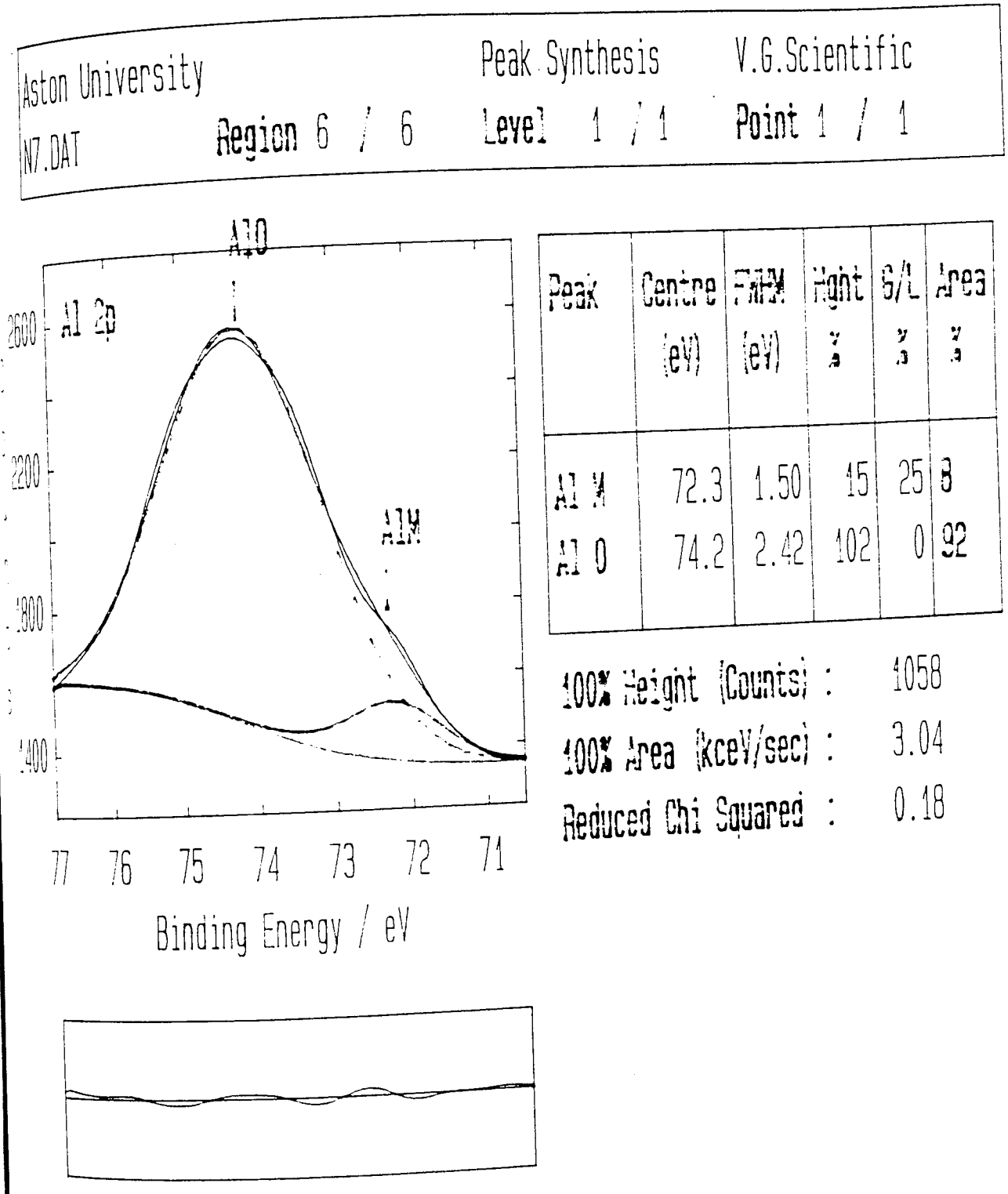

Figure 113. XPS spectra for aluminium on the worn surface of a ZA-27 pin tested at 1 m/s and 6 kgf load.

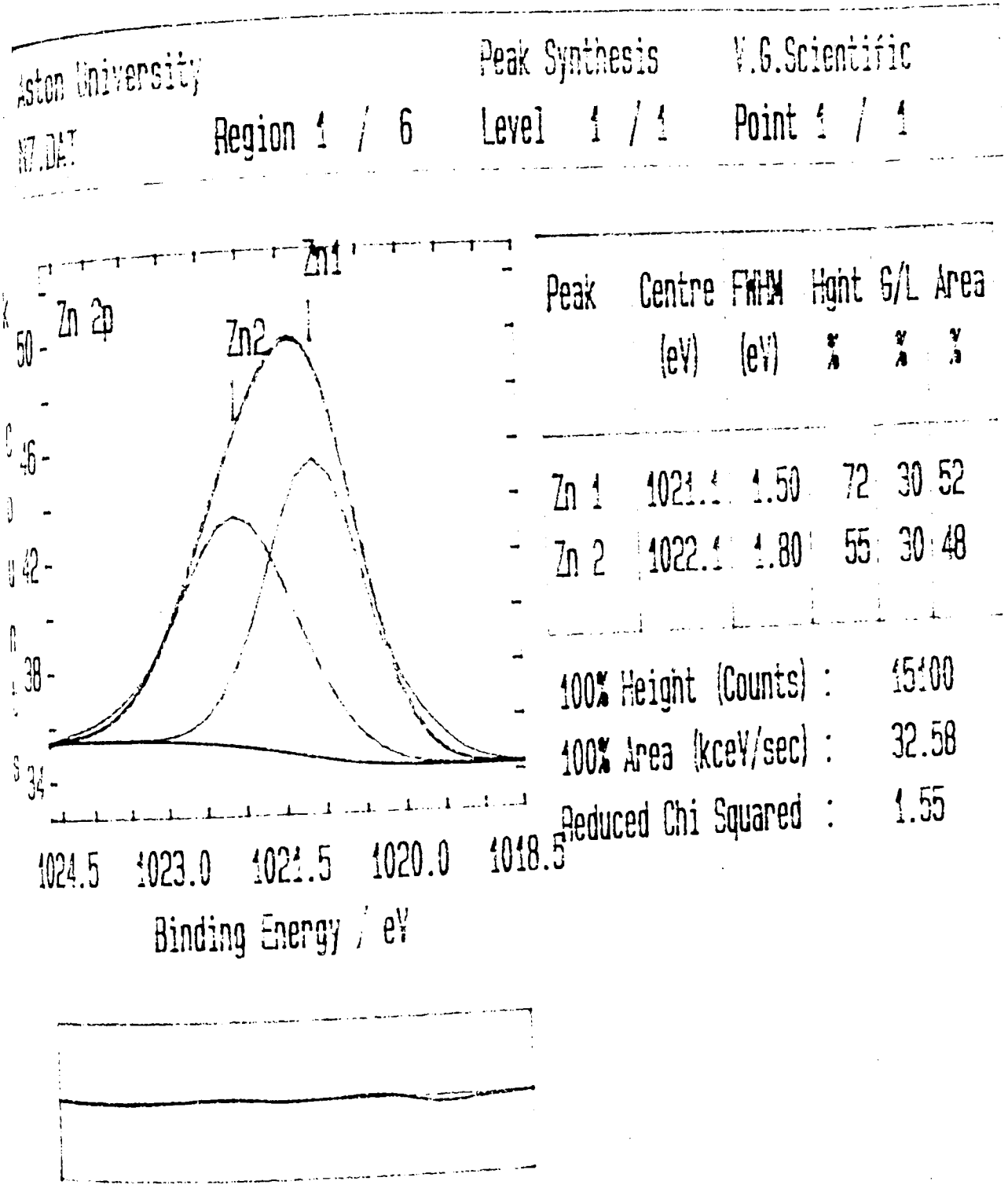

WORN SURFACE OF ZA-27 PIN (7)

Figure 114. XPS spectra for zinc on the worn surface of a ZA-27 pin tested at 1 m/s and 6 kgf load.

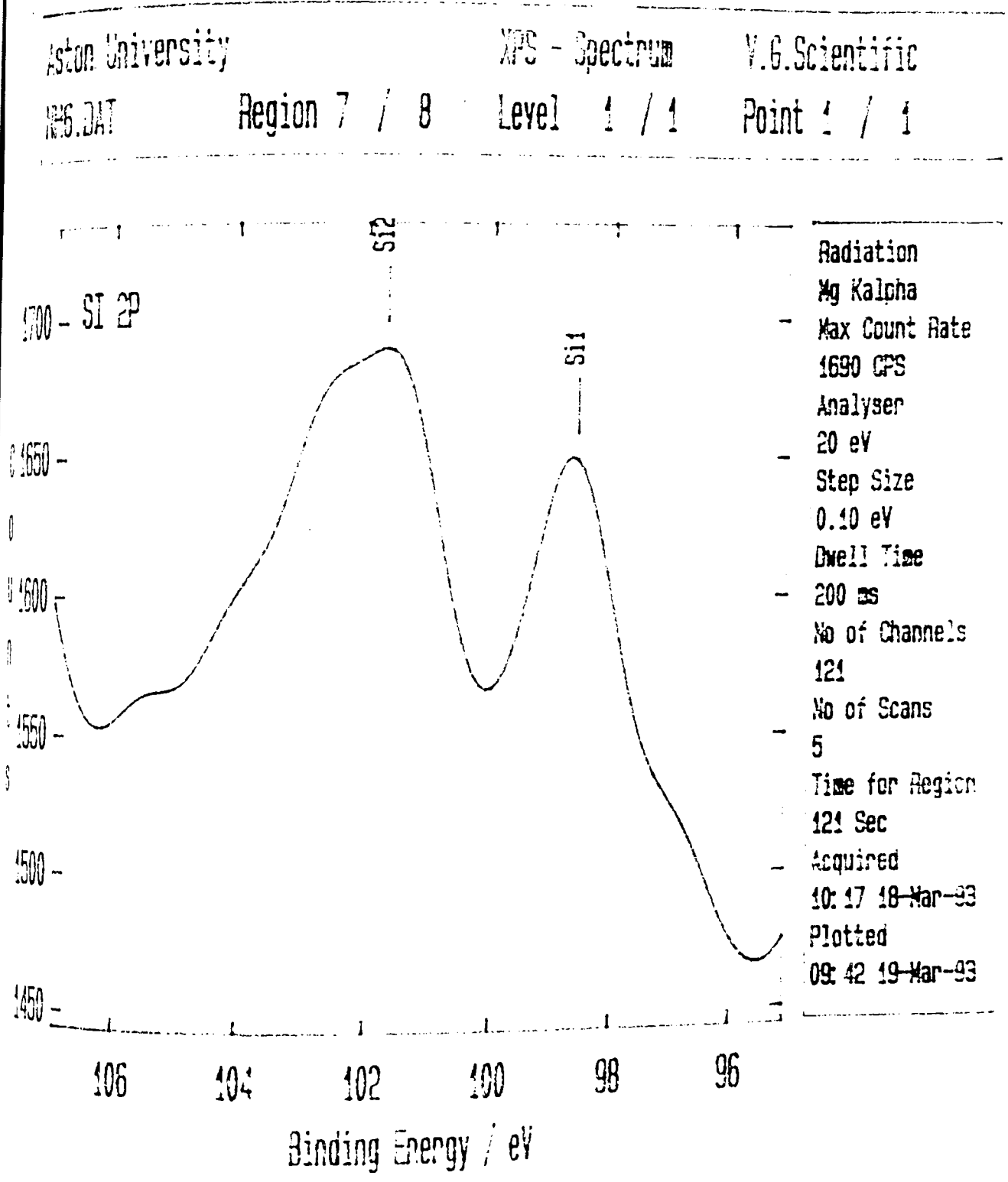

WORN SURFACE OF HAZCA PIN (H6)

Figure 115. XPS spectrum for silicon on the worn surface of a HAZCA pin tested at 0.5 /s of speed and 15 kgf load.

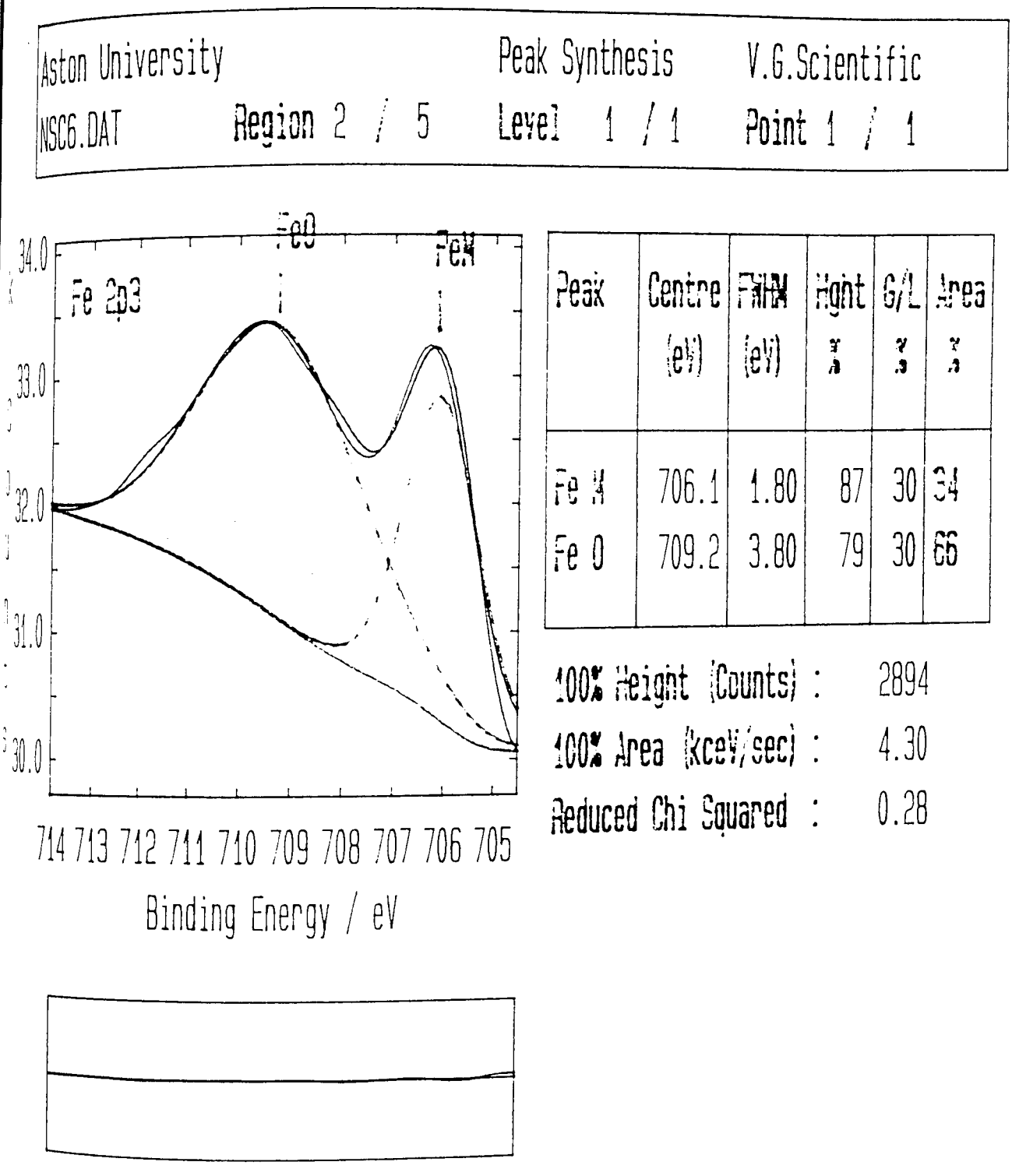

Figure 116. XPS spectra for iron on the worn surface of a Super Cosmal pin tested at 0.5 m/s speed and 15 kgf load.

4.5 DISCUSSION

It is very well known that wear is proportional to both the normal load and sliding distance. This linear relationship derives from surface topography due to the fact that the effect of an increase in load is to give a proportionate increase in the true contact area. Similarly, the effect of an increase in the slid distance is to give a proportionate increase in the number of wearing contacts. However, for purely elastic contact Archard [59] proposed the wear rate as proportional to $W^{0.6}$ where W is the applied load and recently Sarkar [55] found the wear rate of aluminium-silicon alloys as proportional to W^{α} where α had a value between 0.4 to 0.6. Therefore the first aspect to discuss is about the type of relationship between wear rate and load that was established by the alloys tested in this work.

Within the range of load applied, the wear rates of the ZA-27 alloy were demonstrated to obey a linear relationship with load at all imposed sliding speeds. In the case of the Super Cosmal and HAZCA alloys wear rates were proportional to load at 0.25, 0.50 and 2 m/s, but at 1 m/s of speed, being the relationship linear at low loads, there was a load value at which the curve deflected to a more accelerated rate. It is thought that this departure from linearity does not necessarily mean that the Wear Law is not applicable to this particular case, instead the sudden change in slope simply signifies that a change of dominant mechanism has occurred. Therefore a new constant of proportionality is established. In the literature, the load that marks the transition from low to high wear rate is called transition load.

From the Archard Wear Law, $Q = K\frac{LS}{H}$, a wear rate equation in terms of the real area of contact can be written as w=KA for most of individual wear mechanisms. It is clear that the knowledge of the factors influencing the wear coefficient K is important in elucidating the mechanisms of wear of a particular case. Two examples of proposed equations for K were given in the literature review of this Chapter.

Based on the wear rate curves obtained in this work, the wear behaviour of the alloys is compared to each other by comparing the coefficient of wear (K) calculated by multiplying the slope of each curve in $mm^3/mm.kgf$ by the hardness of the bulk material in kgf/mm^2. Table 7 show the results of this exercise.

Table 8. Experimental wear coefficients

Sliding Speed (m/s)	Wear Coefficient K x 10^{-5}			
	ZA-27	Super Cosmal	HAZCA	Bronze
2	8.0	10.0	13.5	-
1	0.8	11.2 (a)	22.5 (b)	48
		1.7	1.1	48
0.5	1.1	1.0	0.9	50
0.25	1.7	2.8	2.9	75 (c)
				2.2

(a) From 7 to 15 kgf load

(b) From 5 to 15 kgf load

(c) From 2 to 4 kgf load.

Low coefficients of wear enclosed in thick lines appear to correspond to one type of wear while coefficients of wear ten or more times higher than the first ones to another type of wear.

The fact that low coefficients of wear increase with decreasing speed was found by Quinn [48] in his equation for oxidational mild wear but this of course, is not a sufficient reason to attribute wear of ZA-27, Super Cosmal and HAZCA at low speeds to oxidative mild wear.

However, the worn surface appearance of low wear rate pins revealing the existance of a dark, smooth and apparently hard surface layer together with shallow surface spalling and few grooving marks along the sliding direction, seem to be typical features of the oxidate type of wear mechanism. This mechanism is well explained by Quinn [48] as a sequence of changes during sliding that starts with a short period of initial severe wear to achieve conformity and create large areas of contact after which, due to a sufficient amount of frictional heating oxidation of the particular plateaux in contact occurs. Then the film of oxide builds up until it reaches a critical thickness and becomes unstable and is removed. The plateaux where oxidation occurs appears smooth and present surface cracks perpendicular to the direction of sliding and also marks of flake removal leaving virgin surface beneath. These features can be clearly seen in Figures 95, 96, 111 and 102.

Surface layers were demonstrated to be a complex mixture of oxides and elements of the mating surface that acted as a protection against metal to metal contact between asperities of both sliding elements.

The constitution and properties of this protective surface layer seem to be of prime importance with regard to the resistance to sliding wear of the ZA-27, Super Cosmal and HAZCA alloys.

According to the surface analysis of worn pins, the predominant oxides on all worn surfaces were aluminium and iron oxides. On ZA-27 pins however, the content of zinc oxide was more significant. For reasons not studied in this work, the surface film on ZA-27 pins seemed to be thicker and more stable than that on the other two alloys.

It seems that the oxidational theory explains well the occurrence of mild wear in the three Zn-Al based alloys but also there are evidences of transference of material between the rubbing surfaces giving rise to a complex structure of the surface layer on the wearing pin. Iron was transferred from the disc counterface in relatively large quantities (more in ZA-27 than in Super Cosmal and HAZCA) mostly in the oxide state. The oxide state of iron as detected by AES analysis was FeO which means that local temperatures during rubbing were higher than 800°C. Another interesting feature of the surface layer in silicon-containing alloys was the occurrence of a certain amount of it as silicides. The formation of this and maybe other compounds was due to a kind of mechanical alloying during prolonged sliding.

Even though wear of the zinc-aluminium pins was not of the severe type at 0.25 m/s of sliding speed, it was higher than that of 0.5 and 1 m/s. This can be explained as due to insufficient interfacial temperature for the formation of sufficient quantity of surface film to dominate the area of contact.

For the oxidative type of wear to occur, it needs adequate conformity between sliding faces so that large areas could come into contact. This must not have occurred in our system at a sliding speed of 2 m/s when no conformity could be achieved due to the severity of other surface interactions like ploughing, abrasion and maybe adhesion which became dominant over any oxidational process so that wear progressed by mechanical mechanisms. As an example of this, Figures 99, 104 and 109 show clear signs of gross plastic flow of material which eventually produced loose metallic flakes and adhered flakes to the counterface.

Regarding the variation of coefficients of friction with changes in the sliding conditions, relatively high coefficients of friction were associated with low wear rates. As low wear rates were associated with the build-up of a surface layer of oxides, possibly the mechanism of

fracture of such films was responsible for that increase in friction force. This in a way agrees with Bowden and Tabor [60] theory of friction where the coefficient of friction was said to be the ratio of the critical shear stress at the interface and the plastic yield pressure of the underlying metal.

On the other hand in situations of more severe wear, coefficients of friction decreased due to partial or total absence of protective film which led the asperity interaction to be related to deformation and flow of thermally softened base material.

Regarding the influence of microstructure and mechanical properties of ZA-27, Super Cosmal and HAZCA alloys upon their wear characteristic an approximate analysis can be divided into two points:

1. Oxidative mild wear. Mild wear appears to be dependent on the thickness, composition and stability of the protective surface film rather than on the mechanical properties of the substrate. However the ability of the alloy to achieve and maintain conformability with the counterface during sliding seemed to depend on the mechanical properties of the alloy. ZA-27 being more ductile and stronger than Super Cosmal and HAZCA, was demonstrated to have a thicker and more stable surface layer. It was possible to observe this characteristic, comparing the behaviour of the three alloys at a sliding speed of 1 m/s. ZA-27 presented a mild regime within the whole range of loads tested while Super Cosmal and HAZCA only maintained this regime up to a transition load when the oxide film was no longer the predominant contact.surface.

   The wear behaviours of Super Cosmal and HAZCA alloys during dry sliding were practically similar at speeds of 0.5 and 0.25 m/s, but at 1 m/s a higher content of silicon in the HAZCA alloy had a negative influence on the surface and sub-surface properties so that the transition load was reduced.

2. Severe wear. Wear rate curves showed that wear at 2 m/s of sliding speed was of the severe type where plastic flow, metallic transfer and abrasion were the prime topographic features in all alloys. In this situation ZA-27 alloy showed a slightly better performance despite the higher hardnesses of the silicon containing alloys. This reflected the difficulty of looking for a correlation of wear with mechanical properties when both situations are sensitive to different states of stress.

The virtue of the presence of hard particles uniformly distributed on the structure, ε-phase particles in ZA-27 alloy, and ε, T' and primary silicon particles in Super Cosmal and HAZCA was to impart anti-scuffing resistance when they rubbed against steel.

4.6 CONCLUSIONS

1. At sliding speeds of 0.5 m/s and 0.25 m/s, Super Cosmal and HAZCA alloys showed a mild type of wear within a range of loads up to 15 kgf. This behaviour was similar to that shown by the ZA-27 alloy under the same testing conditions. The bronze material, on the other hand, suffered very severe wear under the experimental conditions applied to all materials.

2. At a sliding speed of 1 m/s, the ZA-27 alloy still showed mild wear behaviour in the complete loading range (0-15 kgf), while the Super Cosmal and HAZCA alloys experienced a transition from mild to severe wear when loads larger than 7 kgf and 5 kgf respectively were applied.

3. The low wear rates of all zinc-aluminium-based alloys tested in the present work, were identified as of the oxidative type due to the occurrence of a protective surface film as a dominant area of contact and from which wear debris was produced.

4. The protective surface film was found to be a complex mixture of aluminium, zinc and iron oxides and metallic elements derived from both sliding materials.

5. The thickness and stability of the protective surface layer was thought to be dependent on the mechanical properties of the alloy. ZA-27 being stronger and more ductile than Super Cosmal and HAZCA presented a more stable surface layer.

6. A sliding speed of 2 m/s produced a severe type of wear in all alloys. Plastic flow, abrasion and adhesion became dominant over the oxidational process.

CHAPTER 5

BEARING CHARACTERISTICS OF HIGH ALUMINIUM ZINC-BASED ALLOYS UNDER BOUNDARY CONDITIONS OF LUBRICATION

5.1 LITERATURE REVIEW

5.1.1 Introduction

A plain journal bearing is a tribological system that consists basically of a sleeve of bearing material wrapped around a rotating shaft and designed to support a radial load in the presence of a lubricant [61]. Figure 117 shows the essential features of the system.

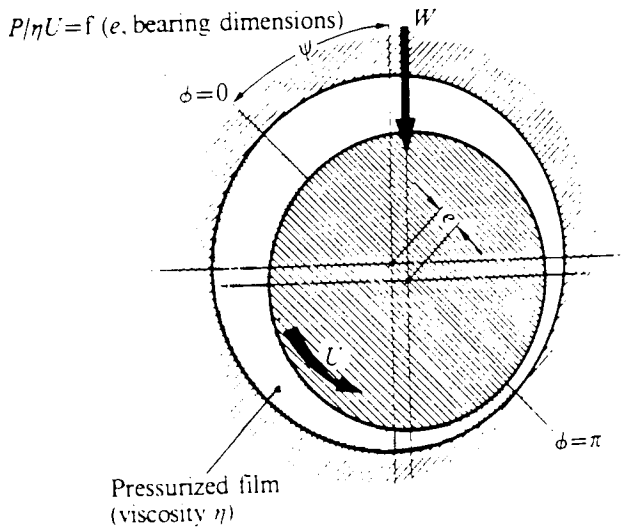

Figure 117. Journal bearing system.

Where:

ψ	=	Attitude angle
c	=	Radial clearance
e	=	Eccentricity
U	=	Journal linear velocity
W	=	Load
r	=	Radius of journal
ϕ	=	Angular position of a point in the lubricant wedge
η	=	Viscosity of the lubricant.

In normal operation, a converging wedge of lubricant generates sufficient pressure to support the load hydrodynamically.

Sommerfeld developed a journal-bearing mathematical analysis based on the Reynolds' equation for lubrication, and formulated fundamental concepts that form the basis for any design procedure for hydrodynamic behaviour.

The general equation:

$$\frac{P}{\eta U}\left(\frac{c}{r}\right)^2 = -\frac{6}{\cos\psi}\int f(\varepsilon,\phi)\cos\phi d\phi$$

shows the existence of a relationship between the parameters of the bearing (load, speed, viscosity) and the eccentricity, the attitude angle and the extent of the film.

The term $\frac{P}{\eta U}\left(\frac{c}{r}\right)^2$ is known as Sommerfeld Number. The form $\frac{\eta N}{P}\left(\frac{r}{c}\right)^2$, is also used as Sommerfeld Number, specially in the U.S.A. Other authors call the expression the Bearing Parameters.

Due to the difficulty of solving the Reynolds' equation in two dimensions, Sommerfeld assumed that the bearings were infinitely wide, but Ocvirk introduced another approach for narrow bearings, arriving at the following general equation:

$$\frac{P}{\eta U}\left(\frac{c}{r}\right)^2\left(\frac{d}{b}\right) = \frac{\varepsilon\pi}{\left(1+\varepsilon^2\right)^2}\sqrt{1+0.62\varepsilon^2}$$

where: $\frac{c}{r}$ = clearance ratio

$\frac{d}{b}$ = breadth ratio

Consequent analysis established the coefficient of friction as a function of the eccentricity:

$$\mu = 2\left(\frac{d}{b}\right)^2\left(\frac{c}{r}\right)\frac{1}{\varepsilon}\frac{\left(1+\varepsilon^2\right)^{3/2}}{\sqrt{1+0.62\varepsilon^2}}$$

which expression was found to be tolerably accurate for most practical values of $\frac{P}{\eta U}$ (60).

If the load is raised or the speed reduced, the eccentricity increases, the attitude angle decreases and the coefficient of friction increases. This reduces the minimum film thickness so that with further increasing of load or decreasing of rotational speed, complete or partial breakdown of hydrodynamic conditions occurs. On the other hand at very light loads and high rotational speeds, the journal will rotate almost concentrically within the bearing.

5.1.2 Lubrication Regimes

Figure 118 illustrates how the state of lubrication and frictional resistance in a journal bearing are influenced by changes in the three main parameters that govern its performance. This curve is best known as Stribeck Curve. In its abscissa η is the viscosity of the lubricant at the operating temperature of the bearing in Pa.s x 10^{-3}, N is the number of continuous revolutions/second (or m/s) and P is the bearing stress (load) given in MPa (62,52).

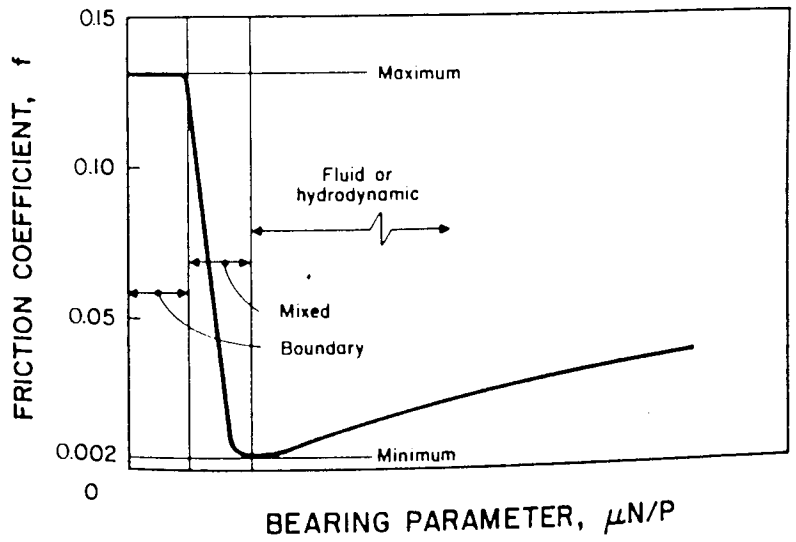

Figure 118. Idealised Stribeck Curve for journal bearings (51).

The Stribeck Curve consists of three lubrication regimes:

a) Hydrodynamic or fluid lubrication, where a complete thick film of lubricant separates journal and bearing. Here the friction is dependent only on the shear properties of the lubricant.

b) Boundary lubrication, where some metal to metal contact occurs only separated by a thin film of lubricant and characterised by high friction almost uninfluenced by changes in speed, load or viscosity.

c) Mixed lubrication, characterised by a rapid fall in friction as the bearing parameter is increased. This regime is a mixture of hydrodynamic and boundary conditions.

5.1.3 Boundary Lubrication

Boundary lubrication according to a definition given by Campbell [62] is lubrication by a liquid under conditions where the solid surfaces are so close together that appreciable contact between opposing asperities is possible. The friction and wear in boundary lubrication are determined predominantly by interaction between the solids and the liquid. The bulk flow properties of the liquid play little or no part in the friction and wear behaviour.

This severe lubrication regime is generally maintained by the use of special surface films which interpose themselves between the sliding junction to prevent severe wear and adhesion. Rabinowicz [63] proposed that in boundary conditions load is supported by a combination of lubricant film and by asperities which manage to penetrate this film, where the frictional force is a combination of shear in the adhesive metal junctions and shear between lubricant films, i.e.

$$F = \alpha A_r S_m + (1-\alpha) A_r S_l$$

where F is the frictional force, α is the fraction of real area of contact (A_r) which is penetrated, S_m is the metal shear strength and S_l is the lubricant shear strength.

Surfactant additives are normally used in boundary lubricants to prevent adhesion by interposing a stable low shear film between the load bearing surfaces. The action of these additives takes place through complicated physico-chemical features like physisorption, chemisorption and polymerisation. The optimum molecular structure for a boundary lubricant consist of a long straight hydrocarbon chain with an active radical at one end. Compounds having such structure occur naturally in animal and vegetable oils, but they are noticeably absent in mineral oils. This situation is normally remedied in the case of mineral oils, by

adding a small percentage of an active polar compound such as oleic acid, stearic acid and others [64].

5.1.4 Plain Bearing Materials

Plain bearings constitute a very delicate part of numerous machinery and engines. Most commercial industrial bearings operate in the boundary or mixed regimes at some points during their operating life. Therefore the virtues of a material forming the bearing surface become important.

Plain bearing materials have to satisfy a number of material properties and tribological conditions depending on their application; the following are the most important [65]:

1. High strength to resist deformation by steady and fluctuating loads.
2. Low friction and low wear rate to minimise frictional heating, seizure and damage of the shaft.
3. Conformability to compensate for imperfection in shaft geometry.
4. Embeddability to absorb dirt and debris carried by the lubricant.
5. Wettability to hold an oil lubricant film with tenacity.
6. Good thermal conductivity to dissipate frictional heat.
7. Good corrosion resistance against acid products of oil decomposition.
8. Low cost and availability.

Lubricated journal bearings, which during their life span have to support more or less extended periods of solid to solid contact, function adequately largely by virtue of their tribological properties such as resistance against microwelding and wear rate [66].

Conventional materials currently used for high duty plain bearings are copper-lead alloys and leaded bronzes. Relatively new bearing materials for severe conditions are the three main aluminium-based alloys; namely, Aluminium-Tin, Aluminium-Lead and Aluminium-Silicon alloys and two mainly zinc-based alloys, the ZA-12 and the ZA-27 alloys.

5.1.5 Zinc-based Alloys as Plain Bearing Materials

Marczak and Ciach [54] reported that a zinc-based alloy containing approximately 40% Al and 2% Cu exhibited better properties than CuPb30 and CuSn10 alloys when tested as sleeve bearings on a model equipment.

A family of zinc-based alloys containing 27 to 70% Al, 0 to 5% Cu and 0 to 5% Si known as the Alzen alloys are claimed to compare well with tin bronzes. Of this range of alloys, that with 30% Al and 5% Cu, Alzen 305 has been manufactured in the U.K. in a wide range of applications [21].

Savaskan and Murphy [67] reported the lubricated wear behaviour of a number of alloys based on Zn-25% Al with silicon or copper ternary additions using a special pin-on-ring method and compared with that of SAE 660 bronze and SAE 73 brass. It was concluded that Zn-Al-Si alloys had the best wear behaviour. The wear resistance increased with the amount of silicon.

Monotectoid Zn-Al based ternary alloys were also studied by Murphy and Savaskan [21] as wear resistant bearing materials in an automobile engine application. Bushes made of alloys containing 38% Al and 1.9% Cu and 35.6% Al and 8.4% Si were tested in as-cast and heat treated conditions together with a phosphor bronze bush and an unbushed cast iron valve rocker. The monotectoid Zn-Al alloy containing silicon was found to be comparable with or superior to that of cast iron and bronze in this application. This was attributed to the presence of discrete silicon particles in the Zn-Al matrix.

Finally it is worth mentioning an evaluation of the ZA alloys for bearing applications carried out by Barnhurst and Farge [52] under an extensive research programme sponsored by the Noranda Research Centre, Canada. Full bearing tests were conducted on a specially constructed test rig where continuously cast and sand cast ZA-12 and ZA-27 alloys and lead-tin bronze were examined. The bearing performance of the alloys was evaluated as a function of the casting technique and the conditions of the journal. Loads as high as 7-14 MPa and speeds as low as 0.3 m/s were used in the presence of a grease lubricant supplied on a semi-continuous basis. The best performance was shown by the sand cast ZA-27 alloy combined with a journal of hardness 40-45 Rc and surface roughness of 0.4 - 0.6 μm c.l.a. The resistance to wear was found to be related directly with the general hardness of the material and the amount of copper rich ε phase present in the microstructure. An example of the type of Stribeck Curves obtained in this work is given in Figure 119.

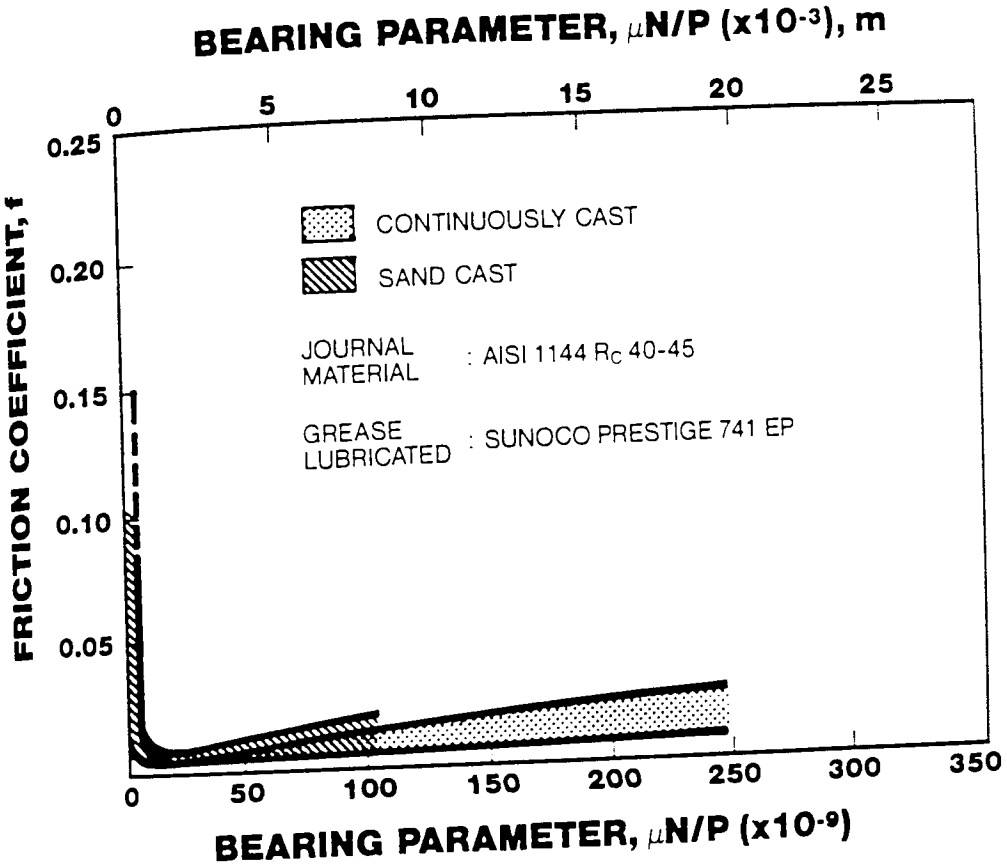

Figure 119. Stribeck Curves for continuously cast and sand cast ZA-27 alloy [52].

Other comparative tribological studies [68,53] on ZA-27 and bronze sleeve bearings also reported favourable results for the zinc-based alloy.

5.2 AIM OF THE LUBRICATED WEAR-TESTING WORK

Apart from other favourable properties and characteristics, the good wear resistance under severe dry sliding conditions shown by the Super Cosmal and HAZCA alloys, make these alloys seem favorable alternative bearing materials, particularly in those situations where the journal-bearing system works on prolonged periods of metal to metal contact.

The objective of this part of the work was to study the behaviour of the Super Cosmal and HAZCA alloys in a sleeve bearing simulation test with boundary lubrication. The alloys were to be compared with standard ZA-27 and bronze SAE 660.

The aims of the present study were thus:

1. To generate Stribeck curves to establish the conditions of load, journal speed, and lubrication at which the system worked on a regime of boundary lubrication.

2. To run the tests for a sufficient duration at conditions of relatively high friction (boundary lubrication) in order to evaluate wear by mass losses.

5.3 EXPERIMENTAL PROCEDURE

5.3.1 Full Plain Bearing Test Rig

In order to study the performance of the Super Cosmal, HAZCA, ZA-27 and bronze as full plain bearings under high load and low speed conditions, a test rig was designed and built by the author. The test rig was modelled on an old system of pulleys and belt quoted by Davis and Krok [69] in a pioneer work on sleeve bearing testing machines.

The parts and functions of the testing rig illustrated in Figure 120 are described as follows: The test bearing was clamped in a concentric floating housing, and loaded against the shaft under a radial vertical loading system . When the shaft rotated it exerted a force to overcome the friction resistance at the bearing-shaft interface. This force produced a moment which tended to tilt the floating housing about the shaft axis in the direction of rotation. This friction torque was amplified by an arm mounted on the housing itself and measured by a cantilever load cell. Load was applied to the loop via a frictionless second pulley, so that additional resistance for the housing to tilt was minimised and the loading line of action maintained vertical. This arrangement is more clearly shown in Figure 121. Four active strain gauges were placed on the cantilever and connected into a Wheatstone Bridge-amplifier circuit, the output of which was recorded by a potentiometric chart recorder. Oil for lubrication was gravity fed from an overhead container to the bearing-shaft interface through a radial hole in the bearing. The shaft was driven by a drive unit of continuous speed variation. Rotational speeds on the 25.4 mm diameter shaft ranged from 120 to 840 rpm.

Frictional forces were calibrated on the chart recorder by applying static loads on the cantilever load cell. For a gain of 20 in the Bridge amplifier and at 200 mV of full scale on the chart recorder, the relationship calculated from a linear calibration curve was:

1.27 mm movement on the chart = 1N force on cantilever

Applying a balance of moments about the shaft axis, the frictional force in the bearing-shaft interface could be calculated with the following expression:

$$F_r = \frac{547}{127} \cdot \frac{\Delta x}{1.27} \quad (N)$$

where Δx was the mean displacement value of the fluctuating friction track.

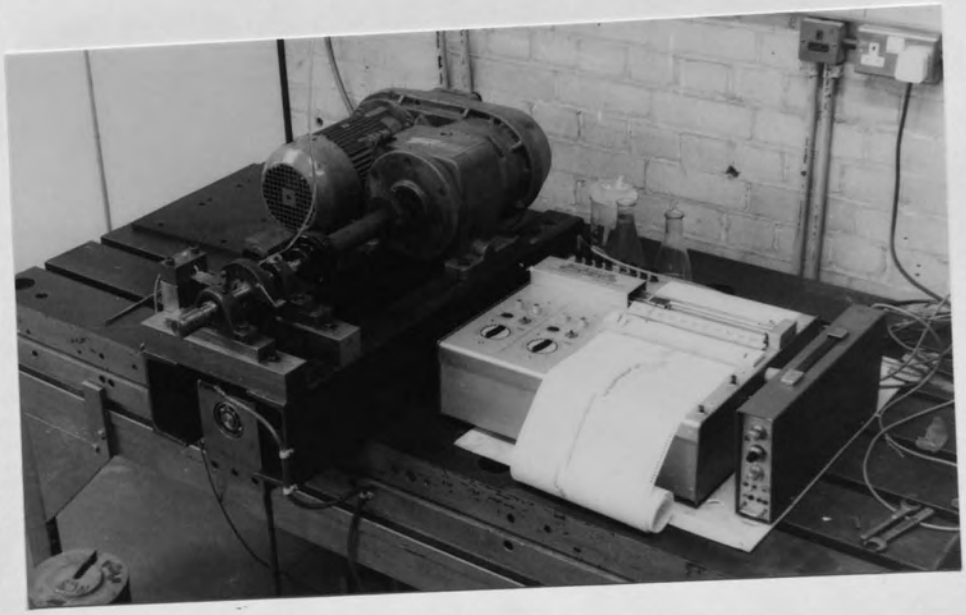

Figure 120. Plain bearing testing rig.

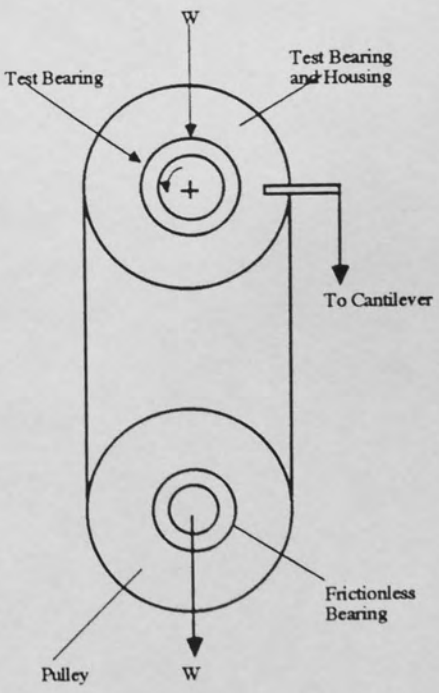

Figure 121. Loading system of the bearing testing machine.

5.3.2 Tribological Elements

Sleeve Bearings

Test Super Cosmal, HAZCA and ZA-27 sleeve bearings were machined to dimensions from sand cast bars produced according to casting methods discussed in Chapter 2. A continuously cast bar was used to produce the bronze test bearings.

Final dimensions for all bearings were the following:

Outer diameter	38.1 mm
Internal diameter	25.4 mm
Width	12.7 mm
Diametral clearance	0.04 - 0.06 mm
Surface finish	1.3 - 1.5 μm c.l.a.

Shaft

Shafts were machined from EN24 steel bars and then hardened to 57-58 Rc. The final diameter of 25.4 mm and surface finish of 0.3 - 0.4 μm c.l.a were obtained by grinding.

Lubricant

In order to run the journal bearing system at insufficient conditions of lubrication forcing the transmission of load via partial solid-to-solid contact, a light spindle oil was used as lubricant. Some of the physical characteristics are the following:

Shell Tellus oil R10

Viscosity grade, ISO 3448		10
Kinematic viscosity, cst,	at 20°C	21
	at 40°C	10
	at 100°C	2.5
Density at 15°C, kg/l		0.87
Flash point, °C		153

5.3.3 Test Procedure

Composition of Stribeck Curves

Bearing Parameters (Sommerfeld Numbers) to be used in the test calculated for combinations of three levels of load and six levels of shaft linear speed are tabulated in Table 9. The absolute viscosity of the lubricant taken into account was that at 40°C, i.e. $\eta = 0.0087$ Pa.s.

Table 9. Bearing Parameters

Shaft Speed m/s	**Bearing Parameter x (10^{-3}) m**		
	1.68 MPa	**2.88 MPa**	**4.00 MPa**
0.15	0.80	0.50	0.36
0.25	1.35	0.80	0.56
0.38	2.00	1.20	0.86
0.51	2.70	1.60	1.15
0.71	3.80	2.20	1.60
1.12	6.00	3.50	2.52

Once the test bearing was cleaned and mounted on the assembly, oil was run for several minutes before starting the machine. Then with the system still unloaded the motor drive was started and the oil flow was set at 120 drops/min.

The test started by loading the bearing with a constant load of 541N (1.68 MPa) and increasing the speed from 0.15 to 1.12 m/s at regular intervals of 10 minutes. For each period of time friction forces were measured so that a first $\mu - vs - \frac{\eta N}{P}$ curve could be obtained.

Repeating the same procedure at loading stresses of 2.88 MPa (930N) and 4.00 MPa (1285N), various curves were plotted until a constant curve was obtained.

It was realised that this method of obtaining Stribeck curves was a measure of the running-in performance of the test bearing material.

Wear Evaluation

In the previously determined Stribeck curves, the examination 0.15 m/s speed and 4.00 MPa (1285N) load, was found to correspond to a high friction boundary regime for all alloys. However, keeping the system running at this regime was found to be dependent on the lubrication rate.

In order to evaluate wear, new bearings were run for a period of 12 hours at a shaft speed of 0.15 m/s and a loading stress of 4.00 MPa, maintaining a constant a coefficient of friction of 0.10 - 0.15 by adjusting the flow of lubricant. Temperature rise was also monitored with a thermocouple attached to the bearing wall. Wear was evaluated by mass losses measurements.

5.4 EXPERIMENTAL RESULTS

Stribeck Curves

The specifically designed rig for sleeve bearing testing was demonstrated to be able to reliably produce both fluid and boundary lubrication regimes by varying the bearing parameter $\frac{\eta N}{P}$. Since the position of Stribeck curves was dependent on the roughness of the mating surfaces, it was possible to follow a step by step running-in process of the alloys until variations of friction coefficient as a function of bearing parameter were constant.

Figures 122 to 125 show the running-in curves for bronze, ZA-27, Super Cosmal and HAZCA bearings respectively. The running-in ability of the three zinc aluminium-based alloys was superior than that of the bronze material. However, ZA-27 bearings showed coefficients of friction significantly lower than those of the Super Cosmal and HAZCA bearings. Also the critical bearing parameter at which hydrodynamic lubrication started, was the smallest for ZA-27 bearings. Super Cosmal and HAZCA bearings showed slightly bigger values of critical bearing parameter. Bronze in turn, presented the biggest value of critical $\frac{\eta N}{P}$.

Final Stribeck curves confirmed that at a bearing parameter of 0.36×10^{-3} (m) (4.00 MPa stress, 0.15 m/s speed) a condition was attained in which the oil film broke down and the coefficient of friction was correspondingly high due to metallic contact in the bearing-shaft interface.

Wear Evaluation

As mentioned in the test procedure, wear was evaluated through mass loss measurements when bearings were run for a period of 12 hours under poor lubricating conditions keeping coefficients of friction in the range of 0.10 - 0.15.

Experiments were performed in duplicate. Discrepancies were of the order of 5% in zinc-based bearings and 10% in bronze bearings. The average value of mass losses, together with the volumetric wear rate calculated using the materials' density are presented in Table 10.

Table 10. Mass and volumetric wear rate of Super Cosmal, HAZCA, ZA-27 and bronze alloy in a bearing simulation test.

Bearing Alloy	Mass Loss mg/12h	Volumetric Wear mm^3/h
Super Cosmal	6.88	0.168
HAZCA	8.20	0.202
ZA-27	10.47	0.175
Bronze	253.18	2.34

Increments of bearing temperature during the test are shown in Figure 126. The first two hours of test reflected also the running-in ability of the alloy.
The zinc aluminium-based alloys ran-in rapidly and tended to come into a low friction regime so that a reduction of lubricant flow from 120 drop/min to 60 drop/min was necessary. On the contrary, for bronze bearings the lubrication rate was increased to 160 drop/min to avoid excessive temperature rise and coefficients of friction higher than 0.15.

Finally, after termination of the tests, the test shafts were inspected and the surface roughness of the track measured. Tracks corresponding to ZA-27 presented no particular feature and no difference in roughness compared with the rest of the test shaft. Tracks corresponding to Super Cosmal and HAZCA appeared evidently marked with an increase in surface roughness from 0.3 to 0.35 μm c.l.a. In the case of bronze bearings roughness of the wear track on the shaft also suffered an increase to 0.35 μm c.l.a. but this was due to bronze transfer.

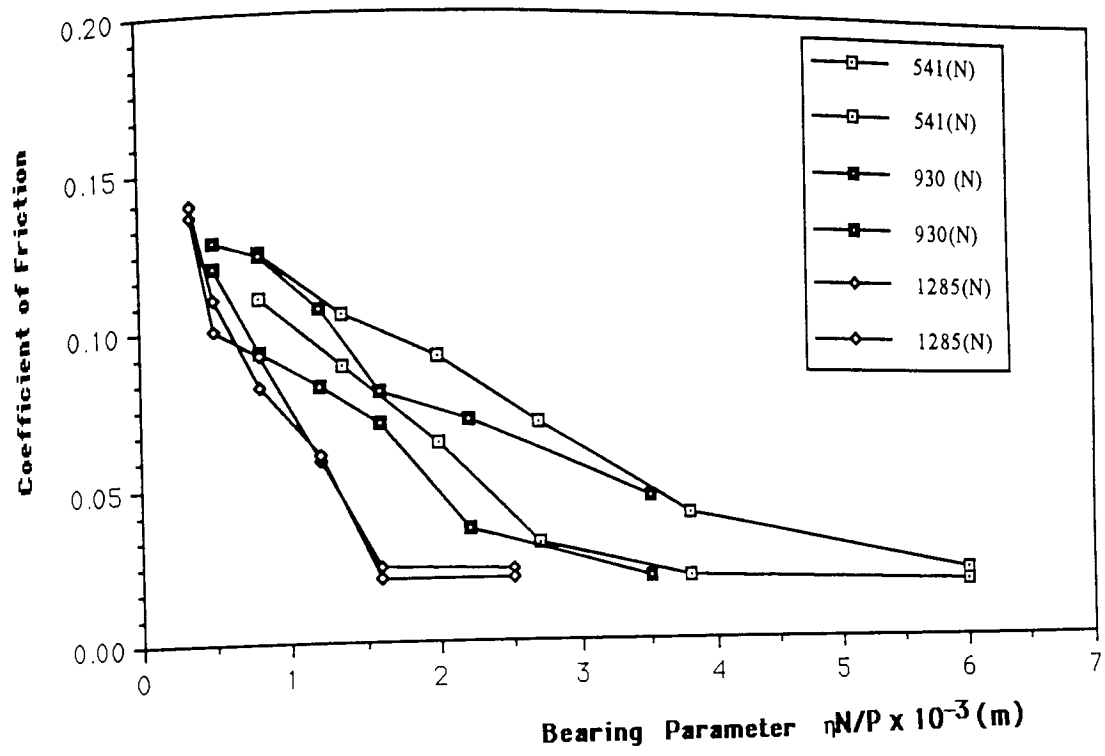

Figure 122. Stribeck curves for bronze bearing.

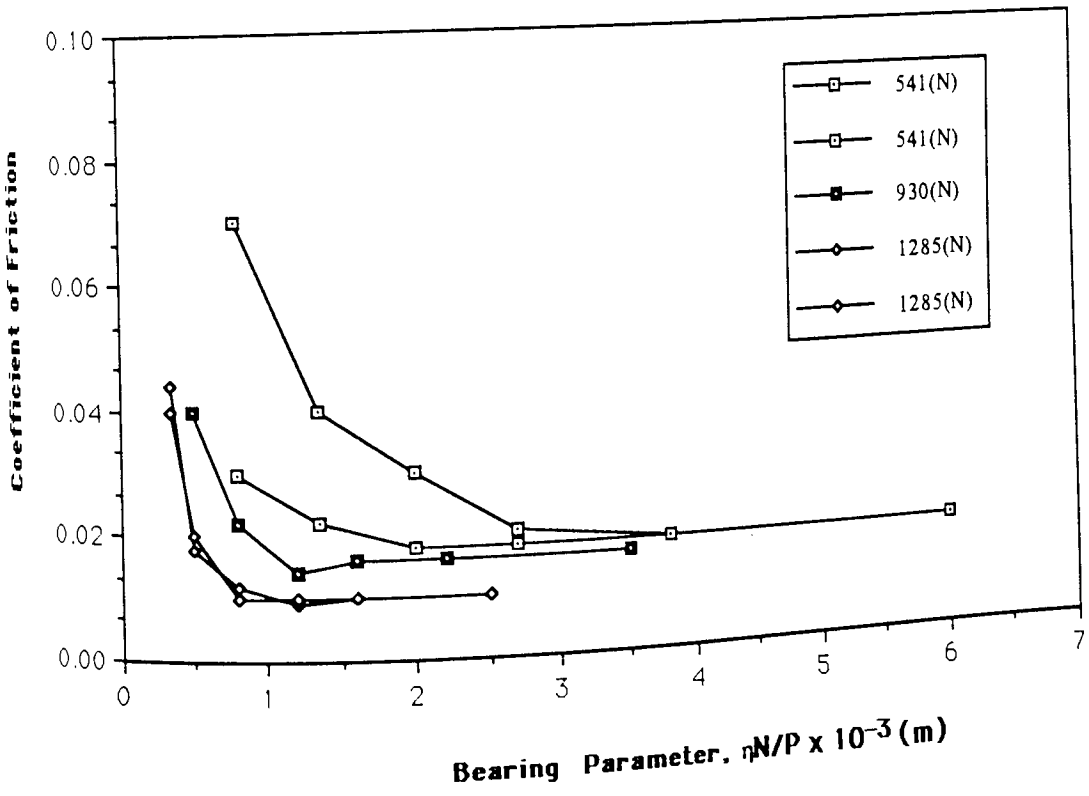

Figure 123. Stribeck curves for ZA-27 bearings.

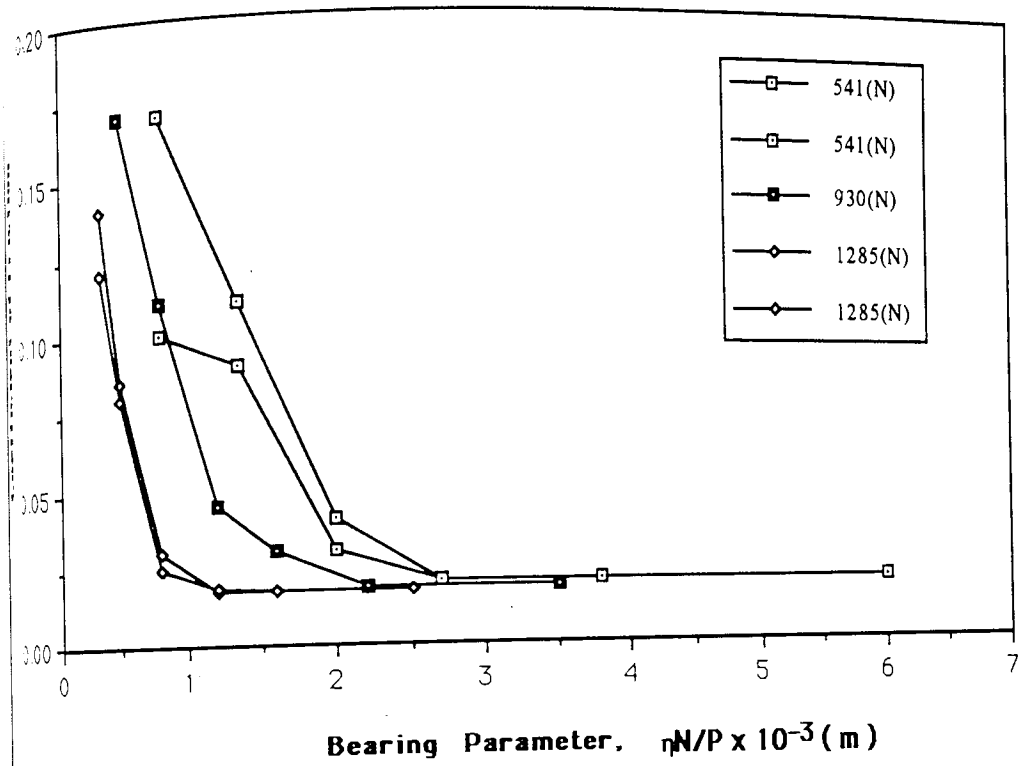

Figure 124. Stribeck curves for Super Cosmal bearings.

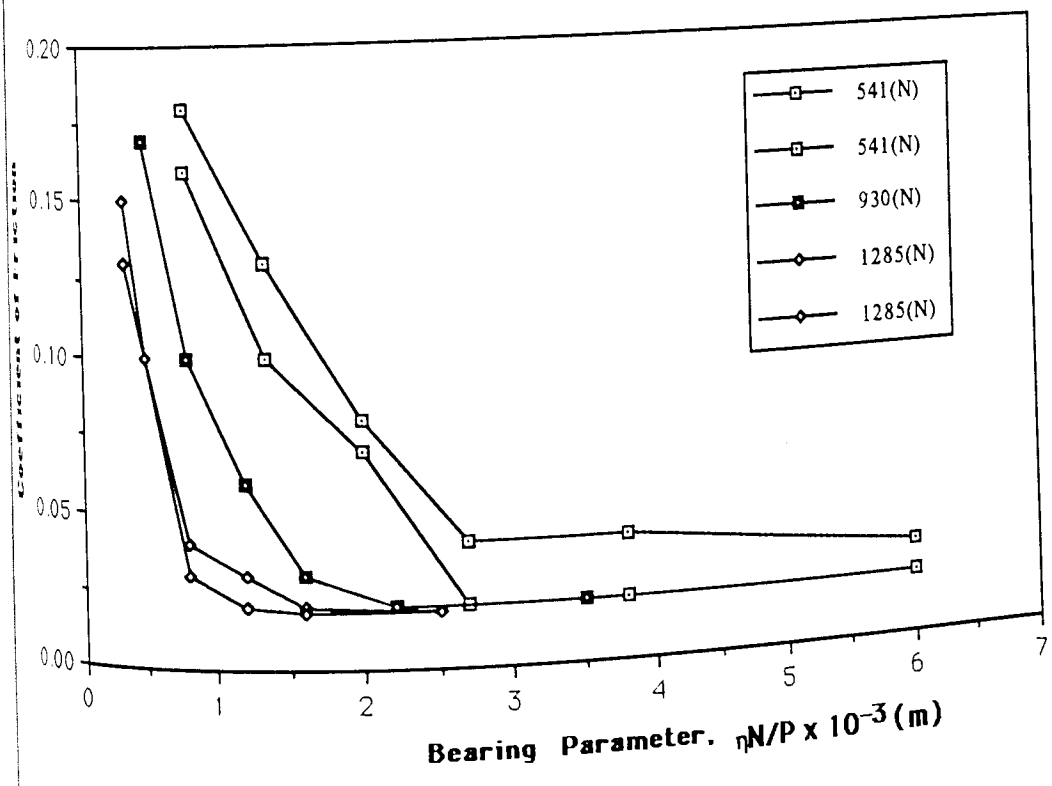

Figure 125. Stribeck curves for HAZCA bearings.

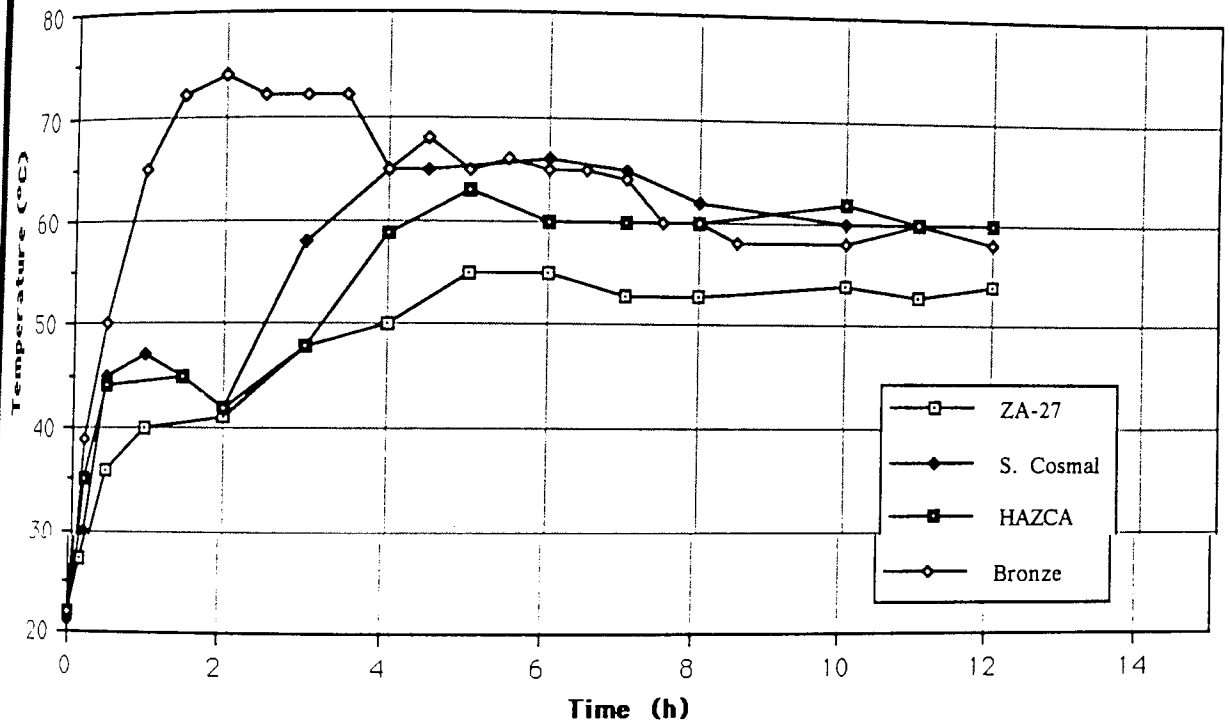

Figure 126. Bearing temperatures for Super Cosmal, HAZCA, ZA-27 and bronze bearings tested under similar conditions of load and speed.

5.5 DISCUSSION

Stribeck curves showed that lower speeds and higher loads at poor lubrication conditions can be tolerated well by the Super Cosmal and HAZCA alloys similarly to the ZA-27 alloy.

In dry sliding tests mild wear of Super Cosmal, HAZCA and ZA-27 was attributed to an oxidational process which produced a protective film on the rubbing surface of samples. Oxidative mild wear of these alloys could occur under lubricated conditions due to the large amounts of dissolved oxygen in the lubricant as well as the oxygen present in the surroundings.

Unfortunately a detailed study of wear debris has not been carried out in the present work but a qualitative observation of the lubricant coming out from zinc-aluminium bearing showed the presence of only very fine dark particles typical of oxidational mild wear of metals. Also black patches of impregnated oxide film were evident on the wear surface of the test bearings. In contrast, oil from bronze bearings presented small flakes of metallic material probably due to a machining process in which shaft asperities continuously removed finely divided material from the wearing surface.

Although wear rates of Super Cosmal and HAZCA bearings were comparable with those of ZA-27 bearings, their coefficients of friction were higher. This was due to the presence of hard silicon particles which probably were standing proud of the matrix. As a result of higher coefficients of friction equilibrium bearing temperatures were also higher in Super Cosmal and HAZCA bearings than those in ZA-27 bearings.

The fact that HAZCA alloy exhibited the same behaviour as the Super Cosmal alloy, showed that a larger content of silicon in zinc aluminium-based alloys did not increase their wear resistance.

Although a slight damage of the shaft by the micro-abrasion action of silicon particles was noticed, the beneficial effect of silicon was to prevent scuffing under severe conditions of metal to metal sliding contact.

5.6 CONCLUSIONS

1. Super Cosmal and HAZCA bearings were demonstrated to run-in similarly to ZA-27 alloy under the same conditions of lubrication.

2. In full bearing test, a loading stress of 4.00 MPa and a shaft speed of 0.15 m/s under conditions of lubricant starvation were satisfactorily tolerated by Super Cosmal and HAZCA bearings in a similar manner as the ZA-27 alloy. The experimental conditions were too severe for the bronze bearing material.

3. Under identical load, speed and lubrication conditions, Super Cosmal and HAZCA bearings were found to run at higher coefficients of friction than ZA bearings.

4. No differences in behaviour as bearing materials were found between the Super Cosmal and the experimental HAZCA alloy.

CHAPTER 6

GENERAL DISCUSSION AND CONCLUSIONS

The objective of the present work was to study the suitability of two high aluminium zinc-base alloys as materials in plain bearing applications mainly from the viewpoint of their wear behaviour in dry and boundary-lubricated conditions. Also as important was considered the determination of their mechanical properties, the analysis of their metallurgical structure and their casting behaviour when they are produced by the sand casting process.

Bearings must have sufficient mechanical strength to support the load. Tensile strength at ambient temperature of the Super Cosmal and HAZCA alloy was found to be 310 and 270 MPa respectively. These values are superior to Al-based bearing materials in which the U.T.S. ranges from 90 to 200 MPa [65]. They are also superior to the traditional bronze (SAE 600) (240 MPa), but inferior to the ZA-27 alloy for which U.T.S. was 350 MPa. If the comparison is made in terms of strength to weight ratio the result is very favourable to the Super Cosmal and HAZCA alloys (Table 6).

Considering a reported strength value of 245 MPa for a Zn-60% Al binary [2], it is clear that the combined effect of silicon and copper was beneficial in increasing strength to 310 MPa in the Super Cosmal alloy. The microstructure of this alloy showed that silicon was mainly associated with Al-rich α phase in strengthening this matrix. On the other hand, the zinc-rich η phase was strengthened by the concentration of copper-rich particles in that area. The HAZCA alloy did not achieve higher strength than the Super Cosmal in spite of its higher content of silicon and copper. It seems that the presence of larger amounts of primary silicon and other intermetallics were detrimental to the strength of the alloy.

The low impact strength shown by both alloys may be a drawback in respect of their suitability for bearings supporting fluctuating loads but not so for steady loaded bearings for which they are perfectly suitable.

Low wear rates and low friction are important selection criterion for bearings especially when load is supported by solid-to-solid contacts, i.e. boundary lubrication. In the sleeve bearing simulation tests where a light spindle oil with no additives was used as a lubricant, Super Cosmal and HAZCA bearings were found to perform similarly to ZA-27 bearings and far better

than bronze (SAE 660) test bearings. Wear rates for the zinc-aluminium-based materials were very low in a relatively prolonged test at coefficients of friction as high as 0.10 - 0.15.

There are two main reasons for the satisfactory behaviour of the Super Cosmal and HAZCA alloys as bearing materials;

a) The combined anti-scuffing action of copper-rich intermetallic phases ε and T' and silicon particles standing proud of the matrix.

b) The build-up of a surface film of oxides and other elements that act as protection against metallic contact. This fact was verified in exaggerated conditions of dry sliding. High loading stresses at low sliding speeds were found to be tolerated by Super Cosmal, HAZCA and ZA-27 test pins due to an oxidative wear mechanism. The predominance of this mechanism depends on the stability of the surface film and this in turn, appeared to be dependent on the strength of the underlying metal. ZA-27 being the strongest and toughest preserved the oxidative mechanism at more demanding conditions, for example at a sliding speed of 1 m/s, at which the Super Cosmal and HAZCA alloy experienced a transition from mild to severe wear as a consequence of surface film breakdown. The transitional load was higher for the stronger Super Cosmal. The virtue of the zinc-aluminium materials in boundary lubricated conditions was to maintain as prevalent the oxidative mechanism of wear.

Friction, particularly in boundary lubricated journal bearings is a measure of the tendency towards microwelding and scuffing. ZA-27 bearings showed the lowest friction coefficients of all material at constant lubricant flow hence the temperature rise on the bearing journal system was also the lowest. The friction of silicon containing bearings was higher due to the sliding contact of hard silicon particles with the steel counterface as a result of which a slight increase in surface roughness in the journal occurred.

Super Cosmal and HAZCA are multiphase alloys, the structure of which consisted mostly of a hard Al-rich matrix with small amounts of soft zinc-rich phase and discrete hard particles. The dirt embeddability of those structures is not as good as that of the ZA-27 alloy since occasional signs of abrasion on the bearing surface were noticed.

It has been demonstrated that wear in ZA alloys was dependent on the amount and distribution of copper-rich ε particles in the structure [52] so that sand castings were more wear resistant than permanent mould or continuously casting materials. Sand casting of Super Cosmal and HAZCA alloy produced copper-rich ε and T' particles along with hard silicon particles, but the influence of these particles on strengthening the matrix seem to be more important for the overall wear behaviour of these alloys.

The ease of fabrications is another important factor on bearing material selection. Provided careful pattern and risering design is applied, sand casting of high aluminium zinc-based alloys was found not to be problematic due to the positive influence of silicon on reducing the temperature range of solidification, increasing fluidity, improving feeding efficiency, reducing gravity segregation and eliminating underside shrinkage.

The main general conclusions that could be drawn from this work are the following:

1. The experimental HAZCA alloy showed an equivalent behaviour with Super Cosmal alloy in respect of both casting and tribological tests.

2. Super Cosmal and HAZCA alloys proved to be a viable alternative as bearing materials. Their wear resistance under boundary lubrication conditions were found to be practically equal to that of the ZA-27 alloy and superior to that of bronze bearings.

   Features such as low wear rates, very fine wear debris and an absence of scuffing were typical of a mild oxidative type of wear in lubricated conditions.

3. The above mentioned oxidative mechanism was responsible for a mild type of wear in zinc-aluminium alloys in dry sliding tests at conditions of low speeds and high loads. A surface layer complex in structure and mainly comprised of aluminium, iron and zinc oxides and metallic or intermetallic particles coming from the mating surfaces was found to the predominate in the area of contact. Finely divided wear debris resulted from the removal of this material by delamination.

4. The metallurgical structure of the HAZCA alloy differed from the structure of the Super Cosmal in that it contained less ß phase, the decomposition of which had been retarded by the influence of magnesium, and also in the presence of a larger number of primary silicon particles, ε and T' particles. This alloy also contained curved blades of an Fe-Si-Zn compound which were absent from Super Cosmal

   The general structure of both alloys consisted of a multiphase dendritic structure of predominant cored Al-rich matrix surrounded by decomposed ß phase and pools of interdendritic zinc-rich η phase. Primary and eutectic silicon particles appeared distributed throughout the structure mainly in Al-rich areas, and copper-rich ε and T' particles appeared associated with zinc-rich eutectic pools.

5. The HAZCA alloy exhibited lower tensile strength than the Super Cosmal, (270 MPa and 310 MPa respectively). They both were found to have low toughness (7J), but the HAZCA alloy was harder than the Super Cosmal. The tensile strengths of both alloys compared well with many commercial aluminium-based alloys but were inferior to that of the ZA-27 alloy.

   Furthermore, the strength of HAZCA and Super Cosmal alloys were shown to be strongly dependent on porosity content and microstructural fineness.

6. When cast in sand moulds, proper directional solidification, rapid cooling rates and effective melt degassing constituted the most important factors to achieve soundness in Super Cosmal and HAZCA castings, and hence to obtain the best of their properties. The castability of both these alloys was superior to ZA-27, but they were more sensitive to the presence of porosity.

7. Taking into account their low specific gravity, the high aluminium zinc-based alloys had the highest strength to weight ratios of any zinc alloy.

REFERENCES

1. **R.J. Barnhurst**
   Zinc and Zinc Alloys.
   ASM Metals Handbook 10th Edition, 1990, pp.527-542.

2. **Y. Mae and A. Sakono-Oka**
   New Die Casting Alloy with High Damping Capacity.
   Metallurgical Society of AIME, 1985, Paper No. A85-18.

3. **E. Gervais, H. Levert and M. Bess**
   The Development of a Family of Zinc-Based Foundry Alloys.
   AFS Transactions, Vol 88, 1980, pp.183-194.

4. **H. Nieswaag**
   Some Developments in Casting Technology.
   Giesserei, Vol 74, 1987, pp. 11-115.

5. **C. R. Loper, Jr. and T.E. Prucha**
   Feed Metal Transfer in Al-Cu-Si Alloys.
   AFS Transactions, Vol 98 1990, pp. 845-853.

6. **J. Campbell**
   Castings.
   Butterworth-Heineman, 1991.

7. **M. Sahoo and L.V. Whiting**
   Foundry Characteristics of Sand Cast Zn-Al Alloys.
   AFS Transactions, Vol 92, 1984, pp. 861-870.

8. **F. Habiby and M.J. McNallan**
   Macrosegregation and Underside Shrinkage in Sand Cast Zinc 27% Aluminium Alloy (ZA-27).
   AFS Transactions, Vol. 92, 1984, pp. 263-269.

9. **R.J. Barnhurst, E. Gervais and F.D. Bayles**
Gravity Casting of Zinc-Aluminium Alloys Solidification Behaviour of ZA-8, ZA-12 and ZA-27.
AFS Transactions, Vol. 91, 1983, pp. 569-584.

10. **O. Ayik, M. Ghoreshy, M. Sahoo and R.W. Smith**
Solidification and Foundry Studies of Zn/Al Alloys.
Journal of Crystal Growth, 1986, pp. 594-601.

11. **R.J. Barnhurst and E. Gervais**
Gravity Casting of Zinc-Aluminium (ZA) Alloys: Dependence of Mechanical Properties on Soundness, Microstructure and Inclusion Content.
AFS Transactions, Vol. 93, 1985, pp. 591-601.

12. **M. Sahoo, L.V. Whiting and D.W.G. White**
Control of Underside Shrinkage in Zinc-Aluminium Foundry Alloys by the Addition of Trace Elements.
AFS Transactions, Vol. 93, 1985, 475-479.

13. **P.R. Beeley**
Foundry Technology.
Butterworths, 1980.

14. **A. Potervin and P. Bastien**
Fluidity of Ternary Alloys.
Journal Institute of Metals , 1934, pp. 45-56.

15. **F.R. Mollard, M.C. Flemings and E.F. Niyama**
Understanding Aluminium Fluidity: The Key to Advanced Cast Products.
AFS Transactions, Vol. 91, 1983, pp. 647-652.

16. **G. Lang**
Giesseigenschaften und Oberflächenspannung von Aluminium un Binären Aluminiumlegierungen.
Part I, Aluminium, Vol. 48, No. 10, 1972, pp.664-672.

17. **R.J. Barnhurst, E. Gervais and F.D. Bayles**
Gravity Casting of Zinc-Aluminium Alloys Solidification Behaviour of ZA-8, ZA-12 and ZA-27. AFS Transactions, Vol. 91, 1983, pp. 569-584.

18. **M. Sahoo and L.V. Whiting**
Foundry Characteristics of Sand Cast Zn-Al Alloys.
AFS Transactions, Vol. 92, 1984, pp. 861-870.

19. **R.J. Barnhurst**
Gravity Casting Manual for Zinc-Aluminium Alloys.
Noranda Technology Centre, 1989, p. 13

20. **R.J. Barnhurst and D. Jacobs**
Gravity Casting of Zinc-Aluminium Alloys: Development of Foundry Parameters for Casting in Sand.
AFS Transactions, Vol. 96, 1988, pp. 321-328.

21. **S. Murphy and T. Savaskan**
Comparative Wear Behaviour of Zn-Al Based Alloys in an Automotive Engine Application.
Wear, 98, 1984, pp. 151-161.

22. **A. Kearney and E.L. Rooy**
Aluminium Foundry Products.
Metals Handbook, 9th Edition, pp. 123-126.

23. **G. Fortina**
Correlation Between Castability, Hot Tearing Tendencies and Solidification Properties of Aluminium Casting Alloys.
AFS International Cast Metals Journal, June 1980, pp. 25-29.

24. **H. Iwahori**
Behaviour of Shrinkage Porosity Defects and Limiting Solid Fraction of Feeding on Al-Si Alloys.
AFS Transactions, Vol. 93, 1985, pp. 443-452.

25. **M.C. Flemings, S.Z. Uram and H.F. Taylor**
Solidification of Aluminium Castings.
AFS Transactions, Vol. 110, 1960, pp. 670-684.

26. **G.R. Goldak and G. Parr**
A High-Temperature X-Ray-Diffractometer Study of the Zinc-Aluminium System in the Region 40-75 wt% Zinc.
Journal of the Institute of Metals, Vol. 92, 1963, pp. 230-233.

27. **J.E. Hatch**
Aluminium: Properties and Physical Metallurgy.
American Society for Metals, 1984, p.48.

28. **S.W.K. Morgan**
Zinc and its Alloys and Compounds.
Ellis Horwood Limited, 1985, p.159.

29 **L.A. Willey**
Aluminium-Copper-Zinc.
Metals Handbook, 8th Edition, Vol.8, American Society for Metals, 1973.

30. **S. Murphy**
Solid-Phase Reactions in the Low Copper Part of the Al-Cu-Zn System.
Z. Metallkunde, Vol.71, 1980, pp. 96-102.

31. **S. Murphy**
The Structure of the T' Phase in the System Al-Cu-Zn.
Metal Science, Vol.9, 1975, 163-168.

32. **Y. Zhu**
Phase Relationships in Zn-Al Based Alloys.
PhD Thesis. The University of Aston in Birmingham, 1983.

33. **N. Mykura, Y.H. Zhu and S. Murphy**
Solid-State Reactions in Zn-Al Based Alloys.
Canadian Metallurgical Quarterly, Vol.25, No.2, 1986, pp. 151-159.

34. **V.A. Toldin, G.V. Kleshchev, D.V. Shumilov and A.J. Sheynkman**
A Generated Scheme of the Sequence of Metastable Phases in Al-Zn Alloys.
Fiz. Metal. Metalloved, Vol.40, No.6, 1975, pp. 1223-1226.

35. **W.V. Youdelis and G.W. Dallen**
Effect of Magnesium and Copper on the Decomposition Kinetics and Mechanical Properties of Zinc-Aluminium Alloys.
Conference of Metallurgists. The Canadian Institute of Mining and Metallurgy,1966, Paper 40.

36. **R.J. Barnhurst and E. Gervais**
Gravity Casting of Zinc-Aluminium (ZA) Alloys: Dependence of Mechanical Properties on Soundness, Microstructure and Inclusion Content.
AFS Transactions, Vol. 93, 1985, pp. 591-601.

37. **D. Nevison**
Zinc and Zinc Alloys.
Handbook of Metals, 9th Edition, p.787.

38. *Zinc as an Engineering Material.*
Leaflet of the Brock Metal Company.

39. **J.C. Weiss and C.R. Loper**
Primary Silicon in Hypereutectic Aluminium-Silicon Casting Alloys.
AFS Transactions, Vol. 95, 1987, pp. 51-62.

40. **H. Fredrikson, H. Hiller and N. Lange**
The Modification of Aluminium-Silicon Alloys by Sodium.
Journal of the Institute of Metals, Vol.101, 1973, pp. 285-299.

41. **S. Murphy, T. Savaskan**
Metallography of Zinc-25%Al Based Alloys in the As-Cast and Aged Conditions
Pract. Met. 24, 1987, pp. 204-221.

42. **A.M. Zahra, C.Y. Zahra, J. Dutkiewicz and R. Ciach**
The Influence of Cu and Mg Additions on the Decomposition of Al (40-50)% Zn Alloy during Isothermal and Continuous Heating.
Journal of Materials Science, 25, 1990, pp.391-398.

43. **R.D. Arnell, P.D. Davies, J. Halling and T.L. Whomes**
Tribology. Principles and Design Applications.
McMillan Education, 1991.

44. **T.S. Eyre**
Wear Characteristics of Metals.
Tribology International, October 1976, pp. 1-10

45. **D.A. Rigney, L.H. Chen, M. Naylor and A.R. Rosenfield**
Wear Processes in Sliding Systems.
Wear, 100, 1984, pp. 195-219.

46. **M.B. Peterson**
Wear Testing Objectives and Approaches.
Source Book on Control Technology. American Society of Metals, 1978, pp. 40-48

47. **H. Czichos**
A System Analysis Data Sheet for Friction and Wear Tests and an Outline for Simulative Testing.
Source Book on Control Technology. American Society of Metals, 1978, pp. 29-39.

48. **S. Jahanmir**
On the Wear Mechanisms and the Wear Equations Fundamentals of Tribology.
Proceedings of the International Conference on Tribology. The MIT Press, 1978, pp.455-467.

49. **T.F.J.Quinn**
The Classification, Laws, Mechanisms and Theories of Wear Fundamentals of Tribology.
Proceedings of the International Conference on Tribology. The MIT Press, 1978, pp.477-491.

50. **F.A. Barwell**
The Contribution of Particle Analysis to the Study of Wear of Metals.
Wear, 9, 1983, pp.167-181.

51. **J. Halling**
Principles of Tribology.
The MacMillan Press Limited, 1983.

52. **R.J. Barnhurst and J.C. Farge**
Evaluation of ZA-12 and ZA-27 for Bearing Applications.
Proceedings International Symposium on Zinc-Aluminium (ZA) Casting Alloys, 1986, pp.85-105.

53. **V.G.S. Mani, P. Sriram, N. Raman and S. Seshan**
Tribological Studies on Cast Zinc-Aluminium Alloys.
AFS Transactions, Vol.96, 1988, pp.525-532.

54. **R.J. Marczak and R. Ciach**
Tribological Properties of the Concentrated Al-Zn Alloys.
Proc. 1st European Tribology Congr., London, 1973, pp.223-227.

55. **A.D. Sarkar**
Wear of Aluminium-Silicon Alloys.
Wear, 31, 1975, pp.331-343.

56. **R. Shivanath, P.K. Sengupta and T.S. Eyre**
Wear of Aluminium-Silicon Alloys.
Source Book on Wear Control Technology. American Society of Metals, 1978, pp.186-192.

57. **C. Beesley and T.S. Eyre**
Friction and Wear of Aluminium Alloys Containing Copper and Zinc.
Tribology International. April 1976, pp.63-69.

58. **F.A. Davis and T.S. Eyre**
Wear of Plain Bearing Materials with Particular Reference to Role of Soft Phases.
Materials Science and Technology, Vol.7, 1991, pp.746-756.

59. **J.F. Archard**
Contact and Rubbing of Flat Surfaces.
Journal of Applied Physics, Vol.24, 1953, pp.981-988.

60. **F.P. Bowden and D. Tabor**
The Friction and Lubrication of Solids - Part 2.
Oxford University Press, 1964.

61. **F.T. Barwell**
Bearing Systems. Principles and Practice.
Oxford University Press, 1979.

62. **W.E. Campbell**
Boundary Lubrication.
Boundary Lubrication - An Appraisal of World Literature, ASME. Edited by F. Ling, E. Klaus and R. Fein, 1969, pp.87-89.

63. **E. Rabinowicz**
Friction and Wear of Materials.
John Wiley and Sons, New York, 1965.

64. **D.F. Moore**
Principles and Applications of Tribology.
Pergamon Press, 1975.

65. **S.N. Tiwari, J.P. Pathak and S.L. Malhortra**
Aluminium Alloys as Plain Bearing Materials - An Overview.
Light Metals: Science and Technology, 1985, p.139-158.

66. **A.W.J. De Gee**
Selection of Materials for Lubricated Journal Bearings.
Wear, 36, 1976, pp.33-61.

67. **T. Savaskan and S. Murphy**
Mechanical Properties and Lubricated Wear of Zn-25 Al-based Alloys.
Wear, 116, 1987, pp.211-224.

68. **Ph. Delneuville**
Tribological Behaviour of ZnAl Alloys (ZA27) compared with Bronze When Used as a Bearing Material with High Load and Very Low Speed.
Wear, 105, 1985, pp.283-292.

69. **A.J. Davis and T.V. Krok**
Sleeve Bearings - Development of a Testing Machine.
Proceedings Inst. Mech. Engrs., 171, 1958, p.961.